

Ekman Currents In The Antarctic Circumpolar Current

by

Christopher Roach

Bachelor of Science & Bachelor of Antarctic Studies (First Class Honours)
University of Tasmania

A thesis submitted in partial fulfilment of the requirements of the
Doctor of Philosophy (Quantitative Marine Science),
Institute for Marine and Antarctic Studies (IMAS)
University of Tasmania
October 2014



Declaration of Originality

This thesis contains no material which has been accepted for a degree or diploma by the University or any other institution, except by way of background information and duly acknowledged in the thesis, and to the best of my knowledge and belief no material previously published or written by another person except where due acknowledgement is made in the text of the thesis, nor does the thesis contain any material that infringes copyright.

Christopher Roach

October 2014

Authority of Access

This thesis may be made available for loan and limited copying and communication in accordance with the Copyright Act 1968.

Christopher Roach

October 2014

Table of Contents:

Abstract	xi
Acknowledgements	xiv
1. Introduction	
1.1 Background	1
1.2 Motivation and Aims	2
1.3 Thesis Outline	3
2. Background and Literature Review	
2.1 The Southern Ocean: Circumpolar Structure and Dynamics	5
2.2 Subsurface Profiling Floats	10
2.3 Ekman Theory	13
2.4 Previous Observational Studies	19
3. Detecting and Characterizing Ekman Currents	
3.1 Introduction	54
3.2 Datasets	54
3.3 Method	59
3.4 Observed Ekman Spirals	65
3.5 Ekman Transport	71
3.6 The Effect of Stratification On Ekman Currents	83
3.7 Discussion and Conclusions	93
4. Examining Wind Driven Flow in the Frequency Domain	
4.1 Overview and Introduction	95
4.2 Datasets	96
4.3 Rotary Spectral Analysis	98
4.4 The Models	100
4.5 Method	105
4.6 Results: ADCP Observations	112
4.7 Results: EM-APEX Floats	122
4.8 Wind Energy Input	134
4.9 Conclusion	136
5. Numerical Modelling of Ekman Currents	
5.1 Introduction	141
5.2 The Models	141
5.3 Performance Metrics	153
5.4 Model Configuration	155
5.5 Shipboard ADCP Results	157
5.6 EM-APEX Results	170
5.7 Explaining The Differences In Model Performance	176
5.8 Conclusion	182
6. Discussion and Conclusions	
6.1 Summary	185
6.2 Discussion and Conclusions	188
6.3 Further Work	193
7. References	197
8. Appendix 1: Supplementary Material For Chapter 3	202
9. Appendix 2: Supplementary Figures For Chapter 5	209

List of Figures:

Chapter 2:

Figure 2.1: Major currents and other features of the Southern Ocean.	5
Figure 2.2: Schematic map of the principal fronts of the Southern Ocean.	6
Figure 2.3: Schematic diagram of the overturning circulation.	8
Figure 2.4: Bathymetry (Smith and Sandwell, 1997) of the Kerguelen Plateau with the major fronts and topographic features marked.	9
Figure 2.5: Schematic of flow in the Kerguelen Plateau region.	10
Figure 2.6: Outline of a typical Argo float cycle	12
Figure 2.7: Mean velocity spiral from 9 profiles taken over 6 periods of steady drift between the 8 th of July and the 3 rd of September 1958.	20
Figure 2.8: Coherence (top) and phase (bottom, positive indicates clockwise rotation) between 10m level and all other depths.	22
Figure 2.9: Daily mean velocities relative to Flip (top) and corrected for Flip's drift velocity (bottom).	23
Figure 2.10: Coherence (top) and phase (bottom, positive indicates clockwise rotation) between wind stress and velocity shear.	24
Figure 2.11: Histograms of the angle between wind direction and drifter heading stratified by month (left) and by wind speed (right).	26
Figure 2.12: Drifter trajectories.	28
Figure 2.13: Mean observed Ekman profile (A) compared with output from a numerical model incorporating density stratification (B). Mean transport estimated from observations compared with that estimated from the wind stress using the 'classical' Ekman transport equations (C).	31
Figure 2.14: Mean observed (top) and simulated (bottom) current profiles for data stratified by time of day into daytime (0800-2000 local time) and night time (2000-0800 local time).	32
Figure 2.15: Mean diurnal current cycle at 5m depth (observed, left; modelled, right).	33
Figure 2.16: Cross-basin transport per unit depth.	35
Figure 2.17: Basin integrated transport per unit of mixed layer depth.	36
Figure 2.18: Mean cross-track ageostrophic velocity plotted as a function of depth normalized by mixed layer depth (MLD) and thermocline depth (TTC).	37
Figure 2.19: Transfer functions from FASINEX in a wind relative reference frame (downwind equating to the x axis).	40

Figure 2.20: Observed (solid vector) and theoretical (dashed vector) Ekman transport.	42
Figure 2.21: Observed mean Ekman spiral (left) and theoretical Ekman spirals computed from decay scales estimated amplitude decay (right, top) and the rate of rotation (right, bottom).	43
Figure 2.22: Eddy viscosity profile inferred via Equation 2.7 from observed shear and stress.	44
Figure 2.23: Observed mean current profile (solid black vectors) and mean wind stresses (Nm^{-2}) from four reanalysis products.	45
Figure 2.24: Observed mean current profile (solid black vectors) and mean transports computed from four reanalysis products.	46
Figure 2.25: Mean eddy viscosity profile inferred from observed mean stress and shear.	47
Figure 2.26: Schematics of the 9 conceptual models from Elipot and Gille (2009).	48
Figure 2.27: Estimates of eddy viscosity (a); viscosity gradient (b) and boundary layer depth (c) for all models; error bars indicate mean absolute deviation. Model performance as measured by the minimum cost function value (d).	50
Figure 2.28: An example transect across the Drake Passage showing velocities (ms^{-1}) obtained inferred from density profiles (a) or obtained from ADCP observations (b and c).	51
Figure 2.29: Mean profile of log current magnitude and phase (a, relative to the shallowest observation) using a constant geostrophic velocity (small symbols, dashed lines) or a constant geostrophic shear (large symbols, solid lines). Hodograph and standard error ellipses (b) for the mean Ekman current profile.	52
Chapter 3:	
Figure 3.1: Location of profiles from 8 EM-APEX floats (coloured circles).	55
Figure 3.2: Time-mean inertial filtered profile (left) and an example inertial filtered profile (right).	56
Figure 3.3: Inertially filtered current speed (ms^{-1}) as a function of depth and time from floats 3760 (top) and 3762 (bottom).	57
Figure 3.4: Examples of hodographs of individual EM-APEX float velocity profiles displaying Ekman-like (top row) and reversed (bottom row) spirals.	66
Figure 3.5: Hodographs of observed Ekman spirals when averaged over all profiles (top row) and all profiles displaying Ekman-like spirals (bottom row).	67
Figure 3.6: Cumulative Distribution Function plots of fitted geostrophic shear ("Shear 1" green; "Shear 2" in black) and shear observed between 100m and 200m (purple).	69

Figure 3.7: Profiles of mean cumulative Ekman Transport relative to a reference level of 200m for the no shear; “shear 1” and “shear 2” cases.	72
Figure 3.8: Wind-relative vector plots of mean Ekman transport with 95% confidence intervals (ellipses).	73
Figure 3.9: Decomposition of Ekman transport by type of spiral present and normalized by the fraction of dataset each represent for no shear (a, left) and “shear 1” (b, right) cases.	74
Figure 3.10: Transport with reversed spirals and strong shear profiles removed at 14m depth.	75
Figure 3.11: Histogram of downwind transport (a, left) and scatter plot of downwind transport against zonal shear (b, right).	76
Figure 3.12: Time series of observed and simulated transport magnitude (top) and heading (bottom) for float 3760.	78
Figure 3.13: Wind-relative transport heading computed from synthetic Ekman spirals of varying “compression” from 1:1.5 to 1:3 for amplitude decay scales (Damp) between 25m and 93m.	79
Figure 3.14: Mean current speed profiles of Ekman currents and Stokes drift (a, left). Mean transport (vectors) at 14m with and without Stokes drift explicitly removed from each velocity profile (b, right).	81
Figure 3.15: Mean wind-relative 14m transport vectors using CERSAT (grey) and NCEP (red for wind only; blue for wind combined with correcting for Stokes Drift) winds for the “No Shear” and “Shear 1” cases (solid and dashed lines, respectively).	83
Figure 3.16: Profiles of Ekman transport by component (left; black lines indicate the crosswind component and grey lines indicate the downwind component) and magnitude (right) against fraction of Mixed Layer Depth for both the no shear case (top) and “shear 1” case (bottom).	85
Figure 3.17: Profiles of the difference in Ekman transport between 0.05MLD intervals against fraction of MLD by component (left; black lines indicate the crosswind component and grey lines indicate the downwind component) and magnitude (right) for both the no shear case (top) and shear case (bottom).	86
Figure 3.18: Profiles of R_i (left) and N^2 (right) for Float 3760 profile 42 (top) and Float 3761 profile 80 (bottom).	87
Figure 3.19: Maximum depth of ‘sustained’ dynamic instability plotted against mixed layer depth.	88
Figure 3.20: Ekman decay scales vs bulk Richardson Numbers (R_b) for decay scales estimated from current amplitude (left) and current rotation (right).	89
Figure 3.21: Mean viscosity amplitude profiles by depth (a, left) and multiple of MLD (b, right).	90

Figure 3.22: Mean viscosity profiles (no-shear left and shear right) as a function of fraction of mixed layer depth (MLD). Linear fits to viscosities in the mixed layer, ocean interior and over the entire profile are shown.	91
Figure 3.23: Mean viscosity profiles (no-shear left and shear right) as a function of fraction of mixed layer depth (MLD). Exponential fits to viscosities in the mixed layer, ocean interior and over the entire profile are shown.	92
Chapter 4:	
Figure 4.1: Ship track of the RV James Cook during the survey phase of the SOFINE voyage (blue) superimposed over ETOPO bathymetry (Amante and Eakins, 2009).	96
Figure 4.2: Schematics of the 9 spectral models. From Elipot and Gille (2009a).	101
Figure 4.3: 24m Ageostrophic current anticlockwise autospectra estimated from float observations approximating geostrophic currents with: (i) a combination of a deep reference velocity and shear as fitted in Chapter 3 (Red); (ii) surface currents estimated from AVISO SSH fields (grey) or (iii) a deep reference velocity (Blue).	109
Figure 4.4: 24m Ageostrophic current anticlockwise autospectra estimated from shipboard ADCP observations approximating geostrophic currents with: (i) surface currents estimated from AVISO SSH fields (red) or (iii) a deep reference velocity (blue).	110
Figure 4.5: ADCP current autospectra ($\log_{10}(\text{m}^2\text{s}^{-2}/\text{Cycle-per-day})$) vs depth.	113
Figure 4.6: Ship wind and 23.55m current autospectra.	113
Figure 4.7: The wind-current cross-spectrum at 23.55m (real component top, imaginary component bottom) estimated from shipboard observations.	114
Figure 4.8: Coherence squared as a function of both depth and frequency (top) and at 23.55m (bottom) for the shipboard ADCP data.	115
Figure 4.9: Fitted Parameters (k , panel 1; dk/dz panel 2; BLD panel 3) and cost function values (panel 4).	116
Figure 4.10: Absolute value of the observed transfer function at 23.55m and the transfer functions for the three best performing models.	117
Figure 4.11: Parameter estimates and cost function values for fits at constant frequencies of -1.4, -0.7, 0.7 and 1.4 CPD.	118
Figure 4.12: Observed and fitted transfer functions vs depth for frequencies of (from left to right) -1.4, -0.7, 0.7 and 1.4 CPD.	119
Figure 4.13: Parameters fits with low frequencies suppressed and using a deep reference velocity as a proxy for geostrophic currents.	120
Figure 4.14: Parameter estimates from constant depth spectral fitting at depths between 23.55m and 79.55m.	121
Figure 4.15: Wind stress and current autospectra at 24m estimated from EM-APEX float data.	123

Figure 4.16: EM-APEX mean current autospectrum ($\log_{10}(\text{m}^2\text{s}^{-2}/\text{Cycle-per-day})$) vs depth	123
Figure 4.17: EM-APEX wind-current cross-spectrum at 24m (real component top, imaginary component bottom).	124
Figure 4.18: EM-APEX wind-current cross-spectrum at 24m (real component top, imaginary component bottom) plotted over 1-2CPD.	124
Figure 4.19: Parameter fits and Cost Function Values for fits to EM-APEX float data.	125
Figure 4.20: Absolute value of transfer function vs depth for observed transfer functions (blue) and the best fitting models (red) at -1.4, -0.7, 0.7 and 1.4 CPD.	126
Figure 4.21: Absolute value of the observed transfer function (blue) and best performing model (1B, red) at 24m.	127
Figure 4.22: Fitted Parameters for 24m fits with (1) AVISO SSH derived geostrophic current; (2) AVISO SSH derived geostrophic current, low frequency ($<0.1\text{CPD}$) signal excluded; (3) 200m reference velocity as a proxy for geostrophic current.	128
Figure 4.23: Parameters fitted to ageostrophic data at 14m, 24m, 50m and 74m. The ageostrophic current was isolated from the observations using an AVISO SSH based geostrophic current.	129
Figure 4.24: Wind stress-autospectra obtained from shipboard instrumentation; CERSAT blended reanalysis-satellite winds and NCEP/NCAR reanalysis winds for the shipboard (top) and float data (bottom).	130
Figure 4.25: Parameter values and Cost Function Values for the constant depth fits to the EM-APEX float data using CERAT blended winds and NCEP reanalysis winds.	131
Figure 4.26: Bootstrap wind autospectra estimated from the EM-APEX float data colour-coded by the float ID number.	132
Figure 4.27: Mean wind autospectrum computed after removing bootstrap estimates obtained from the three short lived floats.	133
Figure 4.28: Comparison of fitted model parameters (viscosity in Panel 1; viscosity gradient in Panel 2 and BLD in Panel 3) when considering all EM-APEX data and when excluding the three short lived floats.	133
Figure 4.29: Estimated surface cospectra evaluated from model 1B; 23.55m observed transfer function and 23.55m cospectrum. Solid lines indicate anticyclonic frequencies and dashed lines	135
Figure 4.30: Cyclonic and anticyclonic co-spectra integrated from 0 to 2CPD. Thick lines denote anticlockwise (anticyclonic) frequencies and thin lines clockwise frequencies	136
Chapter 5:	
Figure 5.1: KS test statistics for velocity distributions at 23.55m depth (top) between all infinite depth Ekman models and shipboard observations. Correlations between observed and modelled mean velocity profiles (bottom) for all infinite depth Ekman models	158

Figure 5.2: PDF plots of 23.55m zonal (top) and meridional (bottom) velocities at viscosities between $2.5 \times 10^{-3} \text{m}^2 \text{s}^{-1}$ and $0.2 \text{m}^2 \text{s}^{-1}$.	160
Figure 5.3: QQ plots of zonal (top) and meridional (bottom) velocities. Symbols indicate quantiles at 0.5% intervals; dashed lines are extrapolated from a linear fit to the 1 st to 3 rd quartiles of the data.	162
Figure 5.4: Time mean wind-driven (top) and stokes-coupled (bottom) current profiles.	164
Figure 5.5: Modelled (grey curve) and observed current autocorrelation as a function of time-lag for the u (left) and v (right) components at 23.5m over a range of viscosities for three different LEMs (top, 'classical'; middle, shear coupled, and bottom, Stokes coupled).	165
Figure 5.6: KS test statistics for velocity distributions at 24m depth (top) between all finite depth Ekman models with a BLD of 105m and shipboard observations.	167
Figure 5.7: KS test statistics for velocity distributions at 24m depth (top) between all finite depth Ekman models with a BLD of 336m and shipboard observations. Correlations between observed and modelled mean velocity profiles (bottom) for all finite depth Ekman models with BLD of 336m.	168
Figure 5.8: KS test statistics for velocity distributions at 24m depth (top) between all infinite depth Ekman models and EM-APEX observations. Correlations between observed and modelled mean velocity profiles (bottom) for all infinite depth Ekman models.	171
Figure 5.9: KS test statistics for velocity distributions at 24m depth (top) between all 105m BLD Ekman models and EM-APEX observations. Correlations between observed and modelled mean velocity profiles (bottom) for all 105m BLD Ekman models.	172
Figure 5.10: KS test statistics for velocity distributions at 24m depth (top) between all 336m BLD Ekman models and EM-APEX observations. Correlations between observed and modelled mean velocity profiles (bottom) for all 336m BLD Ekman models.	173
Figure 5.11: PDF plots of u (left) and v (right) components of Ekman currents for float observations and all three PWP models.	174
Figure 5.12: QQ plots for all PWP models.	175
Figure 5.13: Histograms of wind stress amplitude for insitu shipboard winds (grey); NCEP/NCAR reanalysis winds interpolated onto the ship track (red) and NCEP/NCAR winds interpolated onto the float tracks (black).	177
Figure 5.14: KS test statistics for velocity distributions at 24m depth (top) between the infinite BLD Ekman model run with varying vertical resolution and ADCP observations. Correlations between observed and modelled mean velocity profiles (bottom) for the infinite BLD Ekman models	178

Figure 5.15: Time variable (top, measured by KS test statistic) and time-mean (bottom) model performance for wind forcing data with temporal resolutions between 5 minutes and 12 hours.	179
Figure 5.16: Time variable (top) and time mean (bottom) model performance of the constant viscosity infinite BLD linear Ekman model forced with time-series of various gridded wind products interpolated onto the shiptrack.	181
Appendix 1:	
Figure A1.1: Temperature ($^{\circ}\text{C}$) as a function of depth and time from floats 3760 (top) and 3762 (bottom).	202
Figure A1.2: Salinity (PSU) as a function of depth and time from floats 3760 (top) and 3762 (bottom).	203
Figure A1.3: Scatter plots of Ekman decay scales (D_{amp} , left; D_{rot} , right) as a function of wave period (top) and wave height (bottom).	204
Figure A1.4: Ekman decay scales obtained from current amplitude (D_{amp}) and rotation (D_{rot}) for all EM-APEX profiles plotted as a function of mixed layer depth (top) and thermocline depth (bottom).	206
Figure A1.5: Ekman decay scales obtained from current amplitude (D_{amp}) and rotation (D_{rot}) for all EM-APEX profiles plotted as a function of the 'bulk' N^2 (top) and maximum N^2 (bottom).	207
Appendix 2:	
Figure A2.1: Shipboard 105m BLD Linear Ekman Model Probability Density Functions for viscosities between 0.0025 and $0.2\text{m}^2\text{s}^{-1}$.	209
Figure A2.2: Shipboard 105m BLD Linear Ekman Model QQ plots of zonal (top) and meridional (bottom) velocities for viscosities between 0.0025 and $0.0425\text{m}^2\text{s}^{-1}$.	210
Figure A2.3: Shipboard 336m BLD Linear Ekman Model Probability Density Functions for viscosities between 0.0025 and $0.2\text{m}^2\text{s}^{-1}$.	211
Figure A2.4: Shipboard 336m BLD Linear Ekman Model QQ plots of zonal (top) and meridional (bottom) velocities for viscosities between 0.0025 and $0.0425\text{m}^2\text{s}^{-1}$.	212
Figure A2.5: Float Infinite BLD Linear Ekman Model Probability Density Functions for viscosities between 0.0025 and $0.2\text{m}^2\text{s}^{-1}$.	213
Figure A2.6: Float Infinite BLD Linear Ekman Model QQ plots of zonal (top) and meridional (bottom) velocities for viscosities between 0.0025 and $0.0425\text{m}^2\text{s}^{-1}$.	214
Figure A2.7: Float 105m BLD Linear Ekman Model Probability Density Functions for viscosities between 0.0025 and $0.2\text{m}^2\text{s}^{-1}$.	215
Figure A2.8: Float 105m BLD Linear Ekman Model QQ plots of zonal (top) and meridional (bottom) velocities for viscosities between 0.0025 and $0.0425\text{m}^2\text{s}^{-1}$.	216

List of Tables:

Chapter 2:

Table 2.1: Defining Features of Southern Ocean water masses.	7
--	---

Chapter 3:

Table 3.1: Number of Ekman-like spirals and reversed spirals detected in observed velocity profiles with either linear geostrophic shear or no shear assumed over the Ekman layer, and using either a Nelder Mead simplex search (NM) described in Section 3.3a or a least-squares fit (LS) described in Section 3.3b.	66
--	----

Table 3.2: Estimates of Mean Decay Scales; Eddy Viscosities and RMS residuals using the different methods outlined in section 3.3a and b.	68
---	----

Chapter 4:

Table 4.1: Best performing models and parameters for selected fits to the shipboard ADCP data	137
---	-----

Table 4.2: Best performing models and parameters for selected fits to the EMAPEX data.	138
--	-----

Chapter 5:

Table 5.1: Summary of the key features of all nine models tested during this study.	142
---	-----

Table 5.2: Properties of the four wind datasets tested in section 5.7c.	180
---	-----

Table 5.3: Viscosities corresponding to the minimum KS statistics (best time varying performance) and the maximum correlations between current profiles (best time mean performance) for all infinite depth models run with the insitu shipboard winds.	183
---	-----

Appendix 1:

Table A1.1: Correlations between wave parameters and Ekman decay scales and correlations for fits between wave parameters and the magnitude (\log_{10}) of Ekman decay scales.	205
--	-----

Table A1.2: Correlations between the observed Ekman decay scales and Ekman decay scales obtained from linear or exponential fits to parameters measuring depth and strength of stratification including: maximum N^2 ; the 'bulk' N^2 computed across the mixed layer; the bulk Richardson number; the depth of the thermocline and the depth of the mixed layer.	208
---	-----

Abstract:

The action of wind on the ocean surface results in the formation of Ekman spirals, as proposed by V.W. Ekman in 1905. The spirals display exponential decay of current speed and anticyclonic rotation with increasing depth. Observations of Ekman spirals are extremely rare, and there are few studies that test Ekman theory against observations. Here we present a unique array of velocity profiles from EM-APEX profiling floats, which we use to examine the nature of Ekman spirals in the Southern Ocean and test how well they are described by theory.

Classical Ekman theory assumes the momentum mixing within the upper ocean is set by a constant eddy viscosity. However, previous observational studies have found Ekman spirals to be compressed, with different viscosities estimated from current speed and rotation. This behaviour has been linked to surface trapping of Ekman currents (Price et al. 1987) or could arise due to a failure to consider depth varying geostrophic currents (Polton et al. 2013). We use 1400 profiles of velocity from EM-APEX floats, collected at the northern Kerguelen Plateau as part of the Southern Ocean FINE-structure (SOFINE) expedition during the Austral summer of 2008-9, to investigate whether a constant viscosity parameterization is the best way to represent momentum mixing in the upper ocean, or whether other methods such as a depth-varying viscosity or a mixing scheme linked with stratification (e.g. Price et al., 1986) are more effective. Previous studies of Ekman layer observations have examined either the raw observations, or models of momentum input in the spectral domain or in the time domain. In this study we use all three approaches to build a robust picture of Ekman spirals in the Southern Ocean and their response to wind forcing.

Ekman velocities were isolated from inertial and geostrophic currents in the absolute velocity profiles. Estimates of eddy viscosity and Ekman layer depth were separately obtained from profiles of current speed and heading. Assuming a vertically-uniform geostrophic current the Ekman layer depths from current heading were approximately twice as large as those from current speed decay. This degree of spiral compression has been observed in prior studies. Assuming a linear

geostrophic shear, constant viscosity estimates from current heading and speed decay converged towards a common value, implying a significant reduction in the compression of the Ekman spirals. Including geostrophic shear through the Ekman layer also increased the number of EM-APEX profiles displaying Ekman spiral-like behaviour from 224 to 441, and reduced the RMS velocity residual between fitted and observed spirals. There was no clear relationship between the observed viscosities and mixed layer depth or strength of stratification. This suggests that the compressed spirals observed in previous studies are due to aliasing the geostrophic current into the Ekman spiral (Polton et al. 2013), rather than surface trapping of Ekman currents associated with stratification.

Nine conceptual Ekman models were fitted to the observations in the spectral domain using the method of Elipot and Gille (2009). Application of the spectral technique to shipboard ADCP and *in situ* wind data indicated a constant viscosity model with a finite boundary layer depth (BLD) was the best performing model. Eddy viscosities agreed with Elipot's results for the same latitude bands but the optimal BLD was found to be deeper for the SOFINE region. Examination of Elipot's results indicate that within the latitude band of our study bootstrap, estimates of summer BLDs displayed a greater range of variability than the year round or winter BLDs. This suggests that the deeper BLDs observed in our study were principally due to the timing of SOFINE. A similar analysis using EM-APEX float data and blended reanalysis-scatterometer winds was inconclusive.

To test for the effects of time-varying wind forcing and stratification in the mixed layer, we ran linear and stratified Ekman models with the Price Weller and Pinkel (1986) mixing scheme, forced by both *in situ* shipboard winds and a variety of reanalysis wind data. Model time mean skill was analysed by comparing the correlation between the simulated and observed mean current profiles. Time varying performance was assessed using a two-sample Kolmogorov-Smirnov test and quantile-quantile plots. For the model runs with the shipboard winds, the classical linear time-varying Ekman model offered the best performance. Model runs using 6 hourly reanalysis winds interpolated onto the float tracks performed poorly, preventing a proper assessment of skill of the stratified models relative to the linear Ekman models.

The combined evidence in this thesis suggests that the classical constant viscosity Ekman model offers an adequate representation of the near surface response to wind forcing with a minimal number of parameters.

Acknowledgments:

I would like to acknowledge and thank the following people:

My PhD supervisors: Nathan Bindoff, Helen Phillips and Steve Rintoul. I wish to thank them for the time they invested in discussing my ideas; reading drafts or coming up with suggestions for how to view my more troublesome questions from different perspectives.

The numerous scientists, technicians and crew involved in the Southern Ocean FINE-structure project, without whom I would have no data to play with.

Yueng Lenn for suggesting I look at the effect of geostrophic shear on the Ekman spiral.
Shane Elipot for providing useful advice on how to implement his rotary spectral methods.

The staff and students of IMAS, ACE-CRC, CSIRO Marine and Atmospheric Research and TPAC for the numerous small contributions that keep a project moving and a PhD student no more insane than usual: a social chat here; a suggestion there; the odd bit of IT support or a quiet drink of a Friday evening.

Last, but far from least, my family and friends.

Over the course of my research I have made extensive use of the datasets and tools made freely available to the oceanographic community by a variety of people and organizations; I wish to thank:

Phil Morgan, Lindsay Pender and the other CSIRO staff who developed and made publically available the SEAWATER toolkit for Matlab.

Abderrahim Bentamy for producing the IFREMER/CERSAT blended satellite-reanalysis wind fields which I made extensive use of.

Lana Erofeeva, Gary Egbert and others involved in the development of the TXPO7.2 tidal model.

The European Centre for Medium-Range Weather Forecasts for producing the ERA series reanalysis products.

The National Centers for Environmental Prediction and the National Center for Atmospheric Research for producing the NCEP/NCAR reanalysis datasets.

Finally, I wish to acknowledge that the funding for this research was provided by the Australian government through the Australian Postgraduate Award and from the CSIRO OCE Postgraduate Top Up Scholarship. Funding for the Australian contribution to SOFINE was provided by the Australian Research Council (DP0877098) and the Antarctic Science Program (Projects 3002 and 3228).

Chapter 1: Introduction

1.1 Background

V.W. Ekman's theory of wind forcing on the surface ocean is a corner stone of oceanography (Ekman, 1905). By considering a balance between frictional and Coriolis forces and assuming a constant vertical eddy viscosity, Ekman (1905) derived a set of equations for the latitudinal and longitudinal velocity components as a function of depth. For steady winds the resulting solution is the Ekman spiral, which has a characteristic exponential amplitude decay and anti-cyclonic (anticlockwise in the Southern Hemisphere) rotation with increasing depth. When integrated over the depth of the spiral the Ekman spiral imposes a net transport that is 90° to the wind field. This transport arising from Ekman currents is of significance in the meridional overturning circulation, driving the upwelling of deep waters near 50°S (Speer et al., 2000) and transporting them northward. It is also significant in the formation of Mode Waters (Sallée et al., 2006).

Previous studies using direct observations of profiles of Ekman current have established the validity of the bulk relationship between wind stress and net Ekman transport (Chereskin, 1995, Lenn and Chereskin, 2009, Price et al., 1987). The same studies have also found Ekman-like spirals in data averaged over long time periods in a coordinate frame relative to the wind (Chereskin, 1995, Lenn and Chereskin, 2009, Price et al., 1987). The majority of these studies have found the 'classical' constant viscosity model inadequate, in that the time-mean spirals are compressed; that is the current amplitude decays more quickly with depth than predicted by classical theory. The consequence is that eddy viscosities estimated from the observed amplitude decay, and those estimated from the observed rotation of the spiral are not equal. It has been suggested that this compression is a result of stratification-driven "surface trapping" (Price and Sundermeyer, 1999, Price et al., 1987). However, two more recent studies, one employing spectral methods (Elipot and Gille, 2009a), and a second specifically considering the effect of depth varying geostrophic currents (Polton et al., 2013), indicate that it may be possible to reconcile observed Ekman currents to the 'classical' Ekman model.

In response to the inconsistency between observed and theoretical Ekman spirals discussed above a number of modifications to Ekman theory have been proposed. These include using a slab-like (i.e. velocity constant with depth) Ekman layer (Halpern, 1974, McNally and White, 1985, Wijffels et al., 1994); alternate depth varying eddy-viscosity parameterizations; linking momentum mixing to stratification (Price et al., 1986) and coupling to other processes such as Stokes drift (Heinloo and Toompuu, 2012, Polton et al., 2005) and geostrophic currents (Cronin and Kessler, 2009). These individual modifications to Ekman theory have been compared to observations. However, there have been few coherent efforts to test multiple modifications to Ekman theory against a single dataset; Elipot and Gille (2009a) investigated nine models incorporating a variety of eddy viscosity profiles using rotary spectral techniques but did not investigate any form of coupling with other oceanic processes and were limited to examining a single depth level.

1.2 Motivation and Aims

Ekman currents in the Southern Ocean have seen little observational exploration. Two prior studies (Lenn and Chereskin, 2009, Polton et al., 2013) designed to detect Ekman spirals were both concentrated on the Drake Passage, while Elipot and Gille (2009a) focused on properties on a circumpolar-scale using drogued surface drifter data. As discussed above, even outside the Southern Ocean the vertical structure of Ekman currents is still only poorly understood. Given the role of the Southern Ocean in the global climate, errors in heat and fresh-water transport arising from inappropriate parameterization of the vertical structure of Ekman currents in model simulations could lead to uncertainty in other elements of the climate system. Hence, we seek to improve our understanding of the vertical structure of Ekman currents and to examine the effects of density stratification and coupling with other oceanic processes, and to assess the available theories against observations.

We have access to a unique dataset of approximately 1400 concurrent profiles of temperature, salinity and horizontal velocity with fine vertical (2-5m) and high temporal (8hr)

resolution. These profiles were collected with 8 EM-APEX (Electro-Magnetic Autonomous Profiling eXplorer) velocity profiling floats (Sanford et al., 2005), deployed north of Kerguelen Island during the November-December 2008 Southern Ocean FINE-structure (SOFINE) expedition (Naveira Garabato et al., 2009, Waterman et al., 2012, Damerell et al., 2013, Phillips and Bindoff, 2014). This dataset represents one of the first large-scale deployments of this instrumentation. The float data is supplemented by shipboard ADCP observations taken during the SOFINE cruise; this second dataset offers high temporal resolution (30 seconds between profiles) but reduced vertical resolution. These datasets offer an opportunity to examine Ekman currents from multiple angles; in addition to detecting and characterizing the observed Ekman current we will also use spectral techniques to fit conceptual viscosity profiles and to run numerical Ekman models before comparing the model output to our observations.

1.3 Thesis Outline

This thesis consists of six chapters, opening with the introduction. We then review previous literature examining Ekman currents and Southern Ocean dynamics in Chapter 2.

In Chapter 3 we isolate and characterize the Ekman currents observed in the EM-APEX float data. This allows us to diagnose the “bulk” eddy viscosities and eddy viscosity profiles. We consider the effect of using constant or depth-varying geostrophic currents when isolating the Ekman flow (Polton et al., 2013). We compute the net Ekman transport to see how well it compares to ‘classical’ Ekman theory. Then we consider the effect of stratification on transport profiles; “bulk” viscosities and viscosity profiles.

In Chapter 4 we investigate Ekman currents from a frequency domain perspective. We use rotary spectral techniques (Elipot and Gille, 2009b) to fit theoretical transfer functions to our observational data. By considering the performance of the transfer functions we can then assess the most appropriate combination of eddy viscosity profile and bottom boundary condition for the Ekman layer. These results are useful in assessing the most appropriate parameterization of

momentum mixing. As a secondary benefit, using the best performing transfer function and power-spectra of the wind forcing we can estimate the total wind energy input to the Ekman layer within our area of interest.

In Chapter 5 we examine time domain simulation of Ekman currents with realistic wind forcing. We run two sets of numerical Ekman models with *in situ* and reanalysis wind forcing before comparing the output to our observations of Ekman currents. We use a number of variations of a linear Ekman model to investigate the performance of the best viscosity profiles identified in Chapter 4, and investigate the role of coupling of Ekman currents to Stokes drift and geostrophic shear. Thereafter, we consider three variations on the Price-Weller-Pinkel model (Price et al., 1986) to investigate the effect of surface buoyancy and wind forcing on the density stratification and Ekman currents within the mixed layer. Our conclusions are presented and possible further work discussed in Chapter 6.

Chapter 2: Literature Review and Background Material

2.1 The Southern Ocean: Circumpolar Structure and Dynamics

a. Currents and Fronts

A number of currents play a role in the dynamics of the Southern Ocean. On the northern fringes of the Southern Ocean the subtropical gyres dominate. Further south lies the Antarctic Circumpolar Current (ACC) and adjacent to the Antarctic land mass itself gyres occur in the Weddell and Ross Seas. A map of these features is shown in Figure 2.1.

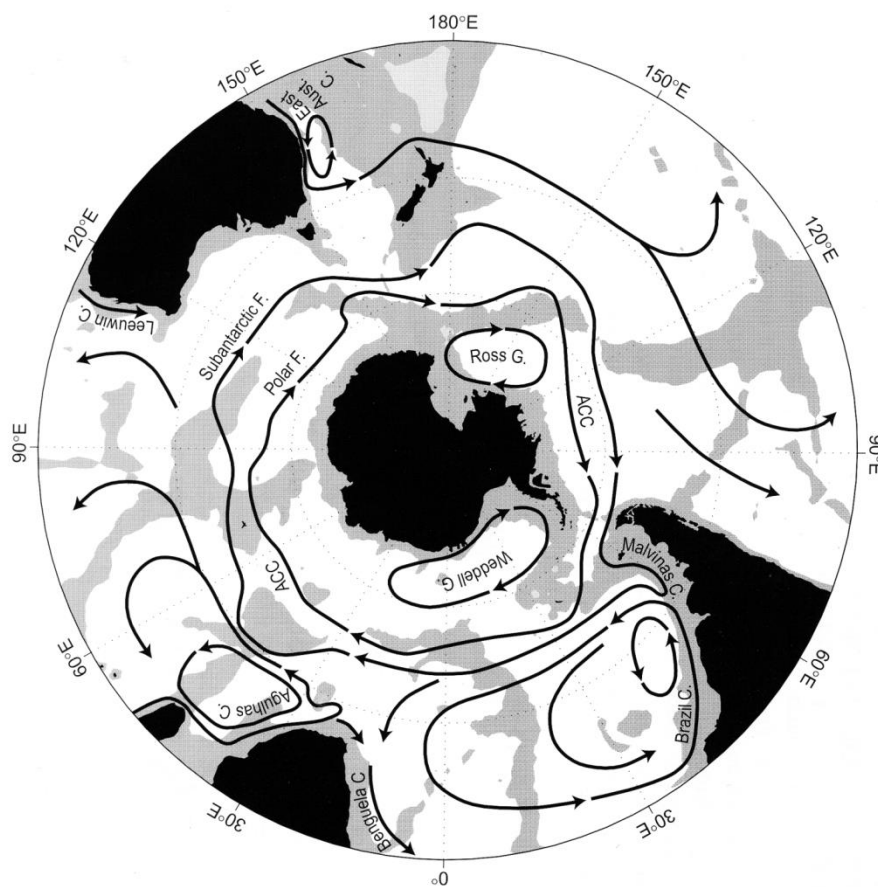


Figure 2.1: Major currents and other features of the Southern Ocean.

From Rintoul et al. (2001).

Of all these currents the ACC is the most significant carrying an average of between $97 \times 10^6 \text{ m}^3/\text{s}$ (Orsi et al., 1995) and $134 \times 10^6 \text{ m}^3/\text{s}$ (Rintoul et al., 2001) of water around the globe and forming a vital link between the ocean basins. The ACC is deep reaching and as a result its path is heavily influenced by the bottom topography.

The boundaries between the various regions of the Southern Ocean are marked by sharp transitions between water masses known as fronts (Stewart, 1997). Generally, four major circumpolar or near circumpolar fronts (Figure 2.2) are recognized (Orsi et al., 1995): the Subtropical Front (STF, blocked by South America); the Subantarctic Front (SAF); the Polar Front (PF) and the Southern ACC Front (sACCf or SACC). The criteria used to define these fronts have varied considerably from study to study, for examples see Belkin and Gordon (1996). This has resulted in discrepancies in the locations of fronts (Sokolov and Rintoul, 2007). In addition to the circumpolar fronts, two minor fronts (the Scotia front and an unnamed front) separate the Weddell and Ross gyres from the ACC.

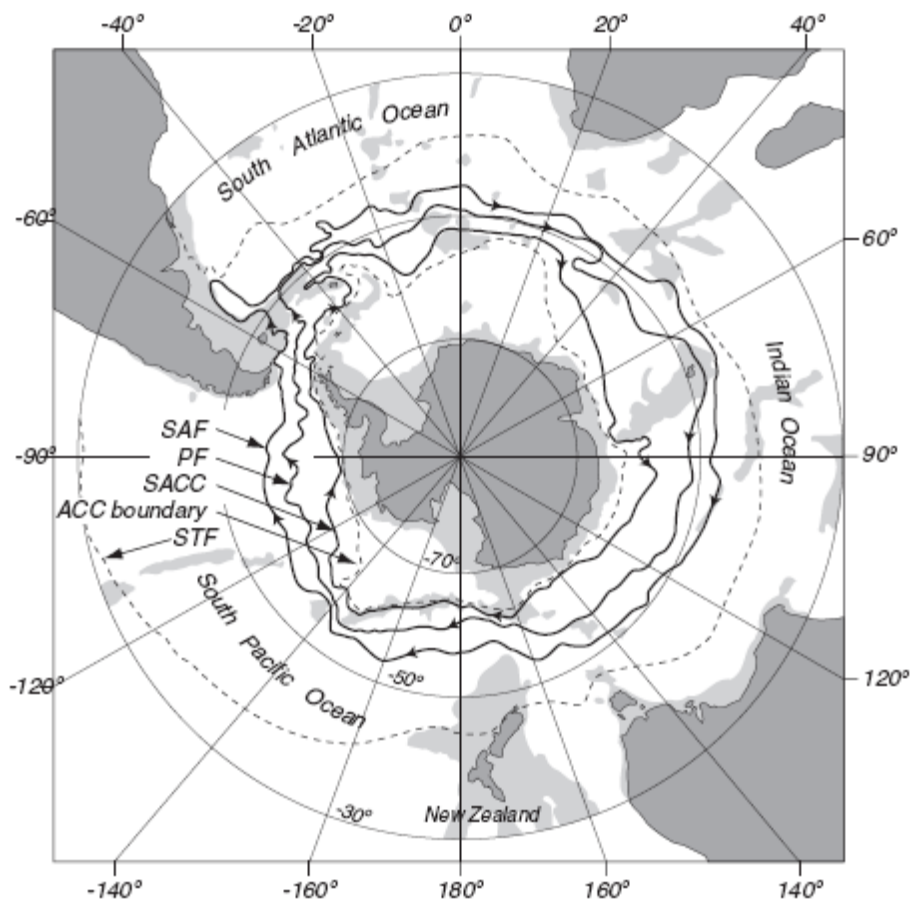


Figure 2.2: Schematic map of the principal fronts of the Southern Ocean. From Stewart (1997), after Orsi et al. (1995). Shaded areas indicate depths of 3000m or less.

Based on studies in the Drake Passage it was long believed that transport along the ACC was concentrated in a number of continuous and deep jets associated with the circumpolar fronts

(Rintoul et al., 2001). The advent of high resolution models; remote sensing of the jets and higher resolution observations have since shown that the ACC is considerably more complex and is actually composed of (Hughes and Ash, 2001): “a complex interweaving of jets, breaking and joining, beginning and ending”. A number of these jets are associated with the temperature and salinity features which older studies have used to define frontal location and are thought to account for some of the discrepancies in frontal positions in those studies. Similar studies (Sokolov and Rintoul, 2007) also indicate that frontal structure is more complex than previously believed.

b. Water Masses

While the circumpolar transport of the ACC is the dominant feature of the Southern Ocean the weaker meridional overturning circulation plays a very significant role in global climate. The circulation is dominated by six major water masses, the names and properties of which are shown in Table 2.1.

<u>Water Mass</u>	<u>Temperature (°C)</u>	<u>Salinity (psu)</u>	<u>Other Characteristics</u>	<u>Sources</u>
Subantarctic Mode Water (SAMW)	4-15	34.2-35.8		(Hanawa and Talley, 2001)
Antarctic Intermediate Water (AAIW)	3-5 (Potential temperature)	34.2-34.4		(Gordon, 2001)
Upper Circumpolar Deep Water (UCDW)	1-2 (Potential temperature)	34.2-34.4	Oxygen minimum	(Gordon, 2001) (Orsi et al., 1995)
North Atlantic Deep Water (NADW)	4	35		(Stewart, 1997)
Lower Circumpolar Deep Water (LCDW)	1-2 (Potential temperature)	34.2-34.4	Salinity maximum	(Gordon, 2001) (Orsi et al., 1995)
Antarctic Bottom Water (AABW)	<-1 (Potential temperature)	34.65-34.75		(Gordon, 2001)

Table 2.1: Defining Features of Southern Ocean water masses.

The densest of these water masses is the cold and saline AABW which originates on the continental margins of Antarctica, most notably in the Weddell Sea. Further up the water column sits the LCDW,

NADW and UCDW, south of the Polar Front both these water bodies extend to the surface. North of the Polar Front the AAIW and subsequently (north of the SAF) the SAMW dominate the near surface layers of the Southern Ocean.

c. The Overturning Circulation

The overturning circulation (Figure 2.3) is largely dependent on the balance between the southwards flow of the deep waters and the northward flow of AABW and surface waters north of the PF (Rintoul et al., 2001). It has been surmised that this process is at least partially driven by Ekman (wind driven) transport: Over much of the Southern Ocean westerly winds dominate (causing northward Ekman transport), reaching a maximum in the vicinity of 50°S; further south winds are weaker and more variable. This results in divergent Ekman transport which causes upwelling of the deep waters.

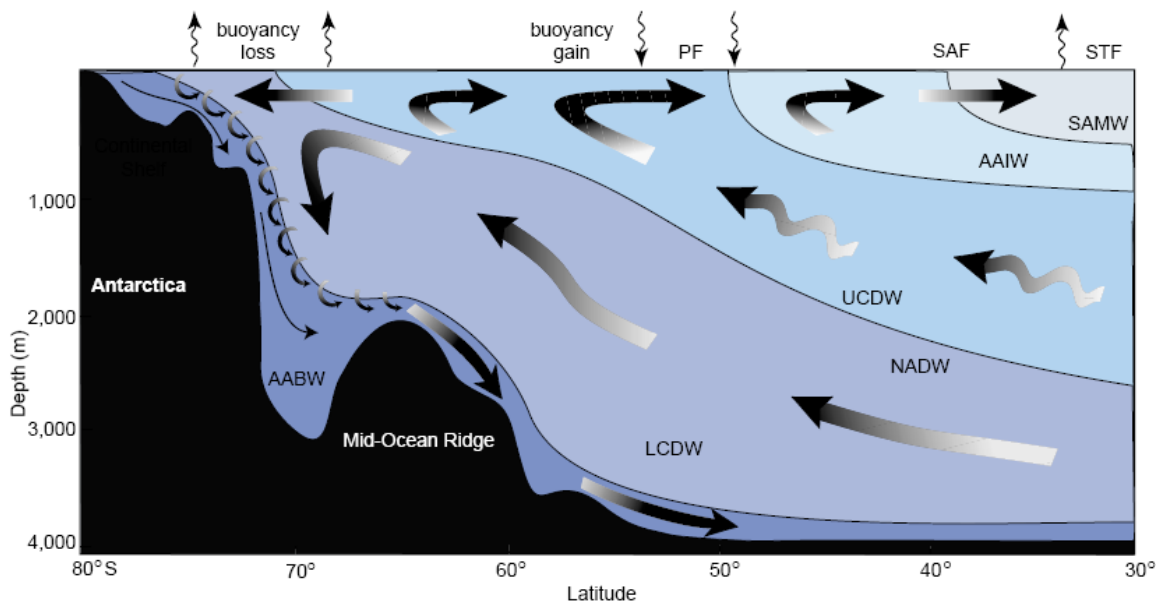


Figure 2.3: Schematic diagram of the overturning circulation. From Speer et al. (2000).

As a result of the circumpolar nature of the ACC, meridional geostrophic transport is confined to regions in which sea floor topography cuts across the ACC. From this it has been deduced (de Szoek and Levine, 1981) that in order to balance northward Ekman flow and heat loss to the atmosphere eddies must contribute to an unusually large portion of the heat transport across

the ACC. Models (Speer et al., 2000) and experiments (Phillips and Rintoul, 2000) seem to confirm this. Areas associated with high eddy intensity include the Kerguelen and Campbell Plateaus.

d. The Kerguelen Plateau Region

The Kerguelen Plateau is a region of shallow water between 70°E and 80°E and extending from approximately 45°S to 65°S (Figure 2.4). The Plateau is split in two by the Fawn trough near 57°S; the plateau north of the trough is typically shallower than south of the trough. It represents one of the few major topographic barriers within the Southern Ocean, driving a bifurcation of the ACC deflecting the Polar and Subantarctic fronts northwards and the Southern ACC front southwards (Park et al., 2008). This bifurcation and deflection of the ACC jets results in intense eddy activity (Meijers et al., 2011b, Phillips and Rintoul, 2000, Rintoul et al., 2001).

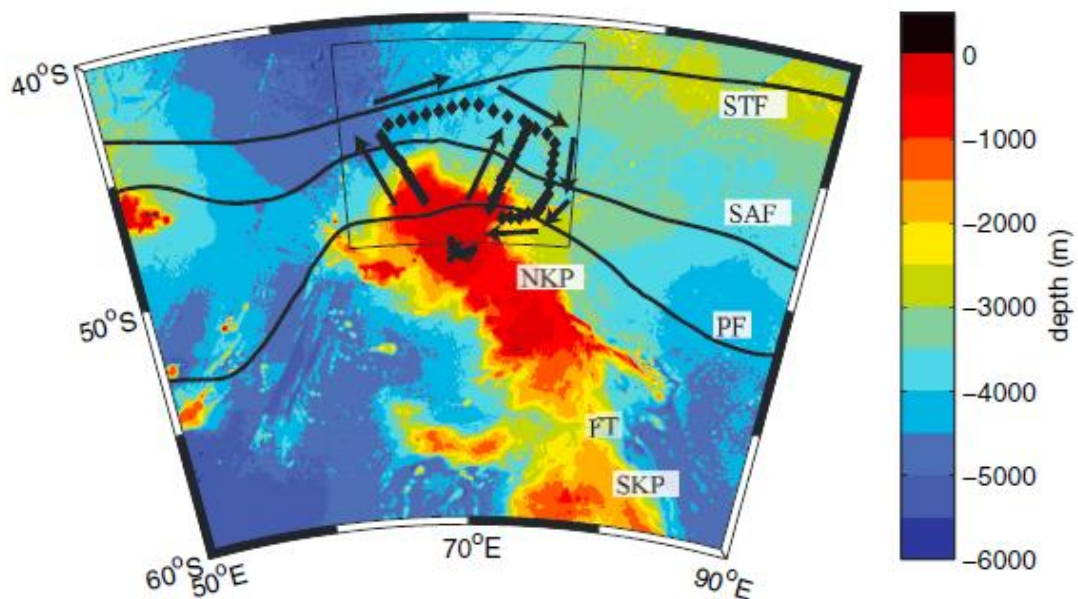


Figure 2.4: Bathymetry (Smith and Sandwell, 1997) of the Kerguelen Plateau with the major fronts and topographic features marked. Fronts are indicated by black lines (north to south: STF, Subtropical front; SAF, Subantarctic front and PF, polar front) while the SOFINE CTD survey is marked with the black diamonds (arrows indicate direction of survey). NKP and SKP mark the Southern and Northern Kerguelen Plateaus; FT marks the Fawn Trough. From (Damerell et al., 2013).

Flow in the Kerguelen region, as reconstructed by Park et al. (2008), is shown in Figure 2.5. Net transport is dominated by jets associated with the major branches of the Subantarctic front to the north of the Plateau and by flow through the Fawn Trough further south. Flow over the Plateau itself is weak.

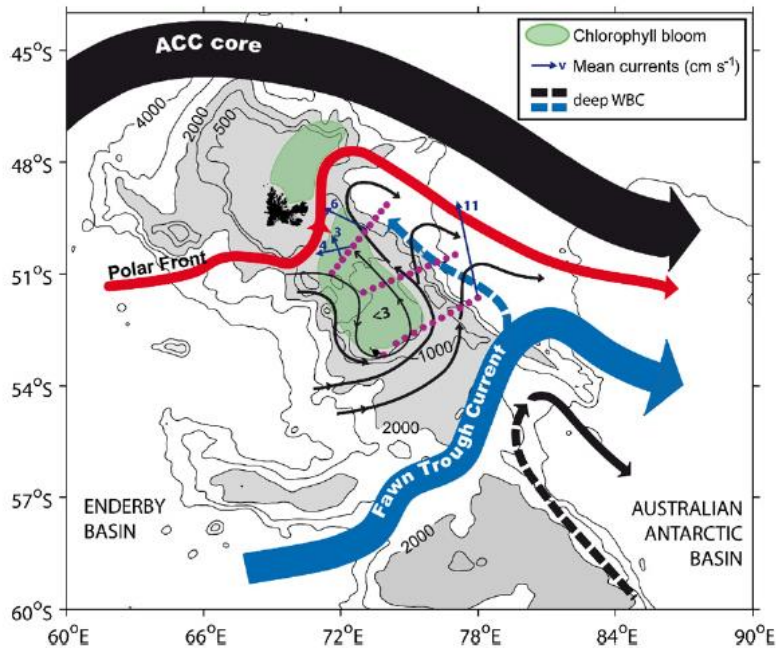


Figure 2.5: Schematic of flow in the Kerguelen Plateau region. Dashed lines indicate deep western boundary currents. Blue vectors with numerals indicate observed current velocities. From (Park et al., 2008)

2.2 Subsurface Profiling Floats

One of the major problems for Oceanographers has been the limitations on quality, quantity, geographic and temporal coverage of data. The development of the expendable bathythermograph (XBT) in the 1960s and the World Ocean Circulation Experiment in the 1990s (Roemmich et al., 1998) have done much to improve the extent and quality of coverage, however many limitations still remain. XBTs are principally deployed from ships of opportunity, and as such, the resulting data is mainly restricted to major shipping lanes and the measurements only provide temperature profiles. The WOCE survey provided high quality data across the entire water column, but even given seven

years of work the spatial coverage remained sparse. The large scale deployment of subsurface profiling floats under the Argo programme has overcome some of these limitations.

The use of sub-surface floats was pioneered by John Swallow in 1955 (Gould, 2002) when he produced the first SOFAR (SOund Fixing And Ranging) floats. Early floats used a frequency in the region of 10kHz giving a detection range of around 5 km (Warren and Wunsch, 1981). By the mid-1970s it had become common to use the SOFAR channel (around 1000Hz) which allowed ranges of up to 700km (Warren and Wunsch, 1981). During the 1980s RAFOS (reverse SOFAR) floats were developed (Gould, 2002). Unlike SOFAR systems RAFOS used receivers fixed to the float and the signals transmitted from fixed stations.

With the advent of the WOCE program during the 1990s RAFOS floats were supplemented by the introduction of Autonomous Lagrangian Circulation Explorer (ALACE) floats (Gould, 2002). ALACE floats could be set to maintain a desired depth for a period of time before surfacing then descending and repeating the process. ALACE floats did not use acoustic tracking; data on the location of a float was obtained solely from fixes obtained by satellite when the float periodically surfaced.

The development of the Argo array was first proposed in 1998 in conjunction with the Global Ocean Data Assimilation Experiment (GODAE) and the Climate Variability and Predictability Program (CLIVAR). The first floats were deployed in 2000 and worldwide coverage was achieved by 2004 (Lebedev et al., 2007). By the end of 2007 the initial target of 3000 active floats had been met.

a. Argo Floats

With the exception of some limited use of fixed profiling devices in the Arctic the vast majority of data collected by the Argo project is sourced from profiling floats. Currently most deployed Argo floats are of three main models: APEX, SOLO and Provor. All of these float models have similar characteristics: a nominal life time of 4 years or between 150 and 170 cycles and a maximum operating depth of about 2000m. All Argo floats use an external hydraulically operated bladder to

control depth. By adjusting the volume of the bladder, the volume and hence density of the float can be changed, allowing the float to rise or sink until neutral buoyancy is achieved.

An Argo float cycle (Figure 2.6) consists of four distinct phases. First is the surface phase during which data is transmitted to satellites.

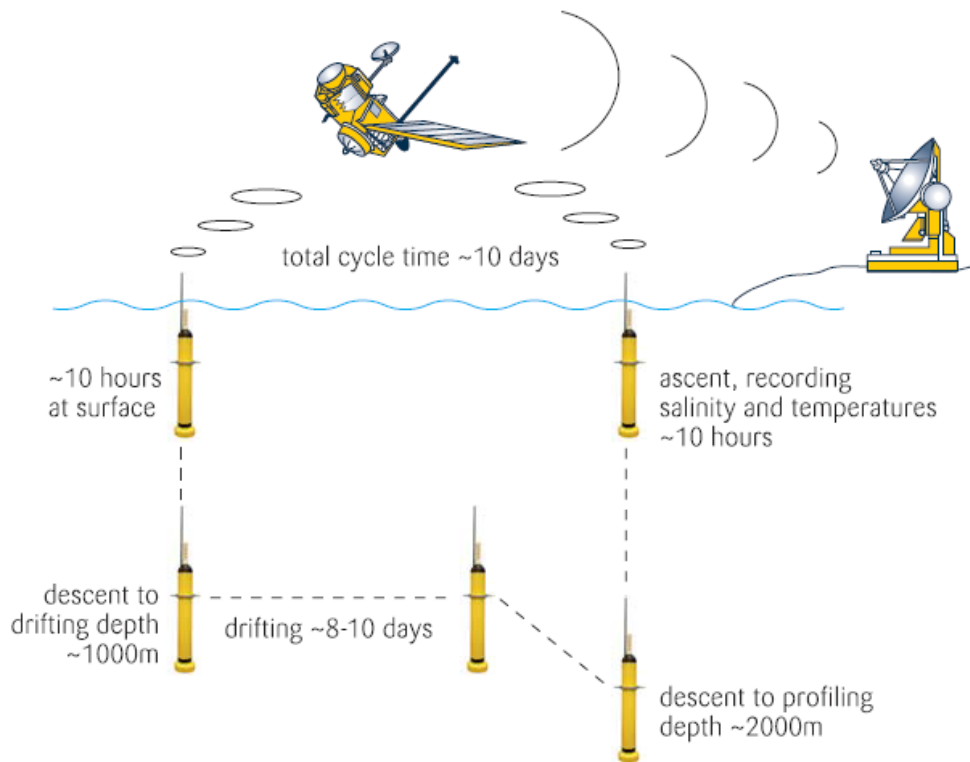


Figure 2.6: Outline of a typical Argo float cycle. From Gould (2006).

This is followed by descent to parking depth and an extended period spent at a parking depth which for 90% of floats is between 1000m and 2000m (Lebedev et al., 2007). Finally, the profiling phase in which temperature and salinity sensors record data while the float ascends to the surface.

Dependent on the intended use of a float the profile may commence at the parking depth or may be preceded by a descent to a greater depth. On average an Argo float cycle lasts for 9.5 days, of which 9 hours are spent on the surface (Lebedev et al., 2007).

b. EM-APEX Floats

EM-APEX (Electromagnetic Autonomous Profiling EXplorer) floats (Sanford et al., 2005) are an enhancement of the APEX sub-surface profiling float manufactured by Teledyne-Webb, which makes

up much of the current Argo fleet. They are equipped with an electromagnetic subsystem including compass, accelerometers and electrodes that measure the motionally-induced electric fields generated by currents moving through the vertical component of the Earth's magnetic field. Two orthogonal pairs of electrodes give two independent measurements of electrical potential difference across the body of the float. As the instrument ascends/descends at approximately $10\text{-}12\text{ cm s}^{-1}$, external fins cause the body to rotate so that the orientation of the electrode axes relative to the instantaneous current is constantly changing. The sampling rate is 20Hz and these data are averaged to 1 second intervals. On-board processing performs a least-squares fit over a moving window of 50 seconds to give one voltage component pair, and the RMS error of the fit. The resulting vertical resolution is 2-4dbar, depending on the float's vertical velocity. Each fit comprises multiple rotations of the float, allowing the large self-potential associated with electrodes to be removed. The electric field measurements are converted to relative velocity components following the method described in Sanford (1971). The unknown constant velocity offset is determined in this case from the GPS locations at each surfacing of the float, as described in Phillips and Bindoff (2014), allowing absolute velocities to be calculated. Further details of the EM-APEX floats are discussed in Section 3.2a.

2.3 Ekman Theory

One of the earliest theories addressing the effect of wind forcing on the ocean was proposed by V.W. Ekman (1905), inspired by Nansen's observations of Icebergs drifting to an angle offset from the wind. Ekman devised his theory by considering a steady horizontal flow driven by constant wind forcing, resulting in a balance between frictional and coriolis forces. By assuming a constant "coefficient of friction" throughout the water column, Ekman was able to obtain differential equations for the longitudinal and latitudinal components of velocity as a function of depth. The coefficient of friction governs the transmission of frictional forces down the water column, and is now usually termed the eddy viscosity. Ekman's equations result in a solution generating an exponential decay in the magnitude of the velocity and an anticyclonic (anti-clockwise in the

Southern Hemisphere) rotation with increasing depth, resulting in the classical Ekman spiral.

Versions of these equations have also been adapted for use with periodic wind forcing (Rudnick, 2003, Rudnick and Weller, 1993). By integrating the Ekman velocity over a selected depth range the resulting Ekman transport of water can be calculated.

Ekman transport can have significant impacts on both biological and climate systems. Ekman transport away from a coastline can produce upwelling of water. While in the open Ocean spatial variability of Ekman transport can result in the phenomenon of Ekman pumping resulting in downwelling of water and Ekman suction driving upwelling. An example of this is the role Ekman transport plays in the meridional overturning circulation by driving the upwelling of deep waters near 50°S (Speer et al., 2000) and transporting them northward. These Ekman flows carry cold water northward, effecting a poleward heat transport and thus contributing to the global heat balance.

a. Derivation of Steady State Solutions:

The derivation of 'classical' steady state Ekman theory involves seven assumptions:

1. The ocean is large and of uniform depth.
2. The ocean has a uniform and constant density throughout.
3. Water can flow freely into and out of the region considered: nearby currents and coastlines are neglected.
4. The curvature of the Earth may be neglected.
5. A steady and uniform wind stress acts on the entire region being considered.
6. The system has had time to achieve a stationary state of motion.
7. Water can be treated as incompressible.

Following Ekman (1905) we consider the x-component of momentum:

$$\frac{\partial u}{\partial t} + u \frac{\partial u}{\partial x} + v \frac{\partial u}{\partial y} + w \frac{\partial u}{\partial z} = -\frac{1}{\rho} \frac{\partial p}{\partial x} + fv + F_x$$

Where: x,y,z denote the longitudinal, latitudinal and vertical coordinates

u, v, w denote the longitudinal, latitudinal and vertical velocities

f denotes the Coriolis parameter

p denotes pressure

ρ denotes density

F_x denotes the frictional force

Note that for the sake of consistency throughout this thesis all notation used to describe Ekman processes will be consistent with Chereskin and Price (2001) and Lenn and Chereskin (2009).

Assumption 5 implies that u and v do not vary as functions of x and y , combining this with assumption 7 in turn implies that w does not vary as a function of z .

Thus:

$$\frac{\partial u}{\partial x}, \frac{\partial u}{\partial y}, \frac{\partial v}{\partial x}, \frac{\partial v}{\partial y}, \frac{\partial w}{\partial z} = 0$$

Hence, the x component of the momentum equation simplifies to:

$$\frac{\partial u}{\partial t} = -\frac{1}{\rho} \frac{\partial p}{\partial x} + fv + F_x$$

The assumption of uniform density (assumption 2) implies that there is no horizontal variation in pressure. Hence:

$$\frac{\partial u}{\partial t} = fv + F_x$$

But the frictional force is a function of density and the horizontal components of stress, T_{xz} and T_{yz} (Stewart, 1997):

$$F_x = \frac{1}{\rho} \frac{\partial T_{xz}}{\partial z}$$

Thus:

$$\frac{\partial u}{\partial t} = fv + \frac{1}{\rho} \frac{\partial T_{xz}}{\partial z} \quad (2.1)$$

Ekman assumed a frictional stress of the form:

$$T_{xz} = \rho k \frac{\partial u}{\partial z} \quad (2.2)$$

Where k is the kinematic eddy viscosity.

Thus, the momentum equation becomes:

$$\frac{\partial u}{\partial t} = fv + \frac{1}{\rho} \frac{\partial \left(\rho k \frac{\partial u}{\partial z} \right)}{\partial z}$$

Assuming k is independent of depth (z):

$$\frac{\partial u}{\partial t} = fv + k \frac{\partial^2 u}{\partial z^2} \quad (2.3)$$

Applying assumption 6, the derivative of u with respect to time must be zero; we obtain a balance between wind stress and the Coriolis force:

$$0 = \frac{fv}{k} + \frac{\partial^2 u}{\partial z^2}$$

Now, consider the substitution:

$$D_e = \sqrt{\frac{2k}{|f|}} \quad (2.4)$$

Hence the expression becomes:

$$0 = \frac{2v}{D_e^2} + \frac{\partial^2 u}{\partial z^2}$$

A similar procedure can be applied to the y -component to yield:

$$0 = -\frac{fu}{k} + \frac{\partial^2 v}{\partial z^2} = -\frac{2u}{D_e^2} + \frac{\partial^2 v}{\partial z^2}$$

The solutions to these partial differential equations take the form (Ekman, 1905):

$$u_{ek} = V_1 e^{\frac{z}{D_e}} \cos\left(\frac{z}{D_e} + c_1\right) + V_2 e^{-\frac{z}{D_e}} \cos\left(\frac{z}{D_e} + c_2\right)$$

$$v_{ek} = V_1 e^{\frac{z}{D_e}} \sin\left(\frac{z}{D_e} + c_1\right) - V_2 e^{-\frac{z}{D_e}} \sin\left(\frac{z}{D_e} + c_2\right)$$

Where V_1 and V_2 denote speeds and c_1 and c_2 denote angles.

Taking z positive upwards it becomes apparent that the first term of each equation decays away from $z=0$ while the second term decays towards $z=0$. Thus V_1 represents the surface velocity (from now on denoted V_{surf}) and V_2 represents a velocity at depth. Hence, assuming an infinitely deep ocean (in practise, a depth much greater than D_e), V_2 can be taken as 0 m/s and so the second term can be neglected:

$$u_{ek} = V_{surf} e^{\frac{z}{D_e}} \cos\left(\frac{z}{D_e} + c_1\right) \quad (2.5a)$$

$$v_{ek} = V_{surf} e^{\frac{z}{D_e}} \sin\left(\frac{z}{D_e} + c_1\right) \quad (2.5b)$$

To determine the value of c_1 we must first find the derivatives by depth of u_{ek} .

$$\frac{\partial u_{ek}}{\partial z} = \frac{V_{surf}}{D_e} e^{\frac{z}{D_e}} \left(\cos\left(\frac{z}{D_e} + c_1\right) - \sin\left(\frac{z}{D_e} + c_1\right) \right)$$

Now consider the case of $z=0$ (i.e. at the surface) with a constant wind stress (T) applied along the y axis. The x component of wind is, thus, zero:

$$0 = T_{xz, z=0} = \rho k \frac{\partial u}{\partial z}$$

Thus, for real and constant eddy viscosity and density the derivative of u_{ek} with respect to z must be zero:

$$0 = \frac{\partial u_{ek}}{\partial z} = \frac{V_{surf}}{D_e} e^{\frac{z}{D_e}} \left(\cos\left(\frac{z}{D_e} + c_1\right) - \sin\left(\frac{z}{D_e} + c_1\right) \right)$$

$$\therefore 0 = \cos\left(\frac{z}{D_e} + c_1\right) - \sin\left(\frac{z}{D_e} + c_1\right)$$

At the surface $z=0$, hence:

$$\therefore 0 = \cos(c_1) - \sin(c_1)$$

Applying a trigonometric identity:

$$0 = \sqrt{2} \sin\left(c_1 + \arcsin\left(\frac{1}{\sqrt{2}}\right)\right)$$

$$\therefore 0 = c_1 + \arcsin\left(\frac{1}{\sqrt{2}}\right)$$

$$\therefore c_1 = \frac{\pi}{4} \text{ radians} = 45^\circ$$

Similarly, for the wind directed along the y axis the y component of stress is:

$$T_{yz, z=0} = \rho k \frac{\partial v}{\partial z} = T$$

Hence, evaluating the derivative of Equation 2.5b at the surface we obtain:

$$T = \sqrt{2} \rho k \frac{V_{surf}}{D_e}$$

Substituting Equation 2.4 for D_e , and rearranging, we obtain an explicit expression for the surface velocity V_{surf} in terms of the wind-stress, density, eddy viscosity and coriolis parameter:

$$V_{surf} = \frac{T}{\sqrt{\rho^2 k f}}$$

The final form of the equations for u (Eqn. 2.5a) and v (Eqn. 2.5b) components of Ekman current velocity display the expected exponential decay and rotation with increasing depth:

$$u_{ek} = V_{surf} e^{-\frac{z}{D_e}} \cos\left(\frac{z}{D_e} + \frac{\pi}{4}\right) \quad (2.5a)$$

$$v_{ek} = V_{surf} e^{-\frac{z}{D_e}} \sin\left(\frac{z}{D_e} + \frac{\pi}{4}\right) \quad (2.5b)$$

2.4 Previous Observational Studies

While laboratory experiments and atmospheric studies (Hesselberg, 1954) confirmed the existence of Ekman spirals it would take over half a century for the first observations of an oceanic Ekman spiral (Hunkins, 1966) and it would not be until the 1970s that instruments became sensitive and reliable enough for detailed examination of both localized Ekman spirals and (on a larger scale) Ekman transport.

Generally, there are three methods by which Ekman theory has been studied observationally:

1. Observations of Ekman transport across hydrographic sections (Chereskin and Roemmich, 1991, Wijffels et al., 1994).
2. Large scale statistical analysis of drogued surface drifter paths (Elipot, 2006, Krauss, 1993, McNally, 1981)
3. Direct observation of velocity profiles (Chereskin, 1995, Lenn and Chereskin, 2009, Weller, 1981).

a. Early Observations

The first reliable observations (Hunkins, 1966) of Ekman spirals in deep waters were not made until 1958 when a series of measurements were undertaken from a station on an ice floe in the central Arctic Sea. Observations were made by the use of a tethered drogue deployed through a hole in the ice. Current heading was determined using the horizontal angle between the tether and north, while observations of the angle between the tether and a vertical plumbline were calibrated against both theory and observations with a conventional current meter to produce estimates of current speeds relative to the ice floe. The drift velocity of the ice floe was estimated from positional fixes obtained by celestial navigation.

A total of 23 velocity profiles from 13 periods of steady wind and steady drift were isolated for analysis. These velocity profiles consisted of 4 to 6 velocity observations over depth ranges from 29 to 61m. Vector plots of mean velocities over each drift period were prepared. At shallow depths (typically around 12m), the majority of these plots display clockwise displacement of near surface

velocities relative to the ice floe and wind velocities and clockwise rotation, both consistent with Ekman theory. At deeper depths velocity amplitude decay and rotation are less consistent, and so do not fit as well to theory.

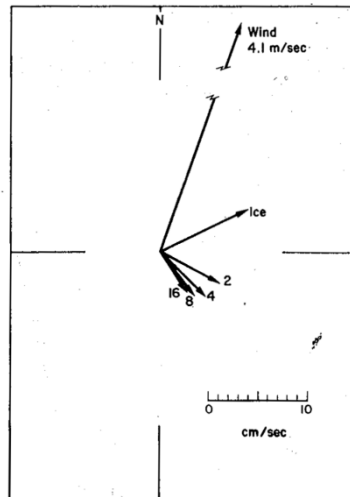


Figure 2.7: Mean velocity spiral from 9 profiles taken over 6 periods of steady drift between the 8th of July and the 3rd of September 1958. Numbers adjacent to vectors denote depth in meters. From Hunkins (1966).

While features of these profiles are indicative of Ekman spiral like behaviour, Hunkins (1966) pursued the problem further by considering a mean profile over 6 periods of steady drift (Figure 2.7). The resulting profile has a clearly defined spiral rotating clockwise and decaying with increasing depth. Additionally, Hunkins (1966) compared this mean spiral to the combination of a thin under-ice boundary layer and a theoretical Ekman spiral with $k=23.8\text{cm}^2/\text{s}$ (not shown). Aside from a slight offset, probably arising from the geostrophic component of velocity, the two spirals matched well. This led Hunkins (1966) to conclude that the 'classical' constant eddy viscosity Ekman theory was adequate.

In 1971 Halpern (1974) undertook a study of mixed layer responses in the North Pacific using a mooring deployed at 47° N 128° E in 2700m of water. The mooring was equipped with a wind recorder, one air thermistor and nine thermistors placed between the surface and 55m. Four current meters were installed on the mooring in such a way as to place two (8 and 16m) in the mixed layer, one (26m) at the top of the thermocline and one (46m) at the base of the thermocline. The

experiment ran for 32 days from the 4th of August to the 5th of September, however the 16m current meter failed after 27 days hence limiting examination of currents to that time period. During the experiment two cold fronts passed over the mooring on the 20th of August and the 1st of September, otherwise winds only occasionally exceeded 5m/s.

The passage of the 20th of August 'storm' drove considerable changes in the mixed layer. The temperature structure of the water column changed considerably: the mixed layer deepened from around 18m to 25m; the upper 10m displayed cooling of about 1°C and waters between 20 and 30m warmed (by 2°C at 23m and 0.6°C at 30m). Despite these changes, the net heat content of the upper 50m varied by less than 5%. Based on a combination of this minimal change in heat content and surface observations, Halpern concluded that the temperature redistribution was principally driven by vertical mixing rather than horizontal advection.

Examination of the velocity observations indicated strong coupling between the wind and mixed layer currents and a weaker coupling between the wind and deep currents and hinted at a slab-like (vertically-uniform horizontal velocity) response in the mixed layer. While no indications of an Ekman spiral were detected, observations of flow at 8m and 16m (14cm/s and 12cm/s) during a storm on the 20th and 21st of August were generally in line with a mean velocity of 14cm/s computed by assuming wind-derived estimates of Ekman transport were evenly spread over the 0-20m depth range. Observations of current headings at the same depth for the same time period yielded a clockwise deflection relative to the wind heading of around 120°. Halpern (1974) deemed that these observations were consistent with Ekman theory but were not strong enough to be taken as confirmation.

b. Weller (1981)

Developments over the course of the 1960s and 1970s allowed the introduction of more sophisticated current meters. During 1977 a set of vector measuring current meters (VMCMs) were deployed from the free-drifting research platform *Flip* in deep waters off California.

Observations of velocities relative to the research platform were made using two pairs of VMCMs on a wire. The wire was payed out and retrieved over the course of two hours, cycling the upper pair of VMCMs between 5m and 70m and the lower pair between 77m and 142m. During each cycle the wire was stopped for 5 minutes at ten preset depths resulting in velocity observations at 21 depth levels. Simultaneous observations of airspeed were made using an anemometer mounted 18m above the surface, this airspeed was corrected to a height of 10m and converted into a wind stress. *Flip's* drift was tracked using the LORAN radio navigation system.

Velocities were sorted into six depth bins (5-15m, 22-40m, 48-67m, 76-89m, 96-110m and 118-142m) and rotary spectra were calculated for positive and negative radial frequencies in each depth bin. Negative (clockwise rotating) frequencies displayed a peak around 0.04 cycles per hour (CPH) which, due to the direction of rotation and proximity to the local coriolis frequency (denoted f), Weller (1981) attributed to inertial motion. Next, the coherence and phase (probable angle) between specific depth bands and the rest of the water column was calculated. Motion relative to the surface (Figure 2.8) was found to be significantly coherent with motion over the top 40m for a frequency band of -0.1 to 0.1 CPH.

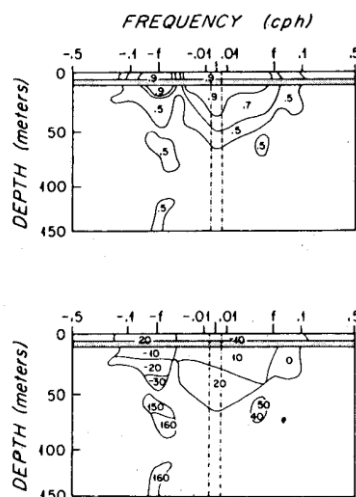


Figure 2.8: Coherence (top) and phase (bottom, positive indicates clockwise rotation) between 10m level and all other depths. From Weller (1981).

For subinertial frequencies phase relative to surface motion was predominantly positive, indicating rotation to the right. This was confirmed by examination of the mean daily velocities for the first five days of the study (Figure 2.9).

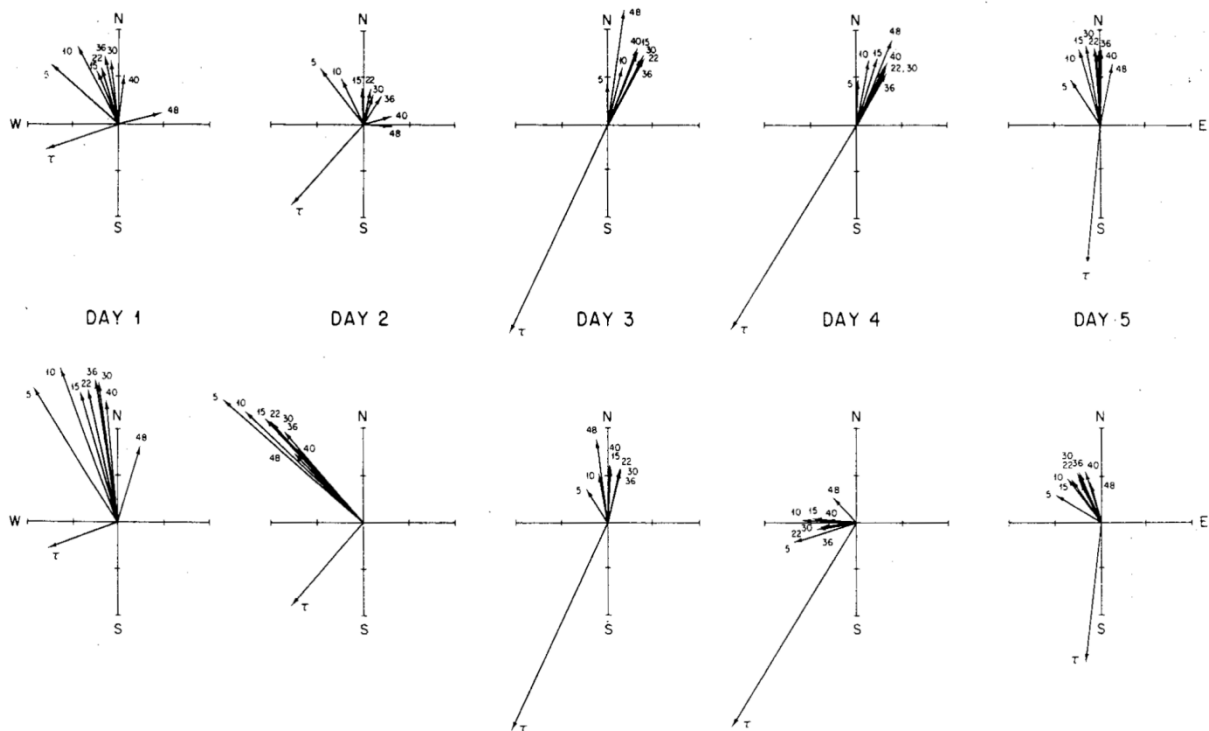


Figure 2.9: Daily mean velocities relative to Flip (top) and corrected for Flip's drift velocity (bottom).

Vectors are labelled with the corresponding depth or, in the case of those indicating wind stresses, τ .

Tick marks on axes are at 0.1m s^{-1} for velocity and 10^{-2}Pa for wind stress. From Weller (1981).

Issues with the number of high quality LORAN fixes per day meant that estimates of *Flip's* drift speed (and hence, absolute rather than relative velocities) could on average be obtained only once per day. This prevented direct investigation of wind stress-velocity relationships using rotary cross spectral analysis as previously applied within the water column. Instead Weller (1981) used the observations of relative velocities to produce time series of velocity shear. Plots of coherence and phase between the wind stress and shear are shown in Figure 2.10. Generally, coherence was significant to a depth of around 40m over a frequency band from -0.2 to 0.2 CPH. Coherence was deepest reaching at low frequencies with the exception of a region of coherence between 70 and 100m depth around the negative (clockwise-turning) inertial frequency. For all positive frequencies and the negative

frequencies between $-f$ and 0 CPH the phase plot indicates that shear is usually to the right of the wind stress. At frequencies less than $-f$ the phase plot indicates shear is usually to the left of wind stress.

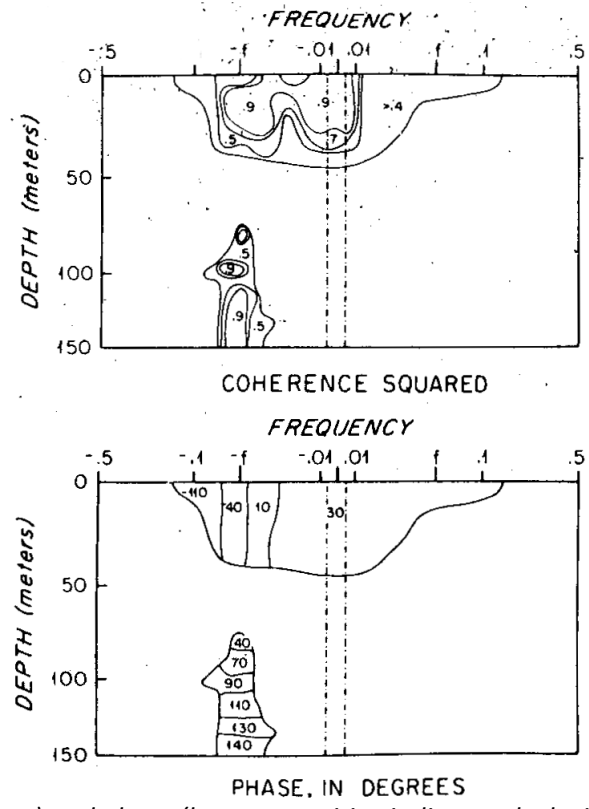


Figure 2.10: Coherence (top) and phase (bottom, positive indicates clockwise rotation) between wind stress and velocity shear. From Weller (1981).

Using a combination of time dependent wind stress and Ekman equations, Weller (1981) attempted to model the velocity structure observed. Using a constant eddy viscosity parameterization, attempts to match the observed phase resulted in an eddy viscosity of between 100 and $500 \text{ cm}^2/\text{s}$, while matching the observed shear required an eddy viscosity of around $50 \text{ cm}^2/\text{s}$. Similarly, simple linearly varying eddy viscosity parameterizations could not be made to match both the observed phase and shear. This inconsistency in estimates of eddy viscosity has also been observed in more recent studies (Lenn and Chereskin, 2009, Price and Sundermeyer, 1999, Price et al., 1987).

c. NORPAX and Related Drifter Studies (McNally, 1981)

With the development of suitable satellite instrumentation (RAMS and ARGOS) during the 1970s the use of surface drifters for ocean observation became practical. One of the notable early deployments of surface drifters occurred during the NORPAX experiment conducted between July 1976 and June 1977. Twenty three drifters with 9 m drogues on 30m lines were deployed and tracked (McNally, 1981). In principal the use of the drogues with large surface area implies that the resulting drift trajectory can be attributed primarily to the velocity at drogue depth rather than to windage on the float. Over the course of the experiment, 80% of the drifters reported the loss of drogues.

Monthly vector averages of drifter speed and direction were calculated for 5° by 5° bins and compared to similarly vector-averaged winds from the Fleet Numerical Weather Centre's synoptic wind analysis dataset (2.5° spatial and 6 hourly temporal grids). These average winds and drift velocities indicated that a 350% increase in drifter velocity during the winter months coincided closely with 500% increase in wind speed during the same period. Additionally, comparisons of mean wind and drifter headings indicated a tendency for the drifter to be deflected to the right of the wind, consistent with the expected direction of deflection with depth and transport from Ekman theory. More detailed consideration of this data indicated that over the period of high wind speed from October 1976 through March 1977 the mean deflection of all drifters was 28° right of the wind, less than the 45° deflection expected for surface Ekman velocities or the 90° deflection expected for net Ekman transport.

A second analysis procedure was also applied. Drifter trajectories were interpolated to produce 4 location fixes per day on the same 6 hourly temporal grid used for the FNWC wind dataset. Wind velocities were then interpolated to each location. A five day running average filter was then applied to the wind and drifter velocities. This data was then sorted by wind speed and date. Histograms of the difference between wind and drifter headings were computed for both (Figure 2.11). The histograms of deflection as a function of wind speed indicate that for weak winds (under 5 knots) deflection is approximately uniformly distributed but for stronger winds a preferred

deflection of float velocities off the wind of between 20° and 30° to the right is established and subsequently displays little sensitivity to further increases in wind speed. The histograms by date show an initial slight preference for rightward deflection, increasing and becoming more clearly defined while moving into the higher intensity winds of October 1976 to March 1977 before subsiding with the weaker winds thereafter. As with the monthly vector mean analysis this behaviour suggests significant correlation between large scale atmospheric forcing and drifter trajectories.

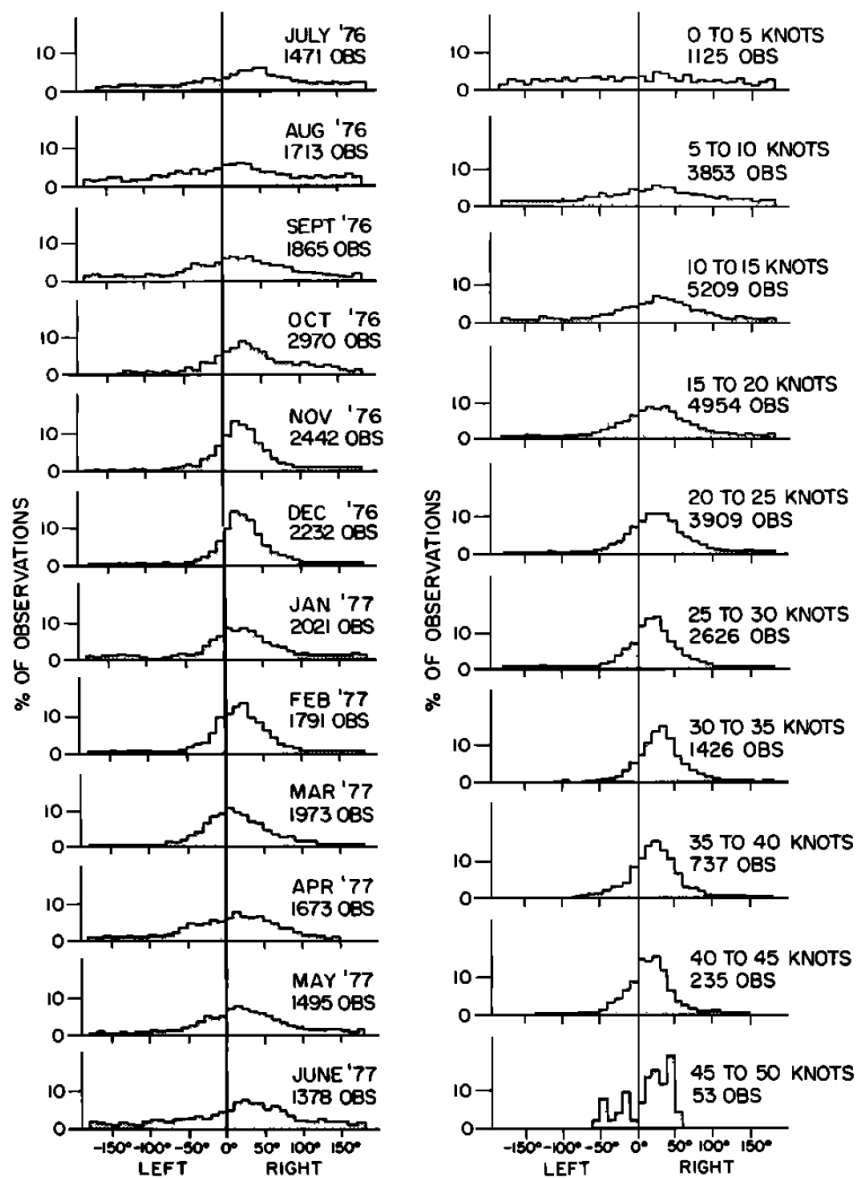


Figure 2.11: Histograms of the angle between wind direction and drifter heading stratified by month (left) and by wind speed (right). From (McNally, 1981).

Finally, McNally sorted the drifter velocities by the status of the drifters' drogues: 4408 measurements occurred while drogues were still attached; 7739 occurred after drogue loss. Calculations of mean speeds gave a value of 9.0cm/s for drogue observations and 8.8cm/s for observations after drogue loss. Averaged over the entire study time, while drogues remained attached drifters moved at 1.4% of the wind speed at 36° to the right of the wind and after drogue loss drifters moved at 1.5% of the wind speed at 34° to the right of the wind. McNally proposed two possible explanations for this observation, the first being a total lack of drogue efficiency (i.e. all velocities are exclusively due to windage) or that there was minimal velocity shear between the surface and 30m depth and by implication no Ekman spiral. Subsequent tests with deep drogues (120-200m) indicated the hypothesis of zero drogue efficiency was unlikely. Thus, McNally concluded that the lack of difference in velocity observations between drifters with and without drogues indicated the presence of little vertical shear in the upper 30m, apparently in contradiction to Ekman theory.

To further pursue this problem McNally and White (1985) performed a repeat deployment of drifters. A total of 12 drifters were deployed in four clusters of three drifters each between 35° N and 38° N along 155° W. Within each cluster, drifters were fitted with drogues at nominal depths of 30m, 60m and 90m. Drifters were tracked using the ARGOS satellite array, providing more daily fixes and less uncertainty in location than the RAMS system used for previous studies. In order to perform analysis against wind data, drifter positions were interpolated to give positions on a regular 6 hourly temporal grid.

Trajectories of all drifters are shown in Figure 2.12. All drifters follow a pattern of a North-South meander followed by Eastward drift until around 150°W, after which the majority of drifters move in a more north-easterly direction. The cluster of drifters deployed at 35° N display continued Eastward drift. Upon switching to a wind based coordinate system the differences in trajectory between the 35° N cluster and the other drifters disappears suggesting that this anomaly was due to differences in wind stress. This plot indicates that overall the drifters experience substantially

greater along-wind displacement than across-wind displacement. Net drift is to the right of the wind but as with the NORPAX study the angle of drift (around 20°) is inconsistent with either the expected net Ekman transport or surface Ekman velocity. There are no clear systematic differences in drift behaviour as a function of drogue depth.

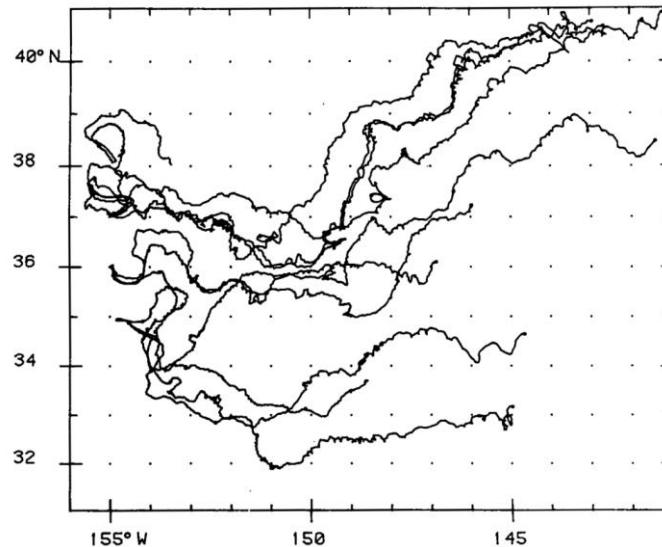


Figure 2.12: Drifter trajectories. From McNally and White (1985).

McNally and White (1985) proceeded to concentrate on the behaviour of the cluster of drifters deployed at 37° N. In all cases the drifters displayed little initial downstream drift with time before each drifter settled into a regime of near-constant downwind displacement rates, all displaying similar drift rates. However, this switch to constant displacement varied as a function of depth – the 30m drogue entered the regime in mid-September, the 60m drifter entered it in early October while the 90m drogue took until mid-October. Similar behaviour was observed for crosswind drift.

An examination of wind stress was unable to account for this behaviour – a number of high wind stress values were observed prior to the 60m and 90m drifters commencing significant downwind drift. However examination of mixed layer depth proved more informative. By producing a time series of mixed layer depths from XBT casts in the surrounding region McNally and White (1985) determined that over the course of the study the mixed layer depth deepened, reaching 25m, 50m and 72m when the 30m, 60m and 90m drifters switched regimes. It should be noted that the

nominal drogue depths reflect the length of an unloaded drogue line, in practise applying a current to the drogue will result in the drogue sitting at a shallower depth. While the drifters used in this study did not have pressure sensors mounted on the drogues (McNally and White, 1985) previous work indicated that a real depth about 80% of the nominal depth (in line with the observed mixed layers depths at commencement of downwind drift) is plausible. Thus McNally and White (1985) concluded that these changes in drift regime reflect the entry of the drogues into the mixed layer.

The behaviour of drifters was modelled by assuming that the crosswind component arose from a slab like wind driven mixed layer and that the downwind component arose exclusively from windage on the exposed hull of the drifter. Removal of the modelled windage-driven downwind velocity reduced total downwind displacement over the study time from around 1500km to 900km, indicating that there are other factors contributing to the downwind drift. The combination of downwind residual and crosswind drift shifts the angle between wind and currents to around 30° likely arising from the difference in the surface area of drogues used in each study. This is in line with the NORPAX measurements (McNally, 1981) but still inconsistent with Ekman theory. The slab-like wind-driven layer model applied to the crosswind component proved more successful by accounting for virtually all the crosswind drift of the 30m and 60m drifter in addition to a significant fraction of crosswind drift for the 90m drifter.

By considering 5-day mean vector averaged velocities of the 60m and 90m drifters prior to the mixed layer depth reaching the drogues and the difference between nominal drogue depth and mixed layer depth, McNally and White (1985) detected clockwise rotating and depth-decaying velocity structures extending from the bottom of the mixed layer. This behaviour is consistent with an Ekman like spiral forming at the base of the mixed layer but the lack of precise data on drogue depth precluded a thorough investigation of these observations.

These two studies (McNally, 1981, McNally and White, 1985) led McNally and White to conclude that a slab-like mixed layer model provided the best representation of near surface wind driven currents. While this seems a logical conclusion from these studies it must be pointed out this

interpretation is based on long-term (multiple month) behaviour and so does not exclude the existence of Ekman like spirals over shorter time frames.

d. The Long Term Upper Ocean Study

Paralleling developments in surface drifter systems, improvements in mooring based observing systems allowed the deployment of more robust and accurate current profilers. These improvements in instrumentation allowed longer time series of subsurface velocities to be collected. An early example of such a study is the deployment of a mooring in the western Sargasso Sea as part of the Long Term Upper Ocean Study in the summer of 1982 (Price et al., 1987). The mooring had a total of 7 Vector Measuring Current Meters mounted at 5, 10, 15, 25, 50, 75 and 100m depth while a number of instruments mounted on the surface buoy recorded meteorological conditions. This mooring returned a time series of 160 days.

A time series of wind stress was estimated using bulk transfer formulae and observations of wind speed and air-sea temperature differences. Meanwhile the wind-driven current was isolated by subtracting from each observation a deep reference velocity (in this case the 50m level) then applying a vector average across all observations from a particular day. Finally, the 160 resulting daily mean velocities were rotated into a wind stress based reference frame and an ensemble average for the entire data set was calculated. This ensemble averaging served to increase the signal to noise ratio.

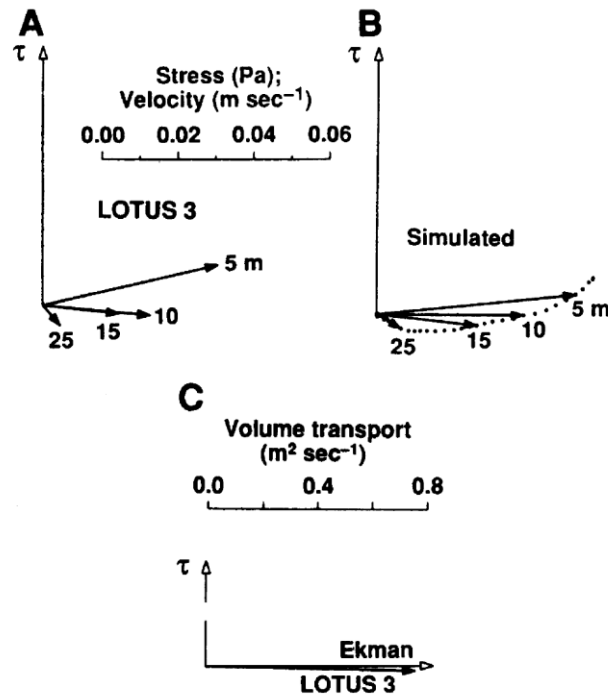


Figure 2.13: Mean observed Ekman profile (A) compared with output from a numerical model incorporating density stratification (B). Mean transport estimated from observations compared with that estimated from the wind stress using the 'classical' Ekman transport equations (C). From Price et al. (1987).

The resulting mean current (Figure 2.13A) takes the form of a rightward rotating spiral decaying with increasing depth, qualitatively consistent with steady-state Ekman theory. Analysis of the amplitude decay seen in this mean spiral generates an eddy viscosity of $6 \times 10^{-3} \text{ m}^2 \text{ s}^{-1}$. The rate of rotation returns a different and incompatible eddy viscosity of $5.4 \times 10^{-2} \text{ m}^2 \text{ s}^{-1}$, almost an order of magnitude greater than the amplitude based estimate. Net Ekman transport was estimated from the mean current profile by applying trapezoid rule integration from the surface to 50m. Despite the two incompatible decay scales seen in the spiral the net transport matched theoretical results computed from mean wind stress to within 10% in magnitude and 5° in heading (Figure 2.15C), well within the 20% uncertainty in the theoretical Ekman transport. It was found that 95% of transport occurred in the upper 25m of the water column compared to 90% for a classical Ekman spiral with an eddy viscosity of $6 \times 10^{-3} \text{ m}^2 \text{ s}^{-1}$ (obtained from the estimated e-folding depth) or 67% for the rotational eddy viscosity of $5.4 \times 10^{-2} \text{ m}^2 \text{ s}^{-1}$. Price et al. (1987) labelled this behaviour as 'strong surface trapping' and

suggested it indicated that classical Ekman theory was inadequate as it did not specifically include variations in stratification.

Examination of collocated temperature and salinity data indicated that variations in stratification occurred on both seasonal and daily timescales. The changes in stratification driven by the seasonal cycle of heat fluxes covered a range of 10°C. Daily changes in surface temperature usually ranged over 0.3°C but occasionally exceeded 2°C. These temperature variations in turn drove variations in mixed layer depths. Daily heat flux variations were observed to drive a cycle between a day time minimum mixed layer depth of between 2m and 10m and a night time maximum between 10m and 30m. The influence of these changes in stratification can be seen in the differences in the mean daytime and night time current spirals (Figure 2.14), the night time spiral displays weaker 5, 10 and 15m velocities and more rapid rotation with depth than the daytime spiral.

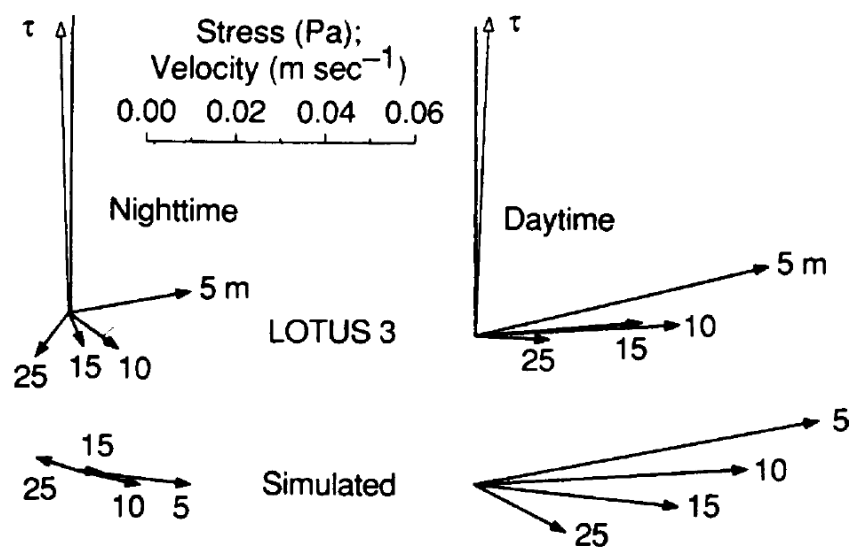


Figure 2.14: Mean observed (top) and simulated (bottom) current profiles for data stratified by time of day into daytime (0800-2000 local time) and night time (2000-0800 local time). From Price et al. (1987).

An additional examination of the effects of diurnal stratification was made by calculating 5m level velocities at 4 hour time intervals through the ensemble mean 'day' (Figure 2.14). This plot indicates a tendency for the 5m velocity to increase in magnitude and rotate to the right through the course of a day (0800-2000) before decaying overnight. Both the mean day and night and 5m level

data suggests that the surface trapping observed in the mean spiral arises predominantly from the shallow mixed layer depths of the daytime component of the diurnal cycle. Price et al. (1987) also constructed a numerical model to simulate the formation of Ekman currents under the influence of stratification. This model was able to create good matches to the total mean spiral (Figure 2.13B), the daytime mean spiral and the 5m diurnal current cycle (Figure 2.15).

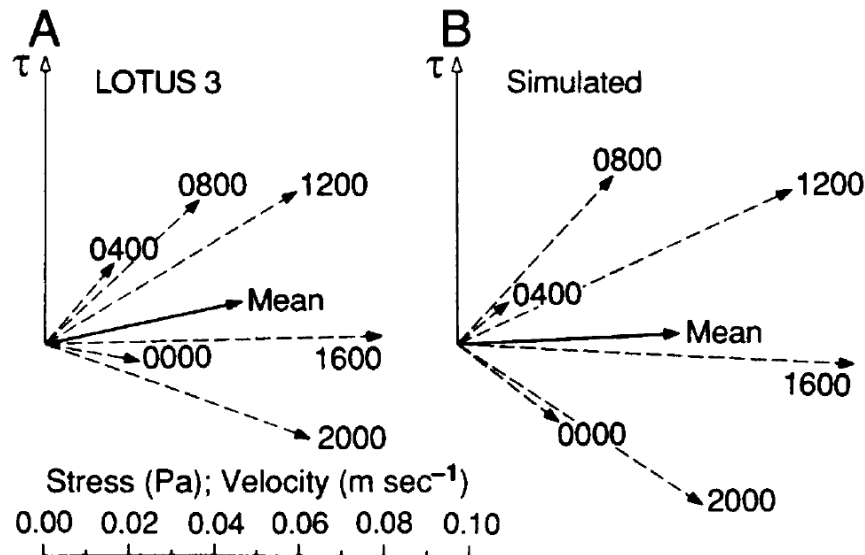


Figure 2.15: Mean diurnal current cycle at 5m depth (observed, left; modelled, right). From Price et al. (1987).

Price et al. (1987) confirmed that the classical wind stress to Ekman transport relationship holds over long time frames. It also demonstrated that the effect of stratification on the vertical structure of wind driven currents is significant, reinforcing the idea that the constant eddy viscosity parameterisation is inadequate. Further examination of data from later phases of LOTUS was undertaken by Schudlich and Price (1998) with similar results.

e. Cross-Basin Transect Estimates of Ekman Transport (Chereskin and Roemmich, 1991, Wijffels et al., 1994)

By the late 1980s the velocity structure of wind driven flows remained unclear: despite several direct observations of spiral like behaviour (Hunkins, 1966, Price et al., 1987, Weller, 1981), other observations pointed towards a slab like response (McNally, 1981, Davis et al., 1981b, Davis et al.,

1981a). The question of the penetration of wind driven transport into the ocean interior also remained, while observations (McNally, 1981, Price et al., 1987) suggested Ekman transport was insignificant below the mixed layer, the limited number of studies did not yet allow a firm conclusion. In an attempt to answer these questions Chereskin and Roemmich (1991) examined data taken from a transect between Senegal and French Guinea in March 1989. Over the course of the transect ADCP observations, wind observations and 84 CTD casts were taken.

The ADCP observations provided profiles of velocity shear over a depth range of 26m to 300m. Similarly geostrophic shear was estimated between adjacent CTD casts by application of the thermal wind equations. The cross track component of the ADCP observations were then averaged between CTD cast locations to generate collocated ADCP and geostrophic profiles. Assuming the ageostrophic component of velocity tended to zero at a reference depth of 250m, Chereskin and Roemmich (1991) subtracted the geostrophic velocity profiles from the ADCP profiles to generate profiles of ageostrophic velocity. From the ageostrophic velocities transport was then calculated. Net ageostrophic transport was found to be predominantly to the north. Examination of transport integrated across the basin (Figure 2.16) indicated that the ageostrophic component displayed a strong near surface maximum before decaying with depth with a second, weaker, maximum around 150m depth. In total the ageostrophic transport in the upper 100m was calculated to be 12Sv with error bars of 5.5Sv. This was compared with wind stress based estimates of transport derived both from shipboard observations and from climatology data. The former yielded an estimate of 8.8 ± 1.9 Sv while the latter yielded an estimate of 13.5 ± 0.3 Sv. Chereskin and Roemmich (1991) concluded these figures were indicative of general agreement between Ekman theory and the observations.

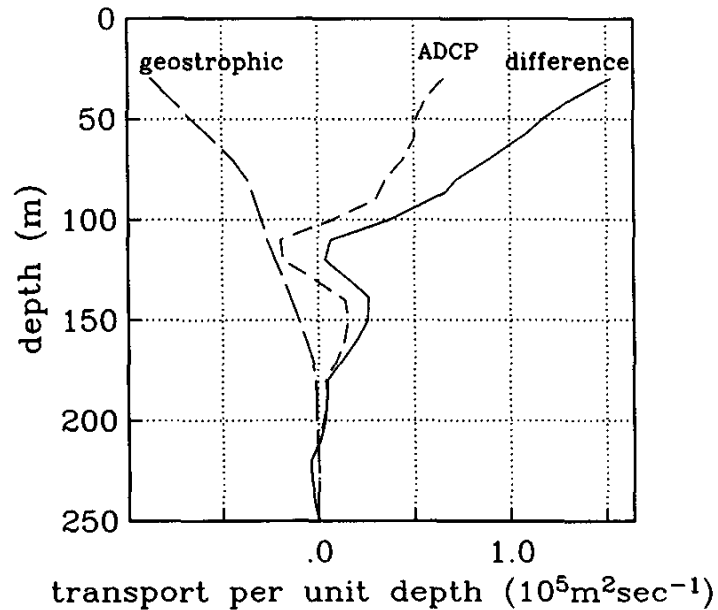


Figure 2.16: Cross-basin transport per unit depth. The solid line (labelled difference) corresponds to the ageostrophic component. From Chereskin and Roemmich (1991).

To investigate the penetration depth of wind driven transport relative to the mixed layer Chereskin and Roemmich (1991) produced profiles of transport on a depth axis normalized by the local mixed layer depth before creating plots of basin integrated transport (Figure 2.17). Plots are shown for two different definitions of the mixed layer depth: variations of 0.1°C and 1°C from the surface temperature respectively. Slab-like behaviour would be expected to manifest as vertically uniform transport from the surface to 1.0 (fraction of mixed layer depth) before a sudden drop to zero transport. Besides a short stretch of vertical uniform transport at very shallow depths (approximately 0-0.3) arising from extrapolation of transport at the shallowest observations (26m) to the surface, neither definition of the mixed layer displays a slab-like response. Instead a near linear decrease towards 0Sv at depth with increasing depth is observed between 0.3 and 1.2 normalized depth units for 1°C definition and 0.3 to 2.0 normalized depth units for 0.1°C definition. In both cases this behaviour is indicative of a significant level of Ekman transport below the mixed layer.

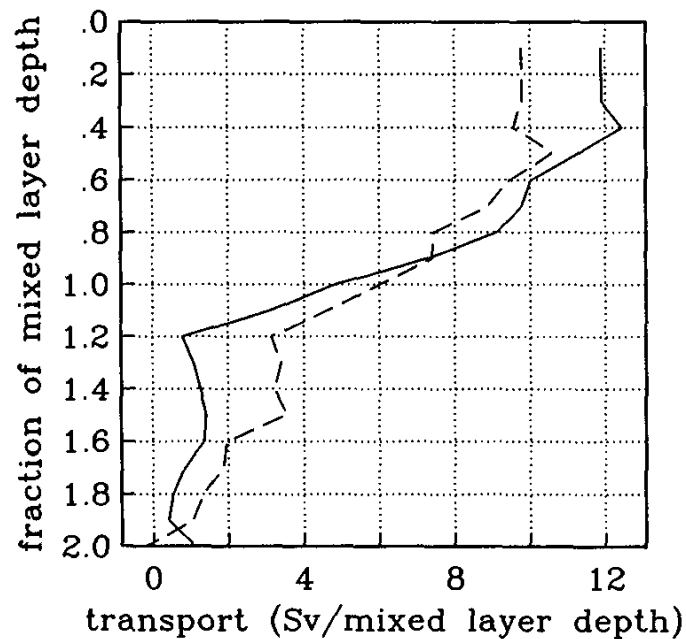


Figure 2.17: Basin integrated transport per unit of mixed layer depth. The mixed layer depth was defined as the depth at which at which temperature varied by 0.1°C (dashed curve) or 1°C (solid curve) from the SST. From Chereskin and Roemmich (1991).

Following Chereskin and Roemmich (1991) Wijffels et al. (1994) examined a transect across the Pacific at 10°N taken between February 9 and May 10 1989. First a mixed layer defined by a variation of 0.1°C was applied, which yielded similar results to Chereskin and Roemmich (1991), apparently excluding a slab-like mixed layer. However, isolated velocity profiles frequently displayed a region of weak shear near the surface and regions of strong shear further down. Thus, Wijffels et al. (1994) repeated this work with a more stringent definition of mixed layer depth (a density change of 0.01kg m⁻³) and with the depth of the top of the thermocline (defined by a density gradient of 0.01kg m⁻⁴). Plots of cross-transect velocity as a function of normalized mixed layer depth and normalized thermocline depth (Figure 2.18) indicated that unlike the temperature based mixed layer definition used by Chereskin and Roemmich (1991) the density based mixed layer definition displays a slab-like response between the surface and 90% of mixed layer depth.

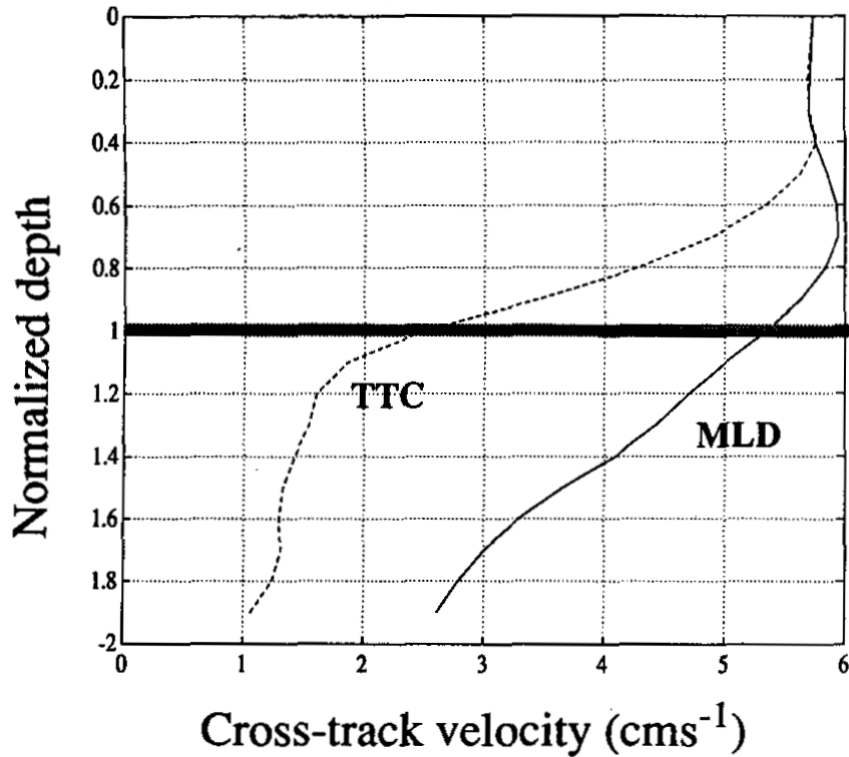


Figure 2.18: Mean cross-track ageostrophic velocity plotted as a function of depth normalized by mixed layer depth (MLD) and thermocline depth (TTC). From Wijffels et al. (1994).

Somewhat unexpectedly, rather than a rapid change in velocity at the base of the mixed layer, these results indicated a steadier change and hence considerable penetration of momentum beyond the mixed layer depth. The thermocline depth based definition on the other hand displays a response more in line with the Atlantic results (Chereskin and Roemmich, 1991). Comparisons between the temperature and density based mixed layer criteria subsequently suggested that the temperature based definition tended to fall closer to the thermocline depth than to the density derived mixed layer depth. Wijffels et al. (1994) also calculated Ekman transport across the transect. The hydrography based estimate of $6.2 \pm 1 \times 10^{10} \text{ kgs}^{-1}$ matched reasonably well with the wind observation based estimate of $5.2 \pm 1 \times 10^{10} \text{ kgs}^{-1}$.

While these two studies (Chereskin and Roemmich, 1991, Wijffels et al., 1994) further supported the relationship between wind stress and net Ekman transport, neither was able to clarify details of the wind-driven velocity structure. The Atlantic study by Chereskin and Roemmich (1991)

indicated the absence of a slab-like layer whereas Wijffels et al. (1994) did detect a slab-like mixed layer overlying a sheared 'transition' layer.

f. Sensitivity to High Frequency Winds

The studies of Ekman currents discussed so far have largely concentrated on comparing observations to steady state Ekman theory. In practise sensitivity to time-varying wind forcing can significantly change the response of Ekman currents. One such study intended to address this was performed by Rudnick and Weller (1993).

Combining the vectorial form of the linear momentum equation and the wind-stress-eddy viscosity relationship, Rudnick and Weller (1993) assumed a solution sensitive to the radial frequency of the wind forcing:

$$\vec{u}(t, z) = \vec{U}(z)e^{i\omega t}$$

Where $\vec{u}(t, z)$ denotes the total vectorial wind-forced velocity, $\vec{U}(z)$ the velocity response relative to the wind heading and ω denotes the radial frequency of the wind.

For $f+\omega > 0$ (and thus $\omega > -f$) the solution obtained by Rudnick and Weller (1993) was:

$$\vec{U}(z) = u_0 e^{(1+i)\left(\sqrt{\frac{|f+\omega|}{2k}}\right)z}, \quad u_0 = \frac{T(1-i)}{\rho\sqrt{2k|f+\omega|}}$$

This result gives a surface velocity 45° to the right of the wind and rotation further to the right of the wind with increasing depth, qualitatively in line with a northern hemisphere 'classical' Ekman spiral.

For $f+\omega < 0$ (thus, $\omega < -f$) the resulting solution was:

$$\vec{U}(z) = u_0 e^{(1-i)\left(\sqrt{\frac{|f+\omega|}{2k}}\right)z}, \quad u_0 = \frac{T(1+i)}{\rho\sqrt{2k|f+\omega|}}$$

Unlike the classical Ekman spiral this solution results in a surface velocity 45° left of the wind and rotation to the left. In both cases the decay scale is a function of not just the eddy viscosity and coriolis parameter, but also the radial frequency of the wind forcing.

Additionally the total geocentric acceleration was defined as:

$$A \equiv \frac{\partial \vec{u}}{\partial t} + i f \vec{u}$$

Geocentric acceleration is used in this case as it filters inertial oscillations. The component of geocentric acceleration coherent with the wind stress was modelled as:

$$\hat{A} = a \frac{T_0}{\rho}$$

Where T_0 is the surface wind stress and a is the transfer function (m^{-1}) determined as a function of ω for each current meter by minimizing the mean square difference between modelled wind-coherent geocentric acceleration and the observed total geocentric acceleration.

A 102 day long data set from the Frontal Air Sea Interaction Experiment (FASINEX) and a 160 day dataset from LOTUS were selected for examination. The FASINEX data was recorded at five moorings deployed in the North Atlantic between February and May 1986. All moorings had 7 current meters within the top 160m of the water column and one current meter mounted at 700m, while two moorings also had current meters mounted at 1000 and 4000m. The LOTUS time series on the other hand consisted of data from two moorings operational during May through October 1982: a surface mooring with current meters mounted between 5m and 100m and a subsurface mooring with current meters irregularly distributed between 129 and 4007m with the majority of current meters concentrated towards the top of the mooring (129m-328m).

Wind stresses were estimated for both datasets using bulk parameterizations before rotary spectral analysis was applied. In both cases the resulting power spectra were generally similar, both displaying a slight tendency for clockwise rotating frequencies to be more energetic than anticlockwise rotating frequencies. Geocentric acceleration was also estimated using the expression

outlined above before transfer functions were calculated for four frequency ranges -0.5 to -0.083 cycles per hour (super inertial, clockwise rotating fourier components), -0.083 to -0.028 CPH (near inertial, clockwise rotating fourier components), 0.028 to 0.083 CPH (near inertial, anticlockwise rotating fourier components) and 0.083 to 0.5 CPH (super inertial, anticlockwise rotating fourier components). Plots of FASINEX transfer functions are shown in Figure 2.19 grouped into four depth ranges. Generally these results show a turning with depth consistent with the predictions for each frequency band, both within each depth range and between depth ranges and a general trend of surface intensification.

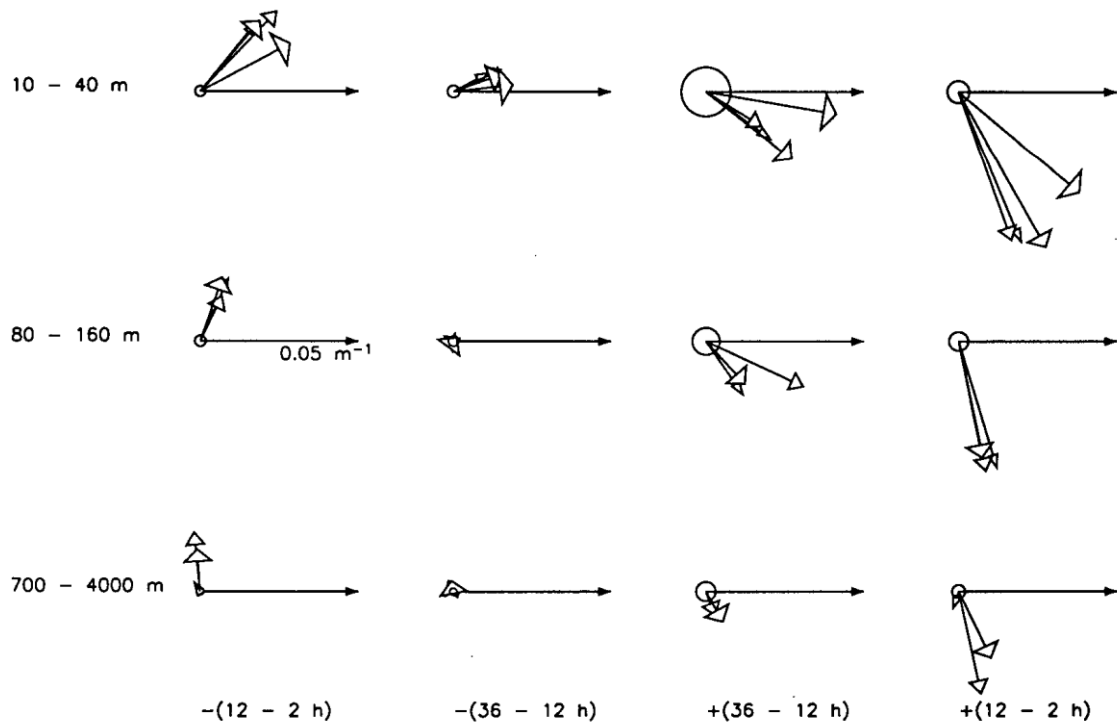


Figure 2.19: Transfer functions from FASINEX in a wind relative reference frame (downwind equating to the x axis). Transfer functions are grouped into three depth ranges (rows) and four frequency bands (columns). From Rudnick and Weller (1993).

Unexpectedly the FASINEX data displays significant responses at extreme depth (700-4000m). Rudnick and Weller suspected this deep response arose from the transmission of mooring motions down the tether used to anchor the mooring to the seafloor. A correction scheme was developed which assumed that below a reference depth (taken as 80m for FASINEX) any wind driven

response arose from mooring motion rather than Ekman currents. Following the application of this correction, transport estimates for FASINEX were found to be in good agreement with theory and the resulting geocentric acceleration spirals turned to the left for clockwise rotating high frequency forcing and to the right in other cases. Application to the LOTUS data proved less successful: while the rotation of the spirals remained consistent with theory, the transport estimates did not match as well, suggesting that while the wind driven response is in the right direction, it is too small.

g. ADCP Mooring Studies

In addition to the ship-board surveys, Acoustic Doppler Current Meters were soon adopted for deployment on moorings. Such instruments have proven of value in both shallow waters (Yoshikawa et al., 2010, Liu et al., 2007) and the open ocean (Chereskin, 1995, Lenn and Chereskin, 2009).

The first application of mooring mounted ADCPs to Ekman currents was undertaken as part of the Eastern Boundary Current (EBC) experiment conducted in 1993 (Chereskin, 1995). A mooring with a downward looking ADCP and closely spaced thermistors (between the surface and 150m level) was deployed in deep water at 37.1° N, 127.6° W. The ADCP was mounted at a depth of 2m and was configured to produce velocity measurements at 4m intervals between 8m and 164m. Velocities were measured for a five minute period three times an hour before one average velocity for each 5 minute period was calculated. Random error in the velocity data was determined to be no more than 0.5 cm s⁻¹.

For the analysis, a reference depth of 48m was selected. A mean spiral qualitatively similar to a theoretical Ekman spiral was detected and net transport calculated for both the 48m reference level and a number of alternate reference levels up to 60m depth. In all cases these transport estimates were found to agree with the wind-stress based transport to within the 20% uncertainty arising from errors in the drag coefficient used to calculate the wind stress. Estimates of transport were made on a daily basis and a cumulative transport calculated as a function of time (Figure 2.20) was found to be in general agreement with theory. Chereskin (1995) interpreted this agreement as

indicating that the momentum balance observed during the experiment was close to the steady state linear momentum balance assumed under classical Ekman theory.

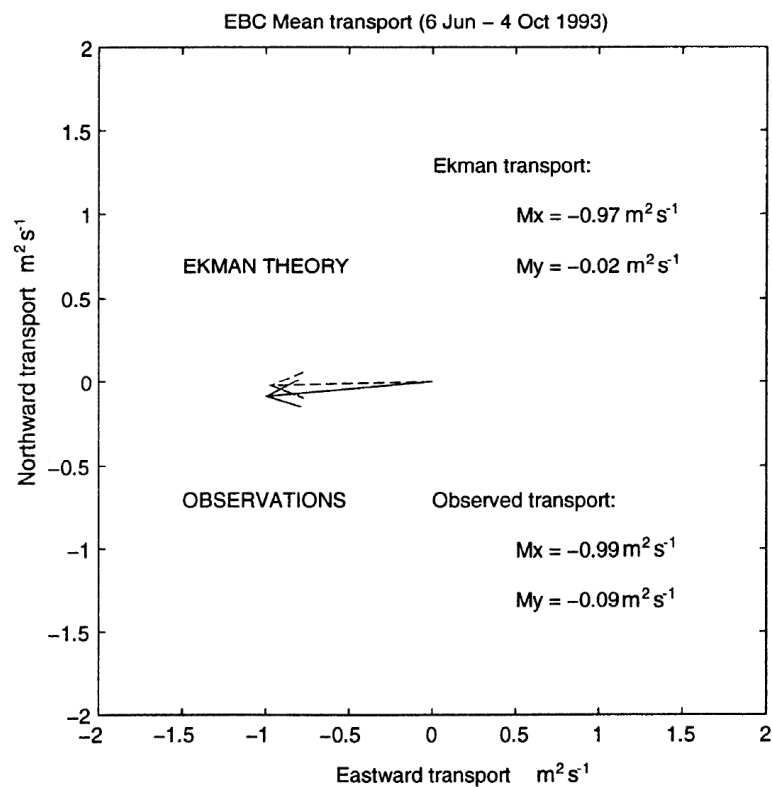


Figure 2.20: Observed (solid vector) and theoretical (dashed vector) Ekman transport. From Chereskin (1995).

Returning to the mean spiral Chereskin (1995) calculated decay scales and eddy viscosities from the observed spiral (Figure 2.21). As with several previous studies the spiral was found to be ‘flat’: a deeper decay scale (48m) was observed using a rotation based definition (1 radian rotation) compared to the decay scale estimated from amplitude decay (25m). This resulted in a mismatch in eddy viscosity of a factor of 4 ($274 \text{ cm}^2 \text{ s}^{-1}$ for the amplitude based definition and $1011 \text{ cm}^2 \text{ s}^{-1}$ for the rotational definition).

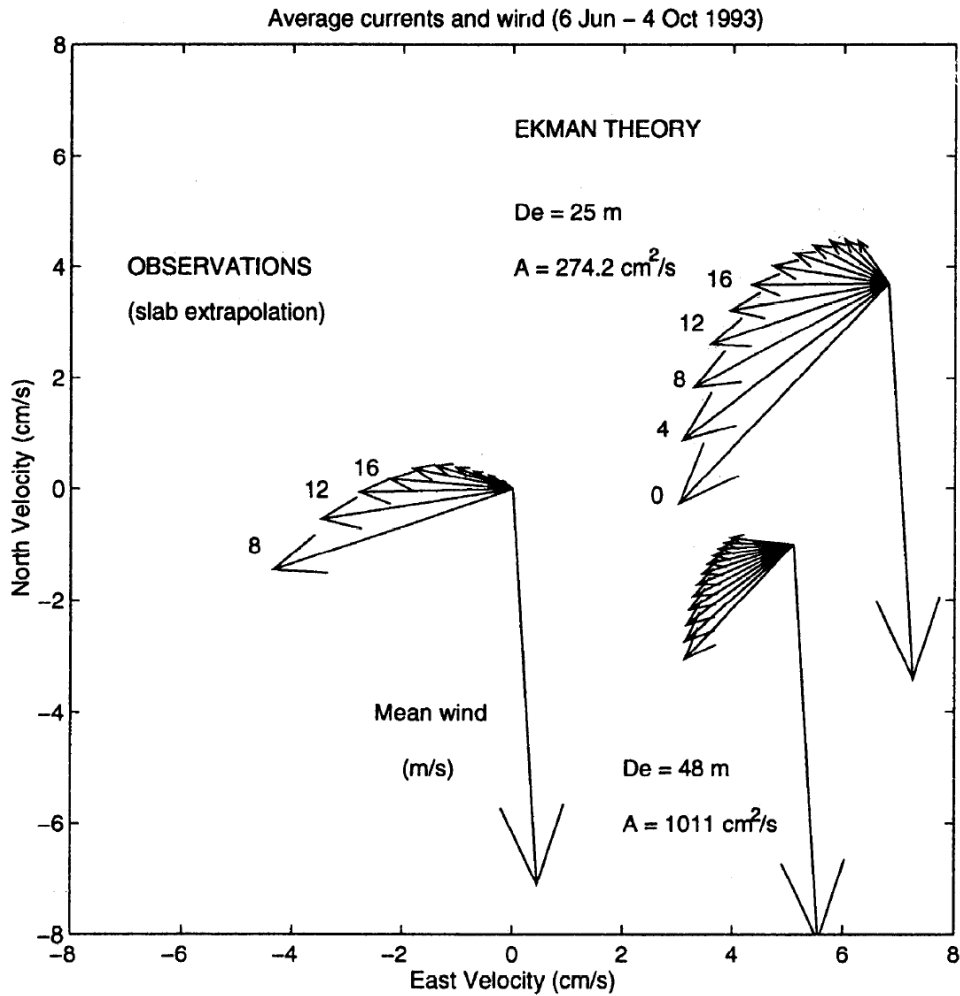


Figure 2.21: Observed mean Ekman spiral (left) and theoretical Ekman spirals computed from decay scales estimated amplitude decay (right, top) and the rate of rotation (right, bottom). From Chereskin (1995).

This mismatch in eddy viscosities raised the question of whether a uniform eddy viscosity was a sensible parameterization. To further examine this question Chereskin (1995) returned to the relationship between stress and shear:

$$T_{xz} = \rho k \frac{\partial u}{\partial z} \quad (2.6)$$

Thus, if shear and stress profiles are available it is possible to calculate a profile of eddy viscosities. Shear by definition was easily obtainable from the velocity observations. Stress on the other had to be estimated from the relationship:

$$T(z) = T_0 - \rho \int_z^0 -2\Omega \times \vec{u}_E dz \quad (2.7)$$

Where $T(z)$ is the stress at depth z , T_0 is the stress at the surface (i.e. the wind stress), Ω is the Earth's rate of rotation and u_E is the Ekman velocity. The resulting eddy viscosity profile when an upper boundary condition requiring $T(z=0)$ be equal to the wind stress is imposed is shown in Figure 2.22. This procedure produced estimates of eddy viscosity of between 100 and 200 $\text{cm}^2 \text{s}^{-1}$ between 10m and 30m, closer to the amplitude based estimate of k from the observed spiral.

Chereskin (1995) concluded that the EBC data indicated that the wind-driven portion of the observed flow was in Ekman balance over time periods greater than a few days; that estimates of Ekman transport from current and winds matched well and that the mean Ekman currents took the form of a smooth, 'compressed' spiral similar to previous observations (Price et al., 1987).

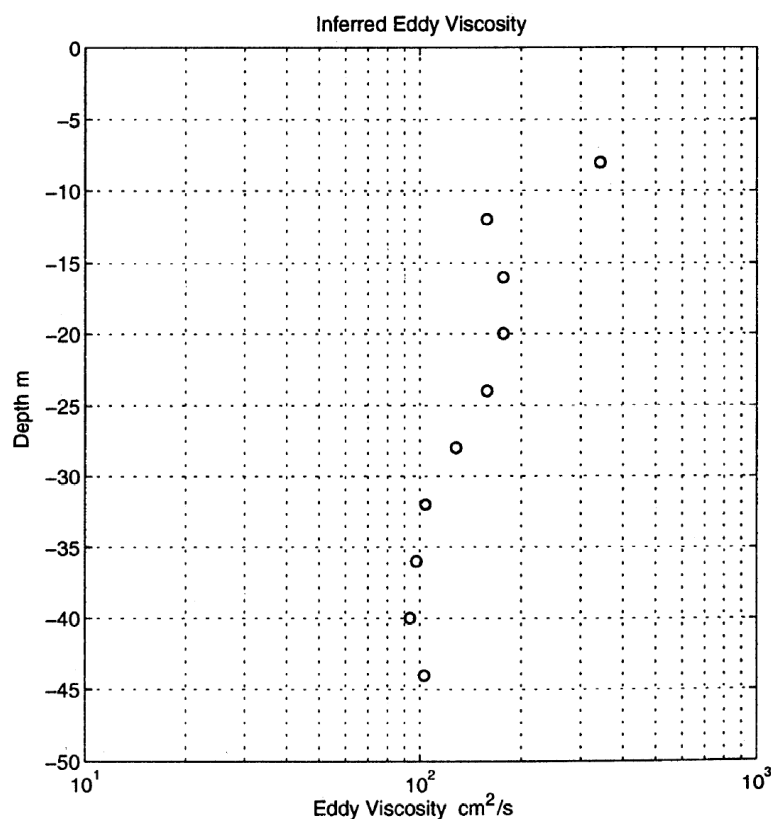


Figure 2.22: Eddy viscosity profile inferred via Equation 2.7 from observed shear and stress. From Chereskin (1991).

h. Previous Southern Ocean Observations

Prior to the start of this project there had been just two studies of Ekman currents in the Southern Ocean: Lenn and Chereskin (2009) investigated Ekman currents using ship-board ADCP observations in the Drake Passage, while Elipot and Gille (2009a, 2009b) used spectral methods to examine surface drifter data. Subsequently, a third study (Polton et al., 2013) was published re-examining the Drake Passage ADCP data used by Lenn and Chereskin (2009) to investigate the effect of depth varying geostrophic velocities on the structure of Ekman currents.

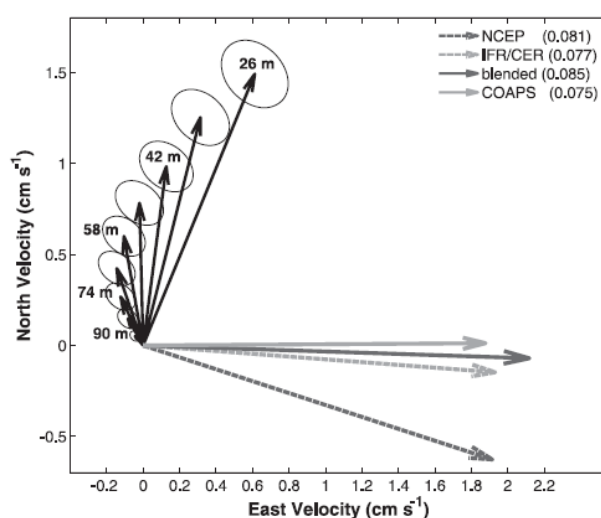


Figure 2.23: Observed mean current profile (solid black vectors) and mean wind stresses (Nm^{-2}) from four reanalysis products. From Lenn and Chereskin (2009).

Lenn and Chereskin (2009) examined data collected by a 153.6kHz ADCP aboard the *Laurence M. Gould* during 156 crossings of the Drake Passage between September 1999 and October 2006. The mean cross-track geostrophic shear was computed from XBT/XCTD surveys and compared with the corresponding mean ADCP observations of shear; the ADCP shear was found to diverge from the XBT shear at approximately the 100m level, suggesting that this depth represented the base of the mean Ekman layer. ADCP currents were then gridded into 25km boxes and averaged to give one profile from each transect per box. Ekman current profiles were then generated by subtracting a deep reference velocity (here taken to be 98m) from each gridded velocity profile. Averaging over all Ekman current profiles resulted in a mean current spiralling anticyclonically and

decaying with depth (Figure 2.23). Least square fits to the amplitude decay and rotation of this mean spiral gave eddy viscosities of 0.0308 and $0.2210\text{m}^2\text{s}^{-1}$ respectively.

Mean Ekman transport was then computed by assuming the velocity was constant between 26m and the surface before integrating the observed Ekman spiral from 98m to the surface. This transport was then compared to transport estimated from a variety of wind products (Figure 2.24). Three of the four products agreed with the observations at the 95% level. Similar analysis over subsets of the dataset by season or latitude did not display agreement with the wind-derived transport estimates.

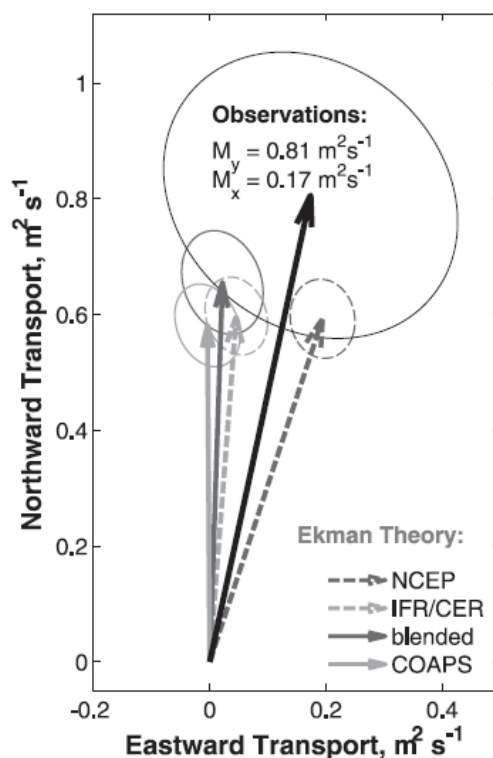


Figure 2.24: Observed mean current profile (solid black vectors) and mean transports computed from four reanalysis products. From Lenn and Chereskin (2009).

Lenn and Chereskin (2009) then computed profiles of viscosity using a similar method to that employed by Chereskin (1995). Varying from Chereskin's method Lenn computed viscosity profiles based upon the vectors rather than magnitude of the stress and shear. Stress and shear were typically found to not be parallel, resulting in a complex eddy viscosity (Figure 2.25). Eddy viscosity

magnitude was found to decrease with depth from approximately $0.1\text{m}^2\text{s}^{-1}$ at 26m to near zero at the base of the Ekman layer. The phase of the viscosities was found to be negative; indicating that at a particular depth stress was offset to the right of the corresponding shear vector. Lenn and Chereskin (2009) suggested that the observed complex viscosity either arose as an artefact of the averaging process (Price and Sundermeyer, 1999) or as the addition of a skewed component to the stress tensor, possibly arising from interactions with internal and surface gravity waves.

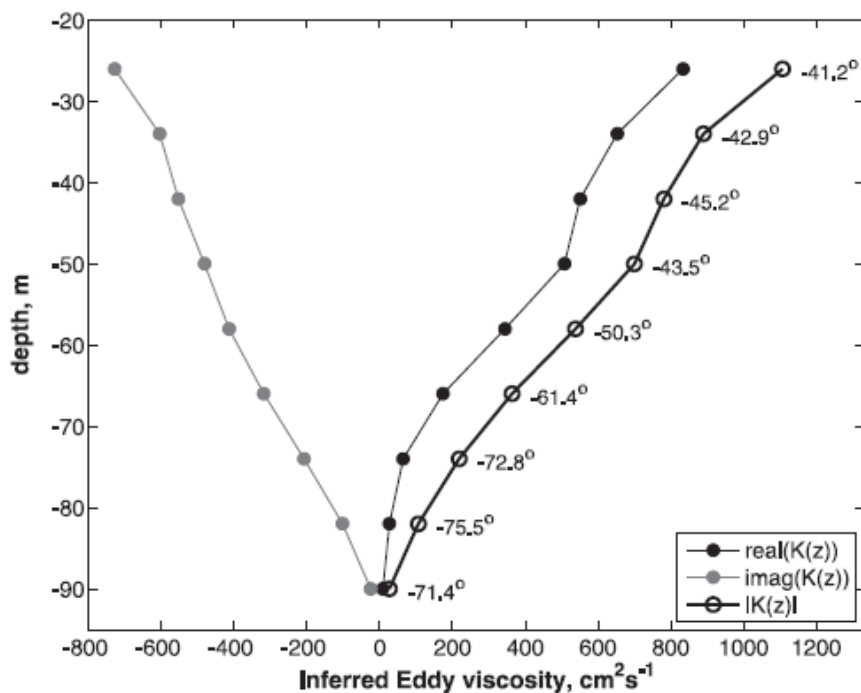


Figure 2.25: Mean eddy viscosity profile inferred from observed mean stress and shear. From Lenn and Chereskin (2009).

Elipot and Gille (2009a) adopted a rotary spectral technique to fit nine conceptual models (Figure 2.26) of Ekman currents to observations taken with drogued surface drifters between 30° and 60° S. Data was sourced from drifters with drogues set at 15m depth deployed during the Surface Velocity Program and the Global Drifter Program; these drifters were tracked by the ARGOS array and resulting trajectories and velocities interpolated at six-hour time intervals.

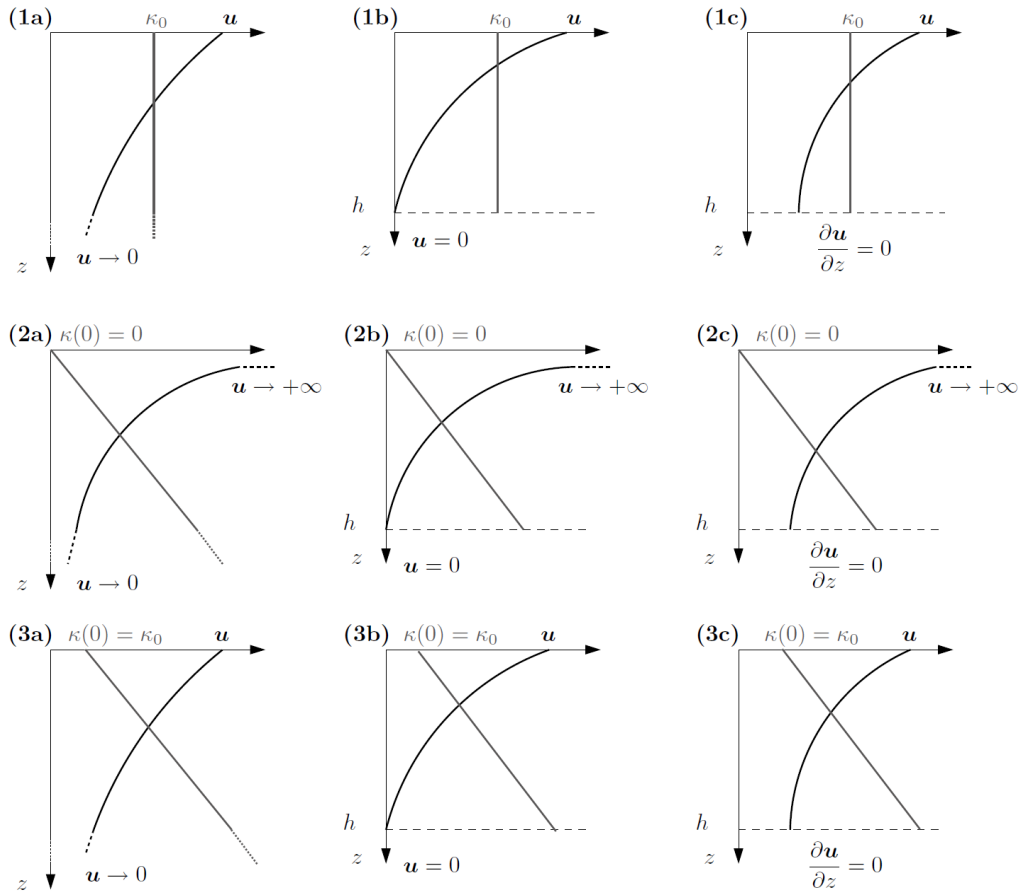


Figure 2.26: Schematics of the 9 conceptual models from Elipot and Gille (2009). These models consist of combinations of three types of viscosity profile with three bottom boundary conditions. Class 1 models (top row) assume a constant viscosity (κ_0); class 2 (middle row) assume a viscosity increasing at a constant rate (κ_1) from 0 at the surface; class 3 (bottom row) assume a viscosity increasing at a constant rate from a non-zero value at the surface. These viscosity profiles are then combined with three bottom boundary conditions: an infinite depth Ekman layer (a, left column); a “one layer” model in which velocity approaches zero at a finite depth, h , (b, middle column) and a “one and a half layer” model in which shear tends to zero at depth h (c, right column).

Elipot and Gille (2009a) isolated trajectories of at least 40 days duration between October 1992 (the start of TOPEX/Poseidon altimetry data) and August 2002 (the end of the ERA-40 reanalysis dataset). These trajectories were then divided into 40-day long segments and sorted into 2° latitude bands. Geostrophic velocities were estimated from a combination of a time varying term estimated from AVISO sea level anomalies and a time mean term derived from the GRACE mean

dynamic topography interpolated onto the drifter tracks. Ageostrophic velocities at 15m depth were then obtained by subtracting the geostrophic velocities from the corresponding velocities estimated from the drifter trajectories. Time series of wind stresses corresponding to each drifter trajectory segment were then obtained from the ECMWF ERA-Interim reanalysis dataset.

For each latitude band the wind-stress autopower-spectrum ($P_{\tau\tau}$) and wind-current crosspower-spectrum ($P_{\tau u}$) were estimated using the periodogram method. The observed transfer function was then defined as the ratio of the cross-spectrum to the auto-spectrum:

$$H_{obs}(\nu, z) = \frac{P_{\tau u}}{P_{\tau\tau}} \quad (2.8)$$

Model parameters were then obtained by fitting transfer functions (H_m) for each of the nine models to the observed transfer function over the frequency (ν) range of -2 to 2 CPD by minimising the cost function (L , the difference between transfer functions weighted by the coherence γ^2) using a simplex search technique:

$$L = \sum_{\nu_k} |H_m(\nu_k) - H_{obs}(\nu_k)| \times \gamma(\nu_k)^2 \quad (2.9)$$

Errors were estimated using a bootstrap method. Further details of the fitting procedure and error analysis are discussed in Chapter 4.

Model parameters and minimum cost function values obtained by this method for each latitude band are shown in Figure 2.27. Class C (one and a half layer) models were typically found to produce viscosity parameters (k_0 and k_1) closely comparable to the corresponding infinite depth models; meanwhile boundary layer depths (h) produced by class C models were found to be deep, varying between 10^3 and 10^4 m, comparable to or greater than the depth of the ocean. This implied that all class C models were effectively 'degenerate' to the corresponding class A models, and therefore offer no meaningful improvement. Disregarding class C models, Elipot and Gille (2009a) determined that single layer models performed better than the infinite depth models, with model 1B

being the best performing followed by model 3B. Interestingly, the classical Ekman model (1A) was found to be the least satisfactory model.

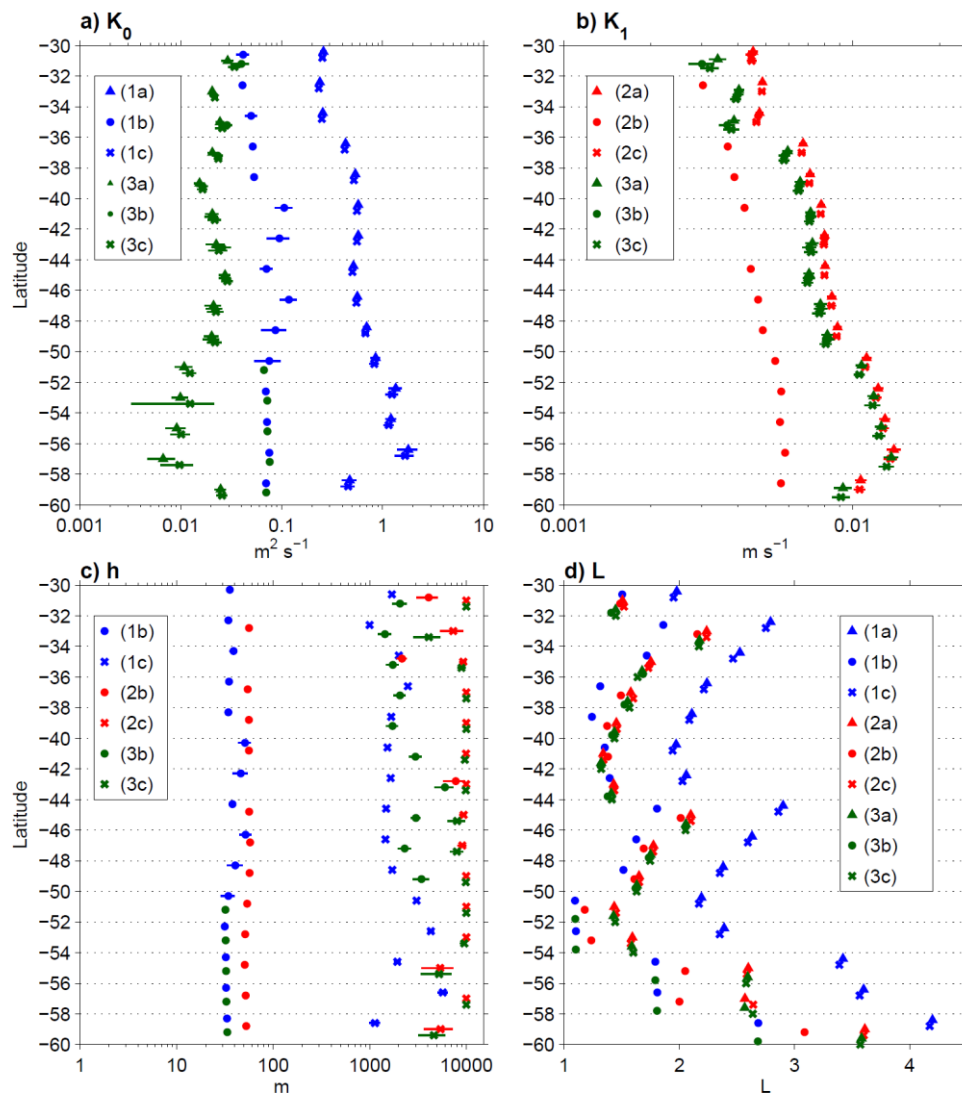


Figure 2.27: Estimates of eddy viscosity (a); viscosity gradient (b) and boundary layer depth (c) for all models; error bars indicate mean absolute deviation. Model performance as measured by the minimum cost function value (d).

Polton et al. (2013) considered the same dataset as Lenn and Chereskin (2009) supplemented with additional data collected on voyages between October 2006 and April 2011. Salinities for the XBT surveys were inferred from a salinity-temperature-depth regression and geostrophic velocities computed from the resulting density profiles. The data was then processed in line with Lenn and Chereskin (2009). Resulting velocity sections across the Drake Passage are shown

in Figure 2.28. The cross-track geostrophic velocity inferred from the XBT data displayed a depth varying structure. Comparison of the ADCP cross-track velocity with the XBT velocity suggests the geostrophic component dominates the cross-track flow. The along-track ADCP velocities were also found to display variability of similar magnitude to the cross-track case, suggesting that it also should be accounted for in the geostrophic current and shear. This behaviour strongly suggests that the vertical structure of geostrophic currents should be explicitly resolved when isolation Ekman currents.

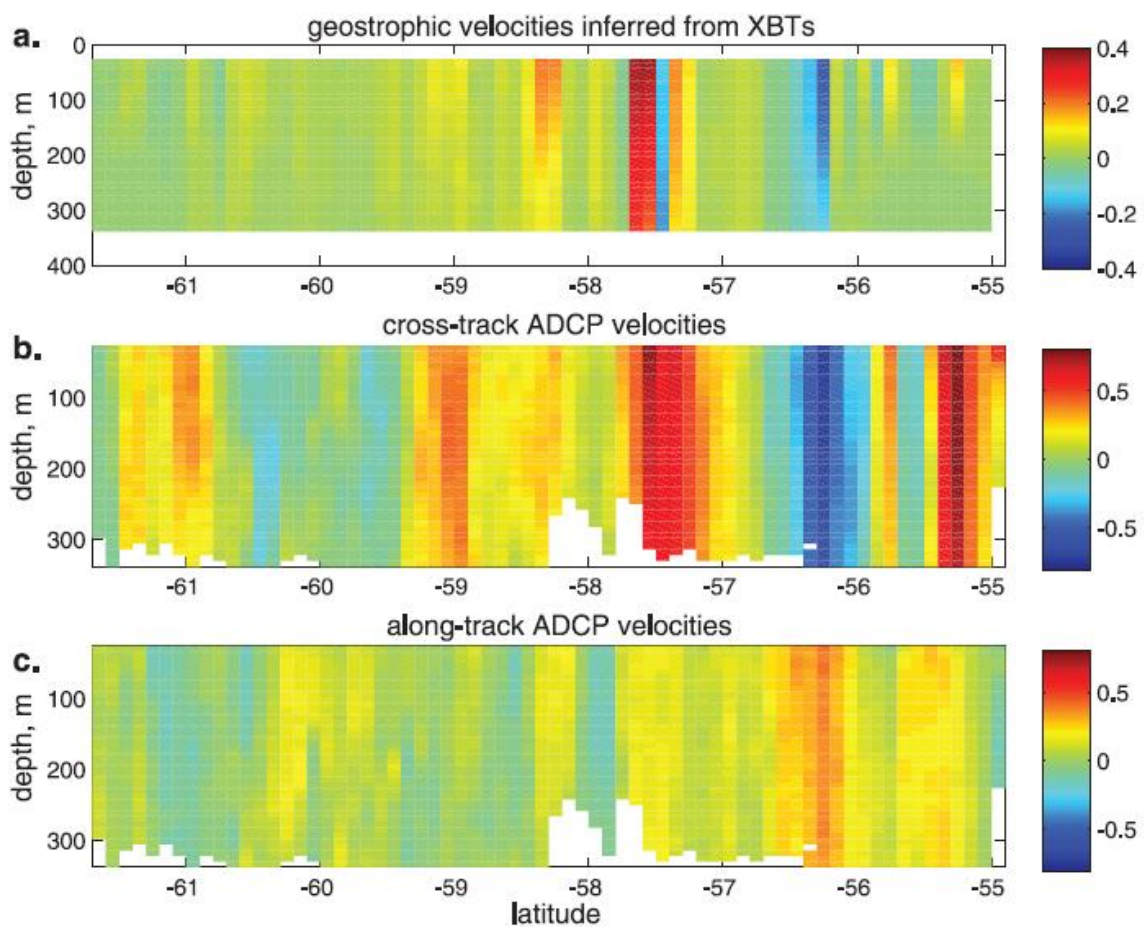


Figure 2.28: An example transect across the Drake Passage showing velocities (ms^{-1}) inferred from density profiles (a) or obtained from ADCP observations (b and c). From Polton et al. (2013).

Polton et al. (2013) then isolated geostrophic shear by sorting the ADCP current profiles into 25x25km grid boxes; in each box a mean current profile was calculated and the mean geostrophic shear obtained from the slope of a linear fit to the mean profile between 150 and 300m. For each

ADCP profile geostrophic currents were then estimated by taking the observed velocity at 150m and extrapolating linearly to the surface using the mean geostrophic shear from the grid-box the ADCP profile was located in. Ekman currents were then obtained by subtracting the extrapolated geostrophic current profile from the observed ADCP velocity profile. Profiles of mean Ekman current phase and log current magnitude (Figure 2.29a, large symbols) obtained using this method displayed closer agreement than when geostrophic shear was neglected (small symbols). The resulting mean current spiral (Figure 2.29b) was found to be consistent with a constant viscosity spiral.

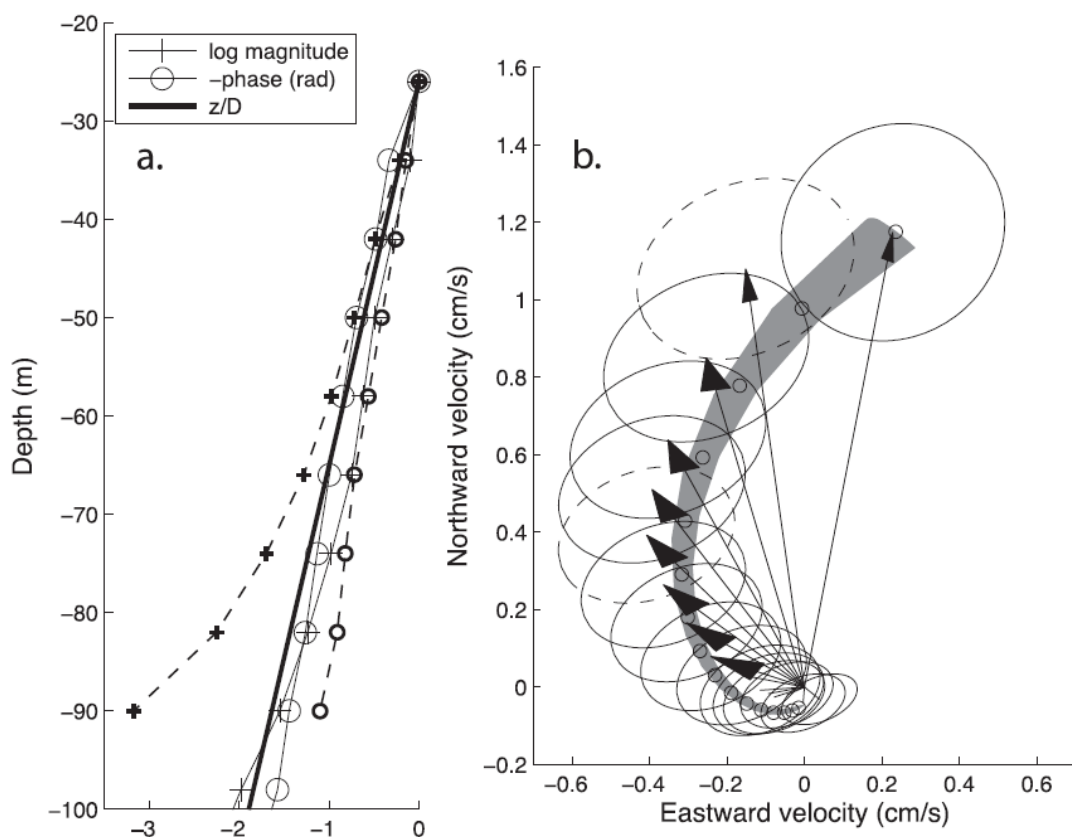


Figure 2.29: Mean profile of log current magnitude and phase (a, relative to the shallowest observation) using a constant geostrophic velocity (small symbols, dashed lines) or a constant geostrophic shear (large symbols, solid lines). Hodograph and standard error ellipses (b) for the mean Ekman current profile. The dark grey region bounds the range of a set of hodographs consistent with a constant viscosity 'classical' Ekman model. From Polton et al. (2013).

These findings indicate that the “compression” of the mean Ekman spiral, previously attributed to stratification induced surface trapping (Price et al., 1987), can arise as a side effect of using a constant geostrophic velocity when isolating Ekman currents. This in turn, suggests that ‘classical’ constant viscosity Ekman theory is adequate and raises questions of whether density stratification is actually relevant to our understanding of Ekman currents.

Chapter 3: Detecting and Characterizing Ekman Currents

3.1 Introduction

Previous studies have established the validity of the relationship between wind stress and net Ekman transport and observed Ekman-like spirals in data averaged over long time periods in a coordinate frame relative to the wind (Chereskin, 1995, Lenn and Chereskin, 2009). However, the vertical structure of both Ekman spirals and Ekman transport is still poorly understood. Previous studies have found the ‘classical’ constant viscosity model inadequate and identified behaviour suggestive of links to stratification in the mixed layer. Additionally, despite the importance of Ekman transport in the Southern Ocean, there have been few previous observational studies in the region (Lenn and Chereskin, 2009, Elipot and Gille, 2009a).

In this chapter we present a dataset of approximately 1400 concurrent temperature, salinity and horizontal velocity profiles. These profiles were collected with 8 EM-APEX (Electro-Magnetic Autonomous Profiling eXplorer) velocity profiling floats (Sanford et al., 2005) deployed north of Kerguelen Island as part of the 2008 Southern Ocean FINE-structure (SOFINE) expedition (Naveira Garabato et al., 2009). We isolate and describe Ekman currents within the EM-APEX data and then proceed to investigate the resulting Ekman transport, with particular attention to its vertical structure and relationship with stratification.

3.2 Datasets

a. EM-APEX Float Velocity Profiles

The data used in this study were collected using eight EM-APEX floats (see Chapter 2, Section 2.2b) deployed north of Kerguelen Island in November 2008 in conjunction with the SOFINE expedition (Figure 3.1). The floats returned over 1400 profiles down to 1800m with samples spaced approximately 3m in the vertical. The horizontal separation of profiles was approximately 2-10 km depending on the mean currents. Within the Kerguelen Island region, all floats took four profiles

(two descent-ascent cycles) per day. Once downstream of Kerguelen Island floats were reprogrammed to produce 'bursts' of four profiles a day with each burst separated by nine days.

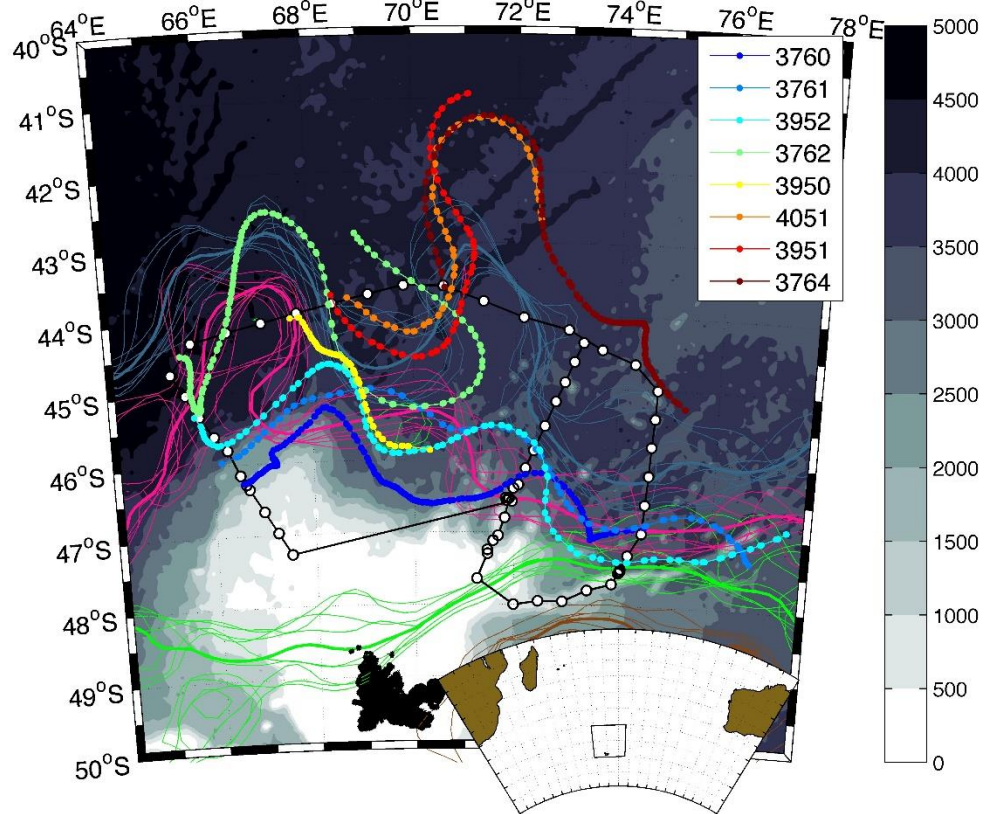


Figure 3.1: Location of profiles from 8 EM-APEX floats (coloured circles). SOFINE cruise track and CTD locations (white circles). Background shading (m) is Smith and Sandwell (1997) bathymetry. Coloured contours from north to south mark the location of the northern (grey), central (pink), and southern (green) branches of the Subantarctic Front, and the northern Polar Front (brown) based on sea surface height (SSH) labels. Weekly and mean front positions (fine and heavy lines, respectively) are shown for AVISO SSH anomalies over the period 18/11/2008-14/1/2009 added to mean dynamic height of 100 dbar relative to 2500 dbar (Sokolov and Rintoul, 2009).

During this study the latitude of the EM-APEX floats ranged from 41°S to 49°S, with inertial periods between 15.9 and 18.2 hours. The profiling mission was designed so that while near Kerguelen Island the pairs of adjacent up casts or down casts were separated by approximately half an inertial period. This profiling allows the isolation and removal of velocities arising from inertial

oscillations. The complex velocity was modelled as the sum of subinertial complex velocity U_M (assumed to be approximately steady over inertial scale periods) and a time varying complex near-inertial velocity U_I .

$$U(t) = U_M + U_I(t) \quad (3.1a)$$

Where:

$$U_I(t) = A_I \times e^{i(\phi - ft)} \quad (3.1b)$$

Given two velocity vectors and the time interval between them we can solve for the subinertial current and for the amplitude (A_I) and phase (ϕ) of the inertial current. Thus, for each pair of profiles spaced approximately half an inertial period apart we found the corresponding subinertial velocity. Calculated subinertial velocities were subsequently linearly interpolated back onto profile locations, producing the dataset used for all subsequent analysis. Only profiles with a time separation within 10% of half the inertial period at their mean latitude were included in this analysis.

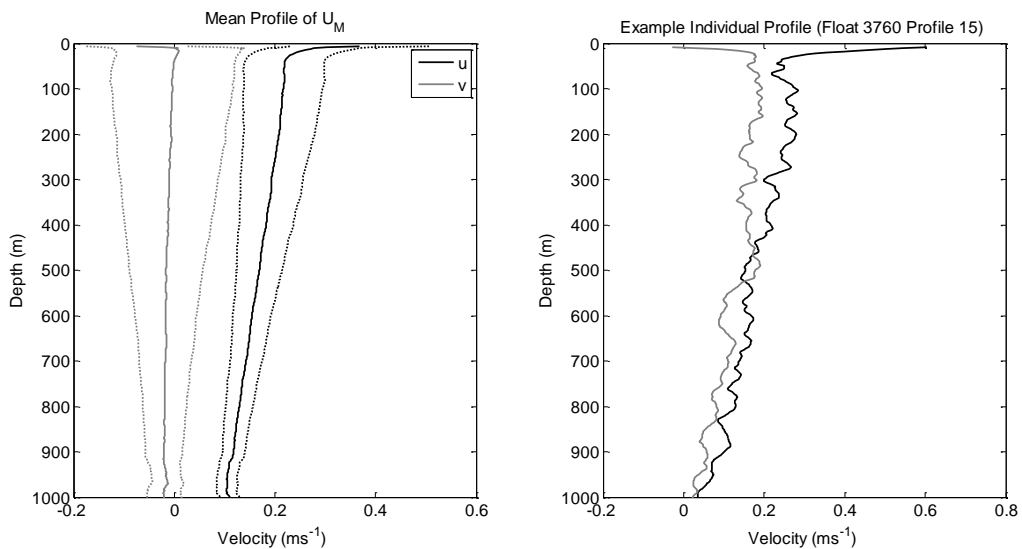


Figure 3.2: Time-mean subinertial profile (left) and an example subinertial profile (right). Grey lines denote the v component and black lines denote the u component. Dashed lines in the time-mean profile indicate the variance of the data about the mean.

The mean non-inertial current profile and an example profile of U_M are shown in Figure 3.2. The time-mean u profile is consistently positive (to the east) as would be expected from the mean

flow of the ACC, while the mean profile of the v component is close to zero over the majority of the water column. Both u and v components display significant variability about the time mean values. Both time-mean and individual cast profiles display higher flow speed within the upper 50m.

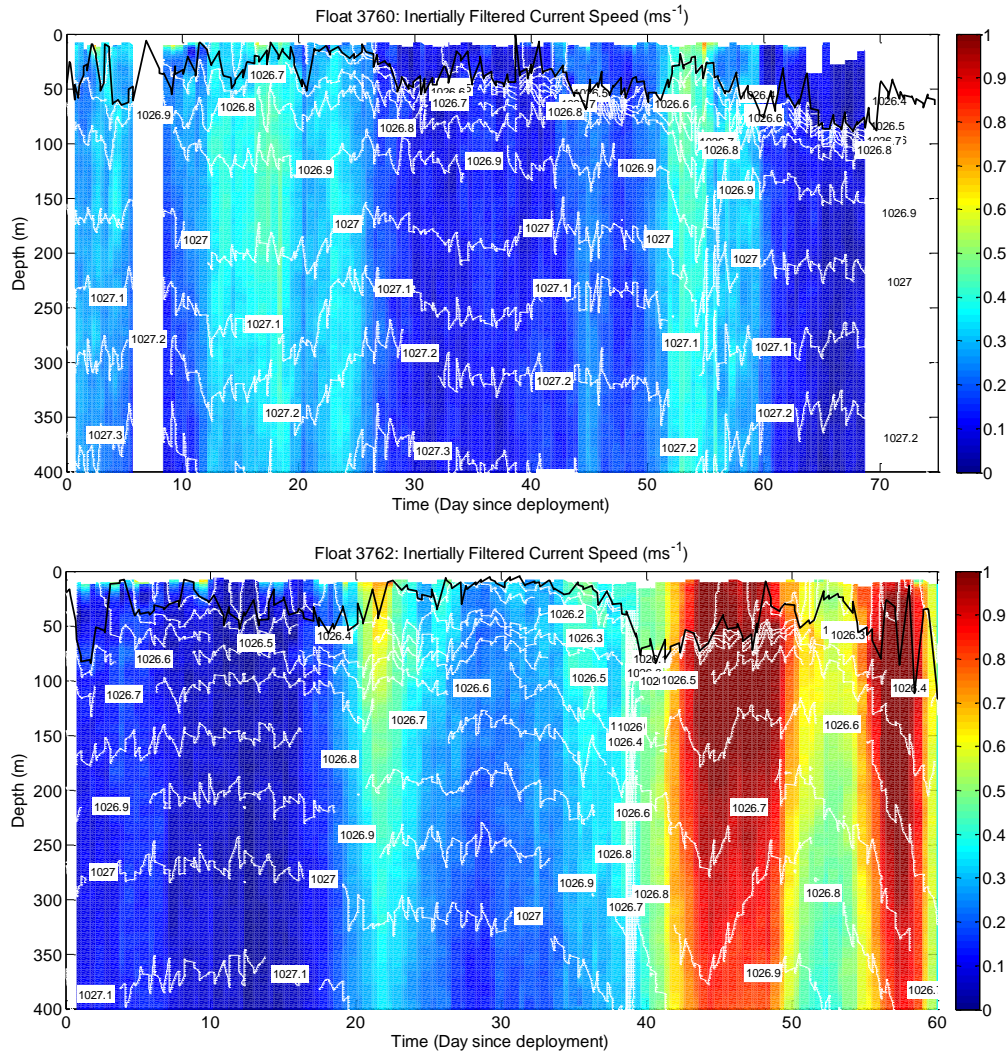


Figure 3.3: Inertially filtered current speed (ms^{-1}) as a function of depth and time from floats 3760 (top) and 3762 (bottom). White contours indicate potential density isopycnals. The black line marks the mixed layer depth using a density criterion of $\Delta\sigma < 0.03 \text{kgm}^{-3}$ relative to the upper-most observation (Sallée et al., 2006).

Examples of current observations as a function of time from the floats are shown in Figure 3.3, corresponding plots of temperature and salinity are shown in Figures A1.1 and A1.2. Float 3760 (Figure 3.3, top) was deployed south of the central branch of the Subantarctic front before drifting closer to the front resulting in a warming and deepening mixed layer. Float 3762 was deployed

between the northern and central branches of the Subantarctic front and ended up following and ultimately crossing the northern branch of the Subantarctic front near the 40 day mark.

b. Wind Data

To examine the wind forcing within the Kerguelen region we used gridded wind fields (Bentamy et al., 2009) produced by the Institut Francais de Recherche pour l'Exploitation de la Mer (IFREMER), Department of Oceanography and the Centre ERS d' Archivage et de Traitement (CERSAT). This dataset was produced by merging QuickSCAT scatterometer winds with SSM/I radiometer wind speeds and ECMWF reanalysis wind fields using an objective method (Bentamy et al., 2009). The resulting 10m wind fields offer 0.25° spatial resolution and 6 hour temporal resolution.

Wind velocities from the blended wind fields were interpolated onto the time and location of each EM-APEX profile and then converted to wind stresses using drag coefficients based on Yelland and Taylor (1996). These wind fields are smoothed both temporally and spatially, and we will return to this point later in this chapter.

c. TPXO7.2 Tides

To investigate the potential for tidal signals to affect our observations we used the TPXO7.2 barotropic tide inverse model with global 0.25° resolution. Details of the model can be found in Egbert and Erofeeva (2002). The model was evaluated to determine tidal velocities at the times and locations of all EM-APEX float profiles.

d. ERA-Interim Wave Data

Mean wave period, significant wave height and mean wave heading were sourced from the ECMWF's ERA-Interim reanalysis dataset (Persson, 2011). This dataset is derived from an atmospheric model coupled to a WAM type ocean wave model (WAMDI Group, 1988), driven by

data assimilated from a variety of sources. The resulting dataset has a 0.25° spatial resolution and a 6 hour temporal resolution.

3.3 Method

a. Isolating Ekman Currents

Ekman currents are the ageostrophic flow field where the primary balance is between the wind stress and the coriolis force. Having filtered near-inertial currents out of the velocity profiles it was necessary to remove the geostrophic component to isolate the Ekman currents. An obvious approach would be to calculate geostrophic velocities from the hydrographic data collected by the floats using the thermal wind equations. In practise, this is impractical as the EM-APEX floats tend to follow streamlines, so that using the thermal wind equations would only resolve the weak cross-stream flow. Hence, we tested two alternative approaches for estimating the geostrophic flow.

First, in line with a number of previous studies (Lenn and Chereskin, 2009, Chereskin, 1995) we assumed there was no geostrophic shear within the upper ocean, and so defined the sub-inertial currents in the Ekman layer to be the sum of the depth-varying Ekman currents (U_{ek}) and a constant geostrophic reference velocity (U_{deep})

$$U_M(z) = U_{ek}(z) + U_{deep} \quad (3.2)$$

$U_{ek}(z) = u_{ek} + i v_{ek}$ was assumed to follow the solution associated with a “classical” Ekman spiral with components u_{ek} (east) and v_{ek} (north) defined as:

$$u_{ek} = V_0 e^{\frac{z}{D_e}} \cos\left(\frac{-z}{D_e} + \theta_0 + \frac{\pi}{4}\right) \quad (3.3a)$$

$$v_{ek} = V_0 e^{\frac{z}{D_e}} \sin\left(\frac{-z}{D_e} + \theta_0 + \frac{\pi}{4}\right) \quad (3.3b)$$

Where the depth, z , is taken as positive upwards; V_0 denotes the surface current speed, θ_0 denotes the wind stress heading (here in radians). D_e denotes the Ekman decay scale, with positive

values corresponding to anticlockwise rotation (as expected from Ekman theory) and negative values corresponding to reversed rotation. U_{deep} is chosen to be the velocity at a level below which the Ekman component should be negligible.

During their study within the Drake Passage, Lenn and Chereskin (2009) used a reference velocity at a depth of 98m based on ADCP measurements of shear from multiple voyages over a period of 7 years. We lack a long record of shear in the Kerguelen region independent of the EM-APEX data; instead we selected the deep reference velocity based on mixed layer depth (MLD). Within the Kerguelen region Sallée et al. (2006) indicated MLDs of less than 100m in summer and up to 200m in winter. On this basis the reference velocity to be used as a proxy for the geostrophic velocity for each profile was defined as the observed velocity at 200m. For the rest of this paper we shall denote this method of defining the geostrophic velocity the “No Shear” case.

For each profile two Nelder-Mead (NM) simplex searches (Nelder and Mead, 1965) were run over the 0-50m depth range to search for the parameters V_0 , θ_0 , and D_e which minimized the cost function, L:

$$L = \sum_{0m}^{50m} |U_{\text{fit}}(z) - U_M(z)|$$

The first set of solutions with the Nelder-Mead algorithm assumed an Ekman component with anticlockwise rotation (as expected in the Southern Hemisphere), and the other solution assumed an Ekman component with clockwise rotation. Initial inputs for both simplex searches were taken to be an Ekman decay scale of 20m, a surface velocity with speed estimated from the upper-most ocean velocity observation and heading based upon the wind stress. For each profile we selected the NM fit which produced the smaller L for our subsequent analysis. Note the solution of this system of equations is intrinsically non-linear since the surface current speed, current heading and Ekman decay scale appear inside the terms on the right side of Equation 3.3a and 3.3b.

The assumption of a constant geostrophic velocity within the mixed layer is not supported by observations undertaken during SOFINE (Phillips and Bindoff, 2014). In these observations the

ACC displayed strong depth-varying flow. Additionally, geostrophic flow and mean wind displayed similar mean headings. It is therefore possible that depth-varying geostrophic flow has been included in our estimate of the Ekman velocity. In light of this we considered two cases (henceforth denoted as “Shear 1” and “Shear 2” cases) in which we assumed the complex near surface sub-inertial currents (U_M) could be described as the sum of an Ekman component (U_{ek}), a constant reference velocity (U_{deep} , here taken as the velocity at the 200m level) and a component arising from a constant geostrophic shear:

$$U_M(z) = U_{ek}(z) + U_{deep} + \frac{dU_{geo}}{dz} \cdot z \quad (3.4)$$

In line with the no shear case two Nelder Mead simplex searches were run to fit parameters V_0 , θ_0 , D_e and the linear shear across the Ekman Layer (i.e. $\frac{dU_{geo}}{dz}$ is constant). Initial inputs for V_0 , θ_0 , D_e were taken as per the no shear case, while those for the shear components were taken as the shear between the 100m and 200m levels. We selected the 100-200m geostrophic shear as a first guess based upon previous studies and decay scales observed in the “no shear” fits (section 3.4a), both of which suggest Ekman currents should be weak below 100m depth. The probability distribution of the geostrophic shear is discussed in Section 3.4a (Figure 3.6).

For “Shear 1” we assumed the Ekman component typically consisted of a “classical” spiral and, hence, took the solutions generated by the NM fit initialized assuming anticlockwise rotation. For the “Shear 2” case we considered the possibility of the Ekman component often displaying reversed rotation as seen in frequency domain solutions of the Ekman equations (Elipot and Gille, 2009a) and Chapter 4. Hence, for each profile we considered NM fits initialised with both clockwise and anticlockwise rotation and took the solution from whichever one of the two displayed the minimal residual. It is worthwhile noting that despite the assumed starting conditions both the “Shear 1” and “Shear 2” Nelder-Mead fits can produce both Ekman-like and reversed spirals.

Having obtained estimates of the parameters discussed above we next examine the performance of the “No Shear” and both shear cases and identify any individual profiles that display Ekman spirals. The classical Ekman spiral can be separated into a velocity amplitude component decaying exponentially with increasing depth and a unit vector component rotating anticlockwise as a linear function of increasing depth:

$$|u_{ek}(z) + iv_{ek}(z)| = V_0 e^{\frac{z}{D_e}} \quad (3.5a)$$

$$\theta(z) = \frac{z}{D_e} \quad (3.5b)$$

The fraction of variance (R^2) values in each observed profile of current speed and heading captured by the Nelder-Mead fits of Equations 3.5a and 3.5b were calculated and used as diagnostics to quantify the presence of rotation and amplitude decay with depth. If the R^2 for the fit to current amplitude exceeded 0.75, and the rotational R^2 exceeded 0.5 and the decay scale D_e was less than 500m, the profile was classified as displaying a spiral and the direction of rotation was obtained. Eddy viscosities (k) were then calculated from estimated Ekman layer depths and the Coriolis parameter (f) as:

$$k = \frac{D_e^2 |f|}{2} \quad (3.6)$$

Finally, we generated Ekman spirals for all profiles from the fitted Ekman decay scales using the solutions for the “classical” case which assumes constant wind forcing and constant density in the mixed layer. These estimated velocity profiles were subtracted from the corresponding observed velocities to obtain residuals which were then used to assess the performance of the fitting procedures (see Section 3.4a).

b. Estimating Ekman Decay Scales and Eddy Viscosities

Ekman decay depth is a product of the shear fitting procedure outlined above. However, in line with previous studies (Lenn and Chereskin, 2009, Chereskin, 1995) we also obtained estimates of Ekman depth based on the rate of rotation with depth of the horizontal velocity vector, and on the rate of velocity amplitude decay observed in each individual spiral. The parameters for Equations 3.5a and 3.5b were fitted independently of each other to the upper 50m of each velocity profile using a least squares technique. The fits produced two estimates of decay scale, D_{amp} , the amplitude fit (from Equation 3.5a) and D_{rot} the rotational fit (from Equation 3.5b). Analysis and classification of the velocity profiles then proceeded in the same manner as with the fits obtained through the Nelder-Mead method (see Section 3.3a).

c. Calculating Transport

The observed Ekman-like profiles were rotated into a wind-relative reference frame using wind estimates interpolated onto each profile's location and time from the CERSAT blended reanalysis-scatterometer wind fields (Bentamy et al., 2009), and mapped onto a regular 2m depth grid. This suppresses variability arising from variations in wind heading and allows our results to be compared with prior studies (Price et al., 1987, Schudlich and Price, 1998). Volume transport per unit path length (T) was obtained for each velocity profile by integrating observed ageostrophic velocities upwards from 200m to the shallowest velocity observation (z_i):

$$T(z_i) = \int_{200m}^{z_i} U_{ek} dz \quad (3.7)$$

The mean wind-relative transport was calculated by averaging all transport estimates. The observed near surface transport was then compared with estimates calculated from reanalysis winds using the well-established relationship (Chereskin, 1995):

$$T_x = \frac{\tau_y}{f\rho}, \quad T_y = \frac{-\tau_x}{f\rho} \quad (3.8)$$

Where τ_x and τ_y denote components of surface wind-stress and ρ denotes the density of the ocean mixed layer.

For both the observed Ekman transport profiles and the wind based transport estimates, confidence intervals (CI) based on 95% confidence intervals were calculated as:

$$CI = \bar{x} \pm \frac{1.96\sigma}{\sqrt{n}} \quad (3.9)$$

Where \bar{x} denotes the mean value; σ denotes the standard deviation and n denotes the number of degrees of freedom. We assumed one degree of freedom per 4 profiles (approximately one degree of freedom per day). The time-scale associated with this number of degrees of freedom, represents our understanding of the oceanographic noise (e.g. Figure 5.5), and because we are not interested in the relationship to weather events, is shorter than the dominant time period of weather systems of a few days. We did not consider additional degrees of freedom introduced by other factors (e.g. Stokes drift), hence, error bars in later sections may be conservatively wide.

Several studies have suggested that transport within the mixed layer can best be described with a slab-like model (Halpern, 1974, Wijffels et al., 1994), that is transport constant within the mixed layer with little transport occurring deeper in the water column. Other studies (Chereskin and Roemmich, 1991) suggest that this is not the case. To investigate this further we considered mean Ekman velocities and transport in a vertical coordinate system defined in terms of the mixed layer depth. Mixed layer depth was calculated from each EM-APEX density profile using a density criterion of $\Delta\sigma < 0.03 \text{ kg m}^{-3}$ relative to the upper-most observation (Sallée et al., 2006).

d. Local Estimates of Eddy Viscosity

The classical, steady-state Ekman solution (Ekman, 1905) is:

$$ifU_e = \frac{\tau(z)}{\rho} = k \frac{\partial U_e}{\partial z} \quad (3.10a)$$

Where U_e denotes the Ekman velocity in the form $u_e + iv_e$; τ the stress and k eddy viscosity.

This equation can be rearranged to give viscosity in terms of stress, Ekman shear and density (Lenn and Chereskin, 2009, Elipot and Gille, 2009a):

$$k(z) = \frac{\tau(z)}{\rho} \cdot \frac{1}{\left(\frac{\partial U_e}{\partial z}\right)} \quad (3.10b)$$

The stress profile can be estimated by integrating U_e upwards from a deep reference level (h_e):

$$\tau(z) = i\rho f \int_{h_e}^{z_i} U_e dz \quad (3.11)$$

We calculated stress, shear and viscosity from Equations 3.10b and 3.11 for all depth levels in each profile, and then generated a mean viscosity profile over all data. In a similar manner to our preceding analysis of transport we also remapped the resulting profiles into mixed layer depth space, prior to averaging.

3.4 Observed Ekman Spirals

a. Performance of Fitting Procedures

The number of Ekman spirals detected by each fitting procedure is given in Table 3.1 while RMS residuals between observations and fitted spirals for the 14m depth level are given in Table 3.2.

Notably, in all cases we identified not just profiles displaying Ekman-like spirals but also spirals that passed the classification procedure outlined above and displayed reversed rotation. These counter-rotating spirals may be consistent with cyclonic super-inertial wind forcing (Rudnick and Weller, 1993).

Example hodographs (the projection of the current profile onto the horizontal plane) of both anticlockwise and clockwise spirals are shown in Figure 3.4. The Ekman currents averaged over all

observations also displayed Ekman-like spirals. This was the case both for the velocities in a geographic reference frame, and where individual profiles were first rotated into along- and cross-wind components (Figure 3.5) at the time and place of the velocity observation.

	Number of Spirals	
	Ekman	Reverse
NM Shear 1	441	39
NM Shear 2	313	227
NM No shear	224	150
LS Shear 1	445	109
LS Shear 2	359	236
LS No Shear	249	186

Table 3.1: Number of Ekman-like spirals and reversed spirals detected in observed velocity profiles with either linear geostrophic shear or no shear assumed over the Ekman layer, and using either a Nelder Mead simplex search (NM) described in Section 3.3a or a least-squares fit (LS) described in Section 3.3b.

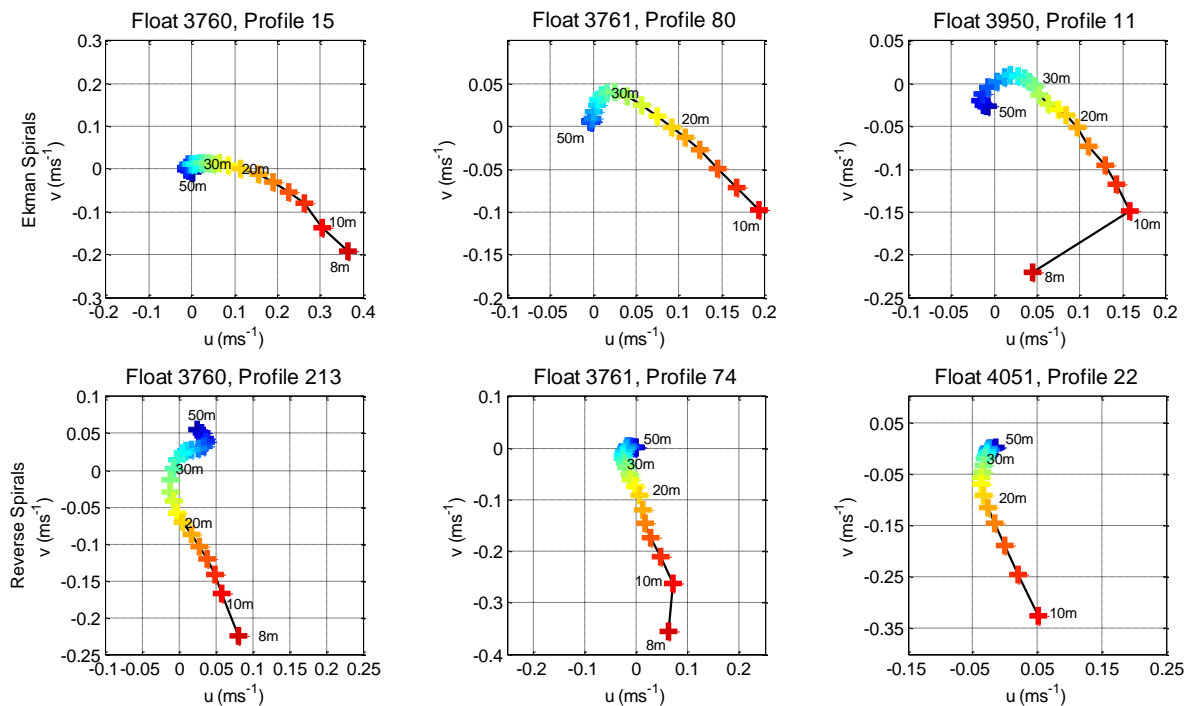


Figure 3.4: Examples of hodographs of individual EM-APEX float velocity profiles displaying Ekman-like (top row) and reversed (bottom row) spirals. Colours represent depths ranging from 8m (dark red) to 50m (dark blue).

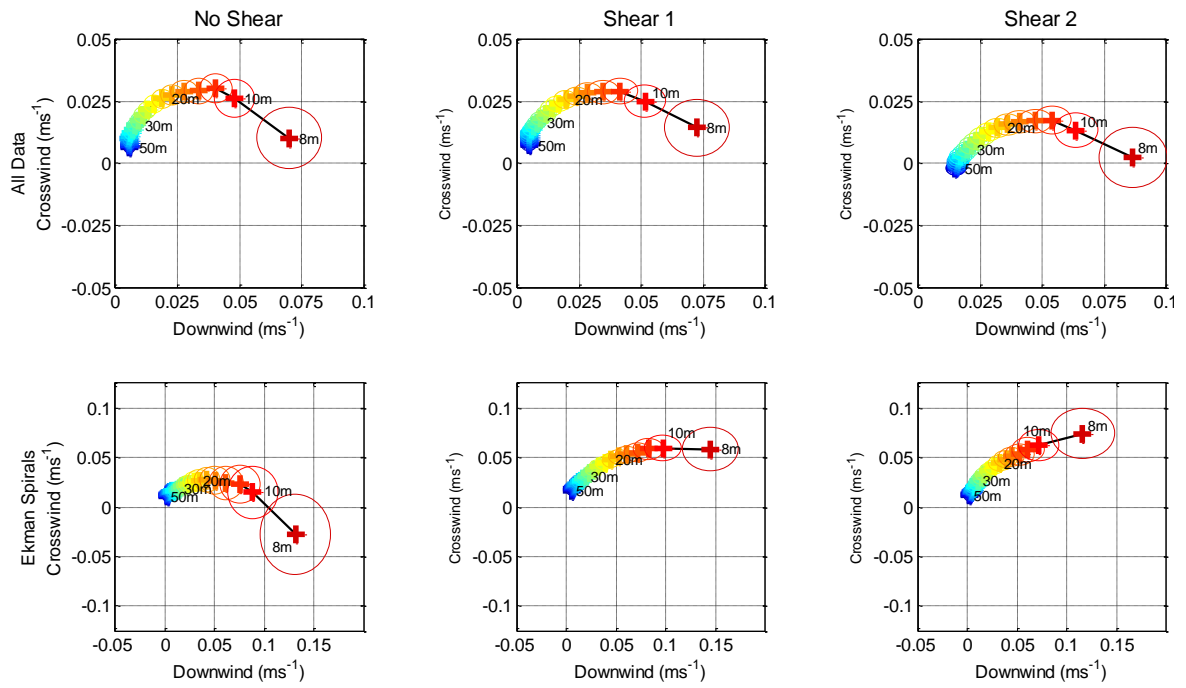


Figure 3.5: Hodographs of observed Ekman spirals when averaged over all profiles (top row) and all profiles displaying Ekman-like spirals (bottom row). Colours represent depths ranging from 8m (dark red) to 50m (dark blue). Ellipses represent 95% confidence intervals.

	<u>No Shear</u>				<u>Shear 1</u>				<u>Shear 2</u>			
	D_e	k	Number	RMS Residual	D_e	k	Number	RMS Residual	D_e	k	Number	RMS Residual
<u>Ekman Spirals</u>	(m)	($10^{-2} \text{ m}^2 \text{ s}^{-1}$)		(ms^{-1})	(m)	($10^{-2} \text{ m}^2 \text{ s}^{-1}$)		(ms^{-1})	(m)	($10^{-2} \text{ m}^2 \text{ s}^{-1}$)		(ms^{-1})
Rot. Fit	42.59±5.36	9.35±2.35	249	0.1376	40.18±4.61	8.33±1.91	455	0.1343	39.01±5.31	7.85±2.13	359	0.1265
Amp. Fit	25.1±2.66	3.25±0.69	249	0.0816	31.07±3.34	4.98±1.07	455	0.1026	31.40±5.31	5.09±1.72	359	0.0691
NM Fit	67.74±15.67	22.92±10.76	224	0.1171	38.53±4.59	7.65±1.82	441	0.0673	34.25±4.61	6.04±1.63	313	0.0557
All Data												
Rot. Fit	93.06±9.70	44.71±9.32	1091	0.1179	70.43±7.77	25.61±5.66	1217	0.1155	75.19±8.27	29.20±6.43	1220	0.1147
Amp. Fit	63.36±6.12	20.73±4.01	1091	0.1467	60.63±5.78	18.98±3.62	1217	0.1319	67.83±8.27	23.77±5.80	1220	0.1381
NM Fit	88.75±8.64	40.7±7.93	1397	0.0958	47.24±3.97	13.38±2.09	1397	0.0624	58.5±4.87	17.69±4.76	1397	0.0516

Table 3.2: Estimates of Mean Decay Scales; Eddy Viscosities and RMS residuals using the different methods outlined in section 3.3a and b. No shear and shear estimates of decay scale come from Equation 3.5a for amplitude and Equation 3.5b for rotation. Ekman spirals is for the analysis based entirely on profiles that fit the definition of an Ekman Spiral (see section 3.3a) and All Data is where all velocity profiles with decay scales of less than 1000m are used including those that do not meet the definition of a spiral and includes reverse spirals. 95% confidence intervals on decay scales were estimated using Equation 3.9, and errors in viscosity estimated by propagating the errors in D_e through Equation 3.6. RMS residuals were computed between observations and fitted spirals at 14m depth

Considered over all profiles that generated a valid decay scale (here taken as less than 1000m) the Nelder-Mead simplex fits (described in Section 3.3a) achieved smaller RMS velocity residuals than the least squares approaches (described in Section 3.3b) that were also tested. Nelder-Mead and least squares fits including shear generally outperformed the no-shear fit using the same technique. The fits with shear also displayed an increased number of Ekman-like spirals compared to the no-shear case. This suggests that to properly isolate Ekman currents, accurate knowledge of the vertical structure of geostrophic currents in the Ekman layer is also important.

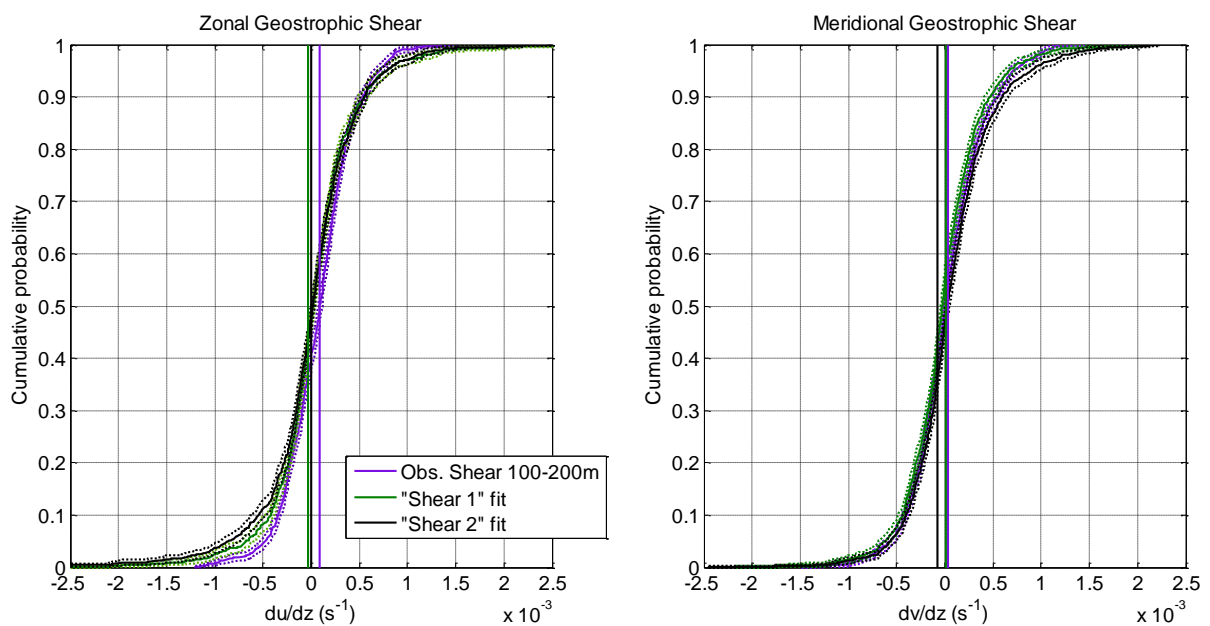


Figure 3.6: Cumulative Distribution Function plots of fitted geostrophic shear (“Shear 1” green; “Shear 2” in black) and shear observed between 100m and 200m (purple). Vertical lines mark the mean value of each distribution. Zonal shear is shown on the left and Meridional shear on the right.

Cumulative distribution functions (CDFs) of the fitted geostrophic shear are shown in Figure 3.6. The Southern Ocean is generally regarded as equivalent barotropic (i.e. current heading is constant through the water column but current speed evolves in a linear manner with depth) in nature (Meijers et al., 2011a) with strong mean eastward flow arising from the ACC jets. Hence, we would expect mean meridional shear close to zero and a positive mean zonal shear. In Figure 3.6 all estimates of meridional shear were close to zero, as expected. However, we found mean zonal shear close to zero. It is likely that this discrepancy is a result of the local oceanography of the Kerguelen

Plateau which features a complex system of eddies and meandering fronts and, based upon recent studies (Phillips and Bindoff, 2014), displays non-equivalent barotropic flow.

The “Shear 1” and “Shear 2” fits produced stronger, negative zonal (westward) geostrophic shear than seen in the observed 100m-200m shear. Otherwise, both Nelder-Mead fits produced geostrophic shear statistically consistent with the observed deep shear.

b. Ekman Layer Depths and Eddy Viscosities

Mean Ekman layer depths and resulting eddy viscosities (Table 3.2) were estimated over all profiles displaying decay scales of less than 1000m and over a subset of profiles identified as displaying Ekman spirals (as defined in Section 3.3a). Mean eddy viscosities obtained from the fits ranged between $3.25 \pm 0.69 \times 10^{-2} \text{ m}^2\text{s}^{-1}$ (no-shear amplitude fit over Ekman like spirals) and $0.447 \pm 0.0932 \text{ m}^2\text{s}^{-1}$ (no-shear rotational fit over all data), consistent with previous observations of 0.0308-0.2210 m^2s^{-1} within the Antarctic Circumpolar Current in the Drake Passage (Lenn and Chereskin, 2009).

Estimates of mean decay scale were found to be consistent over all three fitting methods for the “Shear 1” and “Shear 2” cases. However, in the no-shear case we found statistically significant differences in mean decay scale between the rotational and amplitude fits. This difference in decay scales could indicate a “compression” of the Ekman spiral, as observed in several prior studies (Price et al., 1987, Lenn and Chereskin, 2009, Chereskin, 1995), such that amplitude decays faster than predicted. Investigating this further we considered the ratio of D_{rot} to D_{amp} calculated on a profile by profile basis (rather than the mean basis discussed above). In the “shear 1” case the mean $D_{\text{rot}}/D_{\text{amp}}$ was found to be 1.55 ± 0.16 when just considering the Ekman like spirals and 2.55 ± 0.30 over all profiles with decay scales of less than 1000m. Ratios from the “shear 2” case were similar to the “shear 1” case. Corresponding ratios for the no-shear case were 2.01 ± 0.26 and 3.38 ± 0.40 respectively. These values are broadly consistent with previous studies (Price et al., 1987, Lenn and Chereskin, 2009, Chereskin, 1995), which also found D_{rot} to be around two times larger than D_{amp} . It has been suggested (Price et al., 1987, Price and Sundermeyer, 1999) that this “compression” may

be linked to stratification within the surface layers of the ocean. We discuss links between stratification and Ekman current further in Section 3.6.

3.5 Ekman Transport

a. Mean Transport

The mean profiles of cumulative Ekman transport integrated up from the 200m level (Equation 3.7) are shown in Figure 3.7. Vector plots of mean transport at the 14m level are shown in Figure 3.8. Due to the time needed for an EM-APEX float to ‘spin up’ at the start of its descent, observations are sparse between the 10m depth level and the surface. For example, at 8m depth, less than half the profiles have a valid velocity. Consequently, confidence intervals are wider at shallower levels. The low number of datapoints combined with the “Pandora’s box” of selecting an optimal method of extrapolating from deeper observations of transport to the surface prevents robust and direct comparisons of wind and velocity derived surface transports. Also, tests (not shown) of extrapolating transport to the surface either using a constant velocity or constant shear between the shallowest observation and 0m did not display statistically significant differences to the time-mean 14m observed transport. Thus, the mean transport magnitude calculated from reanalysis winds is instead compared with the observed mean transport at 14m.

Using Ekman velocities isolated as part of the no-shear case the mean transport observed at the 14m level was $0.93 \pm 0.28 \text{ m}^2 \text{ s}^{-1}$. Reanalysis winds gave a mean transport at the surface of $1.01 \pm 0.12 \text{ m}^2 \text{ s}^{-1}$. For the “Shear 1” case mean transport over all data was found to be stronger ($1.18 \pm 0.34 \text{ m}^2 \text{ s}^{-1}$ at 14m) but of similar heading to the no-shear case (Figure 3.8). In the no shear and “Shear 1” cases the observed transport heading averaged over the profiles was found to lie closer to the wind (49° left of the wind) than the theoretical expectation (90° left of the wind). In the “Shear 2” case we obtained a mean transport of $1.95 \pm 1.02 \text{ m}^2 \text{ s}^{-1}$, skewed even further downwind (6° right of the wind).

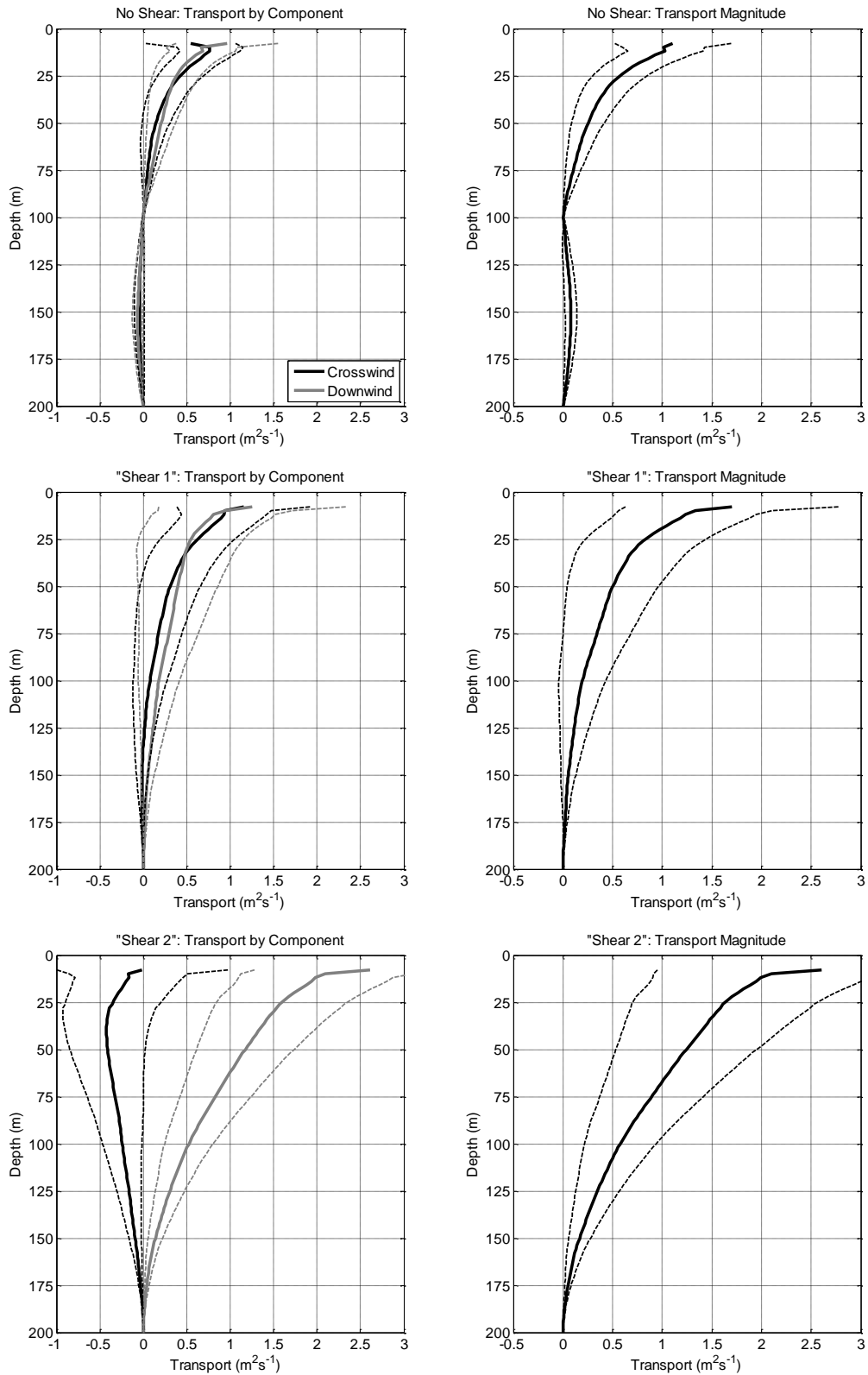


Figure 3.7: Profiles of mean cumulative Ekman Transport relative to a reference level of 200m for the no-shear; "shear 1" and "shear 2" cases. Solid lines indicate the mean transport profiles; dashed lines indicate 95% confidence intervals. Transport is shown by component at the left (positive downwind and to the left of the wind) and in magnitude at the right.

On the basis of these results we concluded that the fitting procedure applied in the “shear 2” case (which gives equal weighting to Ekman-like and reverse spirals) was inadequate; it produced an excessive number of reversed spirals which resulted in a reduced time-mean crosswind transport. For the rest of this chapter any reference to the shear case will refer to the “shear 1” fitting procedure.

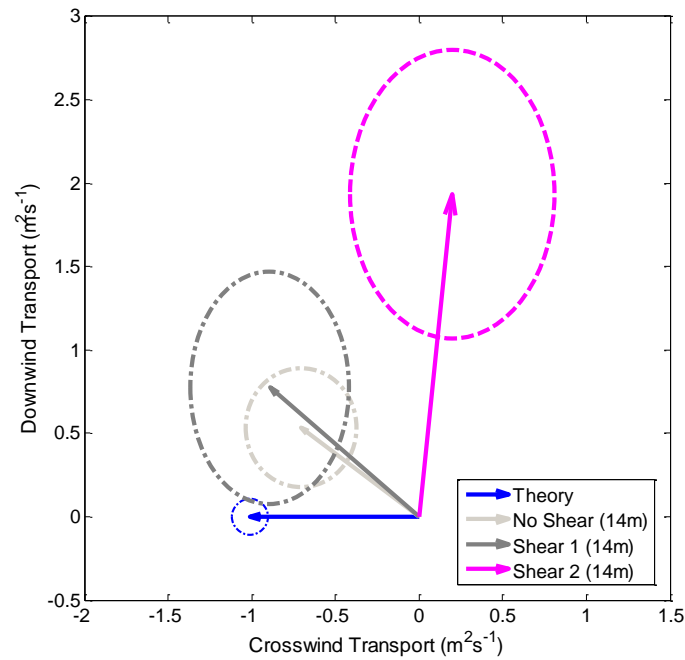


Figure 3.8: Wind-relative vector plots of mean Ekman transport with 95% confidence intervals (ellipses). Blue line is the equilibrium Ekman Transport from the interpolated wind stresses for each profile. Mean Transport from the no shear (light grey) and “shear 1” (dark grey) cases were skewed downwind by approximately 45°. The “shear 2” case (black) which applies a heavier weighting to the possibility of reversed spirals was skewed further downwind.

This downwind skewing of mean transport is a significant difference from classical Ekman theory. To attempt to explain this disagreement we considered the effects on the observations from geostrophic shear; tidal flows; Stokes drift; the ‘compression’ of Ekman spirals described above; and the transient responses to time-varying wind forcing.

A possibility we were unable to investigate is that the downwind transport anomaly may be an artefact arising from the relatively short (around two months) period of high resolution

observations by the floats used in this study; most prior *insitu* studies which successfully identified Ekman spirals have used time series of five months or greater duration. This possibility is supported by Lenn and Chereskin (2009), whose observations proved a good match to theoretical transport in the multi-year average, but also found that the same data when averaged by season did not match the theoretical transport.

b. The Role of Geostrophic Shear and Reverse Spirals

In an attempt to determine the cause of the downwind transport anomaly observed in the no-shear and “Shear 1” case we decomposed the net transport, into a vector sum of transport due to Ekman spirals, reverse spirals and non-spirals (denoted “other”), scaling each component by the fraction of the dataset it represented. In the no-shear case (Figure 3.9a) the majority of the downwind component of transport is associated with clockwise turning (reverse) spirals. Removing those profiles from consideration, the mean transport was found to shift from 48° to 63° left of the wind (Figure 3.10), closer to the theoretical case.

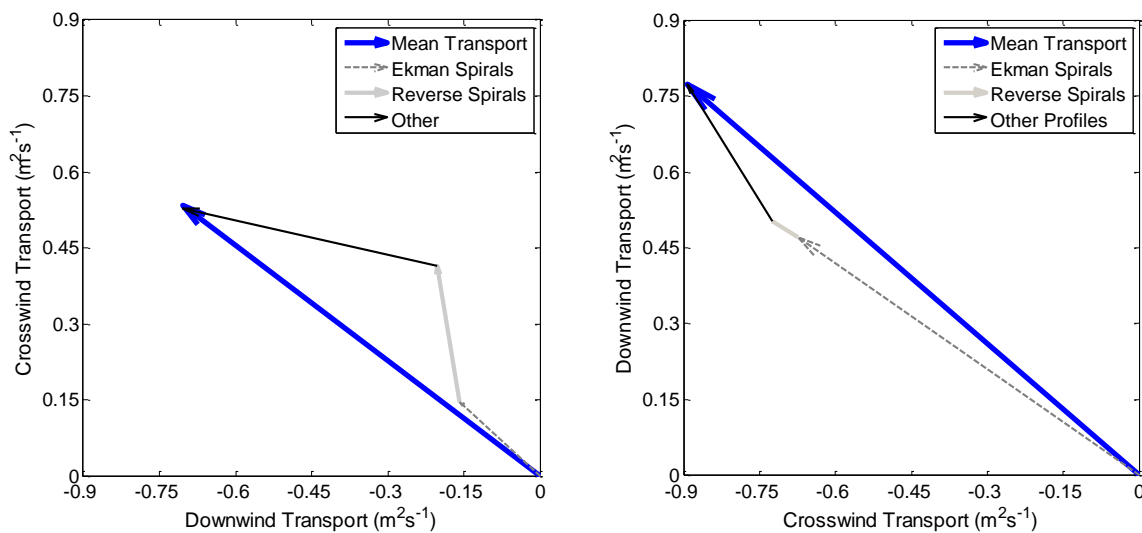


Figure 3.9: Decomposition of Ekman transport at 14m depth by type of spiral present and normalized by the fraction of dataset each represent for no shear (left) and “shear 1” right) cases.

In the “Shear 1” case (Figure 3.9b), transport arising from the Ekman spiral-like profiles was found to account for 75% of the crosswind transport and 60% of the mean downwind transport.

Reversed spirals made only a minor contribution. Excluding reverse spirals and high zonal shear profiles resulted in little change in heading for the shear case.

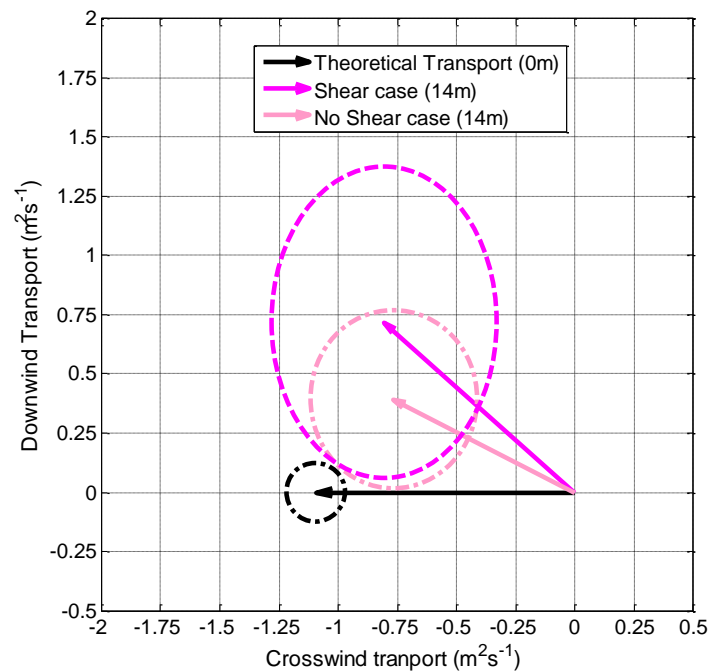


Figure 3.10: Transport at 14m with reversed spirals and strong shear profiles removed, compared to theoretical transport at 0m. Vectors indicate the mean transport and the dashed ellipses the 95% confidence intervals.

A histogram of transport by profile (Figure 3.11a) revealed that much of this mean downwind transport resulted from a few profiles at the far tails of the probability distribution. In a time-mean sense wind heading between 90° and 99° (dependent on if we considered the time-mean wind stress or 'raw' wind), directed close to the zonal component of flow and shear. We found most of the profiles displaying strong downwind transport (Figure 3.11b) were associated with strong zonal shear (here taken as shear outside the two standard deviation range, $1 \times 10^{-3} \text{ s}^{-1}$), resulting in a strong correlation (0.73) between downwind transport and shear. This strong zonal shear is likely to be introduced by errors in the shear fitting procedure. Of the 455 Ekman-like spirals identified by the least square technique, 18 displayed strong positive longitudinal shear ($>0.001 \text{ s}^{-1}$) and 11 displayed strong negative zonal shear ($<-0.001 \text{ s}^{-1}$). Both resulted in strong along-wind transport but of opposite signs.

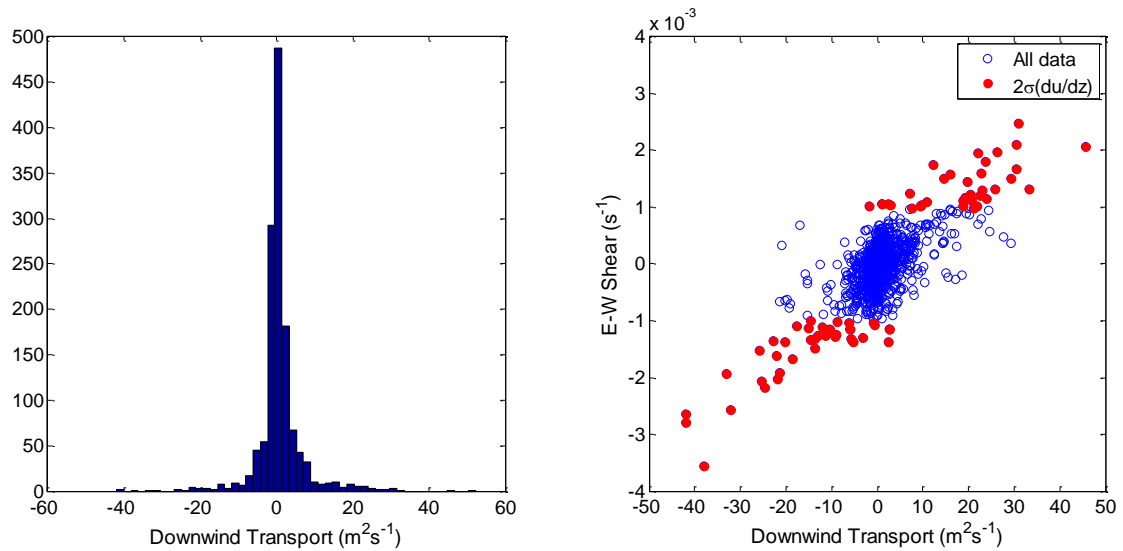


Figure 3.11: Histogram of downwind transport (left) and scatter plot of downwind transport against zonal shear (right). In the scatter plot blue circles denote all data while the filled red circles indicate geostrophic shear outside the two standard deviation range.

Ignoring these profiles with strong shear in addition to ignoring reverse spirals (Figure 3.10), the “shear 1” mean transport remained skewed at 48° left of the wind, comparable with the no-shear case. Mean transport at the surface was skewed further downwind but the 95% confidence intervals implied agreement with the 14m transport. Hence, it is unlikely that the downwind Ekman transport anomaly can be attributed to the inclusion of a residual geostrophic current when integrating current profiles to obtain transport.

c. Tides and Transient Winds

Having excluded contamination by geostrophic shear we considered other sources of the downwind Ekman transport anomaly. We would not expect barotropic tides to account for transport anomaly since they are, by definition, uniform throughout the water column, and hence should be included in the reference velocity we subtract from the observations to isolate Ekman velocities in both the shear and no-shear cases. Secondly, the transport anomaly is based upon data averaged over a wide range of latitude, longitude and time. One would, therefore, expect any tidal signals to be heavily suppressed. Thirdly, barotropic tides from the TPX07.2 model (Egbert and Erofeeva, 2002) within

the Kerguelen region were found to display a mean u-component of -0.0976cms^{-1} and a v-component of -0.1886cms^{-1} . Variability was larger, with standard deviations of 1.945cms^{-1} and 1.199cms^{-1} , respectively. Compared with mean Ekman velocity profiles ($0.79\text{-}8.57\text{cms}^{-1}$ over the upper 50m), mean barotropic tidal velocities are weak, and thus mean tidal transport should have little impact on the observed mean transport. Baroclinic tides may contribute to the transport anomaly, but testing this idea is beyond the scope of this chapter.

We also considered transient wind forcing and compression of the spiral as possible contributors to the downwind skewing. Ekman dynamics are based upon a balance between frictional forces and Coriolis. Given forcing varying on sub-inertial time scales this balance may be disrupted, effectively trapping the Ekman currents in the process of spinning up, leading to modified current profiles and transport, likely with an increased component of transport parallel to the wind, as observed above. The effect of transient wind forcing was examined by forcing a 1D numerical model (described in detail in Chapter 5) of the 'classical' constant viscosity case with observed wind stresses. This model was run for winds along the transects of all 8 EM-APEX floats assuming an eddy viscosity of $0.04\text{m}^2\text{s}^{-1}$ with time steps of 40 seconds, a vertical resolution of 0.5m and a maximum depth of 1000m. The resulting velocity data was filtered to suppress inertial oscillations as outlined in Section 3.2a, consistent with the processing of the profile data before transport was computed between 200m and the surface.

An example time series of transport magnitude and the angle between the simulated transport and the wind for one float (Float 3760) is shown in Figure 3.12. Transport magnitude from the model was close to estimates from the "steady state" Ekman transport equations (Equation 3.8), but showed significant disagreement with the observed transport. In a mean sense the angle between the simulated transport and the wind matched that expected from "steady state" Ekman transport. At any instant, the heading of the simulated transport relative to the wind is not always in agreement with the steady state Ekman transport. However this transient difference is small compared with the differences seen in the observational data.

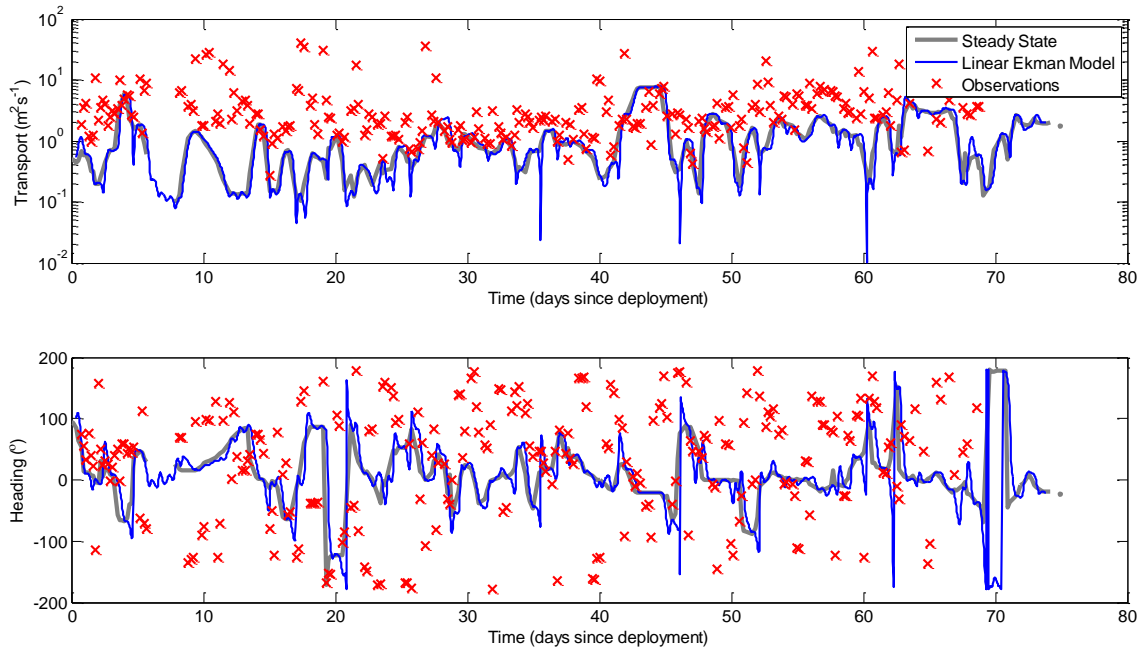


Figure 3.12: Time series of observed and simulated transport magnitude (top) and heading (bottom) for float 3760. Transport magnitude obtained from a 1D numerical model was found to match the steady state Ekman transport relationship closely. The model displayed greater variability in transport heading relative to the wind than expected from steady-state Ekman theory; but less variability than seen in the observations.

The failure to recreate the time-series of observed transport could be dismissed as a limitation of this model when forced with low resolution wind data (see Chapter 5). However, the model's strong agreement with the time-series and time-mean vector of "steady state" transport suggests that the potential disruption of the Ekman balance by high frequency wind forcing cannot explain the downwind transport anomaly.

d. Compressed Spirals and Stratification

"Compression" of Ekman spirals has previously been attributed to density stratification (Price et al., 1987, Price and Sundermeyer, 1999, Chereskin, 1995). To fully examine the effect of a compressed spiral on net Ekman transport one would need to consider a complex model that explicitly includes density stratification (see Chapter 5, Section 5.6c). For this chapter, we examine the effects of

compressed mean spirals in a simplified manner by considering the archetypal Ekman solutions but assuming independent decay scales for rotation and amplitude decay:

$$\mathbf{u}_{ek} + i\mathbf{v}_{ek} = V_{surf} e^{\frac{z}{D_{amp}}} e^{i\left(\frac{z}{D_{rot}} + \frac{\pi}{4}\right)}$$

We created synthetic spirals with decay scale ratios ($D_{amp}:D_{rot}$) between 1:0.25 and 1:5 and calculated the resulting wind-relative transport heading by integrating the computed velocities from 200m to the surface (Figure 3.13). Spirals displaying a level of compression comparable to that seen in our observations (between 1:1.5 and 1:3) were found to display transport at the surface skewed between 88° and 68° left of the wind irrespective of the assumed rotational decay scale.

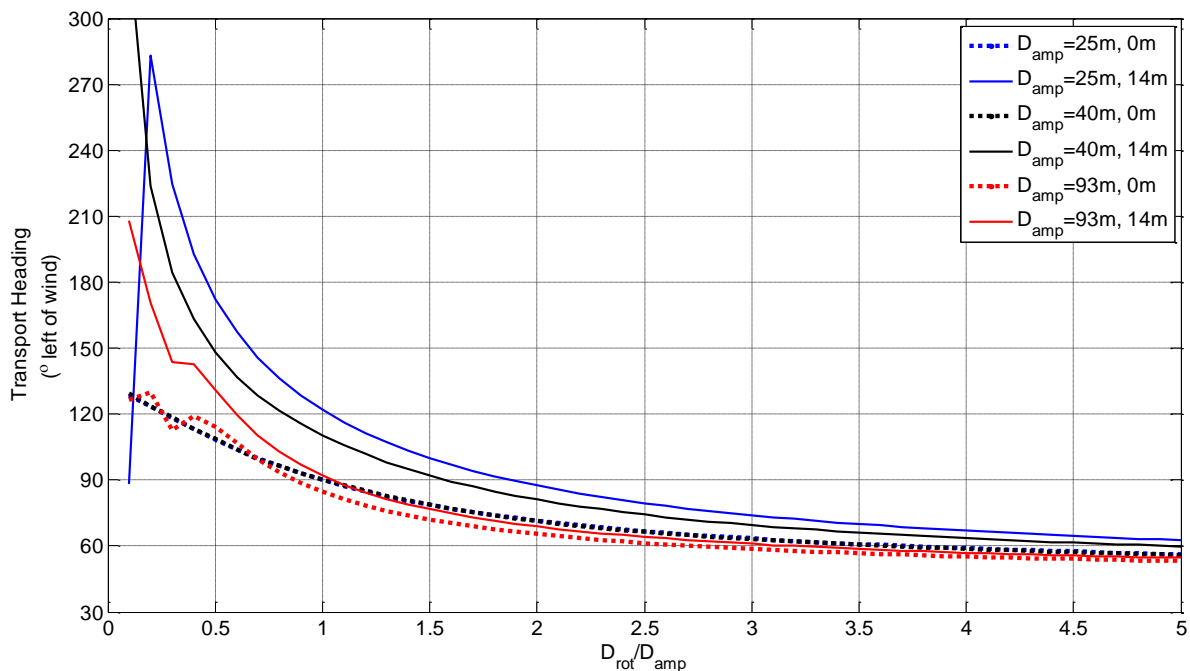


Figure 3.13: Wind-relative transport heading computed from synthetic Ekman spirals of varying “compression” from 1:1.5 to 1:3 for amplitude decay scales (D_{amp}) between 25m and 93m. Solid lines indicate the surface heading while dashed lines indicate the heading at 14m depth.

The level of skewing observed at 14m depth is dependent on the rotational decay scale. Taking D_{amp} as 25m, at the lower limit of the observed decay scales, transport at 14m depth was found to be skewed between 99° (at 1:1.5) and 74° (at 1:3) left of the wind. At a D_{amp} of 40m the transport was skewed between 91° (at 1:1.5) and 70° (at 1:3) left of the wind. Taking D_{amp} as 93m,

corresponding to the largest mean rotational decay scales obtained by the least-square fits described above, transport at 14m depth was skewed between 76° (at 1:1.5) and 61° (at 1:3) left of the wind. These results suggest that a “compressed” Ekman spiral could account for the downwind transport anomaly seen in our observations.

e. Wave Effects

Wave action can impact the Ekman layer by (1) enhancing turbulent mixing through wave breaking; (2) causing a Stokes drift that creates a component of the flow parallel to the wave heading, which could enhance or reduce current speeds that we have diagnosed as Ekman currents or (3) by direct coupling in the form of a Coriolis-Stokes forcing of the surface currents (Polton et al., 2005, Lewis and Belcher, 2004). In the former case one would expect a relationship between Ekman decay scales and either wave height or wave period. We examined these wave properties obtained from the ERA Interim reanalysis for correlations with the Ekman decay scales determined earlier in this chapter. Correlations between Ekman decay scales and local wave heights or wave periods were weak (Appendix 1, section 1). Scatter plots of Ekman decay scales as a function of wave parameters (Appendix 1, section 1) also showed no indication of any solid relationships. These results suggest that wave forcing does not significantly enhance turbulent momentum mixing.

In investigating the direct effect of Stokes drift on our observations we assumed that only monochromatic deep water waves were present. We interpolated the ERA-Interim wave period fields onto the location and time of each float profile before calculating wave lengths using the deep water dispersion relationship:

$$c_p = \sqrt{\frac{g\lambda}{2\pi}} = \frac{\lambda}{T}$$

$$\therefore \lambda = \frac{gT^2}{2\pi} \quad (3.12)$$

Where c_p denotes phase speed; g denotes the acceleration due to gravity (here taken as $9.81\text{m}^2\text{s}^{-1}$);

T denotes wave period and λ denotes wave length.

Vertical profiles of Stokes drift velocities (u_s) were then computed as (Sutherland, 2010):

$$u_s \approx \sqrt{gk^3} A^2 e^{2kz} \quad (3.13)$$

Where A denotes the wave amplitude (here taken as half the significant wave height) and k denotes the wave number ($2\pi/\lambda$).

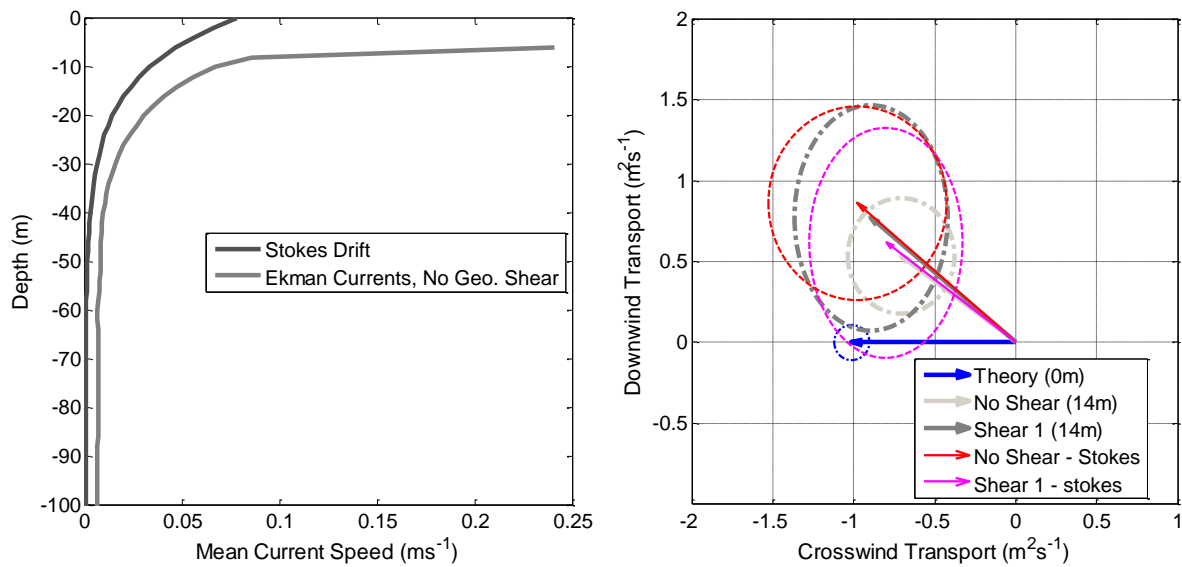


Figure 3.14: Mean current speed profiles of Ekman currents and Stokes drift (a, left). Mean transport (vectors) at 14m with and without Stokes drift explicitly removed from each velocity profile (b, right).

95% confidence intervals are indicated by the ellipses.

Stokes drift speeds calculated from the mean significant wave height and wave period were found to be smaller than, but of comparable magnitude to, the mean Ekman current speeds (Figure 3.14a), and mean wave heading was found to coincide with mean wind heading. The transport calculated from the mean Stokes drift velocity profile was approximately half the magnitude of the observed mean Ekman transport. Assuming the mean Stokes transport was directed downwind it would be capable of accounting for the downwind skewing of the mean Ekman transport, within the uncertainty of the Ekman transport estimates.

We then examined the correlation between surface Stokes transport and Ekman transport at 14m over all profiles before removing Stokes drift from each velocity profile and recalculating mean transport. Correlations between Ekman and Stokes transport were found to be weak in both the no shear and “Shear 1” cases. Removal of Stokes drift from the Ekman currents estimated assuming no geostrophic shear was found to result in the mean transport turning further downwind (Figure 3.14b). However, within the 95% confidence intervals the Ekman transport with and without Stokes drift remained identical. In the “Shear 1” case, explicit removal of Stokes drift reduced the downwind transport anomaly in the mean transport, in turn bringing the 95% confidence interval into agreement with the theoretical transport.

f. Wind Forcing Dataset

As discussed in detail in later sections it is uncertain if the CERSAT blended satellite-reanalysis wind fields are the most appropriate choice for defining wind directions for the float data. Hence, we have repeated the least-squares fits for both the no-shear and “Shear 1” cases using wind directions obtained from the NCAR/NCEP reanalysis. Resulting Ekman transport estimates from all float profiles were then rotated into a wind relative co-ordinate frame and then averaged.

Ekman decay scales and viscosities did not differ significantly from the estimates obtained using CERSAT winds. Mean transport (Figure 3.15) without shear displayed a downwind transport anomaly comparable to the CERSAT results. When including shear the transport anomaly was significantly reduced, bringing the transport into agreement with the theoretical case at the 95% confidence interval. When we explicitly used the NCEP winds and removed Stokes drift mean transport heading was close to the theoretical expectation (Figure 3.15), suggesting that a combination of Stokes drift and wind-field errors account for the observed down-wind anomaly.

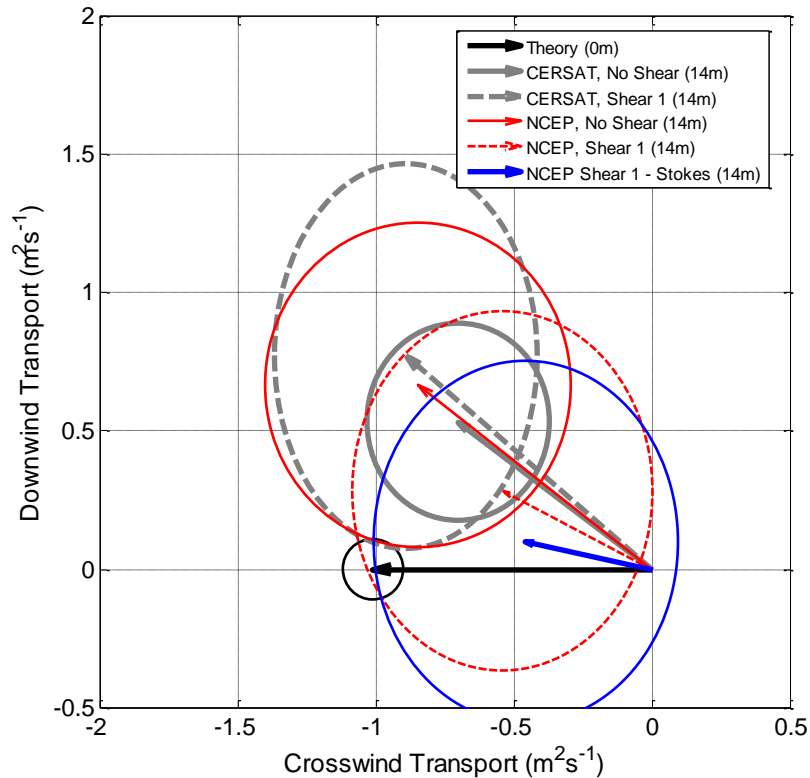


Figure 3.15: Mean wind-relative 14m transport vectors using CERSAT (grey) and NCEP (red for wind only; blue for wind combined with correcting for Stokes Drift) winds for the “No Shear” and “Shear 1” cases (solid and dashed lines, respectively). Again, ellipses indicate 95% confidence intervals.

3.6 The Effect of Stratification On Ekman Currents

A number of previous studies (Price et al., 1987, Price and Sundermeyer, 1999) have suggested that density stratification may have a significant impact on the structure of Ekman currents and the resulting transport. As discussed above we have identified behaviour, notably the “compression” of the mean spirals, consistent with these previous studies. We therefore characterise the structure of the Ekman currents we have observed in terms of properties of the density stratification. The three properties we consider are the depth of stratification (here taken to be the mixed layer depth), the strength of stratification (Buoyancy Frequency squared, N^2) and the stability of stratification (N^2 for static stability and gradient Richardson Numbers for dynamic stability). The square of the buoyancy frequency (N^2), calculated using the code included in the CSIRO Seawater library

(http://www.cmar.csiro.au/datacentre/ext_docs/seawater.htm), was used to define the strength of stratification and Richardson Number (Stewart, 1997) to define the stability of the stratification:

$$R_i = \frac{N^2}{(\partial U / \partial z)^2} \quad (3.14)$$

These are calculated from observed densities and velocity shear on a vertical grid of 2m (note that for the “no geostrophic shear” case we include all shear while in the “shear 1” case we only use the ageostrophic shear). Additionally, we considered the bulk Richardson number (R_b) across the mixed layer interface (Price et al., 1986), which measures the stability of the mixed layer. An R_b of less than 0.65 implies the mixed layer is unstable and will tend to entrain additional water into the mixed layer.

$$R_b = \frac{g\Delta\rho h}{\rho_0(\Delta\mathbf{u})^2} \quad (3.15)$$

Where g denotes the acceleration due to gravity; h the mixed layer depth; $\Delta\rho$ the density difference between the mixed layer and the interior; $\Delta\mathbf{u}$ the difference in velocity across the base of the mixed layer and ρ_0 the surface reference density.

a. Depth and Strength of Stratification

Mixed layer depth (defined in section 3.3c) from the EM-APEX profiles varied between 7m and 330m, with a mean of 43.8m and a standard deviation of 25.2m, during the period 18 November 2008 to 23 May 2009. Profiles of mean MLD-normalized transport (per section 3.3c) for both the no-shear and “Shear 1” cases are shown in Figure 3.16. Plots of the difference in transport between adjacent fractions of mixed layer depth levels are shown in Figure 3.17.

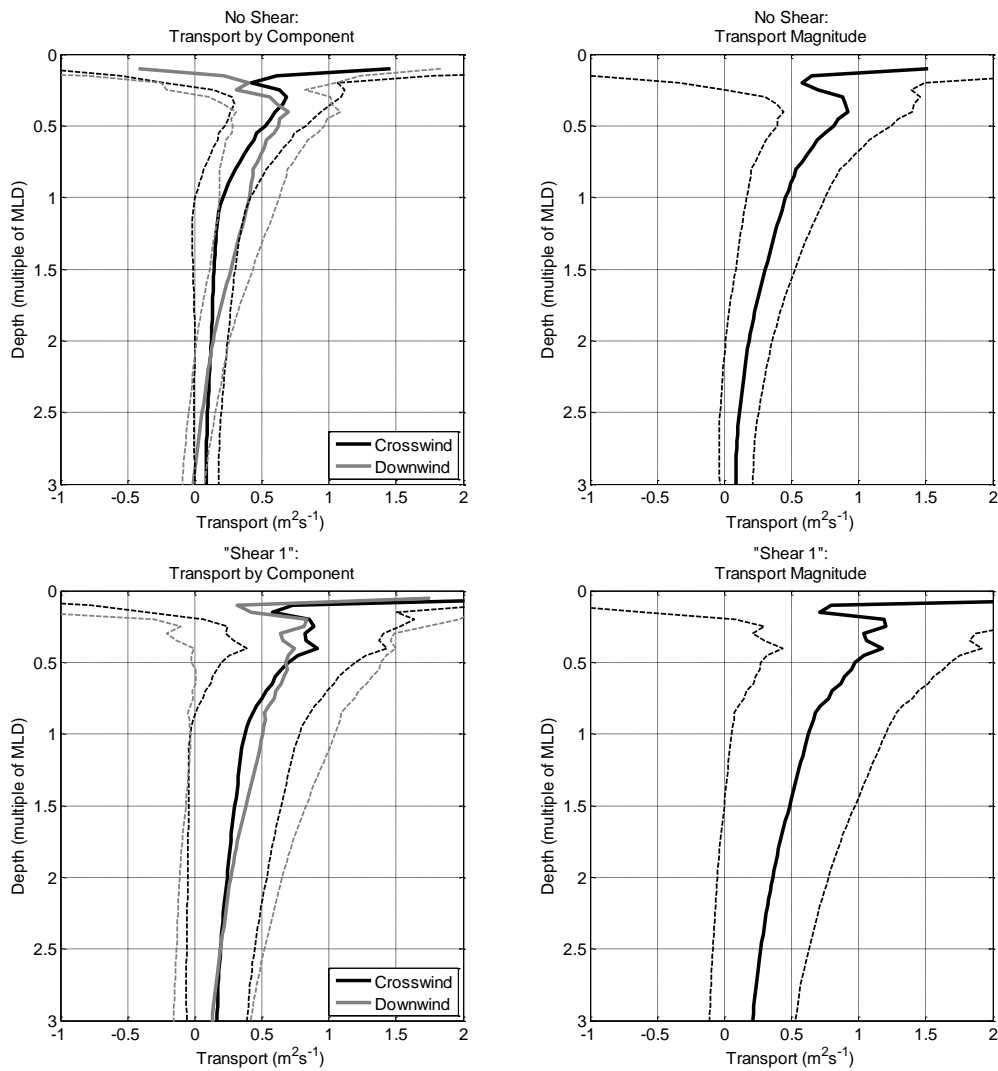


Figure 3.16: Profiles of Ekman transport by component (left; black lines indicate the crosswind component and grey lines indicate the downwind component) and magnitude (right) against fraction of Mixed Layer Depth for both the no shear case (top) and “shear 1” case (bottom). Solid lines indicate the mean profiles while dashed lines indicate 95% confidence intervals.

Transport was surface intensified with over half the transport occurring above the mixed layer (Figure 3.16) and delta-transport rapidly increasing between 1 MLD and the surface (Figure 3.17). Previous studies (Price and Sundermeyer, 1999, Price et al., 1987) have suggested Ekman currents are coupled to stratification by “surface trapping”, which could result in transport profiles similar to our results. It is also possible that this apparent relationship may be largely coincidental. Additionally, the surface intensification of transport within the mixed layer was not consistent with slab-like behaviour identified at lower latitudes in a number of previous studies (Wijffels et al., 1994,

McNally, 1981) with a potential for second order errors in the transports of heat and freshwater by the Ekman Layer in these studies.

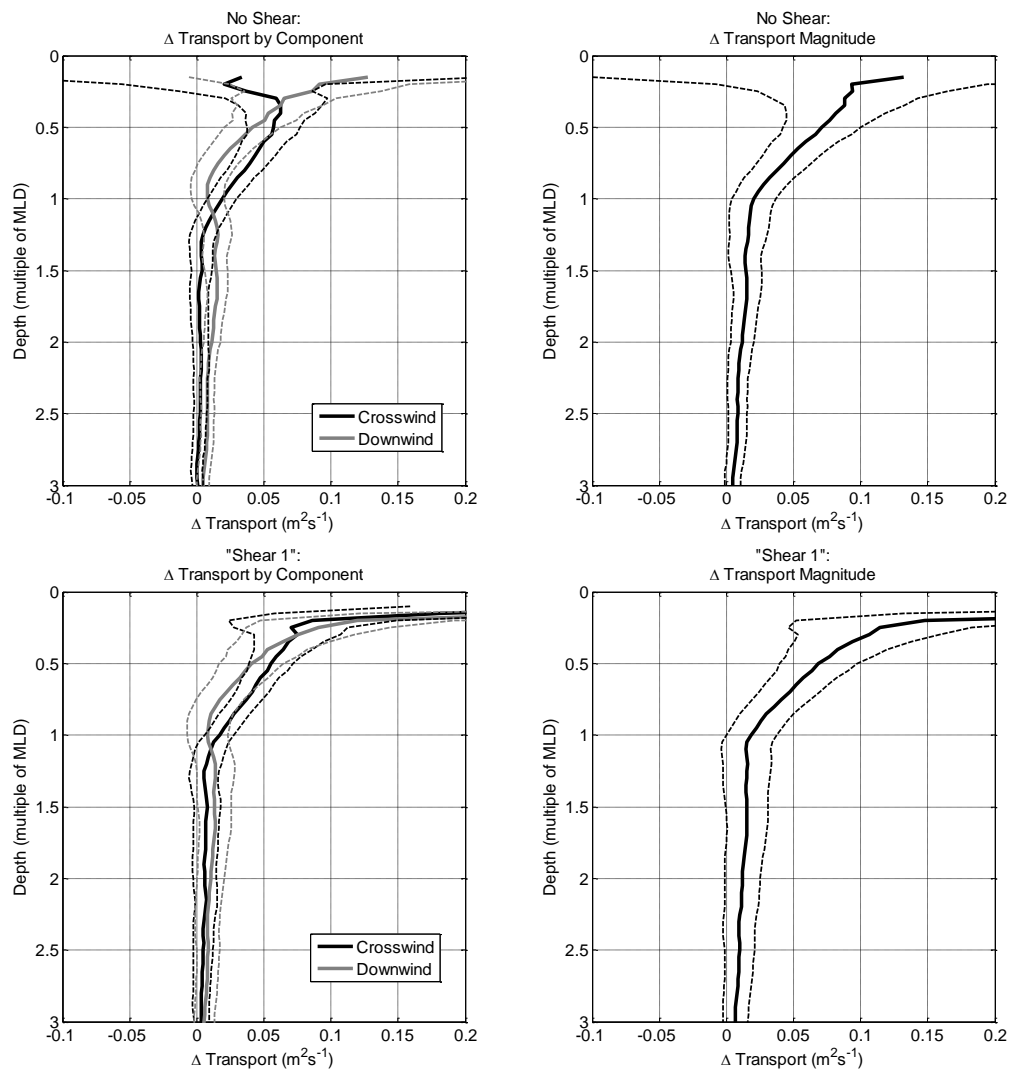


Figure 3.17: Profiles of the difference in Ekman transport between 0.05MLD intervals against fraction of MLD by component (left; black lines indicate the crosswind component and grey lines indicate the downwind component) and magnitude (right) for both the no shear case (top) and shear case (bottom). Solid lines indicate the mean profiles while dashed lines indicate 95% confidence intervals.

Note the enhancement in Δ transport at the surface relative to the mixed layer base.

Plots of R_i and N^2 for two profiles are shown in Figure 3.18. Stratification was generally found to be statically stable ($N^2 > 0$) over the entire depth range. Above the thermocline (defined by the maximum N^2 within the upper 200m) the gradient Richardson numbers were typically found to be

smaller ($O(10^{-3}$ to 1)) than in the interior ($O(1$ to 100)). This tendency for lower R_i near the surface is expected since both Ekman and Stokes shears are surface intensified.

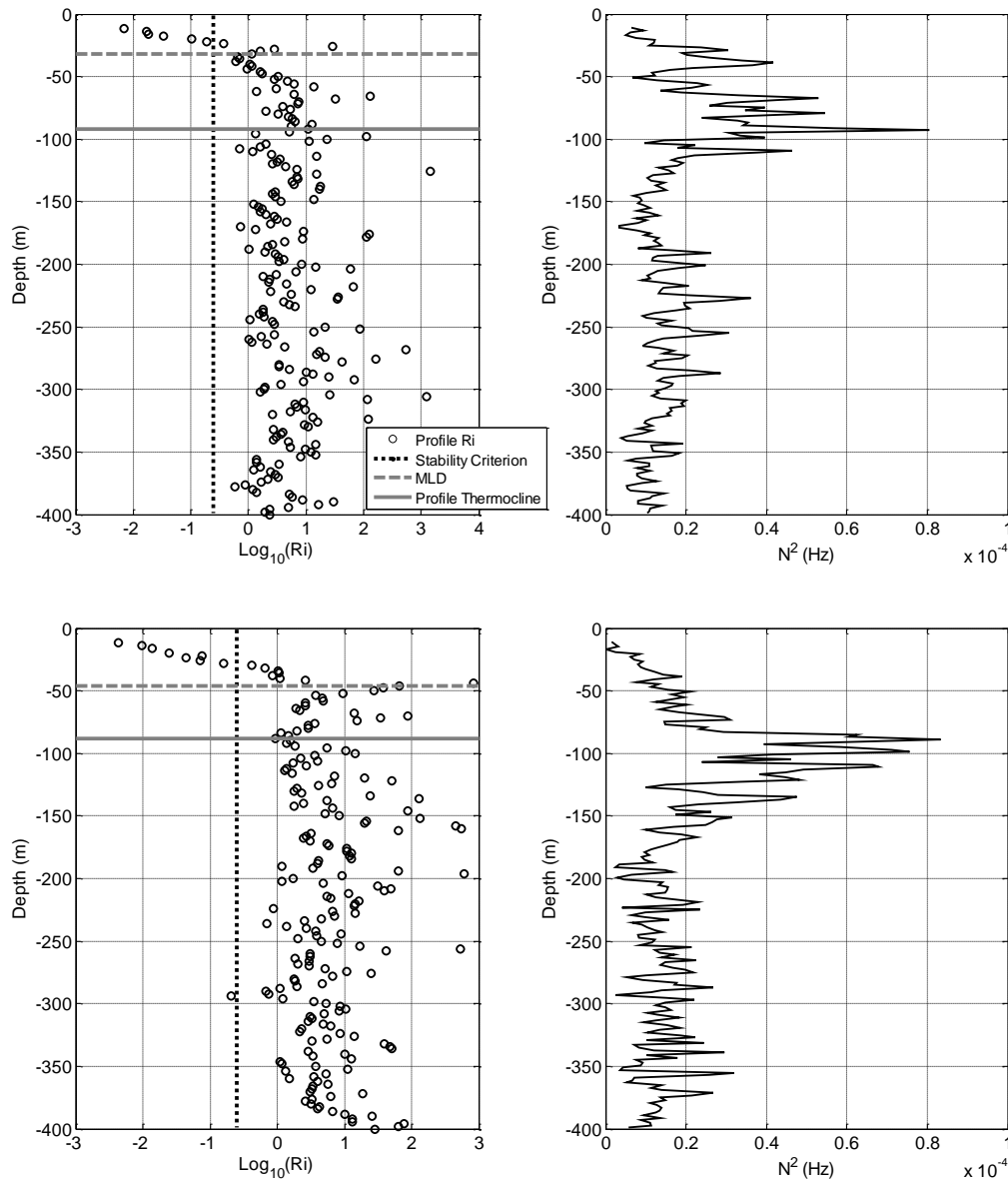


Figure 3.18: Profiles of R_i (left) and N^2 (right) for Float 3760 profile 42 (top) and Float 3761 profile 80 (bottom). The standard criterion for dynamic instability ($R_i < 0.25$) is indicated by the vertical dashed line; MLD and thermocline depth are indicated by the horizontal dashed and solid lines, respectively.

Note that in both cases instability ($R_i < 0.25$) was principally confined to the mixed layer.

Dynamical instability (occurring when $R_i < 0.25$) was rare below the thermocline, and when observed it was confined to small vertical scales (2-4m). Above the thermocline, sustained dynamical instability was found on vertical scales of 10-70m; examination of individual profiles suggested a

linkage between onset of instability and mixed layer depth. This was reinforced when we plotted maximum depth of “sustained” instability (here taken as two or more data-points with $R_i < 0.25$ within a 10m depth range) against MLD (Figure 3.19). Almost all cases of instability occurred at depths equal to or less than the MLD. The maximum depth of sustained dynamic instability displayed no significant relationship to the observed Ekman decay scales.

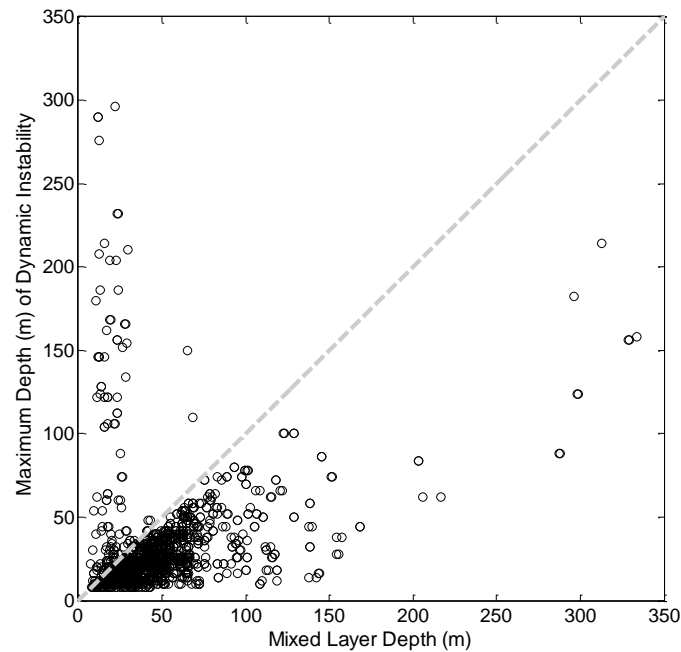


Figure 3.19: Maximum depth of ‘sustained’ dynamic instability plotted against mixed layer depth.

The dashed grey line corresponds to a 1:1 ratio between the depth of instability and the mixed layer depth.

We then examined the relationship between stratification and the vertical structure of Ekman currents (see Appendix 1, section 2 for details) by considering the relationships and correlations between the observed Ekman decay scales and parameters including mixed layer depth; thermocline depth; bulk Richardson number; peak buoyancy frequency and the difference in density across the mixed-layer interface. We found no evidence of linkages between either mixed layer or thermocline depth and the observed Ekman decay scales. Likewise, there is no evidence that the density difference across the mixed layer interface affects the Ekman decay scales. Maximum N^2 was also found to have little impact on the Ekman decay scales.

There is some indication that the decay scales estimated above are related to the bulk Richardson number (Figure 3.20). The magnitude of Ekman decay scales was found to increase in a linear manner as the magnitude of R_b increased. This implies that Ekman decay scales were larger when the mixed layer was more stable. Note, however, that correlations were modest (in the shear case 0.47 for D_{amp} and 0.19 for D_{rot}), implying this result should be treated with caution.

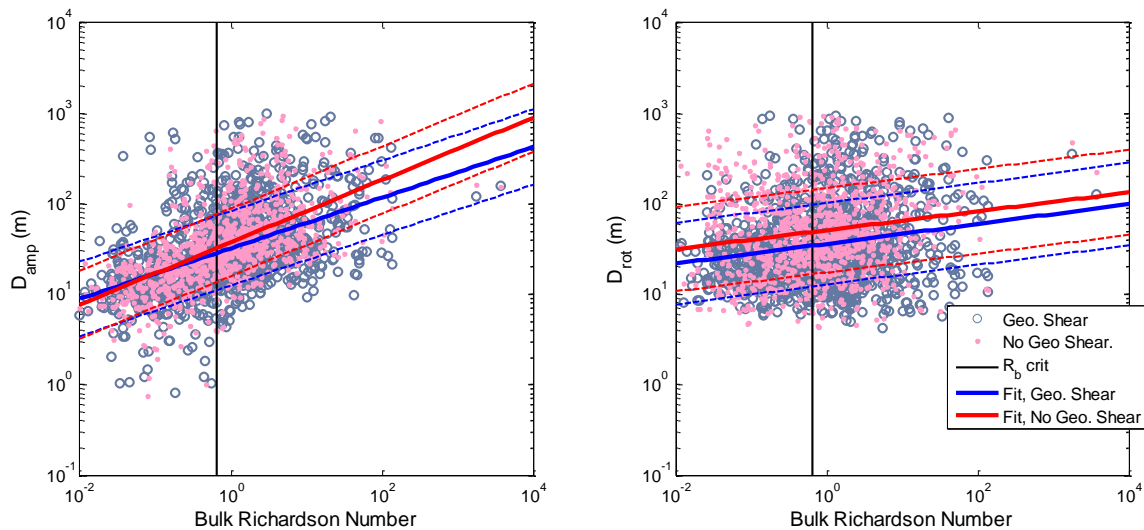


Figure 3.20: Ekman decay scales vs bulk Richardson Numbers (R_b) for decay scales estimated from current amplitude (left) and current rotation (right). Solid red and blue lines represent logarithmic fits to the data; dashed lines indicate confidence intervals estimated from the Matlab polyfit routine. The vertical black line indicates the critical value of R_b (0.65).

b. Local Eddy Viscosities

Eddy viscosity profiles calculated as described in Section 3.3d (Figure 3.21) were found to be of similar magnitude, if somewhat weaker, than comparable observations in the Drake Passage (Lenn and Chereskin, 2009). In general there was a tendency for greater viscosities to be observed closer to the surface and for the shear case to produce larger viscosities than the no-shear case. When considering the viscosity profiles with the vertical coordinate as a proportion of MLD (Figure 3.19b), the no-shear viscosity profile displayed a distinct trend for viscosity to decrease with increasing depth (as a fraction of MLD). Viscosity decreases approximately exponentially from around $10^{-2} \text{m}^2 \text{s}^{-1}$ near the surface to $2\text{-}3 \times 10^{-3} \text{m}^2 \text{s}^{-1}$ at a depth of 2-3 times the MLD. The viscosity profile for the shear

case is more consistent, over the 0-3 MLD range the viscosity is generally around $1-3 \times 10^{-2} \text{m}^2 \text{s}^{-1}$, however, there is still some tendency for smaller viscosities to occur below the mixed layer.

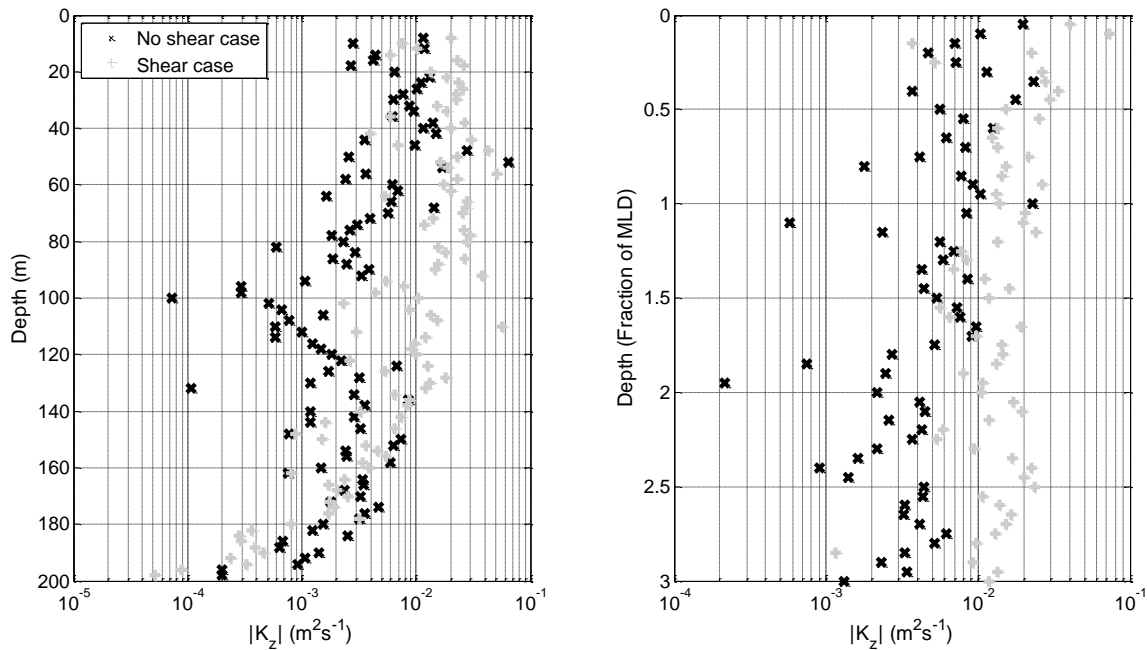


Figure 3.21: Mean viscosity amplitude profiles by depth (a, left) and multiple of MLD (b, right). The no shear case is indicated with crosses, and the Shear case with grey pluses. MLD is mixed layer depth and its definition is given in the text. The vertical component of diffusivity K_z is calculated from

Equation 3.10.

To properly characterize and examine this behaviour we divided the no-shear and shear case mean viscosity profiles into three subsets based upon depth: all data deeper than 0.3MLD; data between 0.3 and 1MLD (denoted “Mixed Layer”) and data between 1.5 and 3MLD (denoted “deep”). We excluded data shallower than 0.3MLD, since much of that data would come from depths only poorly sampled by the EM-APEX floats. Examination of the MLD-normalized viscosity profiles (Figure 3.21) suggested that either linear or exponential fits would provide the best match to the mean current profiles. Linear fits were applied to the viscosity profiles using the matlab polyfit function; the resulting fits and confidence intervals were then plotted as using the matlab polyval function. Exponential fits were applied by using a linear fit to profiles of $\log_{10}(k_z)$ using the polyfit and polyval functions.

Fits to viscosity profiles are shown in Figure 3.22 (linear fits) and Figure 3.23 (exponential fits). Initial examination focusing solely on the mean values of the mixed layer and deep fits, suggested that viscosity values are sensitive to the depth range. Such behaviour could be indicative of density stratification affecting the vertical structure of Ekman currents.

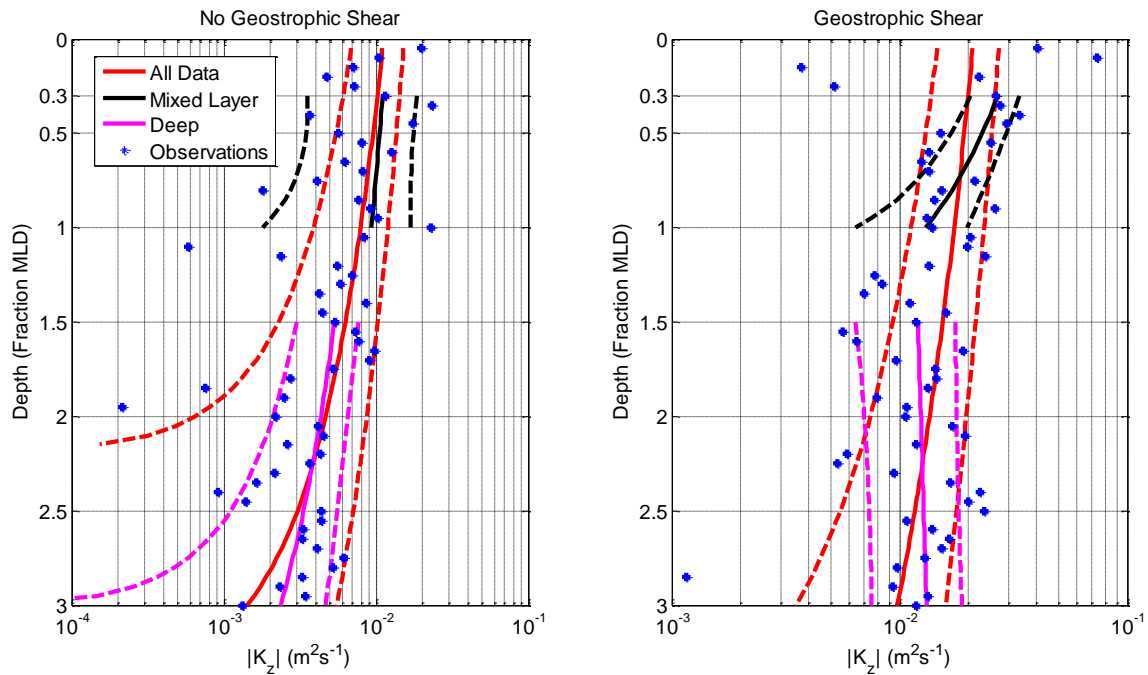


Figure 3.22: Mean viscosity profiles (no-shear left and shear right) as a function of fraction of mixed layer depth (MLD). Linear fits to viscosities in the mixed layer, ocean interior (1.5-3 MLD) and over the entire profile (0-5 MLD) are shown.

However, considering confidence intervals about the mean, we were unable to distinguish a significant difference between any of the mixed layer fits and the corresponding between “all data” fits over the 0.3 to 1MLD interval. Similarly, over the 1.5 to 3MLD interval there was no significant difference between the “deep fits” and the all-data fits. We also found that the confidence intervals did not allow us to distinguish between the linear and exponential all-data fit.

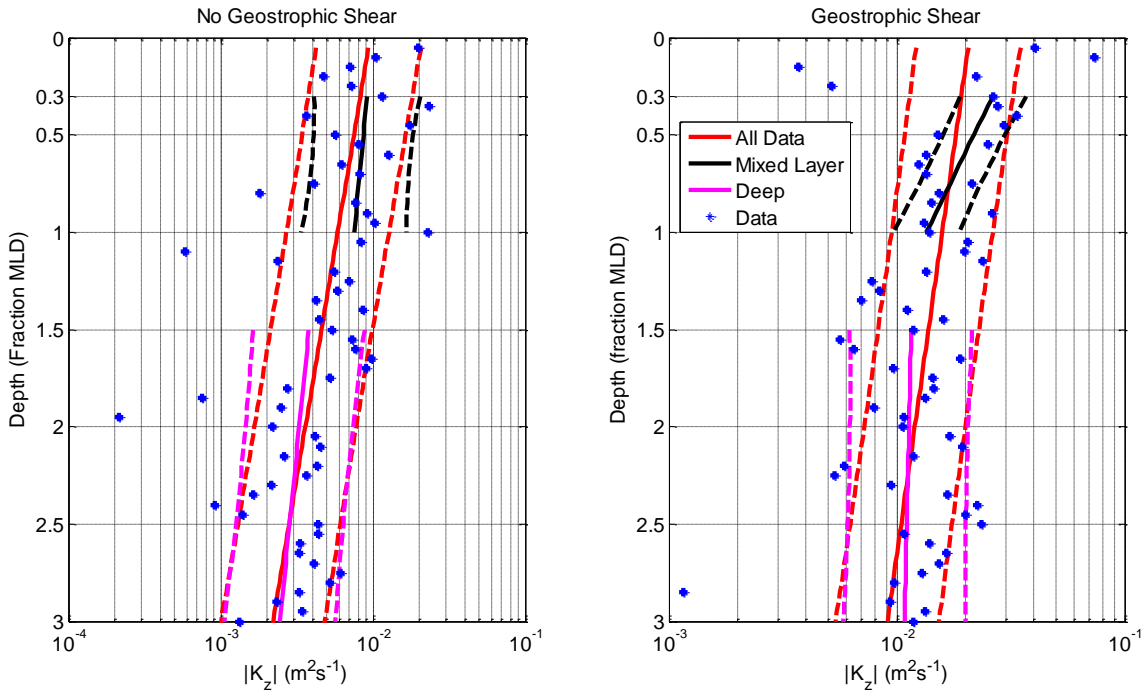


Figure 3.23: Mean viscosity profiles (no-shear left and shear right) as a function of fraction of mixed layer depth (MLD). Exponential fits to viscosities in the mixed layer, ocean interior (1.5-3 MLD) and over the entire profile are shown.

Examining the no-shear case “all data” fits we attempted to identify a range of constant viscosities which would produce agreement with the fit within the confidence intervals over the 0.3 to 3MLD range. No such viscosities could be identified for the linear fit, but for the exponential fit we found that constant viscosities between $3.76 \times 10^{-3} \text{m}^2 \text{s}^{-1}$ and $4.83 \times 10^{-3} \text{m}^2 \text{s}^{-1}$ would satisfy the confidence interval about the exponential fit. Examining the shear case, all-data fits in a similar manner indicated constant viscosities satisfied the confidence intervals between $1.37 \times 10^{-2} \text{m}^2 \text{s}^{-1}$ and $1.60 \times 10^{-2} \text{m}^2 \text{s}^{-1}$ for the linear fit and between $1.14 \times 10^{-2} \text{m}^2 \text{s}^{-1}$ and $1.53 \times 10^{-2} \text{m}^2 \text{s}^{-1}$ for the exponential fit.

There are no statistical differences between these three empirical viscosity models for the water column, and therefore the “Occams razor” approach, we conclude that only a constant viscosity model is required to explain the available observations. It is interesting to note that in both the linear and exponential viscosity models, the observations indicate a tendency for the viscosity to decrease with depth, with generally higher values nearer to the surface layers.

3.7 Discussion and Conclusions

We have detected and characterised Ekman spirals using EM-APEX velocity profiling floats in the Southern Ocean. Eddy viscosities were found to range between 3.2×10^{-2} and $44.7 \times 10^{-2} \text{ m}^2 \text{ s}^{-1}$ (corresponding to decay scales of 25m and 93m), in general agreement with previous studies in the Southern Ocean (Elipot and Gille, 2009a, Lenn and Chereskin, 2009). When we assumed a constant geostrophic velocity within the Ekman layer, mean viscosities (and decay scales) obtained from the rotational least squares fit were found to be significantly larger than those obtained from the current amplitude least square fit, resulting in ‘compressed’ spirals, consistent with prior observations of open-ocean Ekman spirals (Lenn and Chereskin, 2009). This ‘compression’ was also seen when we computed the ratio between decay scales on a float by float basis. If we instead assumed a constant geostrophic shear was present within the Ekman layer, both least square fits (rotation and amplitude decay) were found to produce mean viscosities consistent with each other. Moreover, the “compression” of the spirals (computed on a float by float basis) decreased, with the ratio between the rotational and amplitude decay scales becoming closer to 1:1. Fits with geostrophic shear also captured more individual profiles displaying Ekman-like spirals, and decreased RMS residuals. This behaviour indicates that explicit consideration of the vertical structure of the geostrophic currents is required to properly isolate Ekman currents, and suggests that the ‘compressed’ spirals seen in most prior studies may be an artefact of assuming a constant geostrophic current, as discussed in Polton et al. (2013).

Mean observed transport was found to be of the same magnitude as expected from wind data and steady state Ekman theory. But, in contravention of ‘classical’ steady-state Ekman theory, Ekman transport heading was skewed downwind. The downwind transport anomaly proved surprisingly robust to selection of profiles and is a real feature of the analysis. Transient wind forcing and accidental inclusion of residual geostrophic currents when integrating the Ekman transport were found to have little effect on the downwind transport anomaly. Results suggested that the transport

anomaly likely arose from some combination of the “compression” seen in the Ekman spirals; inclusion of Stokes drift when integrating the Ekman transport, or from errors in the CERSAT wind fields.

We examined the proposed linkage between stratification and Ekman current from a variety of angles. Ekman transport and dynamic instability were largely confined to the mixed layer; while superficially suggestive of ‘surface trapping’ of the Ekman currents by density stratification this association could also be largely coincidental as the mean mixed layer depth and Ekman decay scales are comparable in magnitude. We identified relationships between the magnitude of Ekman decay scales and bulk Richardson numbers, implying that Ekman decay scales tended to be larger when the mixed layer was stable (and, hence, more strongly stratified). We found no firm links between mixed layer depth, thermocline depth or maximum buoyancy frequency and the observed Ekman decay scales. We demonstrated that the “compressed” spirals, previously attributed to stratification driven surface trapping of Ekman currents (Price and Sundermeyer, 1999, Price et al., 1987), could be explained as a side effect of failing to resolve geostrophic shear when isolating the ageostrophic flow (Polton et al., 2013). We conclude that, having found evidence both for and against density stratification affecting Ekman currents, our examination of the effect of stratification on Ekman currents is inconclusive.

Examination of mean viscosity magnitude profiles as a function of MLD normalized depth was initially suggestive of either linear or exponential decay of viscosity with increasing depth. Applications of linear and exponential fits to all depths between 0.3 and 3MLD; just the mixed layer and below the mixed layer (1.5-3 MLD) suggested different behaviour within the mixed layer compared to the interior. However, when we considered the uncertainty around the fits it became clear that these differences were not statistically significant. We subsequently determined it was also possible to reconcile a constant magnitude eddy viscosity with the all data fits.

Chapter 4: Examining Wind Driven Ekman Dynamics in the

Frequency Domain

4.1 Overview and Introduction

While we have detected and described Ekman-like spirals within the latitude and longitude range covered by the SOFINE EM-APEX floats, details of the vertical structure of both the mean and instantaneous spirals did not match classical Ekman theory. Results presented in the previous chapter suggested this could, at least in part, be due to the effects of density stratification. However time variable wind forcing or vertical variation in eddy viscosity may also play a role. To further examine potential effects of these two factors, particularly by allowing for vertical variations, we applied a form of rotary spectral analysis to fit 9 analytic solutions for Ekman type spirals for varying viscosity and boundary layer depths and conditions, in line with a number of previous studies (Weller, 1981, Rudnick and Weller, 1993, Elipot and Gille, 2009a).

We adopted the method previously applied by Elipot and Gille (2009a) to data from surface drifters deployed in the Southern Ocean. The technique involves the estimation of transfer functions using wind-stress auto-spectra and cross spectra between wind-stress and Ekman currents at a constant depth level. By comparing the estimated transfer functions from shipboard ADCP and EM-APEX float observations with transfer functions derived from theoretical combinations of eddy viscosity profiles and boundary conditions we inferred properties of mixing within the Ekman layer. Further analysis (Elipot and Gille, 2009b) arising from this technique also allowed us to make an assessment of the wind energy input within the study region.

This analysis is more comprehensive than earlier work, because it includes a larger range of models than studies prior to Elipot and Gille (2009a) and is extends beyond the single depth level of Elipot and Gille (2009a) to include the water column to 100 metres. Unlike the surface drifter data used by Elipot and Gille (2009a) the EM-APEX and ADCP data provided a time series, and hence power spectra, of ocean currents over multiple depth levels. We used this additional depth

information to assess model performance in a 2D sense, as a function of both depth and frequency (over an interval of -2 to 2 CPD); and to examine the performance of the models over the 0-100m depth range at four frequencies between \pm one inertial period.

4.2 Datasets

a. Shipboard ADCP Data

In addition to the EM-APEX float data discussed in Chapter 3 we investigated shipboard Acoustic Doppler Current Profiler (ADCP) observations obtained during the SOFINE deployment voyage aboard RV *James Cook* during November-December 2008. The ship had two onboard ADCP systems, one operating at 75kHz and a second operating at 150kHz.

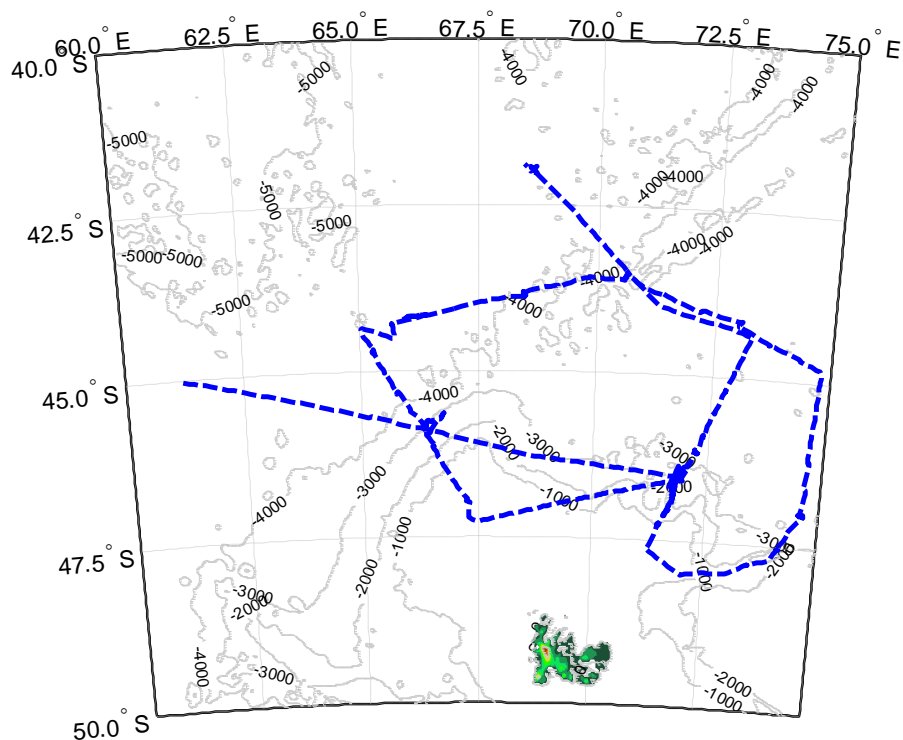


Figure 4.1: Ship track of the RV *James Cook* during the survey phase of the SOFINE voyage (blue) superimposed over ETOPO bathymetry (Amante and Eakins, 2009).

Since the 75kHz system offered relatively poor vertical resolution and did not capture any data above 33m we concentrated on the time-series produced by the 150kHz system. The dataset produced by this instrument ran for 29 days from the 10th of November to the 8th of December 2008

and covered a latitude range from 41S to 48S (Figure 4.1), delivering a dataset with 30 minute temporal resolution down to a depth of 455m. Since the shallowest observed depth and the bin width of the raw data varied over the course of the voyage this study focused on the post-processed time-series which had been mapped onto a regular depth grid, with a primary focus on the 23.55m depth level.

b. Shipboard Winds

Shipboard winds were recorded using an ultrasonic anemometer mounted on a platform near the bow of the vessel. This data underwent quality control; standardising to a nominal 10m height and correcting to absolute wind speed rather than ship-relative airspeed. The final time series of absolute shipboard winds offered 30 second resolution over a period from the 1st of November to the 19th of December 2008. For the purposes of this study we computed a 30 minute resolution running average to match the resolution of the ADCP observations. We then converted the resulting velocity time series to a wind-stress time series using drag coefficients calculated following Yelland and Taylor (1996).

c. EM-APEX Float Data

The EM-APEX float data has been described in detail in the previous chapter. Unlike in the previous analysis, this time we did not filter out inertial oscillations. Despite each float delivering 4 profiles per day the profiling mission was designed to ensure that pairs of adjacent up-casts or down-casts were separated by approximately half an inertial period (8-9 hours). We interpolated the unevenly spaced velocity time-series from each EM-APEX float onto a grid with 6hr time-steps.

d. SSALTO/DUACS Geostrophic Velocity Fields

Maps of surface geostrophic velocity (Dibarboure et al., 2008) were sourced from AVISO. This dataset was derived by merging sea surface height (SSH) data from multiple satellite missions

(including Jason 1 and 2, Topex/Poseidon and Envisat) to generate time varying fields of absolute dynamic topography. In turn, surface geostrophic currents were estimated using a finite difference method (Lagerloef et al., 1999). The resulting velocity fields provide 1/3° spatial and 7 day temporal resolution.

4.3 Rotary Spectral Analysis

a. Fourier Decomposition

The use of rotary spectral techniques depends on representing a vector time series, such as the wind stress or the two components of velocity as a complex Fourier series of oscillations at different frequencies.

$$u(t) + iv(t) = \sum_{k=-\infty}^{k=\infty} u_k(t) \quad (4.1)$$

At each frequency ω_k , the Fourier component is:

$$u_k(t) = C_k e^{2\pi i \omega_k t}$$

Where the Fourier coefficient, C_k , for a dataset sampled over the time period T is:

$$C_k = \frac{1}{T} \int_0^T u_k(t) e^{-2\pi i \omega_k t} dt$$

In effect, the time-series can be represented as a sum of vectors of constant magnitude each rotating at fixed frequencies. From the Fourier coefficient we can then obtain the finite Fourier transform (U_k) of u_k :

$$U_k(\omega_k) = \int_0^T u_k(t) e^{-2\pi i \omega_k t} dt \quad (4.2)$$

Elipot and Gille (2009a) used a periodogram method to estimate power spectra. The time series (here denoted x and y with Fourier transforms X and Y) were split into a number of overlapping

segments of time period T and a Hanning window (Harris, 1978) applied to each segment. Fourier transforms were then obtained for each segment of the two time series. The cross power spectrum between the time series x and y was then estimated as:

$$\widehat{P}_{xy}(\omega_k) = \frac{\langle X_k Y_k^* \rangle}{T} \quad (4.3)$$

Where $\langle \cdot \rangle$ denote the average over all segments of the time series.

The periodogram method employed by Elipot and Gille (2009a) is similar to Welch's method (1967), differing only in minor details. Hence, for the rest of this thesis we will use Welch's method (1967) when estimating power spectra.

b. Transfer Functions

Assuming the ocean currents ($\mathbf{u} = u + iv$) at depth z respond to the wind stress ($\boldsymbol{\tau}$) in a linear manner, the velocity response can be regarded as a convolution of the wind stress with a response function.

Taking a Fourier transform and applying the convolution theorem we obtain:

$$U(\omega, z) = H(\omega, z)T(\omega) \quad (4.4)$$

Where U and T denote the Fourier transforms of \mathbf{u} and $\boldsymbol{\tau}$; and H is the transfer function.

By definition the transfer function must also satisfy (Bendat and Piersol, 1986):

$$P_{\tau u} = H(\omega, z)P_{\tau\tau} \quad (4.5)$$

Where $P_{\tau u}$ denotes the stress-current cross-spectrum and $P_{\tau\tau}$ denotes the wind-stress autospectrum.

Using equation 4.4 to obtain theoretical transfer functions from eddy viscosity profiles is discussed briefly in section 4.4. Computing observed transfer functions from estimated power spectra is discussed further in section 4.5a.

4.4 The Models

During this study we considered the same set of 9 models (Figure 4.2) as applied by Elipot and Gille (2009a). These models included three forms of eddy viscosity profile: 1) constant, 2) linearly increasing with depth from $0\text{m}^2\text{s}^{-1}$ at the surface, and 3) linearly increasing with depth with an offset at the surface. The models also considered three different bottom boundary conditions: A) an infinite-depth Ekman layer; B) an Ekman layer of finite depth with velocity tending to zero at the base of the layer (a so-called “one layer” model), and C) an Ekman layer with shear tending to zero at the bottom of the layer (a “one and a half layer” model). The resulting models were governed by a combination of up to three parameters: the eddy viscosity at the surface, k ; a constant eddy viscosity gradient, $\frac{\partial k}{\partial z}$, (here onwards denoted dk in the text); and the boundary layer depth (denoted BLD in the text and h in some equations) at which the deep boundary conditions were applied.

Elipot and Gille (2009a) obtained theoretical transfer functions by first applying a Fourier transform to the momentum equation to obtain an ordinary differential equation:

$$i(2\pi\omega + f)U(\omega, z) - \frac{d}{dz} \left(K(z) \frac{dU(\omega, z)}{dz} \right) = 0$$

Fourier transforms were also applied to the surface boundary condition and deep boundary conditions. This resulted in a surface boundary condition at $z=0$ of:

$$-K(z) \frac{dU(\omega, z)}{dz} = \frac{T(\omega)}{\rho}$$

In Class 2 models the viscosity tends to zero at the surface, hence, the surface boundary condition was taken as a limit. In other cases (Class1 and 3 models) viscosity is non-zero at the surface; hence, the boundary condition was applied directly.

The deep boundary condition for the infinite depth (type A) Ekman models became:

$$U(\omega, z) \xrightarrow{z \rightarrow \infty} 0$$

And, in turn, the no slip boundary condition in the type B (“one layer”) Ekman models became:

$$U(\omega, z) \xrightarrow{z \rightarrow h} 0$$

And the boundary condition for the type C (“one and a half layer”) Ekman models, in which shear tends to zero at the base of the boundary layer, became:

$$\frac{dU(\omega, z)}{dz} \xrightarrow{z \rightarrow h} 0$$

The eddy viscosity profiles were then applied and the Fourier transform of the momentum equation solved in a form consistent with equation 4.4 subject to the relevant boundary conditions.

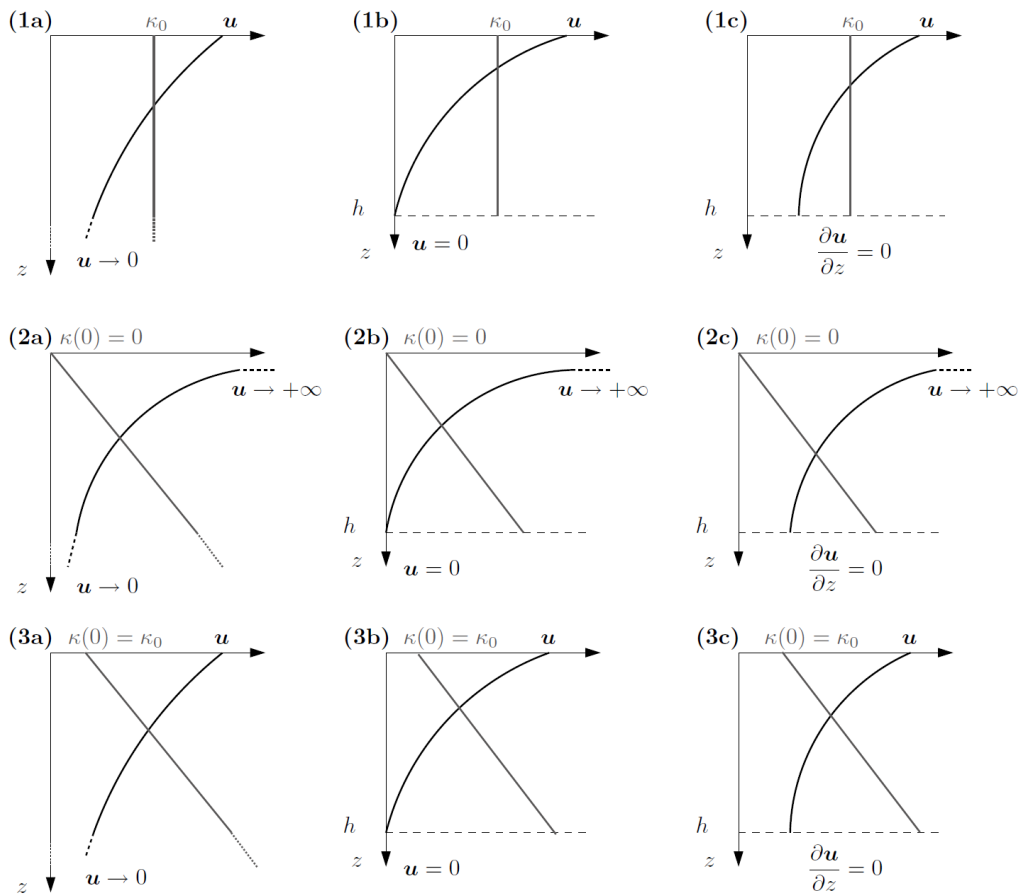


Figure 4.2: Schematics of the 9 models. From Elipot and Gille (2009a).

Derivations of the transfer functions for Class 1 and 2 models have been published in a number of previous papers (Lewis and Belcher, 2004, Madsen, 1977, Thomas, 1975, Weller, 1981) while the Class 3 model transfer functions are derived in Elipot and Gille (2009a). Discussion of the behaviour

of the models as a function of depth and frequency can be found in Elipot (2006) and Elipot and Gille (2009a).

We follow the expressions for theoretical transfer functions given in Elipot (2006) rather than Elipot and Gille (2009a). While both are mathematically identical the expressions given in Elipot's PhD thesis are forms more suitable the optimisation procedure.

a. Constant Viscosity Models (Class 1)

All class one models follow 'classical' Ekman theory by assuming the eddy viscosity (k) is constant with depth. We first define the class 1 model depth scale δ_1 which incorporates an effect from the eddy viscosity and frequency variability:

$$\delta_1(\omega) = \sqrt{\frac{2k}{2\pi\omega + f}} \quad (4.6)$$

To reduce the complexity of the subsequent equations we define the term α as:

$$\alpha = \frac{1+i}{\delta_1} \quad (4.7)$$

Following the derivation outlined in Elipot (2006) the transfer function for the constant viscosity, infinite depth model (Model 1A) is:

$$H_{1A}(\omega, z) = \frac{e^{-\alpha z}}{\rho k \alpha} \quad (4.8)$$

Likewise, for the constant viscosity single layer model (Model 1B) the transfer function is:

$$H_{1B}(\omega, z) = \frac{1}{\rho k \alpha} \frac{\sinh(\alpha(h-z))}{\cosh(\alpha h)} \quad (4.9)$$

Finally, the transfer function for the constant viscosity one and a half layer model (Model 1C) is:

$$H_{1C}(\omega, z) = \frac{1}{\rho k \alpha} \frac{\cosh(\alpha(h-z))}{\sinh(\alpha h)} \quad (4.10)$$

All Class 1 models follow “classical” Ekman theory in assuming eddy viscosity is constant with depth. Hence, the rate of rotation and decay are constant as a function of depth, with the exception of near the BLDs of Models 1B and 1C.

b. Linearly Increasing Viscosity Models (Class 2)

All Class 2 models assume the viscosity increases from $0\text{m}^2\text{s}^{-1}$ at the surface with a constant eddy viscosity gradient, $\frac{\delta k}{\delta z}$, (here onwards denoted dk in the text):

$$K(z) = z \cdot \frac{\delta k}{\delta z}$$

Elipot and Gille (2009a) considered the Class 2 models on the basis of the concept of turbulent mixing length (Prandtl, 1952); as depth increases the size of turbulent eddies becomes larger and so viscosity increases.

Again, for convenience we define three commonly used terms for the following equations.

Firstly, we define the depth scale δ_2 as:

$$\delta_2(\omega) = \frac{\frac{\delta k}{\delta z}}{2\pi\nu + f} \quad (4.11)$$

In the following transfer functions, I_n denotes an n th order modified Bessel function of the first kind.

\mathcal{K}_n likewise denotes a Bessel function of the second kind. The resulting transfer functions are:

$$H_{2A}(\omega, z) = \frac{2}{\rho \frac{\delta k}{\delta z}} \mathcal{K}_0 \left(2 \sqrt{\frac{iz}{\delta_2}} \right) \quad (4.12)$$

$$H_{2B}(\omega, z) = \frac{2}{\rho \frac{\delta k}{\delta z}} \left[\mathcal{K}_0 \left(2 \sqrt{\frac{iz}{\delta_2}} \right) - \frac{\mathcal{K}_0 \left(2 \sqrt{\frac{ih}{\delta_2}} \right) I_0 \left(2 \sqrt{\frac{iz}{\delta_2}} \right)}{I_0 \left(2 \sqrt{\frac{ih}{\delta_2}} \right)} \right] \quad (4.13)$$

$$H_{2C}(\omega, z) = \frac{2}{\rho \frac{\delta k}{\delta z}} \left[\mathcal{K}_0 \left(2 \sqrt{\frac{iz}{\delta_2}} \right) + \frac{\mathcal{K}_1 \left(2 \sqrt{\frac{ih}{\delta_2}} \right) I_0 \left(2 \sqrt{\frac{iz}{\delta_2}} \right)}{I_1 \left(2 \sqrt{\frac{ih}{\delta_2}} \right)} \right] \quad (4.14)$$

The Class 2 models assume a linearly increasing viscosity, and thus, increasing Ekman decay scale with increasing depth. This results in the mean Ekman current profile displaying rapid decay and rotation in the surface waters; however as depth increases the rate of decay and rotation slow.

c. Linearly Increasing Viscosity Models With A Non-Zero Surface Viscosity (Class 3)

Class 3 models assume a linearly increasing viscosity with a non-zero surface viscosity:

$$K(z) = k + z \cdot \frac{\delta k}{\delta z}$$

To simplify the following expressions we define two commonly used terms as:

$$a = 2 \sqrt{\frac{i(z_0 + z)}{\delta_2}} \quad (4.15a)$$

$$b = 2 \sqrt{\frac{iz_0}{\delta_2}} \quad (4.15b)$$

The transfer functions for this class of model are:

$$H_{3A}(\omega, z) = \frac{1}{\rho\sqrt{i(2\pi\omega + f)k}} \frac{\mathcal{K}_0(a)}{\mathcal{K}_1(b)} \quad (4.16)$$

$$H_{3B}(\omega, z) = \frac{1}{\rho\sqrt{i(2\pi\omega + f)k}} \frac{I_0(a)\mathcal{K}_0(a) - \mathcal{K}_0(a)I_0(a)}{I_1(b)\mathcal{K}_0(a) + \mathcal{K}_1(b)I_0(a)} \quad (4.17)$$

$$H_{3C}(\omega, z) = \frac{1}{\rho\sqrt{i(2\pi\omega + f)k}} \frac{\mathcal{K}_1(a)I_0(a) + \mathcal{K}_0(a)I_1(a)}{\mathcal{K}_1(b)I_1(a) - I_1(b)\mathcal{K}_1(a)} \quad (4.18)$$

Similar to the Class 2 models, the Class 3 models display a more rapid rate of rotation and decay near the surface than at depth. However, in this case the rates of decay and rotation with depth are also sensitive to the depth constant component of $K(z)$.

4.5 Method

a. Estimating Power Spectra and Transfer Functions

We estimated the cross-spectra and auto-spectra over a frequency range of -2 to 2 CPD using Welch's Method (Welch, 1967) whereby a time series is split up into overlapping windows, power spectra estimated for each window and then a mean spectrum calculated over all windowed spectra. Note that positive frequencies correspond to anticlockwise and, in this study focusing on the Southern hemisphere, anticyclonic rotation). For both float and shipboard observations we used 10 day windows (40 data-points wide for the floats and 500 data-points wide for the shipboard data). For the shipboard data we used a 75% overlap between adjacent windows to maximize the number of power-spectra estimates from the relatively short time series. Since the float data consists of 8 separate time series, each longer than the shipboard data, a 50% overlap between adjacent windows, in line with Elipot and Gille's method, was adequate.

The shipboard data consists of a single continuous time series of ocean velocities along the ship-track and a corresponding time series of wind stresses. Hence, we were able to apply Welch's

method directly. Unlike the shipboard data the float data consisted of independent time series from each of the floats. Hence, we applied Welch’s method to each float independently. We then averaged over all ‘windowed’ wind-stress autospectra and wind-current cross spectra to obtain a “composite” wind-stress autospectrum and a “composite” wind-current cross spectrum. All individual ‘windowed’ spectra generated for each float were retained for use in the error analysis outlined below.

From Equation 4.5 the observed transfer function was computed as the ratio between the wind stress-current cross-spectrum ($P_{\tau u}$) and wind-stress auto-spectrum ($P_{\tau\tau}$):

$$H(\omega, z) = \frac{P_{\tau u}}{P_{\tau\tau}} \quad (4.19)$$

Uncertainty in the observed transfer function was estimated using a bootstrap method in which $P_{\tau u}$ and $P_{\tau\tau}$ were recalculated multiple times (8 for the ADCP data, 51 for the float data), each time with one windowed spectrum excluded to produce bootstrap power spectra and bootstrap transfer functions ($H_{b,1}$ to $H_{b,n}$). Standard deviations of $P_{\tau u}$ and $P_{\tau\tau}$ were then estimated from the scatter of bootstrap estimates about the corresponding mean value. These standard deviations were propagated through equation 4.19 to obtain the standard deviation of H_{obs} , and 95% confidence intervals were then calculated (Equation 3.9).

b. Fitting Transfer Functions At Constant Depth

We fitted the models discussed above to three subsets of the data; in the first case we duplicated the method described by Elipot and Gille (2009a) in which fits were applied at a constant depth level. To fit each model to the observations a cost function (L) was used. Following Elipot and Gille (2009a) we defined the cost function as the sum over all frequencies of the residual between model transfer function (H_m) and observed transfer functions weighted by the square of the coherence (γ^2):

$$L = \sum_{v_k} |H_m(\omega_k) - H_{obs}(\omega_k)| \times \gamma(\omega_k)^2 \quad (4.20)$$

Where γ^2 was calculated from the observed transfer function, the wind autospectrum and the current autospectrum (P_{uu}):

$$\gamma(v_k)^2 = |H|^2 \frac{P_{\tau\tau}(\omega)}{P_{uu}(\omega, z)} \quad (4.21)$$

Additional penalties to the cost function were applied if the optimisation strayed into a physical parameter space (here taken as $k > 3$, $k < 0$, $dk > 3$, $dk < 0$ or $BLD > 10000m$). In turn dL , the expected uncertainty in L , was estimated by propagating the error in the observed transfer function through:

$$dL = \sum_{v_k} d|H(\omega_k)| \times \gamma(\omega_k)^2 \quad (4.22)$$

Each model was initialised with parameters randomly selected within the parameter space described above, and a Nelder-Mead simplex search was run seeking to minimize the cost function given in equation 4.20. This was repeated 100 times to ensure thorough coverage of parameter space, and hence, maximize the chances of identifying all solutions.

Next we identified unique solutions for each model. In the cases where we found multiple solutions we first considered the cost function value; if one solution displayed a significantly lower L than all other solutions (i.e. $L_1 + dL < L_2$) it was taken as the optimum estimate of model parameters. If multiple solutions with comparable cost function values were detected we then applied a simulated annealing process. Diverging from Elipot and Gille (2009a), optimal solutions were then selected based upon a combination of the minimum cost score returned by the annealing process and the degree of change between the Nelder-Mead and annealing estimates of parameters.

This procedure was repeated, substituting the bootstrap transfer functions $H_{b,1}$ to $H_{b,n}$ in place of H_{obs} . Error bars for each parameter were then estimated as the mean absolute deviation:

$$error = \frac{1}{M} \sum_{k=1}^{k=M} |x_k - x| \quad (4.23)$$

Where M denotes the number of bootstrap estimates retained for the error analysis; x is the optimum parameter estimate from the observed transfer function H_{obs} , and x_k is the parameter estimate from the k^{th} bootstrap transfer function.

d. Fitting Transfer Functions At Constant Frequency

Unlike the surface drifter data used by Elipot and Gille (2009a) the EM-APEX floats and shipboard ADCP data employed in this study provided data over a range of depths. This allows examination of the oceanic response at specific forcing frequencies. Power spectra and transfer functions were calculated independently for time series taken across each depth level (2m intervals for floats, 8m intervals for ADCP data) between the surface and 100m. We then isolated the value of the observed and bootstrap transfer functions over all depth levels at four frequencies; plus and minus the inertial frequency and plus and minus half the inertial frequency.

The optimisation procedure operated in a similar manner as for the constant depth fitting, with the exception that the cost function, L, and uncertainty in the cost function, dL, were calculated at all depths over one frequency:

$$L = \sum_{z_k} |H_m(z_k) - H_{obs}(z_k)| \times \gamma(z_k)^2 \quad (4.24)$$

With the corresponding dL calculated as:

$$dL = \sum_{z_k} d|H(z_k)| \times \gamma(z_k)^2 \quad (4.25)$$

e. Fitting Transfer Functions by Depth and Frequency

As with the fits at constant frequency, power spectra and transfer functions were calculated independently for time series taken across each depth level between the surface and 100m.

The cost function was defined in a similar manner to the above, but was summed over both frequency and depth:

$$L = \sum_{z_k} \left(\sum_{\omega_k} |H_m(z_k, \omega_k) - H_{obs}(z_k, \omega_k)| \times \gamma(z_k, \omega_k)^2 \right) \quad (4.26)$$

dL was calculated in the same manner:

$$dL = \sum_{z_k} \sum_{\omega_k} d|H(z_k, \omega_k)| \times \gamma(z_k, \omega_k)^2 \quad (4.27)$$

f. Isolating Ageostrophic Velocities and Selecting Frequency Bands

Since we wish to investigate Ekman currents we must remove the geostrophic component from the observed velocity time series. Here we have three alternative methods: to use a deep reference velocity as in Lenn and Chereskin (2009); a deep reference velocity plus geostrophic shear estimated in Chapter 3, or to use SSH derived surface velocities interpolated onto float and ship tracks.

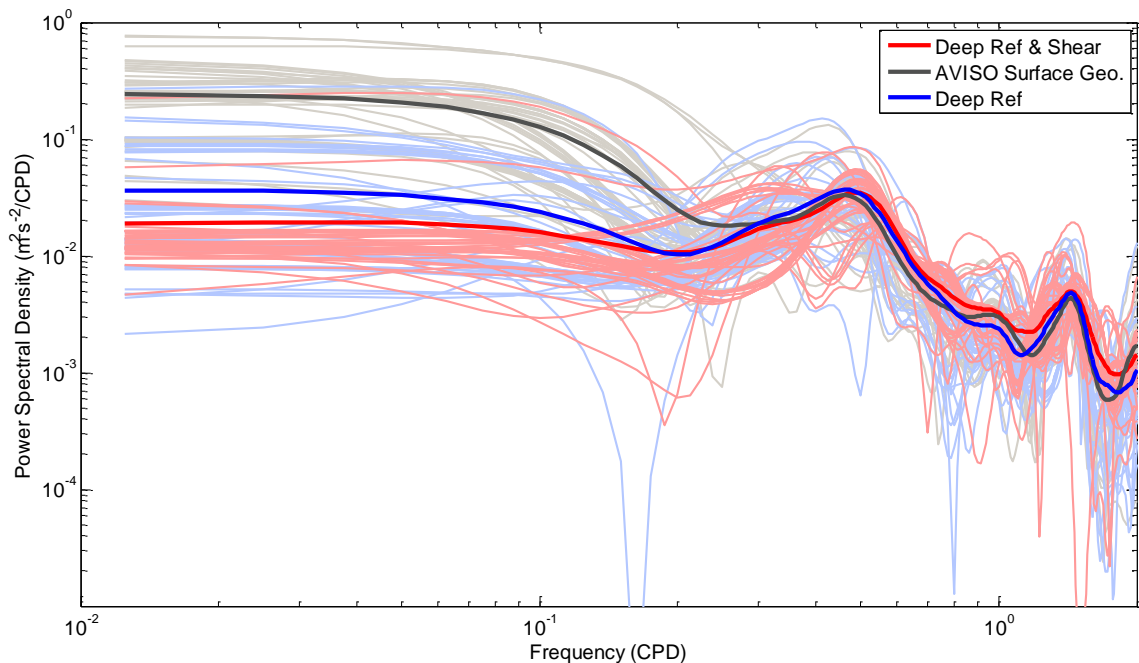


Figure 4.3: 24m Ageostrophic current anticlockwise autospectra estimated from float observations approximating geostrophic currents with: (i) a deep reference velocity and shear (see Chapter 3, Red); (ii) surface currents estimated from AVISO SSH fields (grey) or (iii) a deep reference velocity (Blue). Thick lines denote mean spectra; pale lines denote each bootstrap estimate. Note the general

agreement at high frequencies but significant disagreement between the surface SSH and deep reference velocity approximations at low frequencies (<0.1 CPD).

To determine which of these methods is the most appropriate we calculated autospectra using each of these methods for the float data (Figure 4.3), and using both deep reference velocities and SSH data for the shipboard ADCP data (Figure 4.4).

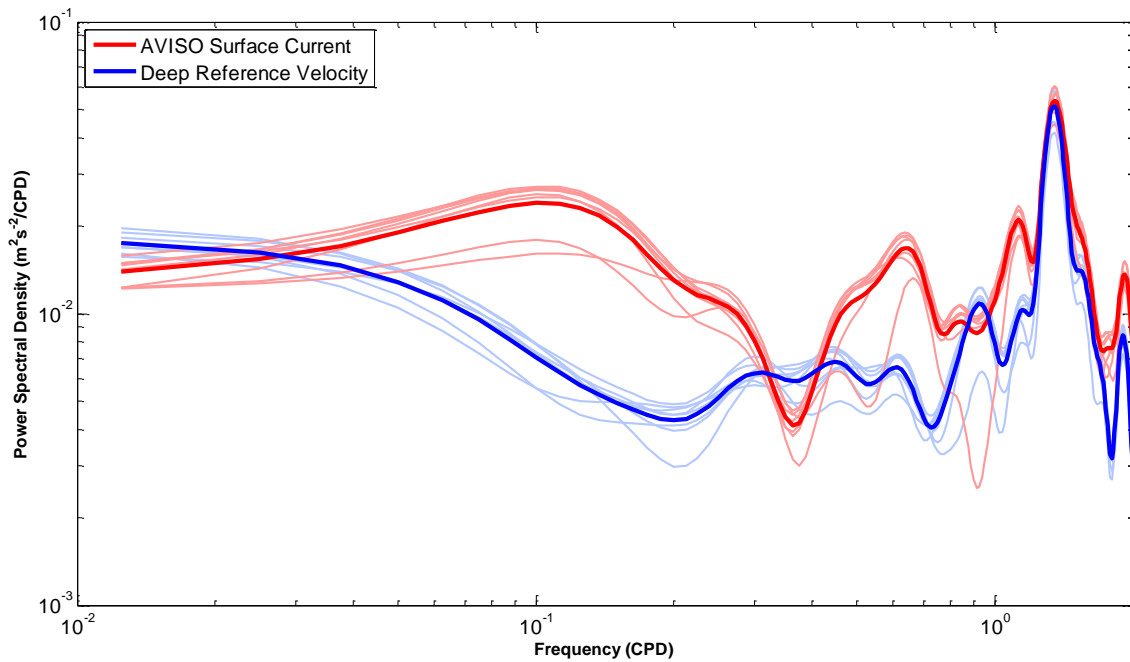


Figure 4.4: 24m Ageostrophic current anticlockwise autospectra estimated from shipboard ADCP observations approximating geostrophic currents with: (i) surface currents estimated from AVISO SSH fields (red) or (iii) a deep reference velocity (blue). Thick, dark lines denote mean spectra; thin, pale lines denote each bootstrap estimate.

All power spectra estimated for each method of removing geostrophic currents are closely comparable at frequencies greater than 0.2 CPD. Inclusion of shear was found to result in only minor differences compared to the use of just a deep reference velocity as a geostrophic proxy. In turn, the use of deep reference velocities was found to attenuate the mean PSD by about an order of magnitude at low frequencies when compared with the SSH geostrophic velocity PSD and previous results given in Elipot and Gille (2009b). Despite this, outlying bootstrap estimates indicate a degree of overlap. It must also be noted that the low frequencies are not well resolved due to the combination of the relatively short period of high frequency observation by the floats (maximum of

70 days of sampling at 4 profiles per day) and the length of the windows used in the spectral estimates. Examination of the shipboard current autospectra shows less disagreement between the two techniques at low frequencies (<0.1 CPD), disagreement of a factor of 2-3 in the middle of the frequency band (0.1-1 CPD) and comparable performance at high frequencies.

As no method was clearly better we opted to maintain consistency with previous studies and use the AVISO SSH currents as the primary proxy for the geostrophic velocity. We also applied a limited analysis (repeating the fitting at constant depth) using a deep reference velocity as a proxy for geostrophic currents to quantify how much difference is made by the definition of geostrophic velocity.

g. Estimating Wind Energy Input

Following Elipot and Gille (2009b) we start with the spectral energy equation (see Elipot's paper for the full derivation) at the ocean surface:

$$P_{\tau u}(0, \omega_k) = i(2\pi\omega_k + f)E + D \quad (4.28)$$

Where E denotes the vertically integrated Kinetic power spectral density in the Ekman layer and D denotes the vertically integrated dissipated power spectral density. Expressions for E and D are given in Elipot and Gille (2009b), but both D and E are purely real terms.

Continuing to follow Elipot and Gille (2009b), we separated the wind-current cross-spectrum into real (C, designated the co-spectrum) and imaginary (Q, designated the quad-spectrum) components:

$$P_{\tau u} = C_{\tau u} - iQ_{\tau u} \quad (4.29)$$

Hence, the co-spectrum is equal to D, the dissipated power spectral density.

$$D = C_{\tau u} \quad (4.30)$$

And the quad-spectrum is related to the kinetic energy of the Ekman layer.

$$-(2\pi\omega_k + f)E = Q_{\tau u} \quad (4.31)$$

From the definition of the transfer function (equation 4.19) at a given depth (z) and frequency, the co-spectrum is related to the wind stress auto-spectrum and the transfer function by:

$$C_{ui}(\omega, z) = R(H(\omega, z))P_{\tau\tau}(\omega) \quad (4.32)$$

Where $R(H)$ denotes the real component of the transfer function.

Our observations were taken at a depth, denoted z_0 , below the surface (23.55m for the ADCP data and 24m for the float data). Equation 4.32 was rearranged to express the surface co-spectrum in terms of the transfer function and the co-spectrum observed at z_0 :

$$C_{ui}(\omega, 0) = \frac{R(H(\omega, 0))}{R(H(\omega, z_0))} C_{ui}(\omega, z_0) \quad (4.33)$$

The surface co-spectrum was calculated using the best transfer function identified in section 4.7. Error estimates were obtained by repeating this procedure for all bootstrap estimates of the co-spectra and transfer function. We then separated the surface cospectra into the cyclonic ($\omega < 0$ CPD) and anticyclonic ($\omega > 0$ CPD) subsets before integrating each from 0 to 2 CPD to obtain the final estimate of wind energy input.

4.6 Results: ADCP Observations

a. Power Spectra and Coherence

The shipboard current autospectrum was plotted across all depths and frequencies (Figure 4.5), and at 23.55m depth (Figure 4.6). The ADCP current autospectrum peaked near the anticlockwise inertial frequency. Outside near-inertial and high clockwise frequencies the spectral density varied between 10^{-2} and 10^{-3} m^2s^2/CPD , making the ADCP current spectrum “flatter” than the EM-APEX autospectrum (section 4.8). The wind-current cross-spectrum (Figure 4.7) demonstrated for signals with $|\omega| < 0.05CPD$, cyclonic and anticyclonic spectra were of comparable strength in both the real (down-wind) and imaginary (cross-wind) components. Over the frequency band of 0.05-0.5CPD, cyclonic frequencies dominate the real component.

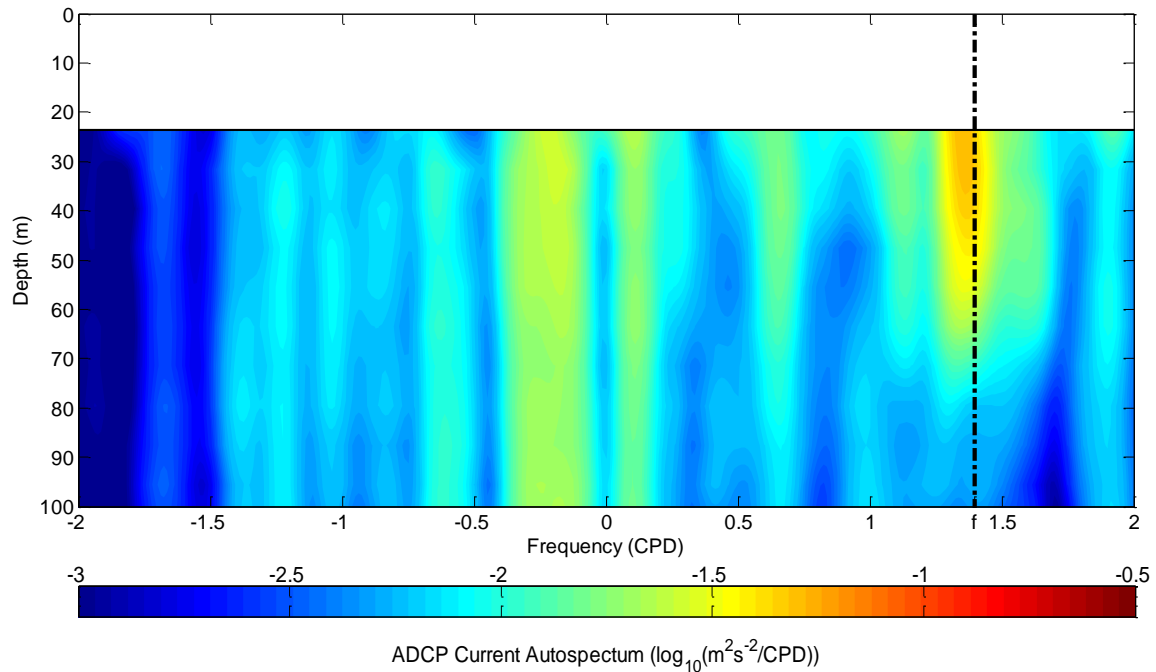


Figure 4.5: ADCP current autospectra ($\log_{10}(\text{m}^2\text{s}^{-2}/\text{Cycle-per-day})$) vs depth. The horizontal black line denotes 23.55m depth level for horizontal fits. The vertical dashed black line marked f denotes mean inertial frequency; note that the inertial frequency is marked in the same manner in subsequent figures.

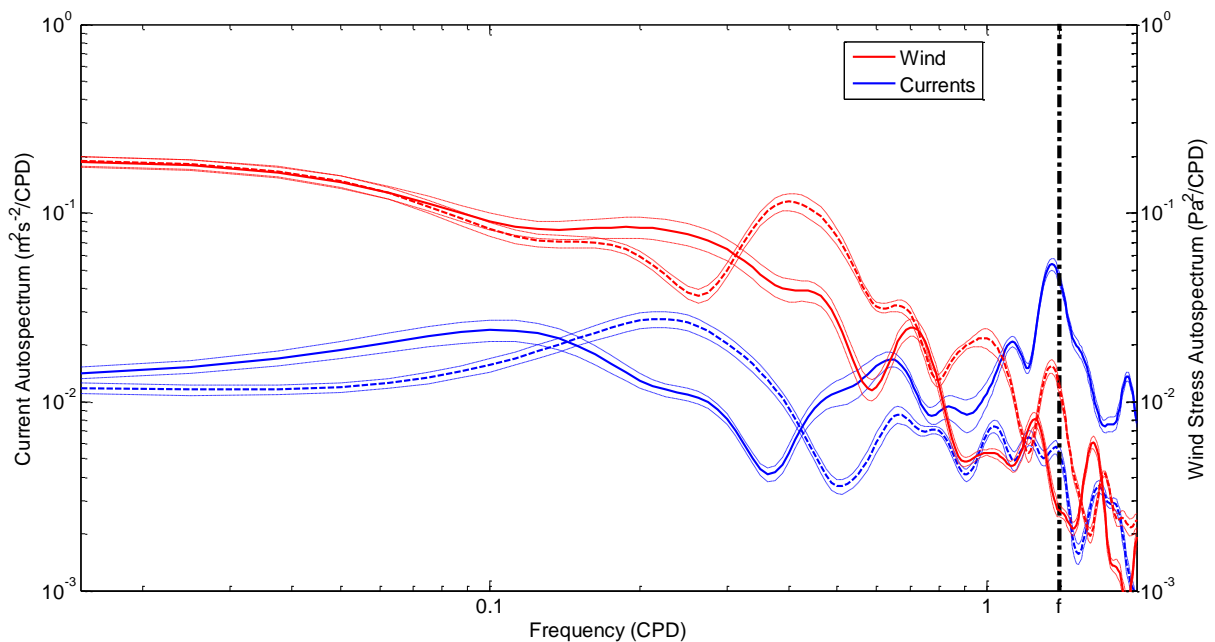


Figure 4.6: Wind stress, and 23.55m current autospectra from the shipboard data described in Section 4.2a. Thick solid lines denote the anticyclonic frequencies; thick dashed lines denote cyclonic frequencies. Thin dashed lines denote 95% confidence intervals estimated over all bootstrap spectra.

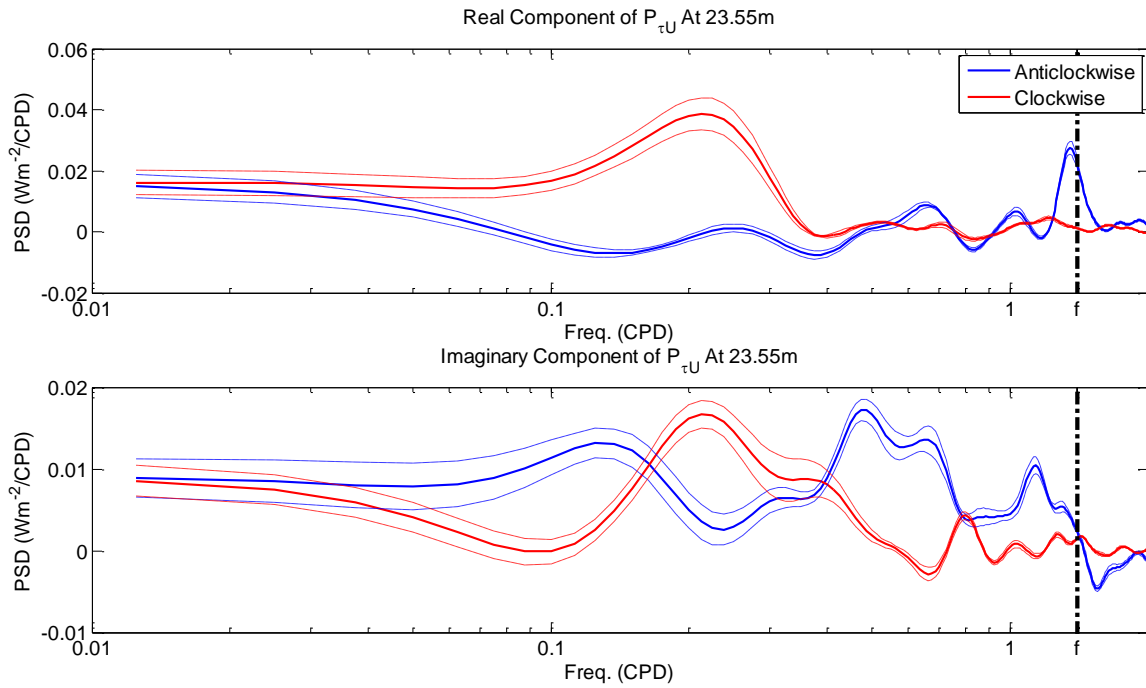


Figure 4.7: The wind-current cross-spectrum at 23.55m (real component top, imaginary component bottom) estimated from shipboard observations. Blue lines denote the anticyclonic frequencies; red lines denote cyclonic frequencies. Dashed lines denote 95% confidence intervals estimated over all bootstrap spectra.

Coherence squared provides a measure of the relation between two signals, in this case the time series of wind stress and ageostrophic current; assuming a linear transfer function. In this case (Figure 4.8) γ^2 displayed a complicated pattern of localized peaks and troughs, with the two most prominent (with $\gamma^2 > 0.6$ at 23.55m depth) occurring near -0.35CPD and around the inertial frequency (1.41CPD). Coherence near these two primary peaks remains high for depths between 23.5m and 80m. In these frequency bands ageostrophic velocities are strongly linked with the wind forcing over a considerable depth range, but away from these frequency bands the currents are only weakly related to the wind forcing.

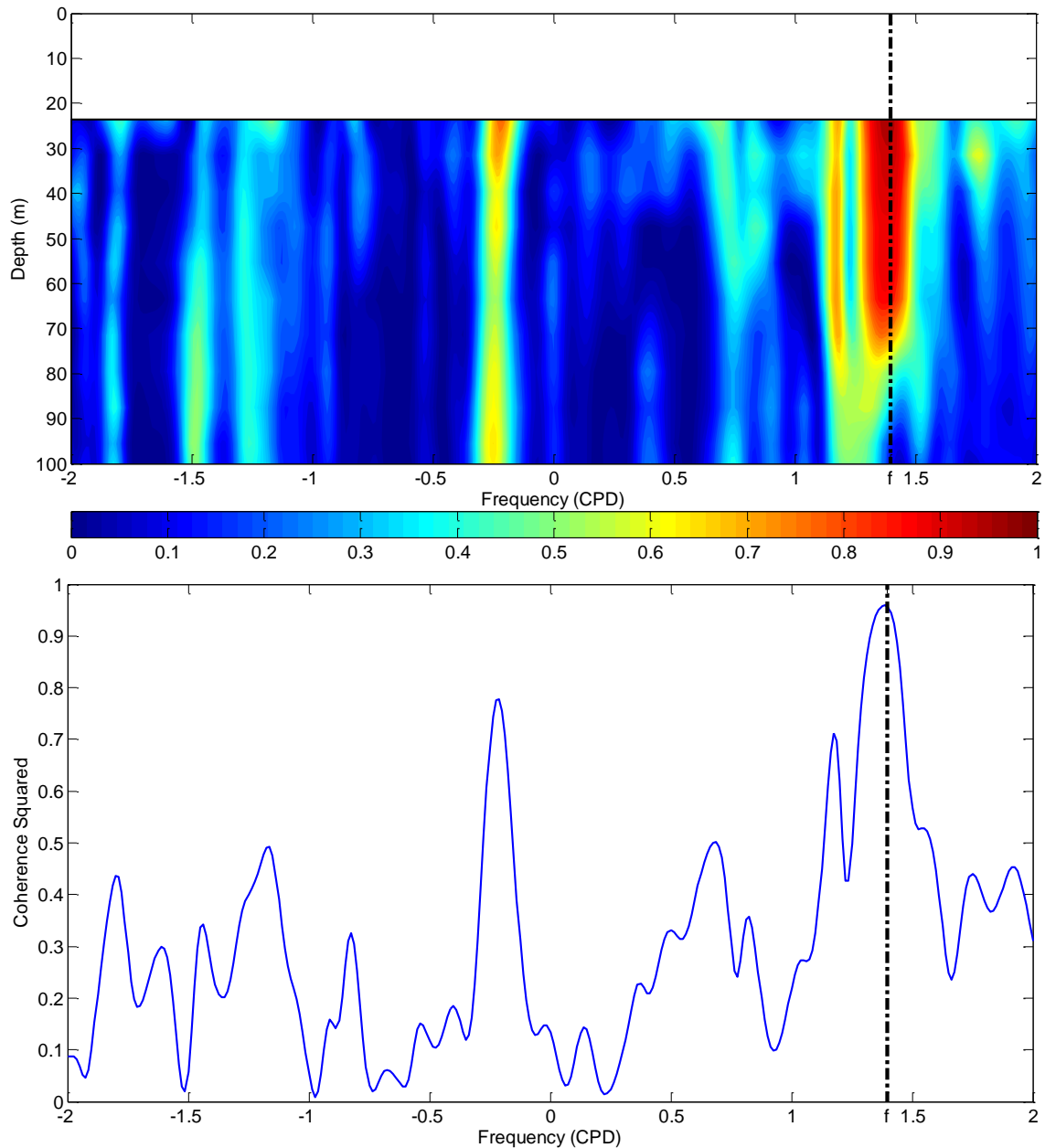


Figure 4.8: Coherence squared as a function of both depth and frequency (top) and at 23.55m

(bottom) for the shipboard ADCP data. When plotted against depth the value of coherence squared is indicated by the colour, ranging from 0 (dark blue) to 1 (dark red).

b. Fitted Transfer Functions: Constant Depth and 2D Fits

Cost function values and fitted parameters for all models are given in Figure 4.9. Models 3B and 3C displayed large uncertainties in viscosity and viscosity gradient, implying that fits of these models to the observations were not reliable. The fits at 23m identified models 1B and 3B to be the best

performing; however model 3B displayed high uncertainty in all parameter estimates. The 2D fit (by frequency and depth over the -2 to 2 CPD and 23.55-100m ranges) also identified model 1B as the best performing. Eddy viscosities for Model 1B were found to be $4.25 \pm 0.60 \times 10^{-2} \text{ m}^2\text{s}^{-1}$ and $4.83 \pm 0.23 \times 10^{-2} \text{ m}^2\text{s}^{-1}$ for the constant depth and 2D fits respectively. Boundary layer depths (BLD) were found to be $104.99 \pm 9.13\text{m}$ and $118.50 \pm 2.86\text{m}$. These eddy viscosities are consistent with results obtained by Elipot and Gille (2009a) but the estimates of BLDs are 2 to 3 times greater than Elipot's circumpolar estimates for a comparable latitude range. Fig. 8 in Elipot and Gille (2009a) indicates greater scatter of BLD estimates during summer, suggesting this difference is likely due to the timing of the SOFINE voyage.

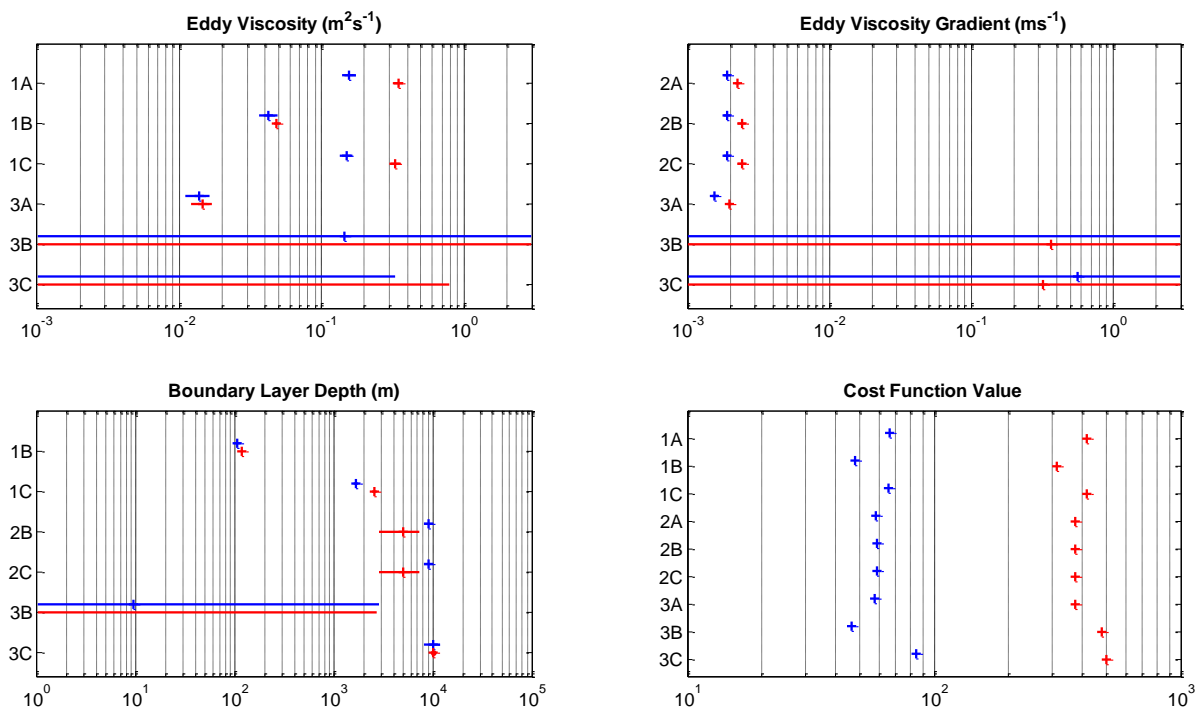


Figure 4.9: Fitted Parameters (k , top left; dk/dz top right; BLD bottom left) and cost function values (bottom right). Plus signs indicate mean values, horizontal lines indicate error bars. Fits over -2 to 2 CPD at 23.55m indicated in blue; 2D fits to 100m indicated in red.

For model 3A and all class 1 and 2 models the 2D fit consistently produced estimates of viscosity and viscosity gradient 10-50% greater than the corresponding results for the 23.55m fit. Models 1A and 1C produced viscosities of around $0.15 \text{ m}^2\text{s}^{-1}$ for the 23.55m fit; and approximately $0.32 \text{ m}^2\text{s}^{-1}$ for the 2D fit. For model 3A the 23.55m fit gave a viscosity of $0.014 \text{ m}^2\text{s}^{-1}$ and the 2D fit

gave $0.024\text{m}^2\text{s}^{-1}$. Estimated viscosity gradients were found to vary over the range $1.5\text{-}2.0 \times 10^{-3} \text{ms}^{-1}$ and $2.0\text{-}3.5 \times 10^{-3} \text{m}^2\text{s}^{-1}$ for the 23.55m and 2D fits respectively. Other than model 1B, all boundary layer depth estimates were between 1600 and 10000m, implying that bottom boundary effects were of little relevance.

Plots of the absolute value of the observed transfer function from the three best fitting models for both the 23.55m fit and the 2D fit are shown in Figure 4.10. While Model 1B for both the constant depth fit and the 2D fit was found to match the key features of the observed transfer function in the anticyclonic sub-inertial to near-inertial domain, it did poorly both in the anticyclonic super-inertial range ($>1.5\text{CPD}$) and over the majority of the cyclonic domain.

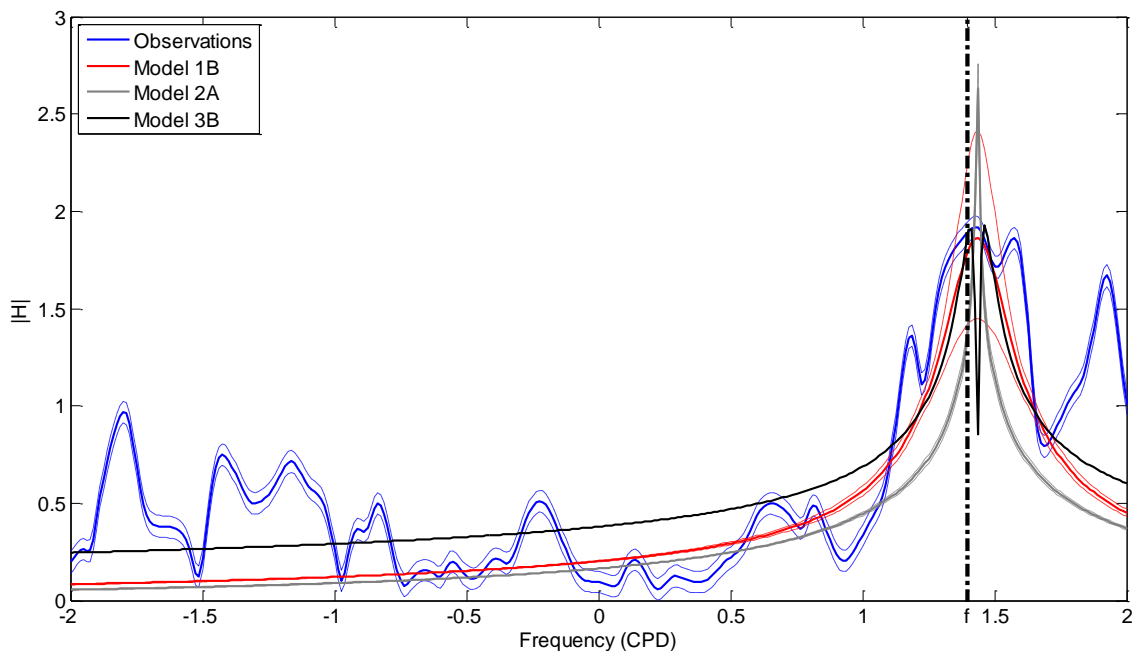


Figure 4.10: Absolute value of the observed transfer function at 23.55m and the transfer functions for the three best performing models. Dashed lines indicate 95% confidence intervals around the transfer functions.

To summarise, both the 23.55m and the 2D fits suggested that a constant viscosity model with a finite BLD and Ekman velocity tending to zero at the BLD (model 1B) provided the most satisfactory fit to the observations. Estimates of eddy viscosity and boundary layer depth were consistent between both of these fits.

c. Fitted Transfer Functions At Constant Frequencies

Parameter estimates and estimated cost function values are given in Figure 4.11. In both sub-inertial frequency fits, all models were found to produce large uncertainties in parameter estimates with error-bars on eddy viscosity, viscosity gradient and BLD often exceeding mean estimates by an order of magnitude. In all cases no model was found to perform statistically better than the rest at the 95% level, however, there was a suggestion of sensitivity to frequency: Class 1 (constant viscosity) models were found to be the best performing as measured by the cost function for both cyclonic and anticyclonic near inertial frequencies, while Class 3 models typically performed better at low frequencies.

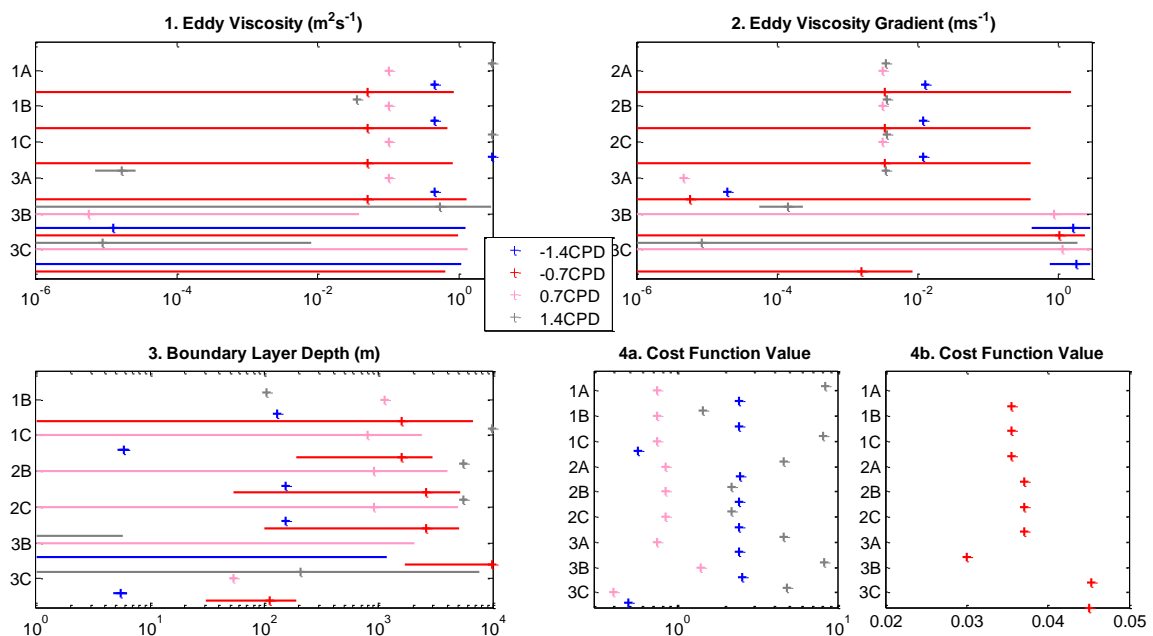


Figure 4.11: Parameter estimates and cost function values (1. Viscosity; 2. Viscosity gradient; 3. BLD; 4a. Cost Function Values for frequencies of -1.4, 0.7 and 1.4 CPD; 4b. Cost function value for -0.7CPD) for fits at constant frequencies of -1.4, -0.7, 0.7 and 1.4 CPD. Plus signs indicate mean values, horizontal lines indicate error bars.

Selected fits and observed transfer functions are shown in Figure 4.12. Near the inertial frequency, model 1B was found to be the most satisfactory, showing not only the best cost function score, but also a good match to the observations over the entire depth range. This fit produced a viscosity of $3.52 \pm 0.18 \times 10^{-2} \text{ m}^2\text{s}^{-1}$ and BLD of $105.47 \pm 1.97\text{m}$, in general agreement to the fit at constant depth.

Model 2C was the second best performing by cost function score in the near-inertial range but proved unsatisfactory when compared to the observed transfer function profile. Models 1C and 3C were found to be the best performing at -1.4CPD and to agree with the observed transfer function within error bars. Both produced extremely shallow ($O(5m)$) boundary layers; the former was also found to display an eddy viscosity at the upper limit of the assumed parameter space while the latter (3C) displayed a viscosity gradient near the upper limit of its parameter-space. The net result in both cases was a transfer function of near constant magnitude with depth. These models, while mathematically acceptable are non-physical. Removing these models from consideration left Model 1B (with k of $0.4436 \pm 0.0333 m^2 s^{-1}$ and BLD of $128.64 \pm 0.92 m$) as the best performing model at -1.4CPD.

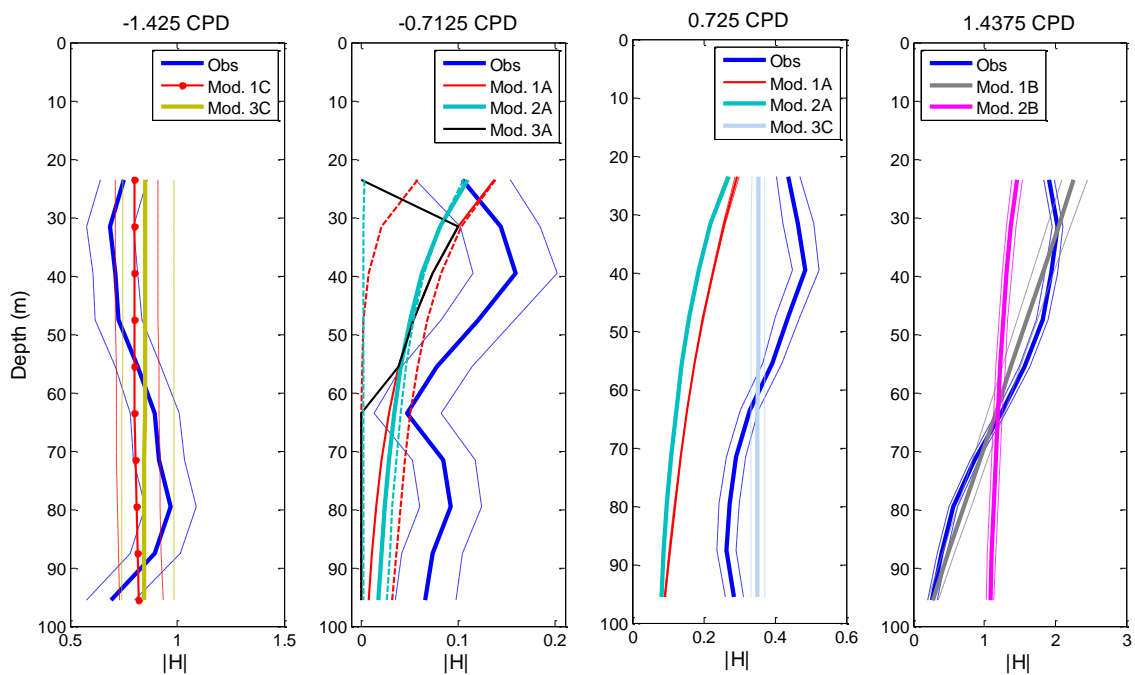


Figure 4.12: Observed and fitted transfer functions vs depth for frequencies of (from left to right) - 1.4, -0.7, 0.7 and 1.4 CPD. Error bars indicated for the observed transfer functions (blue) indicate 95% confidence intervals estimated from bootstrap analysis. Error bars for the fitted transfer functions were estimated by propagating errors in parameter estimates through the theoretical transfer functions.

d. Sensitivity of Fitted Parameters

The estimates of viscosity, viscosity gradient and BLD presented above used a geostrophic velocity determined from sea surface height fields and also included frequency bands which are unlikely to be well resolved with the shipboard data. These factors, together with the depth at which the constant depth fits were applied, have the potential to alter the viscosity, viscosity gradient and BLD values estimated above.

We investigated the sensitivity to frequency resolution of the constant depth fits to the float observations by repeating the fitting procedure with low frequencies (-0.1 - 0.1 CPD) suppressed. The resulting parameter estimates are shown in Figure 4.13. Suppressing low frequency variability was found to have no statistically significant effect on any of the model parameters.

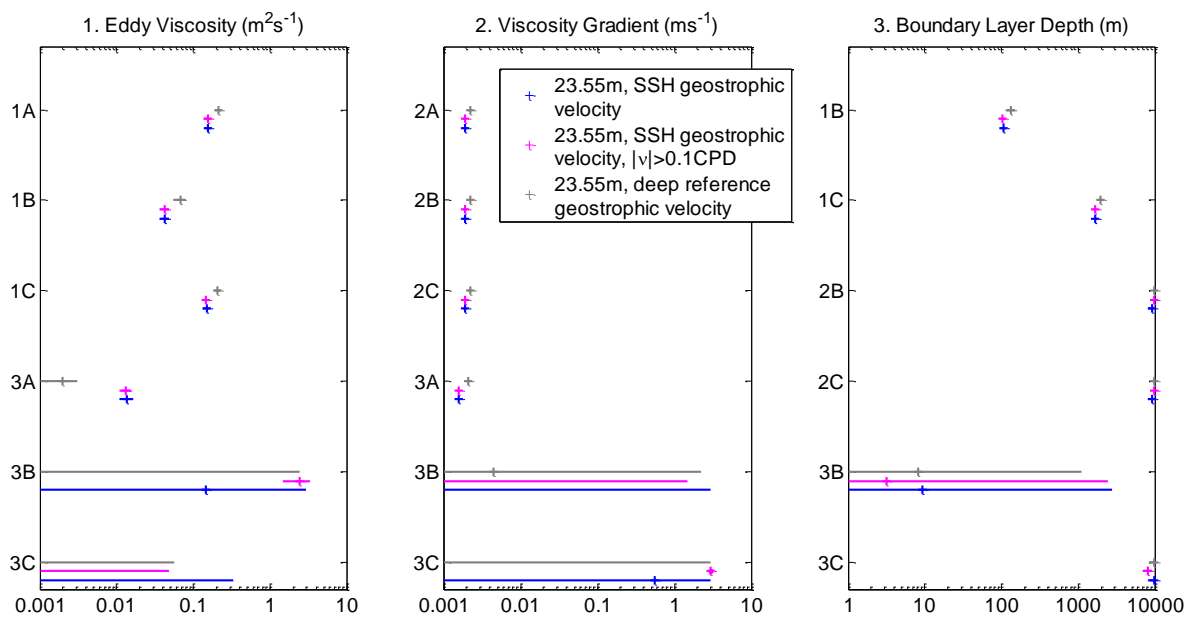


Figure 4.13: Parameters fits with low frequencies suppressed and using a deep reference velocity as a proxy for geostrophic currents. Mean values and uncertainty indicated per figure 4.9.

The sensitivity to geostrophic proxy was assessed by repeating the fitting procedure using deep reference velocities as the geostrophic proxy in place of the SSH derived currents used above. The use of a deep reference velocity as a proxy for the geostrophic currents was found to have significant effect on our estimates of viscosity gradients and boundary layer depths (Figure 4.13). Viscosities obtained from the type 1 (constant viscosity) models were larger than, but of the same

order of magnitude as, viscosities obtained for the same models with the AVISO SSH geostrophic proxy. Model 3A (infinite BLD, linearly increasing viscosity with a non-zero surface offset) produced a viscosity an order of magnitude weaker than was obtained for the same model when using SSH geostrophic currents. Other type 3 models displayed wide confidence intervals, preventing a proper assessment of how the alternate geostrophic proxy impacted the parameter estimates.

We repeated the constant depth fits at a range of depths down to 79.55m (Figure 4.14). All models display agreement in terms of parameter amplitudes between 23.55m and 63.55m. Despite this general agreement, models only reliably achieved a match on all parameters to the constant depth fits above (23.55m) at 31.55m. Excluding models 3b and 3c, we observed a general tendency for mean viscosity, viscosity gradient and BLD estimates to increase with increasing depth. The tendency for models to produce larger parameter estimates at deeper depth levels may be a result of moving from the mixed layer to ocean interior regimes.

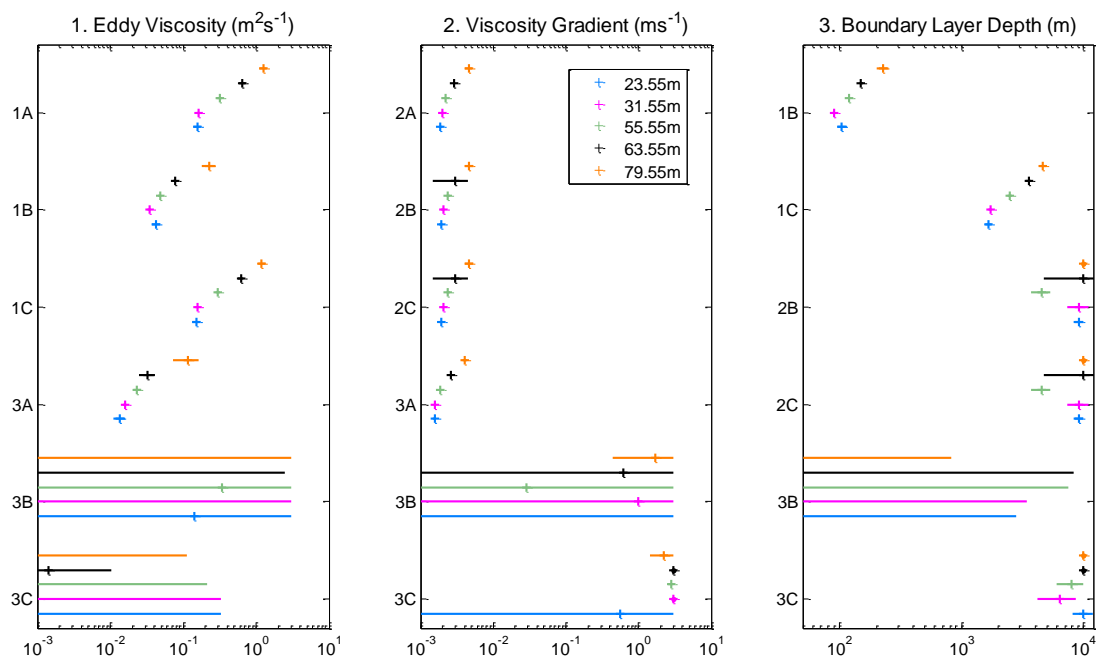


Figure 4.14: Parameter estimates from constant depth spectral fitting at depths between 23.55m and 79.55m. Mean values and uncertainty indicated per figure 4.9.

The spectral fits to the shipboard wind and ADCP data show no significant sensitivity to suppressing low frequency winds. There is a marginal sensitivity to the use of deep reference velocities rather than SSH derived velocities as proxies for the geostrophic currents.

4.7 Results: EM-APEX Floats

a. Power Spectra

Autospectra calculated from winds and 24m currents averaged over all floats are shown in Figure 4.15. The float current autospectrum shows greater variability than the corresponding ADCP spectrum varying from $10^{-1} \text{ m}^2\text{s}^{-2}/\text{CPD}$ at low frequencies to $10^{-4} \text{ m}^2\text{s}^{-2}/\text{CPD}$ at high frequencies. While the EM-APEX power spectrum displays a clear near-inertial response it is significantly weaker than is seen with the ADCP spectrum. The float wind-stress autospectrum was found to be smaller than the shipboard wind-stress autospectrum across the entire frequency range. At frequencies less than 0.1CPD the float autospectrum was a factor of two smaller than the shipboard autospectrum; while at near and super-inertial frequencies the float spectrum is approximately an order of magnitude smaller than for the shipboard observations. Examining the current autospectrum as a function of both depth and frequency (Figure 4.16), we find that the differences compared to the ADCP spectrum (Figure 4.5) discussed above extend to approximately 50m depth.

EM-APEX estimates of the wind-current cross-spectrum are shown in Figure 4.17. Compared to the shipboard cross-spectrum (Figure 4.7), the float spectrum displays much wider error bars at low frequencies and has lower amplitude and less variability at frequencies over 0.2CPD. In Figure 4.18 we present an expanded view of the EM-APEX wind-current cross-spectrum to highlight the near-inertial response; while a near inertial peak is present it is much weaker ($2 \times 10^{-4} \text{ Wm}^{-2}/\text{CPD}$) than in the shipboard spectrum ($3 \times 10^{-2} \text{ Wm}^{-2}/\text{CPD}$).

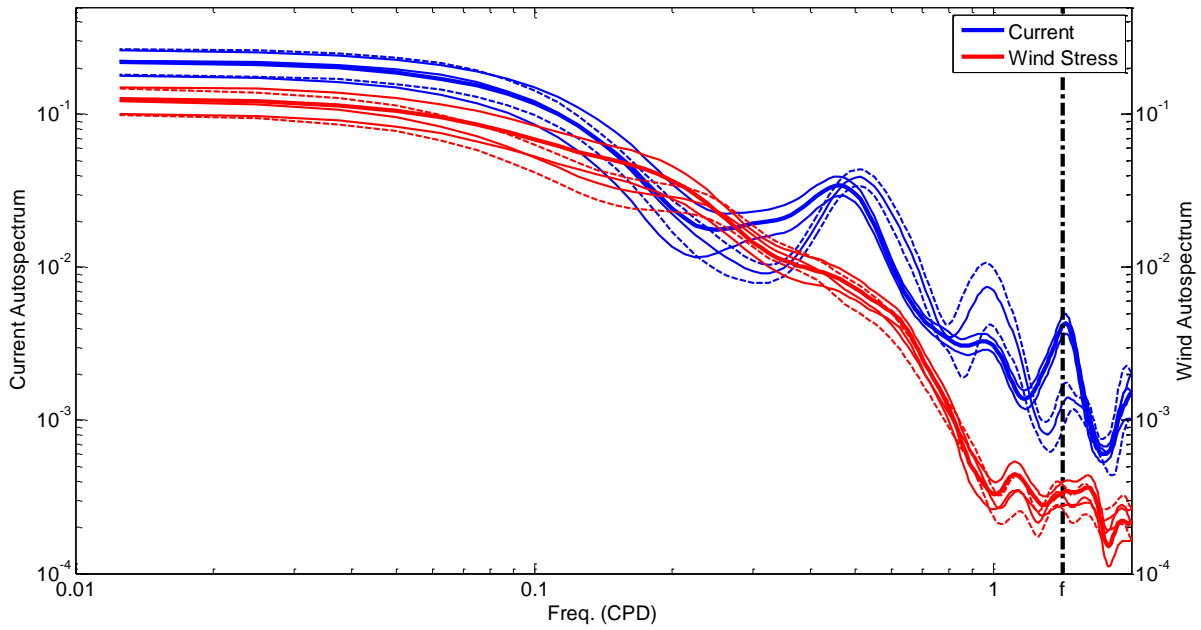
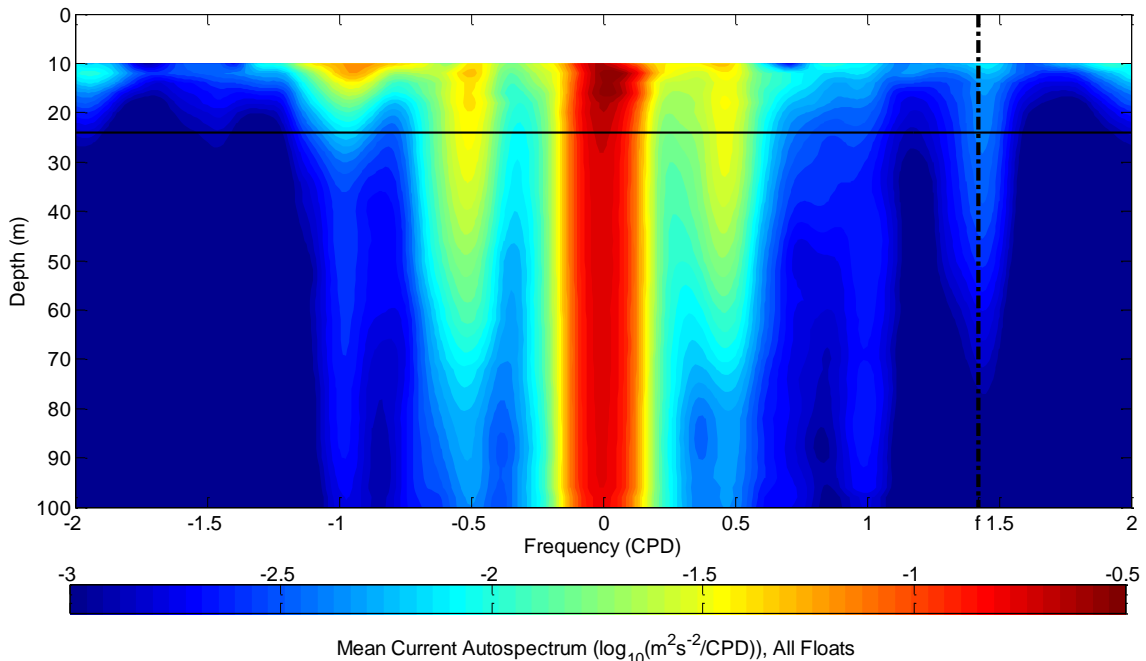


Figure 4.15: Wind stress and current autospectra at 24m estimated from EM-APEX float data. Solid lines denote the mean autospectra, dashed lines indicate the 95% confidence intervals estimated by a bootstrap method.



Mean Current Autospectrum ($\log_{10}(m^2s^{-2}/CPD)$), All Floats
 Figure 4.16: EM-APEX current autospectrum ($\log_{10}(m^2s^{-2}/\text{Cycle-per-day})$) vs depth (mean over all data.). The vertical dashed black line denotes mean inertial frequency over all 8 floats; the horizontal black line denotes depth level for the constant depth fits.

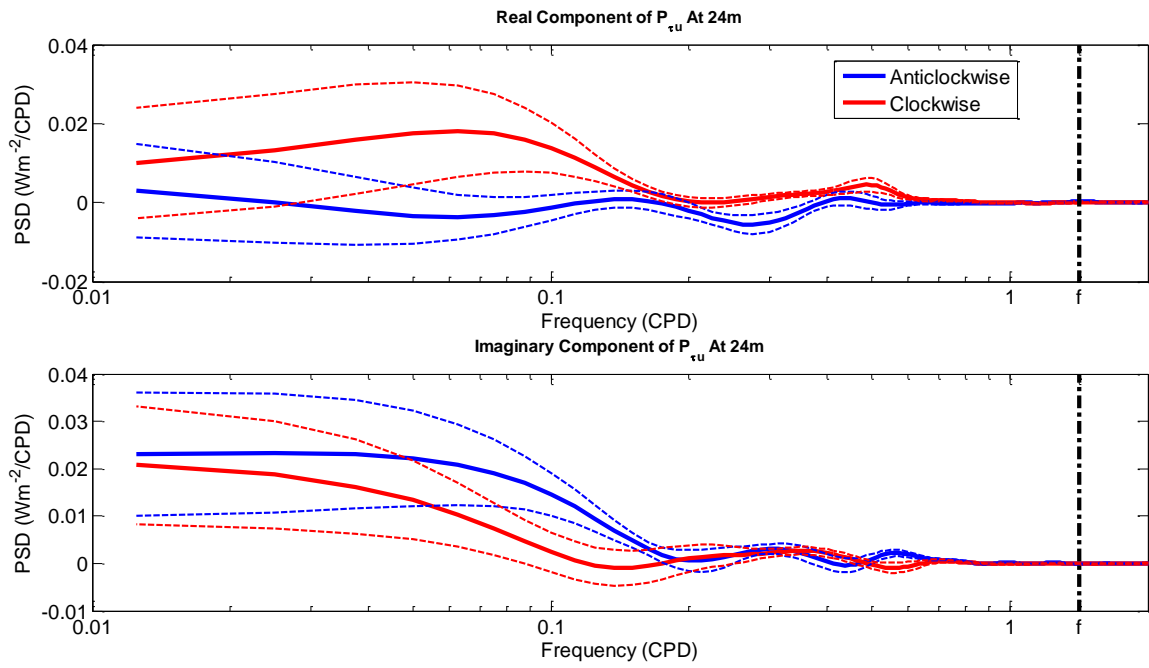


Figure 4.17: EM-APEX wind-current cross-spectrum at 24m (real component top, imaginary component bottom). Blue lines denote the anticyclonic frequencies; red lines denote cyclonic frequencies. Dashed lines denote 95% confidence intervals estimated over all bootstrap spectra.

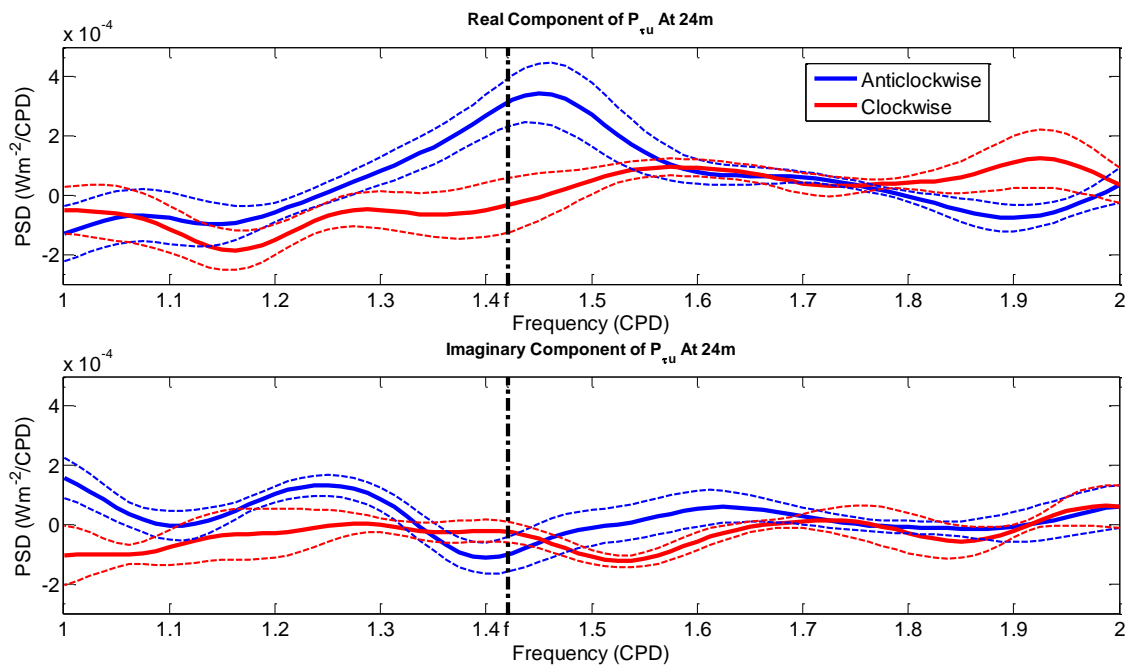


Figure 4.18: EM-APEX wind-current cross-spectrum at 24m (real component top, imaginary component bottom) plotted over 1-2CPD.

b. Fitted Transfer Functions and Parameter Estimates

Parameter values and cost functions obtained from fits to the EM-APEX float data are given in Figure 4.19. Error estimates obtain by the bootstrap method described above were generally found to be large relative to the mean parameter estimates, likely due to the larger variability seen in the float current autospectra (Figure 4.3) than in the corresponding shipboard estimates (Figure 4.4) For both the 1.4CPD and 24m fits, Model 1B was found to be the best performing, with estimated mean viscosities of 0.06 and 0.40 m^2s^{-1} and BLDs of 96 and 336m respectively. Between -1.4 and 0.7CPD fits were consistent in identifying Class 3 models (non-zero surface viscosity linearly increasing with depth) as the most satisfactory.

Mean estimates of viscosity gradients (Figure 4.19, panel 2) were closely consistent within the Class 2 (linearly increasing viscosity) family of models for a single fit but varied between fits; for example, the fit at -0.7CPD gives viscosity gradients of $2\text{-}3 \times 10^{-2} \text{ms}^{-1}$, while the fit at 1.4CPD gives viscosity gradients of $7\text{-}9 \times 10^{-3} \text{ms}^{-1}$ for the same set of models. Meanwhile, mean estimates of viscosity gradient for Class 3 models (non-zero surface viscosity, increasing linearly with depth) displayed no such behaviour.

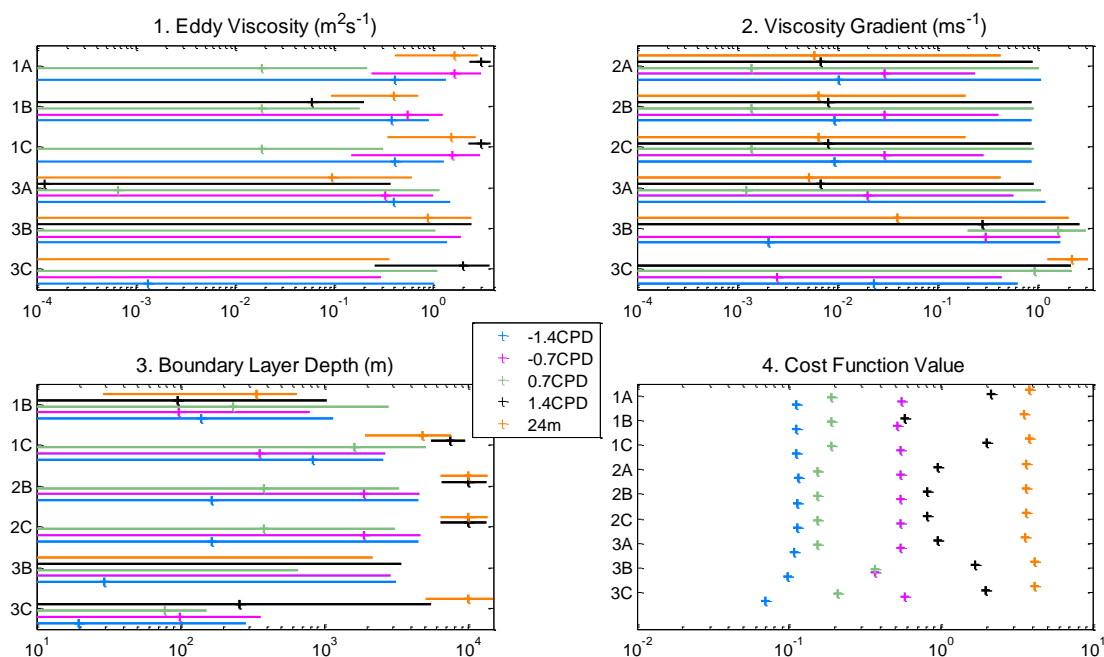


Figure 4.19: Parameter fits and Cost Function Values. Mean values are indicated by the short, vertical lines; uncertainty by the horizontal lines.

Observed transfer functions and the two best fitted models are plotted at each frequency in Figure 4.20. At -1.4, 0.7 and 1.4CPD the best fitted models, as measured by minimum cost function, were found to match the observed transfer function closely over the entire 10-100m depth range. At -0.7CPD model 3B was found to lie right at the lower limit of the error-bars around the observed transfer function, while the second best performing model (1B) lay outside the observed error bars. A similar plot for the 24m fit (Figure 4.21) demonstrates that, as in the shipboard data, model 1B matched the observed transfer function well over the anticyclonic frequencies but captured little of the variability in the cyclonic range.

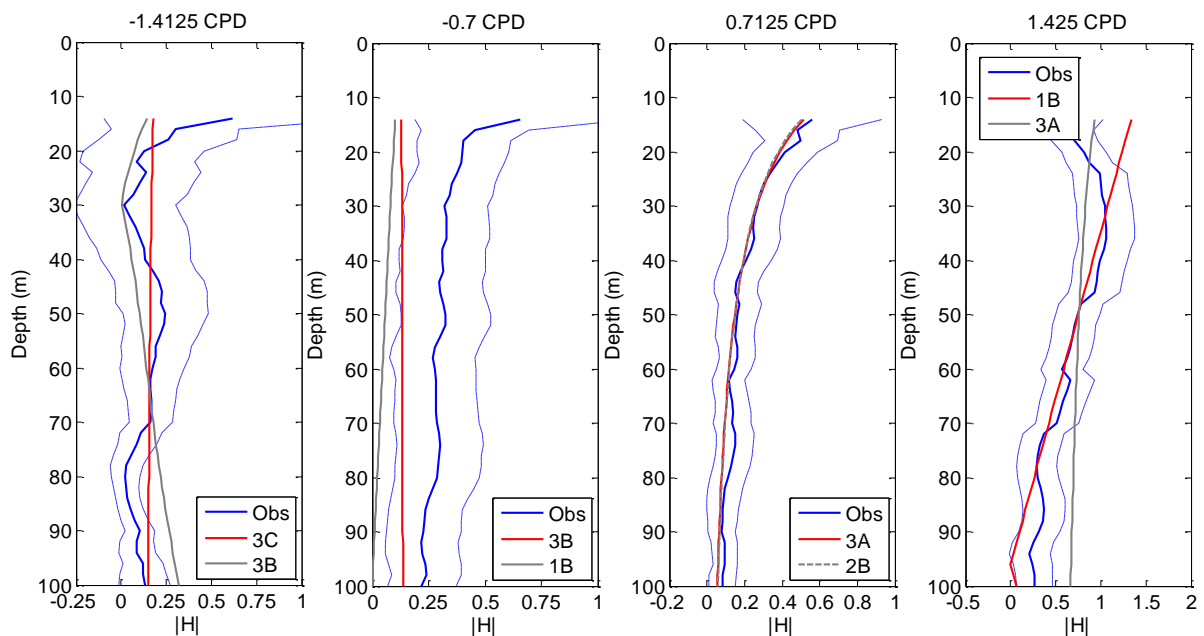


Figure 4.20: Absolute value of transfer function vs depth for observed transfer functions (blue, 95% confidence intervals indicated by dashed lines) and the two best fitting models (red and gray) at near-inertial and half-inertial frequencies.

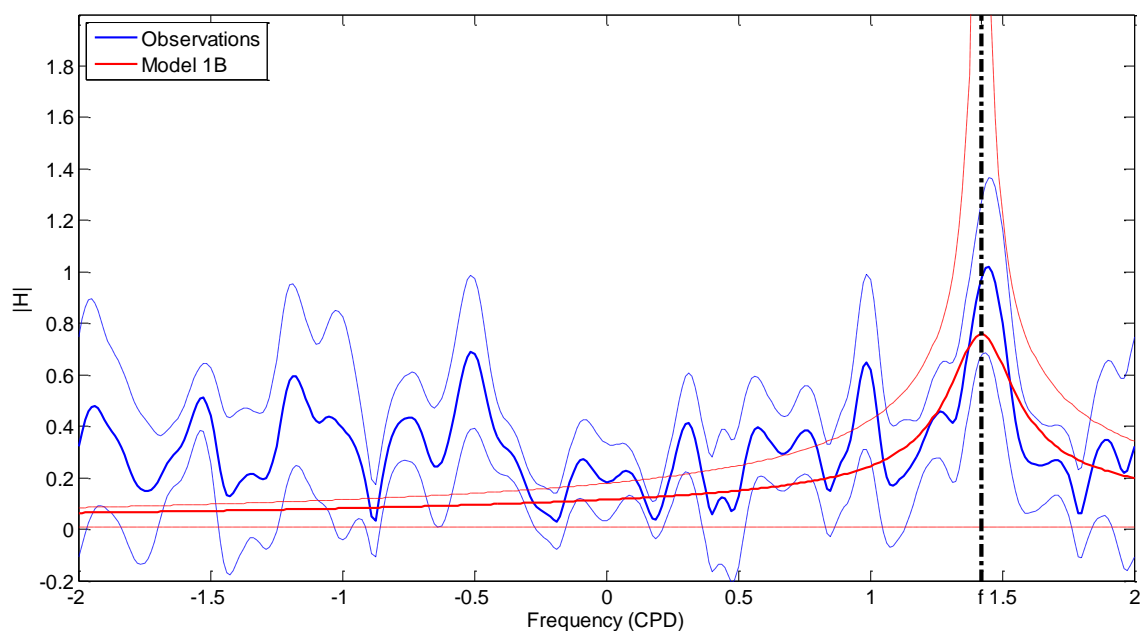


Figure 4.21: Absolute value vs frequency of observed transfer function (blue) and best performing model (1B, red) 24m, -2 to 2 CPD fit. Dashed lines denote the uncertainty about the observed and fitted transfer function.

In summary, in line with the constant depth fits to ADCP data, the corresponding fits of float data suggest model 1B to be the most satisfactory, with eddy viscosities and BLDs comparable in magnitude between both datasets. Similarly, fits at constant frequency found the best performing model depended on the frequency at which the fits were applied; like the fits to ADCP data model 1B was found to perform well at the inertial frequency while Class 3 models were found to deliver the best performance at lower frequencies.

c. Sensitivity of Fitted Parameters to Geostrophic Proxy and Suppression of Low Frequencies

We analysed the sensitivity of the EM-APEX fits in a similar manner section 4.6d. The sensitivity to of geostrophic proxy and suppression of low frequencies is shown in Figure 4.22. Mean parameter estimates for all class 1 and class 2 models show no statistically significant sensitivity to the choice of geostrophic proxy or the suppression of low frequencies. Class 3 models display greater sensitivity in mean parameter estimates, but as discussed above, these models have been found to display large error bars in both shipboard and float data. Hence, we are confident that the choice of geostrophic

proxy and the inclusion of high frequency variability have not significantly affected our estimates of model parameters.

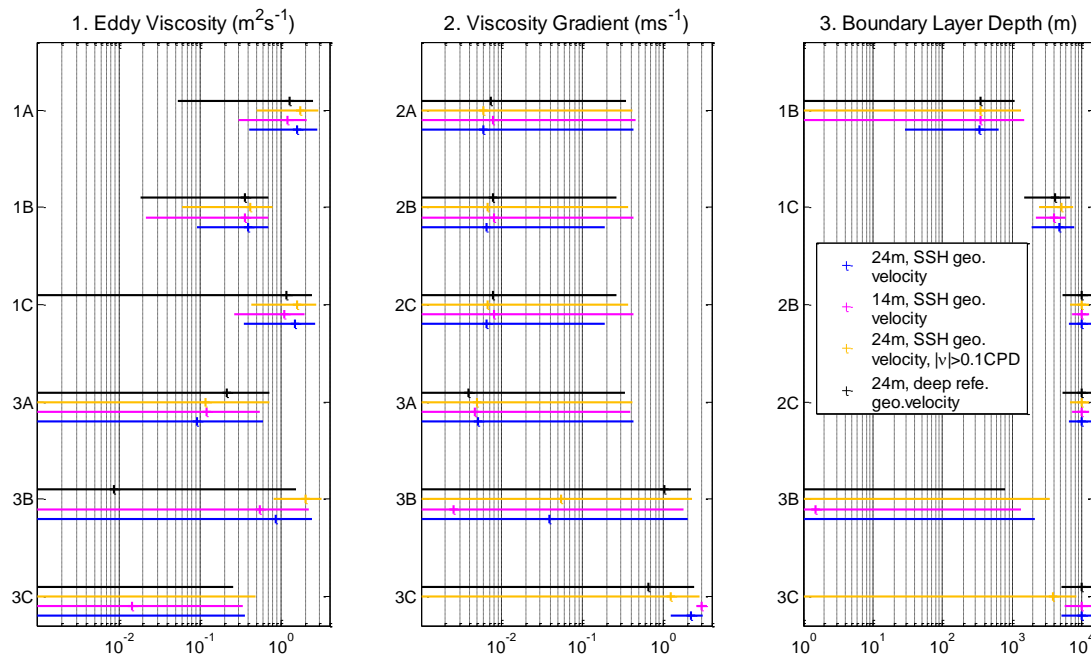


Figure 4.22: Fitted Parameters for 24m fits with (1) AVISO SSH derived geostrophic current; (2) AVISO SSH derived geostrophic current, low frequency (<0.1CPD) signal excluded; (3) 200m reference velocity as a proxy for geostrophic current.

We then repeated the standard constant depth fit at 14m, 24m, 50m and 74m with geostrophic velocities based on ACISO SSH data. Results are shown in Figure 4.23. Estimated mean parameters over class 1 and 2 models were found to be consistent for the 14m, 24m and 50m fits. The fit at 74m depth was found to produce lower mean estimates of viscosity and viscosity gradient for all class 1 and 2 models compared to fits at shallower depths. Estimated BLD was also differed considerably between the 74m fit and shallower depths. Mean mixed layer depth was found to be 43.8m, suggesting this observed inconsistency arises from comparing variability within, or just below the mixed layer to variability within the ocean’s interior.

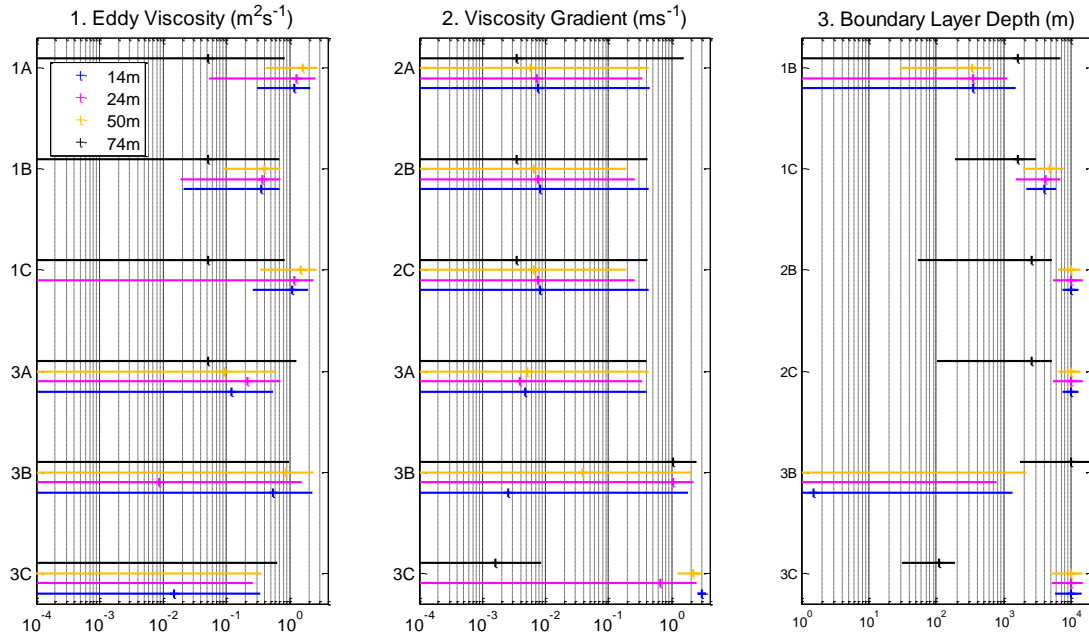


Figure 4.23: Parameters fitted to ageostrophic data at 14m, 24m, 50m and 74m. The ageostrophic current was isolated from the observations using an AVISO SSH based geostrophic current. Panel 1 shows the fitted eddy viscosities; Panel 2 the viscosity gradients and Panel 3 the fitted boundary layer depths.

d. Sensitivity of Fitted Parameters to Wind Fields

As discussed above the parameter values obtained from the fits to the float transfer functions were significantly different from corresponding estimates obtained from fits to the shipboard transfer function. One principal difference between these two datasets was the source of the wind-stresses used to estimate the transfer functions; the shipboard case used *insitu* wind observations whereas the float case made use of the CERSAT reanalysis winds. In Chapter 3 we found the use of wind headings derived from the NCEP/NCAR reanalysis produced a smaller downwind transport anomaly than the same data analysed using winds from the CERSAT blended reanalysis-satellite wind fields. This suggests we need to consider the sensitivity of the spectral fits to our choice of wind data.

The CERSAT winds interpolated onto the shiptrack were found to produce a weaker autospectrum than the *insitu* wind data (Figure 4.24, upper panel). The CERSAT wind spectra for the float tracks displayed a comparable magnitude to the shipboard case. This suggests that the float

wind spectra are also attenuated relative to the (unobserved) 'real' wind spectra along the float tracks, which This raises the possibility that the fits described earlier in this section may display significant sensitivity to the wind data used to estimate wind autospectra and wind-current cross-spectra.

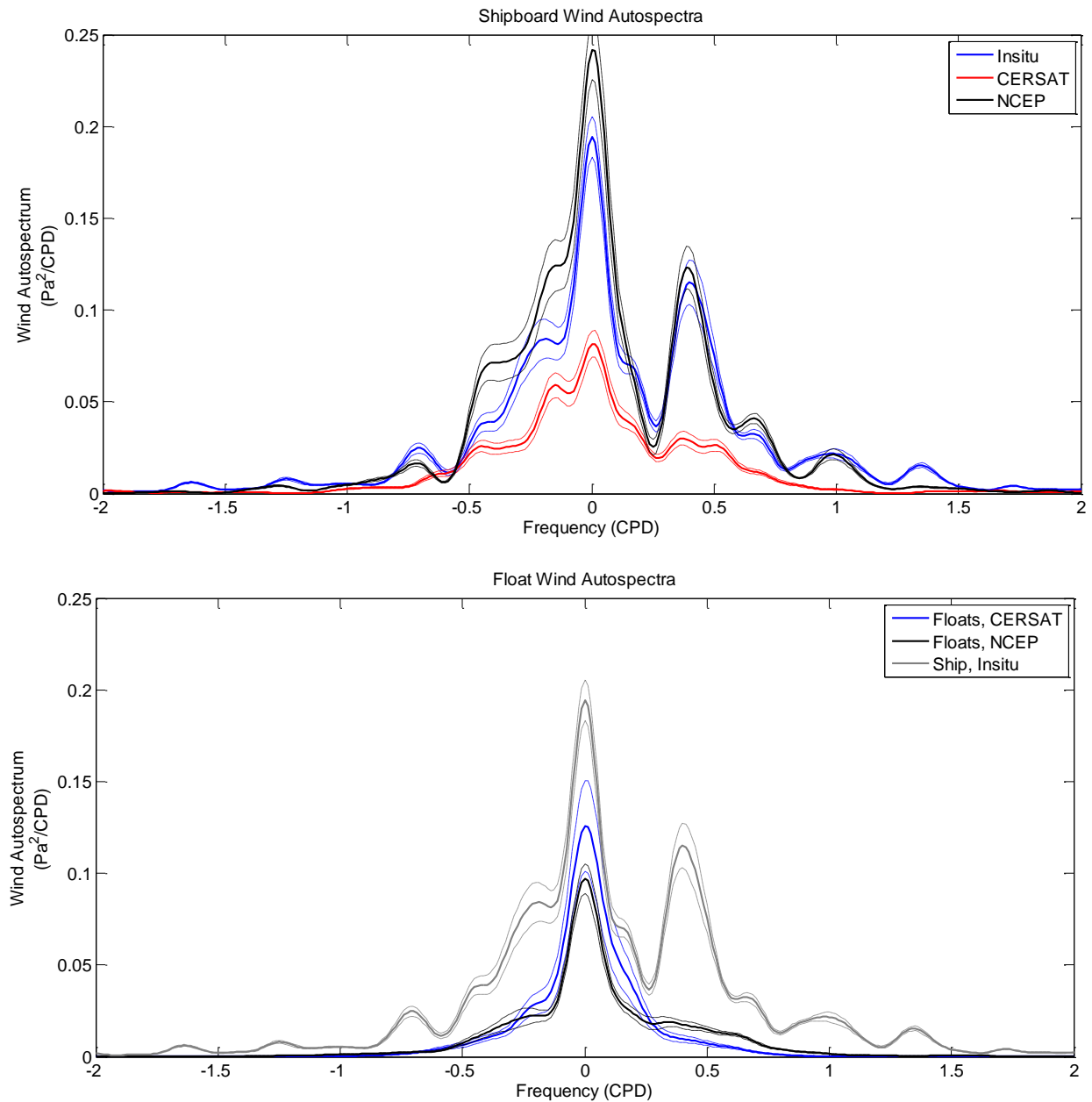


Figure 4.24: Wind stress-autospectra obtained from shipboard instrumentation; CERSAT blended reanalysis-satellite winds and NCEP/NCAR reanalysis winds for the shipboard (top) and float data (bottom). Solid lines denote the mean power spectra while dashed lines denote the 95% confidence intervals.

To address this question we proceeded to examine a number of alternative wind datasets. ERA Interim reanalysis winds and NOAA/NCDC blended satellite winds (Zhang et al., 2006) were found to produce shipboard wind-spectra (not shown) attenuated to a similar degree to the CERSAT blended reanalysis-satellite winds. The NCEP/NCAR reanalysis wind fields were found to produce the closest match to the shipboard *insitu* wind-spectrum (Figure 4.24, upper panel). Hence, we investigated how the choice of forcing dataset affected the spectral fits by rerunning the constant depth fit using wind stresses derived from the NCEP/NCAR reanalysis.

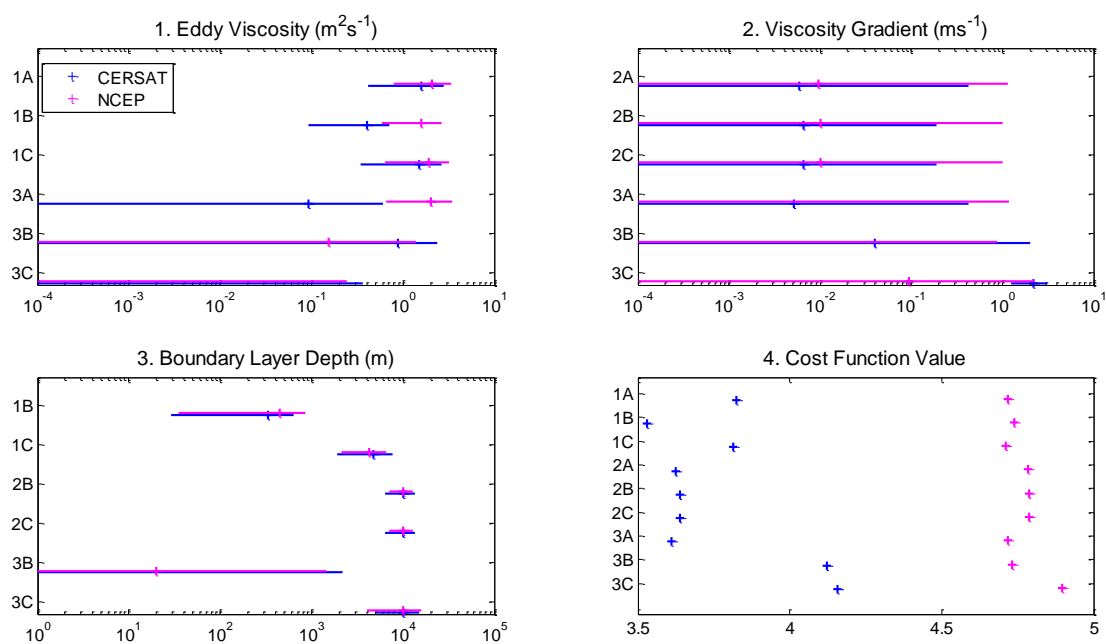


Figure 4.25: Parameter values and Cost Function Values for the constant depth fits to the EM-APEX float data using CERSAT blended winds and NCEP reanalysis winds. Mean values are indicated by the short, vertical lines; uncertainty by the horizontal lines.

NCEP/NCAR reanalysis winds interpolated onto the float track were found to produce an autospectrum (Figure 4.24, lower panel) closer in magnitude to the float CERSAT spectrum than the shipboard *insitu* or NCEP/NCAR autospectra. Examination of wind-stress magnitude as a function of time (not shown) demonstrated that the higher amplitude shipboard spectra were associated with three short duration high wind events. Only one EM-APEX float was active during the time period of these high wind events and no wind events of similar amplitude were seen during the rest of the float record. Hence, this disagreement in wind-spectra amplitude between NCEP/NCAR wind fields

interpolated onto the float tracks and ship track is reasonable. The resulting spectral fits to float data at constant depth with NCEP winds (Figure 4.25) was found to result in no statistically significant changes in model parameters relative to those calculated with CERSAT winds.

e. Sensitivity to Excluding Short-lived Floats

Three of the eight EM-APEX floats delivered fewer than 21 days data, potentially producing low quality and biased estimates of the power-spectra and transfer functions. Examination of bootstrap wind spectra (Figure 4.26) indicates that these floats (3950, 3951 and 4051) produced the lowest amplitude bootstrap wind autospectra. Hence, it is plausible that including these floats in the above analysis would result in an attenuated wind spectrum with resulting errors when computing the observed transfer function.

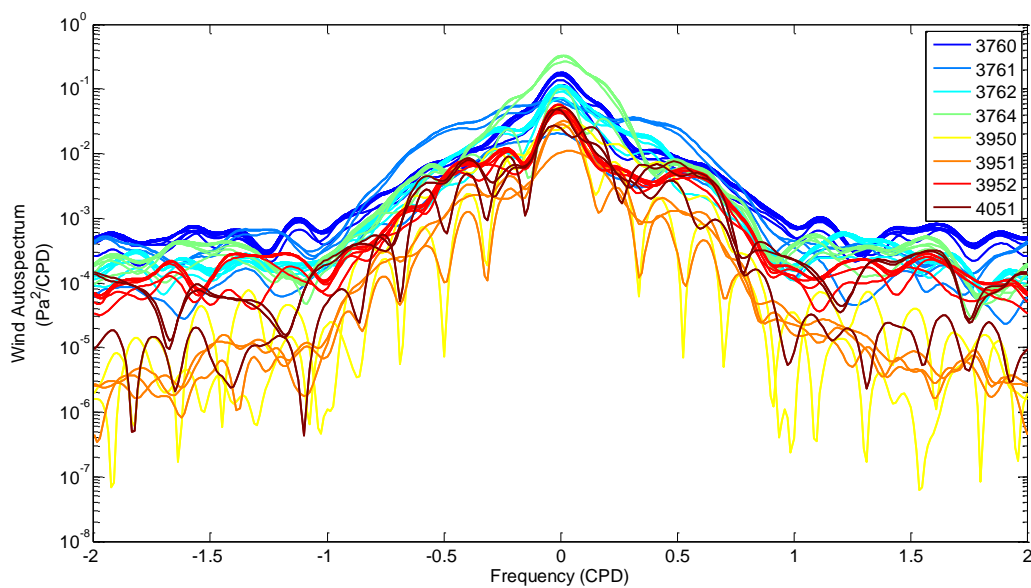


Figure 4.26: Bootstrap wind autospectra estimated from the EM-APEX float data colour-coded by the float ID number.

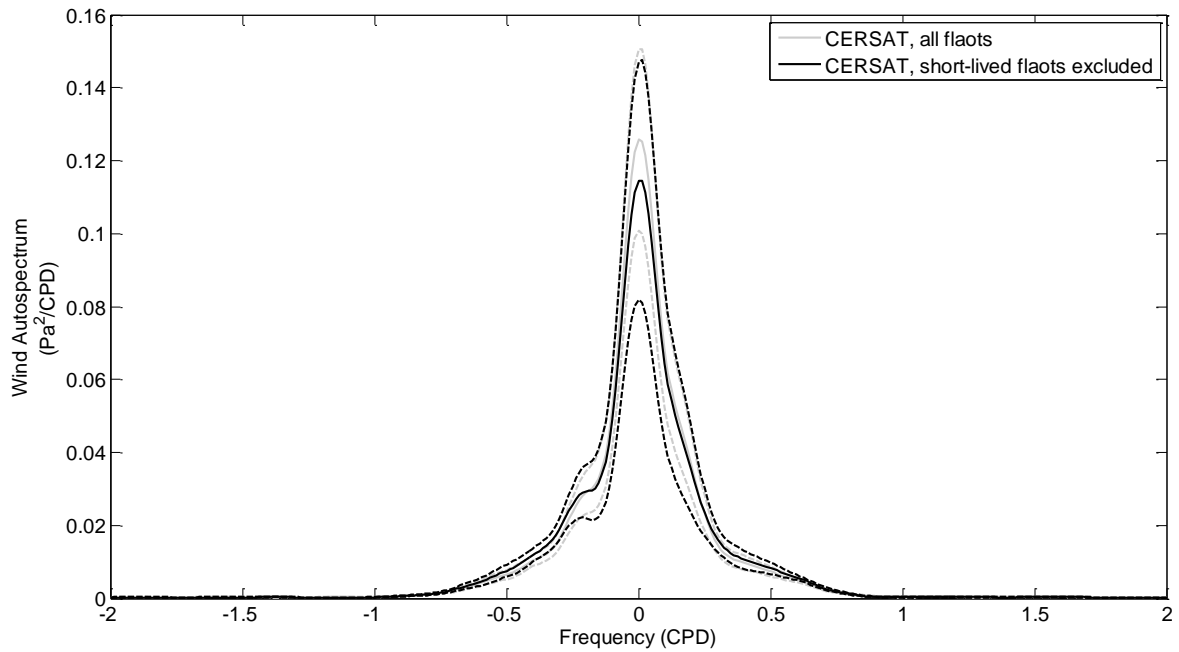


Figure 4.27: Mean wind autospectrum computed before and after removing the three short lived floats. Solid lines denote mean autospectra and dashed lines 95% confidence intervals.

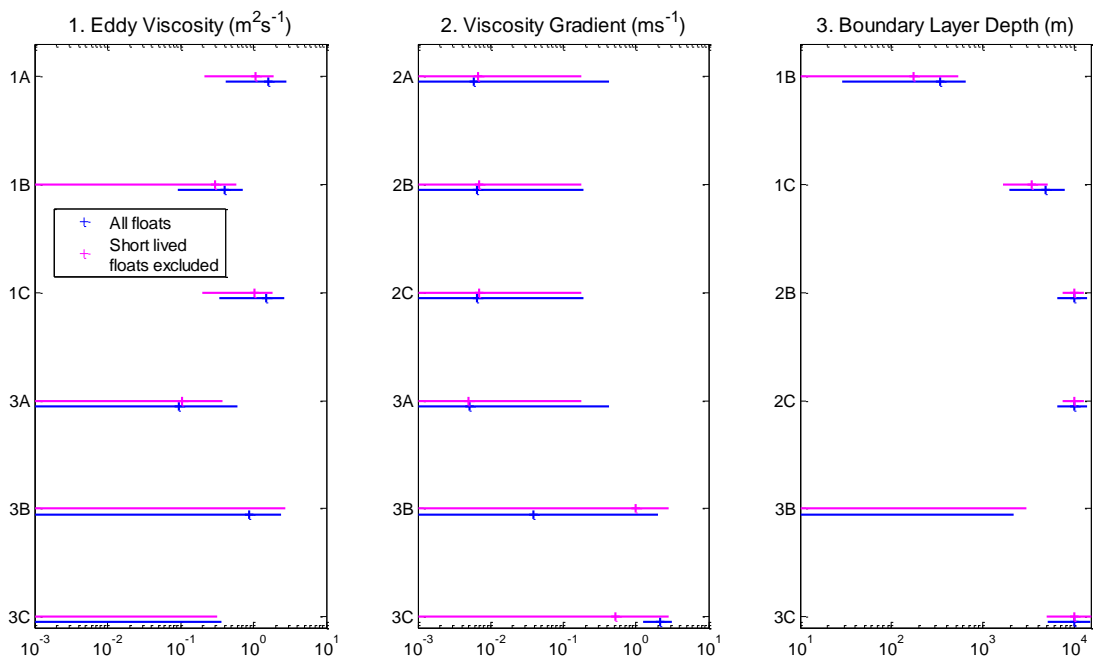


Figure 4.28: Comparison of fitted model parameters (viscosity in Panel 1; viscosity gradient in Panel 2 and BLD in Panel 3) when considering all EM-APEX data and when excluding the three short lived floats.

To examine if the short-lived floats affected our parameter estimates we repeated the 24m constant depth spectral fits without the three short-lived floats removed. The resulting wind autospectrum is

shown in Figure 4.27; unexpectedly removing the three short-lived floats had little effect on the wind spectrum. The fitted parameters are shown in Figure 4.28; we observed no changes in parameters that was significant at the 95% confidence level.

4.8 Wind Energy Input

Previous studies (Wunsch, 1998, Wang and Huang, 2004) found that the Southern Ocean was a hotspot of wind energy input into the ocean, with latitudes south of 40°S accounting for 70% of the globally integrated wind work on the ocean. Most prior studies (Wunsch, 1998, Elipot and Gille, 2009b, Wang and Huang, 2004) concentrated on computing the wind energy input into the Ekman layer on a large-scale circumpolar and long-term basis; our short-term and highly regional dataset offers a complimentary view.

Shipboard estimates of wind energy input were evaluated using Model 1B (constant viscosity, finite BLD) with viscosities and BLDs taken from the 2D and 23.55m constant depth fits. The cyclonic (negative frequencies) and anticyclonic (positive frequencies) co-spectra (Figure 4.29) were then integrated over the frequency band of 0 to 2 CPD to obtain total wind energy input (Figure 4.30). Energy input from the anticyclonic frequencies was found to be greater than the energy input from cyclonic frequencies, in line with results from Elipot and Gille (2009b).

Total energy input to the Ekman layer over the frequency band of -2 to 2 CPD was $45.5 \pm 0.4 \times 10^{-3} \text{ W m}^{-2}$ for the constant depth fit at 23.55m, or $42.7 \pm 0.3 \times 10^{-3} \text{ W m}^{-2}$ when using parameters estimated from the 2D fit. The previous application of spectral techniques to this problem (Elipot and Gille, 2009b) yielded circumpolar estimates of $20\text{-}30 \times 10^{-3} \text{ W m}^{-2}$ over the latitude band of our study. Wunsch (1998) estimated wind energy input into the geostrophic circulation in the Kerguelen Island region to be $18\text{-}24 \times 10^{-3} \text{ W m}^{-2}$. Wang and Huang (2004) found wind energy input into the Ekman layer of around $20 \times 10^{-3} \text{ W m}^{-2}$ over the Indian sector of the Southern Ocean. Our estimates are 50-100% greater than these prior observations.

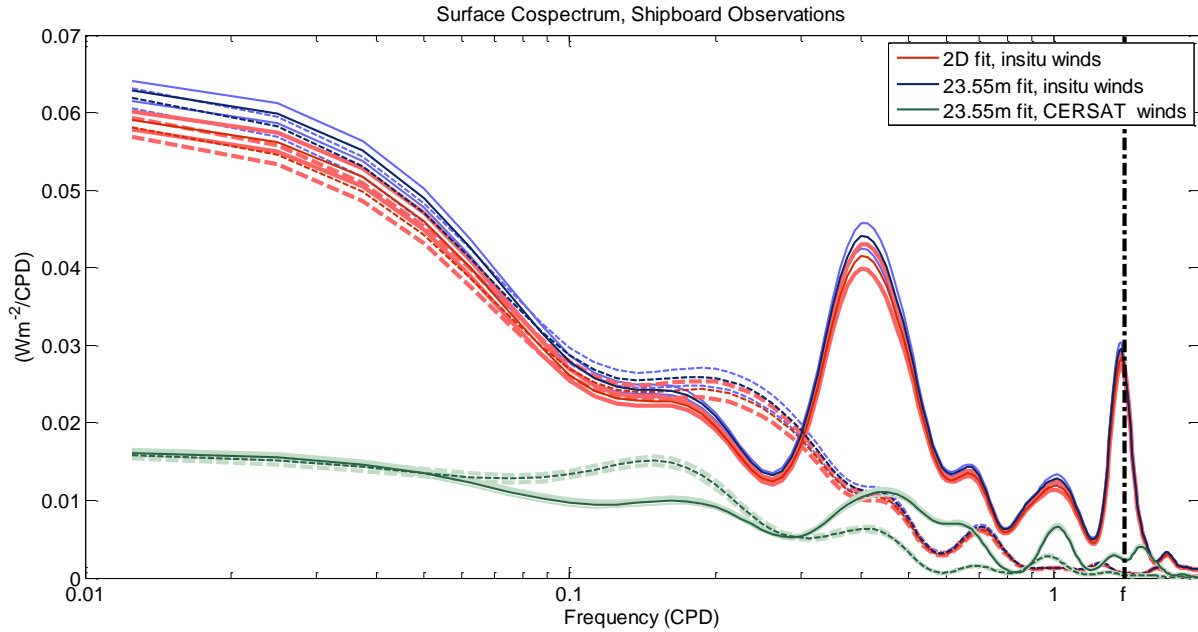


Figure 4.29: Estimated surface cospectra evaluated from model 1B; 23.55m observed transfer function and 23.55m cospectrum, along the shiptrack. Solid lines indicate anticyclonic frequencies and dashed lines cyclonic frequencies. 95% confidence intervals estimated by a bootstrap procedure are indicated by the pale dotted lines.

Wang and Huang (2004) employed spectral techniques combined with a slab-like model of Ekman currents. Elipot and Gille (2009b) used a similar methodology to our study but estimated power spectra over multiple years and on a circumpolar scale. Wunsch (1998) estimated wind energy input by considering the dot product of time mean wind stress and geostrophic velocity fields. In all three cases, the temporal and geographic averaging involved could account for these underestimates, relative to our study, of wind energy input. Another factor which could account for this difference is the wind data used in the study. We employed *insitu* shipboards wind observations while both Wunsch (1998), Wang and Huang (2004) and Elipot and Gille (2009b) used reanalysis wind data. As discussed above, the ship-track wind autospectrum (Figure 4.24, upper panel) from the CERSAT blended satellite-reanalysis data was found to be weaker than the corresponding estimate from the shipboard observations over the majority of the resolved frequency bands. This use of reanalysis winds could potentially work in together with the temporal and spatial averaging to reduce the estimated wind autospectrum. We see an example of this when we compare the

NCEP/NCAR wind stress autospectrum over the ship-track (Figure 4.24, upper panel) and the NCEP/NCAR wind stress spectrum averaged over all floats, covering a larger temporal and spatial extent (Figure 4.24, lower panel).

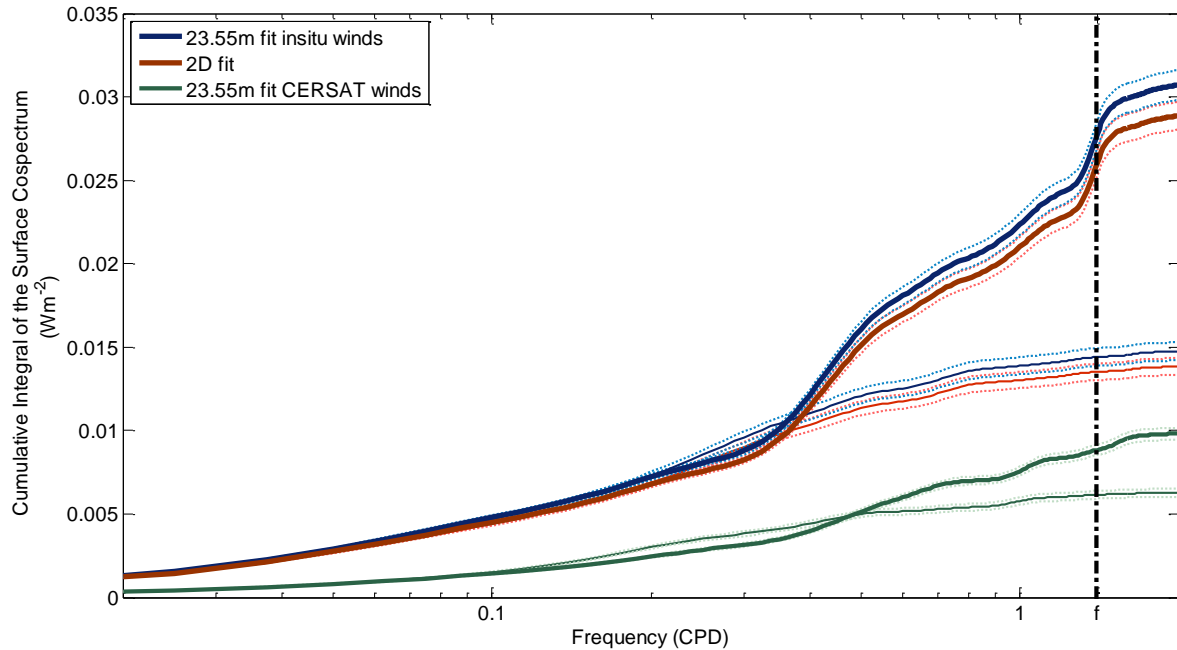


Figure 4.30: Cyclonic and anticyclonic co-spectra integrated from 0 to 2CPD. Thick lines denote anticlockwise (anticyclonic) frequencies and thin lines clockwise frequencies

To examine the effect of using reanalysis wind data we repeated our calculation of wind energy input using power spectra calculated with the CERSAT blended reanalysis-satellite winds in place of the *insitu* winds. Using the model parameters estimated from the 23.55m fit (with *insitu* winds) wind energy input was found to be $16.1 \pm 0.1 \times 10^{-3} \text{ Wm}^{-2}$, closer to but slightly lower than Wunsch's estimate. These contrasting results, using the same oceanic response but differing wind inputs, raises the possibility that prior studies under-estimated wind energy input into the Ocean.

Due to the large uncertainty in the relevant viscosity, viscosity gradient and BLD estimates no attempt was made to estimate wind energy input from the EM-APEX float data.

4.9 Conclusion

We have applied new extensions of the rotary spectral methods as outlined by Elipot and Gille (2009a) to shipboard ADCP and profiling float velocity datasets. Since these profile datasets offered

a view of the ocean's response over multiple depth levels rather than the single depth implicit in the surface drifters used in Elipot and Gille's work we have extended the spectral technique to examine the data both as a function of depth at fixed frequency and in two dimensions as a function of both depth and frequency.

a. Model Performance, Fitted Parameters and Implications for Ekman Currents

Data	Model	k (m^2s^{-1})	dk (ms^{-1})	BLD (m)	
ADCP, 23.55m	1B	$4.25 \times 10^{-2} \pm 6.02 \times 10^{-3}$	-	104.99 ± 9.13	Fig. 4.9
ADCP, 2D	1B	$4.83 \times 10^{-2} \pm 2.28 \times 10^{-3}$	-	118.50 ± 2.86	Fig. 4.9
ADCP, 1.4CPD	1B	$3.52 \times 10^{-2} \pm 1.84 \times 10^{-3}$	-	105.47 ± 1.97	Fig. 4.11
ADCP, 0.7CPD	3C	$2.35 \times 10^{-10} \pm 1.31$	1.17 ± 1.83	53.18 ± 2.63	Fig. 4.11
ADCP, -1.4CPD	3C*	$1.59 \times 10^{-7} \pm 1.09$	1.79 ± 1.04	5.50 ± 0.75	Fig. 4.11
	1C*	3 ± 0.04	-	5.86 ± 0.71	
	1B	0.444 ± 0.033	-	128.6 ± 0.9	
ADCP, -0.7CPD	3A	$5.09 \times 10^{-2} \pm 1.24$	$5.73 \times 10^{-6} \pm 3.98 \times 10^{-1}$	-	Fig. 4.11

Table 4.1: Best performing models and estimated parameters for selected fits to the shipboard ADCP data. The first column records the data the models were fitted to, the second column the best performing model type (as described in Section 4.4), Columns 3 to 5 are the fitted parameters: viscosity(k), viscosity gradient (dk) and boundary layer depth (BLD). A reference back to the relevant figures is given in Column 6. "" denotes a non-physical model.*

The best performing models and fitted parameter values for the ADCP data are shown in Table 4.1. The constant depth and 2D fits to the ADCP velocity data identified model 1B (constant viscosity, finite boundary layer, Ekman velocity tending to zero at the BLD) as the best performing model. Viscosity estimates for both fits were in agreement, while estimates of BLD were generally consistent in magnitude. Fits at constant frequency to the ADCP data also identified model 1B as the best performing model in the near inertial regime with an eddy viscosity and BLD in general agreement with the parameter estimates from the 23.55m and 2D fits of model 1B. Class 3 models

(viscosity increasing with depth with a non-zero offset at the surface) were identified as the most suitable models for the other frequency bands.

The best performing models and corresponding parameters estimated for the EM-APEX float data are given in Table 4.2. Model 1B was found to be the most suitable model when fitted to the constant depth data and the near inertial data. Again, the Class 3 model performed well at cyclonic (clockwise) frequencies.

<u>Data</u>	<u>Model</u>	<u>k (m²s⁻¹)</u>	<u>dk (ms⁻¹)</u>	<u>BLD (m)</u>	
EM-APEX, 24m	1B	0.401±0.31	-	336.43±307.26	Fig. 4.19
EM-APEX, 1.4CPD	1B	0.060±0.14	-	96.09±949.85	Fig. 4.19
EM-APEX, 0.7CPD	3A	6.66 x10 ⁻⁴ ±1.16	1.23 x10 ⁻³ ±1.06	-	Fig. 4.19
EM-APEX, -1.4CPD	3C	1.32 x10 ⁻³ ±1.01	2.29 x10 ⁻² ±0.59	19.45±264.95	Fig. 4.19
EM-APEX, -0.7CPD	3B	1.93 x10 ⁻¹⁷ ±1.87	0.297±1.37	3.81 x10 ⁻¹⁷ ±2909.63	Fig. 4.19

Table 4.2: Best performing models and parameters for selected fits to the EMAPEX data. Columns as per Table 4.1.

Class 1 (constant viscosity) models were found to offer good performance (the lowest cost function value for a given set of fits) when fitted to both ADCP and EM-APEX data at a constant depth level or in the near inertial frequency band (see Figures 4.11 and 4.19 for measures of goodness of fit). Estimated eddy viscosities and boundary layer depths were found to be in close agreement over all model classes and parameters fits.

Class 2 models did not offer the best performance for any of the fits, and more generally offered middling to poor performance (high cost function values). This is likely an effect of the eddy viscosity linearly increasing with depth from 0m²s⁻¹ at the surface. Even with a large viscosity gradient (dk), viscosities are very small near the surface, in turn implying rapid decay and rotation of the Ekman currents in the shallowest part of the mixed layer. Since the EM-APEX floats and the shipboard ADCP did not allow us to examine oceanic velocities within the upper 10m it is likely that we would not be able to detect this rapid current decay and where there are data do not detect the

stretching of the decay scale implied by this class of model. We conclude that the Class 2 models are poorly constrained by the observations, and are the least consistent model of the boundary layer Ekman dynamics assessed here.

Class 3 offered good performance when fitted at constant frequencies away from the inertial frequency. However, we consistently find at least one of the fitted model parameters (k , dk and BLD) display large uncertainty relative to the mean estimate. If these large uncertainties had been confined to the EM-APEX float data or to the constant frequency fits away from the inertial frequency it would suggest the uncertainty was principally a matter of the low amplitude of the mean observed transfer function compared to the variability seen in the bootstrap transfer function. However, we also see Class 3 model parameter estimates with large uncertainties in the ADCP constant depth and 2D fits. This suggests instead that the three parameters viscosity, gradient of viscosity and boundary layer depth (k , dk and BLD) in the Class 3 models have high dependency on each other and it is likely that the estimation procedure is poorly constrained (or ill-posed) by the observations.

The evidence from the fitting of spectral models suggests that either a constant viscosity model (Class 1 models) or a linearly increasing viscosity with a non-zero surface viscosity (Class 3 models) provide the best representation of Ekman currents. However, all Class 3 models display high uncertainty around at least one parameter in all parameter fits. This suggests that the Class 3 models, representing stratified flow, degenerate at times to an ill-posed solution, and thus the evidence for a significant general increase in viscosity with depth is a less robust feature of the data. In Chapter 3 we found evidence that the viscosity decreases with depth (Figure 3.19), although this decrease is within the uncertainty of the confidence interval on the mean viscosity. The lines of evidence from this Chapter and Chapter 3 suggest that a constant viscosity model provides a good representation of Ekman currents, and the time-mean eddy viscosity profile (Figure 3.19). We conclude that of the spectral models examined in this chapter, Class 1 models are the most satisfactory, and from within this class, Model 1B (constant viscosity, finite BLD) is the best.

b. Estimates of Wind Energy Input

Having identified Model 1B as the most adequate model, we computed the resulting wind energy input using parameter estimates derived from the 23.55m constant depth and the 2D fits to ADCP data. Using the *insitu* wind spectrum we obtained wind energy input into the Ekman layer of $45.5 \pm 0.4 \times 10^{-3} \text{ Wm}^{-2}$ and $42.7 \pm 0.3 \times 10^{-3} \text{ Wm}^{-2}$, respectively. These estimates are 50-100% larger than previous large scale estimates (Elipot and Gille, 2009b, Wunsch, 1998, Wang and Huang, 2004).

Repeating our estimates with a wind spectrum derived from the CERSAT blended reanalysis-satellite wind fields we found a wind energy input of around $16 \times 10^{-3} \text{ Wm}^{-2}$, in line with the lower range of previous estimates (Wunsch, 1998, Wang and Huang, 2004). These two results together suggest that the wind energy input is particularly sensitive to the spectral content of the wind field. This difference is unlikely to be due to the time period of these regional measurements and therefore could suggest that closure of the wind budget globally would be improved with wind data with greater temporal resolution.

Chapter 5: Evaluating the Performance of Constant Viscosity Ekman

Models

5.1. Introduction

In the previous chapters we estimated viscosity and viscosity profiles, and fitted a number of conceptual spectral models to the observations. This evidence suggested, against initial expectations, that a constant viscosity parameterization provides an adequate representation of wind-driven momentum mixing within the mixed layer. The results from the spectral fitting also suggested that a finite boundary layer depth may offer superior performance to the ‘classical’ infinite depth Ekman model.

In light of this we tested a family of six constant viscosity linear Ekman models arising from various combinations of boundary layer depth and coupling with geostrophic shear and Stokes drift. We also examined a family of stratified Ekman models using the Price-Weller-Pinkel mixing scheme (Price et al., 1986) to test the effects of density stratification on Ekman currents. All nine models were forced with *insitu* wind-stresses taken along the ship track and blended satellite-reanalysis wind-stresses interpolated onto the float tracks. Model time varying performance was then analysed by considering the statistics of the currents at 24m depth; while time-mean performance was characterized by considering the correlation between the observed and modelled time-mean Ekman velocity profile.

5.2. The Models

During this study we considered a total of nine models (Table 5.1). We first considered a suite of three variations on the ‘classical’ Linear Ekman Model (CLEM), which assumes a constant viscosity and an infinite BLD: 1) the ‘standard’ case with wind forcing only; 2) a version including coupling with geostrophic shear (Cronin and Kessler, 2009) and 3) a version incorporating coupling with Stokes

Drift (Polton et al., 2005). We then considered the same three variations on the finite BLD linear Ekman model (FLEM) with a constant viscosity, which was identified as the best performing spectral model in Chapter 4 and in Elipot and Gille (2009a). These models do not resolve the effect of density stratification beyond confining Ekman currents to a specified boundary layer depth.

We also employed three models using the Price-Weller-Pinkel (PWP) mixing scheme (Price et al., 1986): the first PWP model assumes a heat budget driven only by surface forcing; the second incorporates cross-frontal Ekman transport in the heat budget; and the final PWP model incorporates movement of the heat gradients relative to the floats. These models explicitly resolve the vertical density structure and thereby directly link momentum mixing to stratification. However, these models require additional forcing data including incoming long wave and short wave radiation and the rate of evaporation/precipitation which adds additional potential sources of errors.

Model	Momentum Mixing Parameterization	Coupling	Boundary Layer	Links to SST Gradients
1	Constant Viscosity	None	Infinite	None
2	Constant Viscosity	Stokes	Infinite	None
3	Constant Viscosity	Shear	Infinite	None
4	Constant Viscosity	None	Finite	None
5	Constant Viscosity	Stokes	Finite	None
6	Constant Viscosity	Shear	Finite	None
7	PWP Mixing	None	Infinite	None
8	PWP Mixing	None	Infinite	Meridional Ekman currents
9	PWP Mixing	None	Infinite	Meridional velocity of float drift

Table 5.1: Summary of the key features of all nine models tested during this study.

a. Linear Ekman Models

The derivation of the classical linear Ekman model was discussed in previous chapters. We took a 1D linear Ekman model (Price, 1999) and modified it to take into account time-varying input and variable bottom boundary conditions. The model was constructed on a finite vertical grid. During each time step the current velocity profile (u_t, v_t) is computed from the prescribed viscosity (k) and the velocity profile at the previous time step (u_{t-1}, v_{t-1}):

$$u_t(z) = u_{t-1}(z) + dt \left(k \frac{d^2 u_{t-1}(z)}{dz^2} + f v_{t-1}(z) \right) \quad (5.1a)$$

$$v_t(z) = v_{t-1}(z) + dt \left(k \frac{d^2 v_{t-1}(z)}{dz^2} - f u_{t-1}(z) \right) \quad (5.1b)$$

Where dt denotes the interval of one time step.

Momentum from the wind stress was then added into the surface grid cell, where dz denotes the vertical spacing between grid cells:

$$u_t(0) = u_{t-1}(0) + \frac{\tau_x dz}{k} \quad (5.2a)$$

$$v_t(0) = v_{t-1}(0) - \frac{\tau_y dz}{k} \quad (5.2b)$$

In order to maintain numerical stability the duration of each time step was determined as:

$$dt = \frac{0.4 dz^2}{k} \quad (5.3)$$

This model could be configured with one of two bottom boundary conditions, either a free slip boundary to approximate the infinite depth case or a no slip boundary (velocity set to 0ms^{-1} at the bottom grid level).

b. Including Geostrophic Coupling

The derivation of the ‘classical’ Ekman solutions assumes the oceans have a uniform and constant density, and hence, neglect vertical geostrophic shear from the momentum equation. However, the real ocean features regions of strong density gradients with resulting strong geostrophic flow. Cronin and Kessler (2009) investigated the potential effects of coupling between geostrophic currents and Ekman currents in the tropical North Pacific and determined that a “frontal Ekman” model incorporating coupling with vertically uniform geostrophic shear offered good qualitative agreement with their observations. Within the ACC there are a number of strong fronts with associated strong geostrophic flow; these fronts have been found to display non-equivalent barotropic behaviour (Phillips and Bindoff, 2014), which implies the potential for strong vertical geostrophic shear. In light of this we considered the applicability of Cronin and Kessler’s (2009) “frontal Ekman model” to our region of interest.

The derivation of this model begins with consideration of the linear equations of motion with a buoyancy term:

$$i\mathbf{f}\mathbf{u} = -\frac{1}{\rho_0} \nabla p + \frac{1}{\rho_0} \frac{\partial \boldsymbol{\tau}}{\partial z} \quad (5.4a)$$

$$0 = -\frac{1}{\rho_0} \frac{\partial p}{\partial z} + \frac{g(\rho_0 - \rho)}{\rho_0} - g \quad (5.4b)$$

Assuming that stress and shear throughout the Ekman layer are related by an eddy viscosity leads to the standard surface boundary condition (Equation 2.2, Chapter 2).

$$\boldsymbol{\tau}_0 = \rho_0 k \frac{\partial \mathbf{u}}{\partial z} \quad (5.5)$$

At depths where $k=0$ and $dk/dz=0$, Equation 5.4a reduces to the geostrophic balance:

$$\mathbf{u}_g = \frac{i\nabla p}{\rho_0 f} \quad (5.6a)$$

From Equation 5.4b vertical variations in the horizontal pressure gradient can be related to horizontal buoyancy gradient; as a result geostrophic shear is parallel to density contours.

$$\frac{\partial \mathbf{u}_g}{\partial z} = \frac{i\nabla \left(\frac{g(\rho_0 - \rho)}{\rho_0} \right)}{f} \quad (5.6b)$$

Assuming velocity can be decomposed into geostrophic (\mathbf{u}_g) and ageostrophic (\mathbf{u}_a) components, Equation 5.4b becomes:

$$if(\mathbf{u}_a + \mathbf{u}_g) = -\frac{1}{\rho_0} \nabla p + k \frac{\partial^2 (\mathbf{u}_a + \mathbf{u}_g)}{\partial z^2} \quad (5.7a)$$

Substituting from Equation 5.6a:

$$if(\mathbf{u}_a + \mathbf{u}_g) = if\mathbf{u}_g + k \frac{\partial^2 (\mathbf{u}_a + \mathbf{u}_g)}{\partial z^2} \quad (5.7b)$$

Subtracting \mathbf{u}_g from both sides of the equation yields:

$$if\mathbf{u}_a = k \left(\frac{\partial^2 \mathbf{u}_a}{\partial z^2} + \frac{\partial^2 \mathbf{u}_g}{\partial z^2} \right) \quad (5.8a)$$

Cronin and Kessler (2009) then assumed that the frontal buoyancy structure was vertically-uniform, and by implication (Equation 5.6b) geostrophic shear was constant and the derivative of geostrophic shear was thus zero. This simplifies Equation 5.8a to:

$$if\mathbf{u}_a = k \left(\frac{\partial^2 \mathbf{u}_a}{\partial z^2} \right) \quad (5.8b)$$

Hence, the stress-shear balance is unmodified from the classical Ekman case. However, as geostrophic shear is non-zero it will modify the surface boundary condition:

$$\frac{\partial \mathbf{u}_a}{\partial z} = \frac{1}{\rho_0 k} \tau_0 - \frac{\partial \mathbf{u}_g}{\partial z} \equiv \frac{1}{\rho_0 k} \tau_{eff} \quad (5.9)$$

We obtain a classical Ekman model driven with a modified surface stress (τ_{eff}); specifically the part of the wind stress which that is out of balance with the surface geostrophic stress. Since the modification is confined to the surface boundary condition rather than affecting the stress-shear balance we can apply this modification to both the classical infinite depth Ekman model and the finite-depth Ekman model.

It must be noted that this model is not equivalent to the cases with geostrophic shear considered in Chapter 3; on that occasion we did not incorporate any coupling between geostrophic shear and Ekman currents.

c. Including Stokes Coupling

A number of theoretical studies (Lewis and Belcher, 2004, Gnanadesikan and Weller, 1995, Heinloo and Toompuu, 2012, Perrie et al., 2003) have suggested that some form of coupling may exist between wind-driven currents and wave-driven Stokes drift. Stokes drift acts upon the upper ocean in two ways. Firstly, it deforms the mixed layer turbulence vorticity, in turn driving Langmuir circulation. Secondly, Stokes drift also acts to tilt and stretch the planetary vorticity into the horizontal producing a vortex force in the flow. Following Hasselmann (1970), the interaction between planetary vorticity and stokes drift results in a Coriolis-Stokes force on the momentum balance $\mathbf{f}_{x\mathbf{u}_s}$, (where \mathbf{u}_s denotes the Stokes drift velocity and \mathbf{x} indicates the cross product) which in turn modifies the balance of mean flow within the upper ocean.

We will limit ourselves to examination of a linear Ekman model incorporating Stokes coupling via a modified surface stress boundary condition as developed by Polton et al. (2005). Averaging over wave periods the Coriolis-Stokes forcing appears as an extra term in the horizontal momentum equation:

$$\frac{\partial \boldsymbol{\tau}}{\partial z} = \rho f \mathbf{z} \times (\mathbf{u} + \mathbf{u}_s) \quad (5.10)$$

Polton et al. (2005) decomposed the solution (\mathcal{U}) of the momentum equation (Eqn. (5.10)) into three terms comprised of the ‘pure’ Ekman contribution (\mathcal{U}_e); the Ekman-Stokes component (\mathcal{U}_{es}) and the ‘pure’ Stokes component (\mathcal{U}_s). Assuming a constant eddy viscosity these components were calculated as:

$$\mathcal{U}_e = (1-i)U_e \exp((1+i)z/\delta_e) \quad (5.11a)$$

$$\mathcal{U}_{es} = (1-i)U_e \exp\left((1+i)\frac{z}{\delta_e}\right) \times \left[\frac{U_s \delta_s}{U_e \delta_e} \frac{\frac{1}{2}\delta_e^2/\delta_s^2}{\left(1+i\frac{1}{2}\delta_e^2/\delta_s^2\right)} \right] \quad (5.11b)$$

$$\mathcal{U}_s = \frac{-U_s}{\left(1+i\frac{1}{2}\delta_e^2/\delta_s^2\right)} \exp(z/\delta_s) \quad (5.11c)$$

The Ekman decay scale, δ_e , and Stokes decay scale, δ_s , are defined as:

$$\delta_s = \frac{\lambda}{4\pi} \quad (5.12a)$$

$$\delta_e = \sqrt{\frac{2k}{f}} \quad (5.12b)$$

And the depth averaged Stokes (U_s) and Ekman (U_e) are defined such that:

$$T_s = \int_{-\infty}^0 u_s dz = U_s \delta_s \quad (5.13a)$$

$$T_e = \int_{-\infty}^0 u_e dz = U_e \delta_e \quad (5.13b)$$

Resulting transports are then computed and the net wave-driven transport splits between the Ekman-Stokes and ‘pure’ Stokes components. The partitioning of wave transport between these two components is determined by the term:

$$\delta_e^2 / \delta_s^2$$

When this term is large (i.e. $\delta_e > \delta_s$), as is typical in the open ocean, the Ekman-Stokes transport dominates, and the ‘pure’ Stokes transport and current can be neglected, i.e. $\mathbf{U} = \mathbf{U}_e + \mathbf{U}_{es}$. From this result Polton et al. (2005) obtain an approximate solution:

$$\mathbf{u}_{tot} = \left(1 - \frac{U_s \delta_s}{U_e \delta_e} \right) \mathbf{u}_e \quad (5.15)$$

The Coriolis–Stokes forcing adds an additional component to the ‘classical’ Ekman solution which accounts for the depth-integrated wave transport and has the same variation with depth as the ‘classical’ Ekman solution.

Polton et al. (2005) conclude that the contribution of Stokes drift could be efficiently represented by the classic Ekman model with the surface boundary condition modified so the Ekman spiral is driven by an effective stress consisting of the wind stress plus a stress arising from the Stokes drift (τ_w). Hence the momentum equation becomes:

$$\frac{\partial(\boldsymbol{\tau} + \boldsymbol{\tau}_w)}{\partial z} = \rho f \mathbf{z} \times \mathbf{u} \quad (5.16)$$

Where τ_w is computed as:

$$\boldsymbol{\tau}_w = - \int_{-\infty}^0 \rho f \times \mathbf{u}_s dz \quad (5.17)$$

Since this change is confined to the surface boundary condition rather than affecting the stress-shear balance we can apply this modification to both the classical infinite-depth Ekman model and the finite-depth Ekman model.

Significant wave heights, periods and headings from the ERA-Interim reanalysis dataset were then interpolated onto all float and ship tracks. We then assumed only monochromatic deepwater waves were present before computing profiles of Stokes drift as in Chapter 3 section 3.5e.

c. Price, Weller and Pinkel

The Price, Weller and Pinkel (PWP) model (Price et al., 1986) is a one dimensional numerical model of vertical mixing, initially developed to investigate the response of the upper ocean to the diurnal cycle of heating and cooling. The PWP algorithm is still used in modern ocean models such as HYCOM (Wallcraft et al., 2003).

The PWP model assumes that vertical mixing and radiative processes are driven only by localized surface heat and momentum fluxes. Under these assumptions the heat, salinity and momentum budgets take the standard one-dimensional forms. Hence, the heat budget is defined as:

$$\frac{\partial T}{\partial t} = \frac{-1}{\rho_0 c} \frac{\partial F}{\partial z} \quad (5.18)$$

Where T denotes the temperature, c the heat capacity of water and F denotes the heat flux.

In turn, the freshwater budget is defined as:

$$\frac{\partial S}{\partial t} = - \frac{\partial E}{\partial z} \quad (5.19)$$

Where S denotes salinity and E denotes the fresh water flux.

Finally, the momentum budget is:

$$\frac{\partial \mathbf{u}}{\partial t} = -\mathbf{f} \times \mathbf{u} - \frac{1}{\rho_0} \frac{\partial \boldsymbol{\tau}}{\partial z} \quad (5.20)$$

For this study the model is implemented on a vertical grid of 1m with time steps of 600s. During each time step, surface heat and freshwater fluxes are applied first to the top most grid cell. Next, incoming short wave (subscript SW) and long wave (subscript LW) solar radiation are absorbed by the water column, with a vertical distribution of total incoming solar radiation defined by:

$$I(z) = I(0) \left(I_{SW} e^{-z/\lambda_{SW}} + I_{LW} e^{-z/\lambda_{LW}} \right) \quad (5.21)$$

I(0) denotes the total solar radiation at the surface. I_{SW} and I_{LW} describe the partitioning of incoming solar radiation between short wave and long wave processes; here I_{SW} is taken to be 0.6 and I_{LW} to

be 0.4. The amplitude of the heat input from solar radiation below the surface is determined by λ_{sw} and λ_{LW} (0.6m and 20m).

Density is then computed and adjusted by mixing from the surface down to achieve static stability, such that:

$$\frac{\partial \rho}{\partial z} \geq 0 \quad (5.22)$$

Wind forcing is then absorbed in the mixed layer and the momentum balance (Equation 5.20) is stepped forwards in time. The Richardson number (R_b) across the boundary of the mixed layer (h) is computed as:

$$R_b = \frac{g \Delta \rho h}{\rho_0 (\Delta \mathbf{u})^2} \quad (5.23)$$

If R_b is less than 0.65 the mixed layer is unstable and the model proceeds to entrain and mix deeper levels into the mixed layer until R_b satisfies the stability criterion. Next, the model computes the gradient Richardson number (R_g) over all depths below the mixed layer:

$$R_g = \frac{g \partial \rho / \partial z}{\rho_0 (\partial \mathbf{u} / \partial z)^2} \quad (5.24)$$

The profile $R_g(z)$ is searched to find the minimum value, $R_g(j)$. If $R_g(j)$ is less than 0.25, shear flow instability is presumed to be present and grid levels j and $j+1$ are mixed until stability is achieved. $R_g(z)$ is then recomputed, and this procedure repeated until the entire water column below the mixed layer is stable.

Within the ACC, prevailing winds are typically westerly, resulting in Ekman transport which pushes cold water northwards. The ACC is also dominated by a complicated series of meandering fronts, often associated with strong latitudinal temperature gradients. Both the movement of the fronts relative to the floats and the heat transport arising from Ekman currents could significantly

modify the heat budget involved in the 'basic' PWP model described above. To simplify the problem we will limit ourselves to considering a meridional temperature gradient.

The advective heat fluxes through the northern (q_1) and southern (q_2) boundaries on our region of interest are defined as:

$$q_1(z) = \rho_1(z)C_{p1}(z)v_1(z)T_1(z)$$

$$q_2(z) = \rho_2(z)C_{p2}(z)v_2(z)T_2(z)$$

Hence:

$$\frac{dq(z)}{dy} \approx \frac{q_1(z) - q_2(z)}{\Delta y} \quad (5.25)$$

$$\frac{dq(z)}{dy} \approx \frac{\rho_1(z)C_{p1}(z)v_1(z)T_1(z) - \rho_2(z)C_{p2}(z)v_2(z)T_2(z)}{\Delta y}$$

Given a small Δy we assume the velocity profiles are horizontally uniform. Density and heat capacity are relatively insensitive to small changes in temperature; hence we treat both as constant on a particular depth level.

$$\frac{dq(z)}{dy} \approx \frac{\rho(z)C_p(z)v(z)(T_1(z) - T_2(z))}{\Delta y} \quad (5.26)$$

We first develop the Ekman advection model. In this case the Ekman transport moves cold waters north, up the SST gradient. While this ultimately drives a southwards heat transport via deep return flow we focus on the near surface layer in which this transport will produce cooling. Firstly, we assume that the Ekman currents and horizontal temperature gradient are small below the mixed layer and hence can be neglected. By definition the density of an idealized mixed layer is vertically uniform, which implies that the temperature within the mixed layer should be close to constant with depth. Combined with the assumption of insignificant interior temperature gradient and Ekman velocity, Equation 5.26 simplifies to:

$$\frac{dq(z)}{dy} \approx \rho C_p v_{ek}(z) \frac{\Delta T_{ML}}{\Delta y}$$

Where v_{ek} is the meridional ageostrophic velocity computed by the model.

Integrating with respect to z this becomes:

$$q_{ek}(z) = \rho C_p \frac{\Delta T_{ML}}{\Delta y} \int v_{ek}(z) dz$$

Within the mixed layer $\Delta T/\Delta y$ was obtained from satellite SST observations using datasets described in Section 5.3; below the mixed layer $\Delta T/\Delta y$ was assumed to be $0^\circ\text{C}/\text{m}$, producing a step change in the temperature gradient. For a grid cell of height, Δz , at arbitrary depth level, z_i , the advective heat flux q_a was computed as:

$$q_a(z_i) = \rho C_p \frac{\Delta T_{ML}}{\Delta y} v_{ek}(z_i) \Delta z \quad (5.27)$$

During each time step the resulting Ekman advective flux profile, $q_a(z)$, was computed and applied to the water column after the input of solar radiation and before the mixing procedure.

Above we have assumed that the influence of fronts on the heat budget is confined to the mixed layer and advection arising from Ekman transport. However, in reality ACC fronts are deep reaching and evolve with time. We must also consider the movement of the floats relative to the fronts. The temporal evolution of the fronts is largely captured in the time evolving heat gradient; hence the velocity term will represent only the meridional drift of the float. Matters are potentially complicated by the fact that crossing a front implies moving between water masses with significantly different properties. However, given the relatively slow speed at which the EM-APEX floats drift off streamlines to the flow, it is reasonable to assume that the evolution of the heat budget driven by the temperature gradient should account for most of this effect. The derivation of the frontal PWP model follows similar arguments to the Ekman advection PWP model until Equation

5.26. However, we now assume that the temperature gradient is deep reaching. As a result we obtain an advection term in the heat budget:

$$q_a(z_i) = \rho C_p \frac{\Delta T(z_i)}{\Delta y} v_{drift}(z_i) \Delta z \quad (5.28)$$

Where v_{drift} denotes the meridional velocity of the float's drift.

For this study we will assume the temperature gradient is constant over the upper 200m and zero below. As above this additional heat flux was applied to the model between the input of solar radiation and the mixing procedure.

5.3. Performance Metrics

Before proceeding with the analysis outlined below we first filtered the modelled currents as outlined in Chapter 3 to remove inertial currents and isolate the Ekman velocity profiles. This was done principally to allow direct comparison with Ekman velocity time-series obtained in Chapter 3.

a. Time-Mean Metrics

We consider the time-mean performance of models from two perspectives. Firstly, we calculate the mean current profiles and 95% confidence intervals from the model output. Each modelled mean current profile is then compared with the corresponding observed mean current profile over all data. Secondly, we interpolate the modelled mean current profiles onto the same depth levels as the corresponding observations before calculating the correlation between the profiles for both the u and v velocity components.

b. Time-Varying Metrics

We considered the lagged autocorrelation function and found that observed decorrelation time scale (e.g. Figure 5.5) was of the order of 12-24 hours. We concluded that temporal correlations were not suitable for use with the EM-APEX data as the relatively sparse sampling (4 profiles per

day) significantly increased the likelihood of aliasing noise. Instead we investigated model performance from a statistical view for both the EM-APEX and ADCP velocity data.

To obtain a single cohesive measure of this we applied a two sample Kolmogorov-Smirnov (KS) test to the model and the observed data (Massey, 1951, Rohatgi and Ehsanes Saleh, 1976). The two sample KS test assumes a null hypothesis that the two samples (here the observations and the models) are drawn from the same (unspecified) underlying distribution. We then seek to accept or reject this null hypothesis at a significance level α (i.e. demonstrate that the distributions are not identical at a $1-\alpha$ level). This is done by computing the maximum difference ($D_{n_1n_2}$) between the cumulative distribution functions of the two samples. If this difference exceeds the critical value given in Equation 5.29, then we can reject the null hypothesis:

$$D_{n_1, n_2} > c(\alpha) \sqrt{\frac{n_1 + n_2}{n_1 n_2}} \quad (5.29)$$

Where n_1, n_2 denote the number of samples in each distribution while $c(\alpha)$ is a parameter for a given significance level. For the 95% confidence level we use in this study the value of $c(\alpha)$ is 1.36.

The two sample KS test provides a simple means of determining if the model and observed distributions are the same. However, in the event the distributions do not match, it provides no easy means to tell the difference between a mismatch due to, for example, a handful of outlying datapoints in the *in situ* observations, versus a systematic mismatch. In light of this we turn to quantile-quantile (QQ) plots (Wilk and Gnanadesikan, 1968). QQ plots were constructed by computing the cumulative distribution functions for each dataset, dividing the CDFs into regularly spaced quantiles (here taken at 0.5% intervals) and then identifying the velocities which correspond to each quantile. Observed and simulated velocity values for each quantile were then plotted against each other; a linear fit was then applied to the data between the first and third quartiles (25-75%) and was then extrapolated across the entire range of observed data.

5.4. Model Configuration

a. ADCP Ekman Models

Models were run for viscosities of 0.0025, 0.005, 0.01, 0.0425, 0.1, 0.2 and $0.447\text{m}^2\text{s}^{-1}$. To simplify the model we assumed that latitude, and therefore the Coriolis parameter, could be treated as a constant. This is a reasonable assumption as our data covers a relatively narrow latitude range from 41°S to 48°S . The infinite-depth Ekman models were approximated by using a boundary layer depth of 1000 m with a free slip bottom boundary condition to approximate the effect of an infinite BLD. Finite depth LEMs were configured with a BLD of either 105m or 336m (in line with the fits to the ADCP and EM-APEX data discussed in Chapter 4) and a no slip boundary condition. All linear Ekman models applied to the shipboard ADCP observations were run on vertical grids with dz of 0.5m. Stokes drift was computed (as in Chapter 3) from reanalysis wave period and significant wave heights interpolated onto the ship track before the resulting surface stresses for the modified LEMs were computed as described above. Geostrophic shear was computed from the shipboard ADCP observations using the method outlined in Chapter 3 assuming a reference depth of 200m. Time steps were computed from Equation 5.3. Output was saved to disk for later analysis every 1600 seconds.

To characterise the time varying performance of the model we compared the statistical distribution of modelled currents with the nominal 23.5m ADCP observations. However, the ADCP observations actually represent the currents observed in a 'bin' surrounding the nominal depth. The width of this depth bin varied with the mode in which the ADCP was running and whether RV *James Cook*'s keel was raised or lowered. As a result the 23.5m ADCP observations include contribution from currents between 10m and 30m depth. Hence, it is not appropriate to compare the model time series at 23.5m depth to the observations and we must instead construct a representative time series. We considered two time series; one created by taking the mean velocity over the 10-30m interval at each time step and the other taking the maximum current by amplitude over the 10-30m depth. We found the time series constructed using the maximum current by amplitude produced a

probability density function closer to the PDF produced using the ADCP data; hence, we proceeded with this modelled time series for the subsequent analysis.

Autocorrelation as a function of time lag for each model configuration at a particular viscosity was computed via a bootstrap method; the velocity time-series was split into a number of overlapping segments and the correlation by component as a function of time lag was calculated for each segment. Mean autocorrelation as a function of time-lag and the corresponding 95% confidence intervals were then computed from the bootstrap estimates.

b. EM-APEX Ekman Models

Ekman models for the floats were run with the same viscosities and BLD configurations as the models applied to the ADCP data. As float current time-series were two to three times longer than the duration of the shipboard time-series, applying the same time-steps used in the ADCP model runs was likely to result in excessive run times. Hence, following Equation 5.3, we opted to use a lower resolution vertical grid with dz of 1m.

We considered model performance over all floats rather than on a float by float basis to maximize the number of datapoints available to ensure our analysis of time-varying performance was robust. Time series of simulated and observed velocities were generated in a similar manner to the shipboard case before the output from all floats was aggregated into a single dataset. We then applied the two sample KS test and computed the probability density functions and generated QQ plots. Autocorrelation as a function of time-lag was computed using a similar bootstrap method as applied to the ADCP model runs, only differing in that we took the mean and 95% confidence intervals over all floats. Similarly, the time-mean current profiles were generated by averaging over all floats.

c. PWP Models

The three variations on the Price-Weller-Pinkel model were only applied to the EM-APEX floats.

The PWP models were implemented on a 1m vertical grid with a maximum depth of 1000m and run with 600 s time steps. Wind-forcing, as above, was derived from the CERSAT blended ERA-Scatterometer dataset (described in Chapter 3) and interpolated onto each float trajectory. To simplify the model we assumed that latitude, and by extension the coriolis parameter, could be treated as constant, as we did for the linear Ekman models.

Six hour resolution solar short wave incoming radiation, the outgoing long-wave radiation and precipitation were sourced from the NCEP/NCAR reanalysis product and interpolated onto the time and locations of all EM-APEX profiles. While NCEP/NCAR provides lower spatial resolution compared to the ECMWF ERA reanalysis products, all ERA products offer the relevant data at 12hr temporal resolution, limiting the ability of the model to capture the diurnal cycle in stratification. As diurnal changes in stratification have been proposed (Price et al., 1987) as a major influence on the structure of the Ekman spiral, we judged the improvement in temporal resolution from using NCEP to outweigh the loss of spatial resolution. Meridional SST gradients were obtained from a 24hr-0.25° resolution blended SST dataset derived from Advanced Very High Resolution Radiometer (AVHRR) and Advanced Microwave Scanning Radiometer (AMSR) satellite systems (Reynolds et al., 2007).

5.5. Shipboard ADCP Results

a. Infinite Depth LEMs

The infinite depth linear Ekman models were compared against observed Ekman currents extracted from the ADCP observations by removing the geostrophic shear (as described in Chapter 3) with a deep reference velocity, here taken as the mean between 183.5 and 215.5m. The time varying performance of all infinite BLD Ekman models as measured by the KS test statistic is shown in the upper panel of Figure 5.1. No models produced a KS statistic less than the critical value of 0.049; this indicates that none of the modelled CDFs matched the observed CDF. By a strict definition this would suggest that at the 95% confidence level none of the infinite depth LEMs were able to provide

a proper representation of the Ekman currents; however the observational data set likely contains noise that is not present in the model data.

The classical Ekman model was found to display a minimum zonal KS statistic of 0.075 for an eddy viscosity of $0.005\text{m}^2\text{s}^{-1}$; the zonal KS statistic was found to increase (i.e. model time-varying performance decreased) with increasing viscosity. The corresponding meridional KS statistic was found to display a minimum value of 0.134 at a viscosity of $0.01\text{m}^2\text{s}^{-1}$ and model performance then degraded with increasing viscosity. This tendency for model performance to degrade beyond a particular range of viscosities (here $0.005\text{-}0.01\text{m}^2\text{s}^{-1}$) is logical. If we consider a single depth level a higher viscosity equate to deeper decay scale. Assuming a constant wind stress, this implies that the magnitude of the Ekman velocity is reduced. This is seen clearly in the PDF plots shown in Figure 5.2.

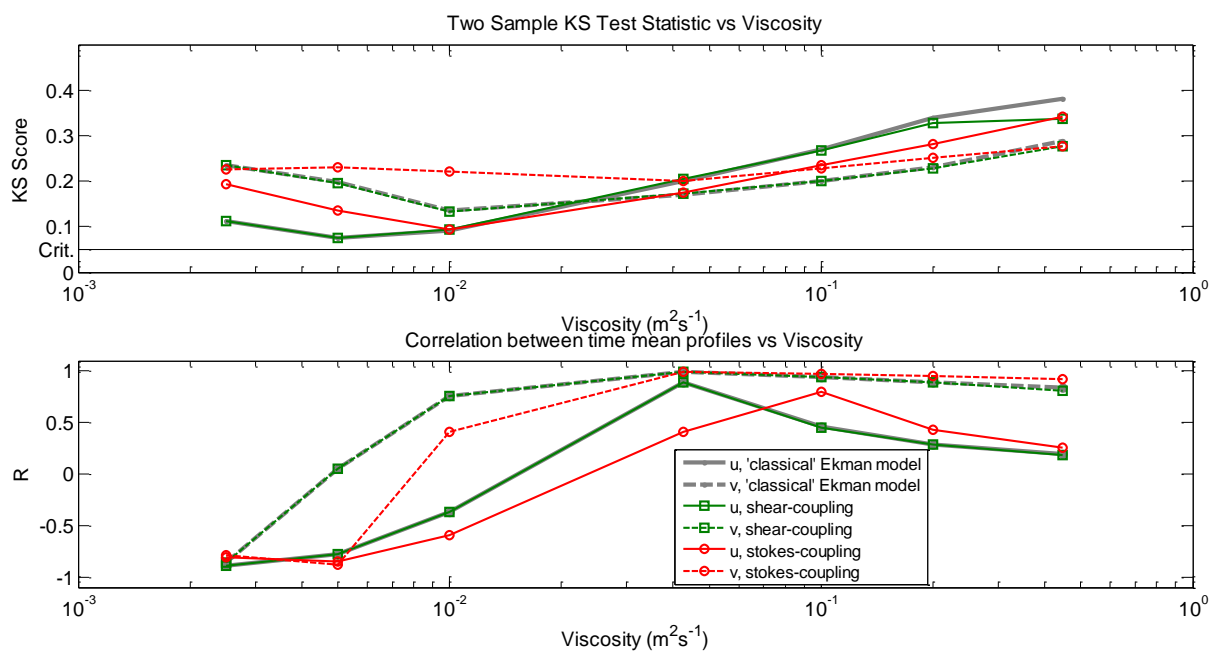


Figure 5.1: KS test statistics for velocity distributions at 23.55m depth (top) between all infinite-depth Ekman models and shipboard observations. Correlations between observed and modelled mean velocity profiles (bottom) for all infinite depth Ekman models. Crit. indicates the critical value for a two sample KS test.

The shear-coupled Ekman model was found to have performance closely comparable to the classical Ekman model for all viscosities less than $0.2\text{m}^2\text{s}^{-1}$. At greater viscosities the shear-coupled model displayed superior performance to the CLEM; however, at these viscosities all models display

very high KS statistics, indicating model skill is low. The Stokes drift coupled Ekman model best matched the observations of zonal velocity at $0.01\text{m}^2\text{s}^{-1}$ with a KS statistic of 0.095; meridional performance was characterised by a minimum KS statistic of 0.201 at a viscosity of $0.043\text{m}^2\text{s}^{-1}$. The stokes-coupled model was found to outperform the CLEM in the zonal component at viscosities of $0.043\text{m}^2\text{s}^{-1}$ and above, but proved inferior to the CLEM in the meridional component over the entire viscosity range. This evidence suggests that of the three models considered here, the classical Ekman and geostrophic shear coupled models are the most appropriate for capturing the time varying behaviour seen in the shipboard observations.

Examination of probability distribution functions obtained from the observations and the models indicated qualitative agreement between observations and the classical Ekman model in the zonal component at viscosities between 0.0025 and $0.0100\text{m}^2\text{s}^{-1}$ (Figure 5.2) despite the modelled PDFs tending to produce a heavier than expected rear (westward) tail. Examination of corresponding PDFs for the meridional component showed agreement in the shape of the PDFs but modelled PDFs were found to display a positive (northward) bias relative to the observations. PDFs displayed heavier tails than seen in the observations.

QQ plots (Figure 5.3) show good agreement at viscosities between 0.005 and $0.0100\text{m}^2\text{s}^{-1}$, with performance decreasing significantly at $0.0425\text{m}^2\text{s}^{-1}$. The QQ plots also suggest that the failure to meet the KS criteria is associated with the tails of the modelled distributions. Concentrating on the linear fit extrapolated from the 1st to 3rd quartiles we see close agreement between the observations and the model output at $0.0100\text{m}^2\text{s}^{-1}$. The shear-coupled model (not shown) was found to display almost identical behaviour to the classical Ekman model at all viscosities.

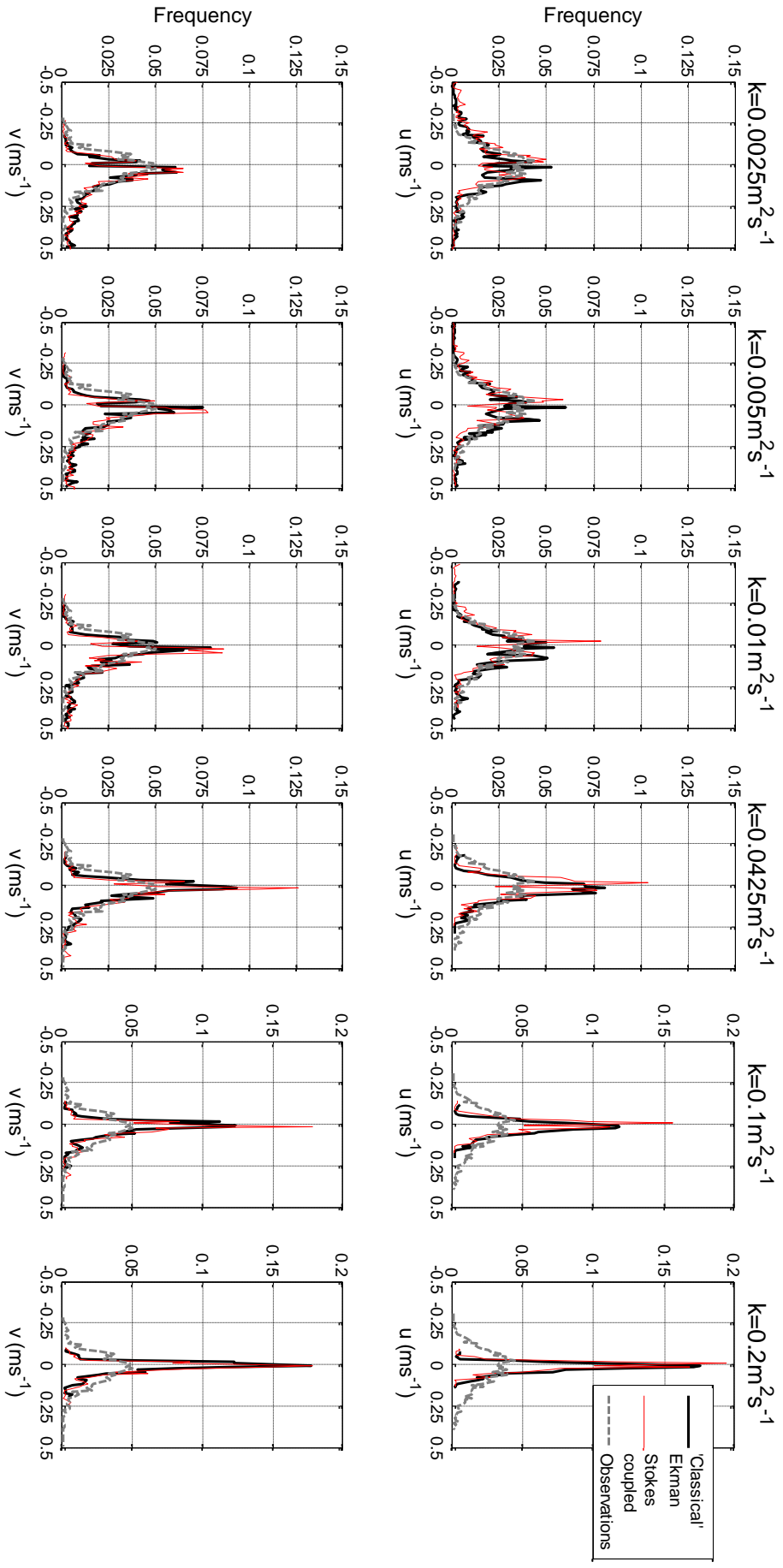


Figure 5.2: PDF plots of 23.55m zonal (top) and meridional (bottom) velocities for infinite BLD models at viscosities between $2.5 \times 10^{-3} \text{ m}^2 \text{ s}^{-1}$ and $0.2 \text{ m}^2 \text{ s}^{-1}$.

Grey line marks the PDFs from observations while black and red denote the classical and Stokes coupled Ekman models respectively.

The Stokes coupled model (Figure 5.2) displayed significant disagreement with the observed zonal PDF at viscosities of 0.0025 and $0.0050\text{m}^2\text{s}^{-1}$ but fair agreement at $0.0100\text{m}^2\text{s}^{-1}$; as above the mismatch was principally characterised by the model displaying a heavy rear (westward) tail. The meridional modelled PDFs displayed a similar northward bias as described above. QQ plots (Figure 5.3) displayed behaviour consistent with the PDFs. Examination of the linear fit extrapolated from the 1st to 3rd quartiles indicated that the Stokes-coupled model generally provided a close match to the corresponding fit to the uncoupled Ekman model. This in turn suggests that the performance of the Stokes model may be more satisfactory than the KS test results indicate.

The heavy tails observed in the PDF and QQ plots of modelled data were found to be associated with high wind speeds. This suggests that the numerical models, and by extension classical Ekman theory, tend to overestimate the oceanic response for strong winds. We speculate that it is likely an effect of wind waves. There are two plausible means by which the wind waves could suppress the Ekman response to strong winds:

1. The formation and breaking of wind waves implies that wind energy (and, hence, momentum) is inputted into the wave field and dissipated instead of transferred via the wind stress into Ekman currents.
2. Studies (Donelan et al., 1993, Fairall et al., 1996, Johnson et al., 1998) indicate that wind waves can affect sea surface roughness and, hence, the surface wind stress. Wind stresses computed in our study use the drag coefficient function from Yelland and Taylor (1996), which does not explicitly include any wave effects. Hence, it is possible that we have overestimated the wind stresses arising from high winds.

Unfortunately, we were unable to pursue this line of inquiry any further. We were limited to using wave parameters obtained from the ERA Interim reanalysis. The spatial (1.5°) and temporal scales (6 hour) of this dataset limit its utility on the fine spatial scales and short time periods needed to examine the effects of wind waves.

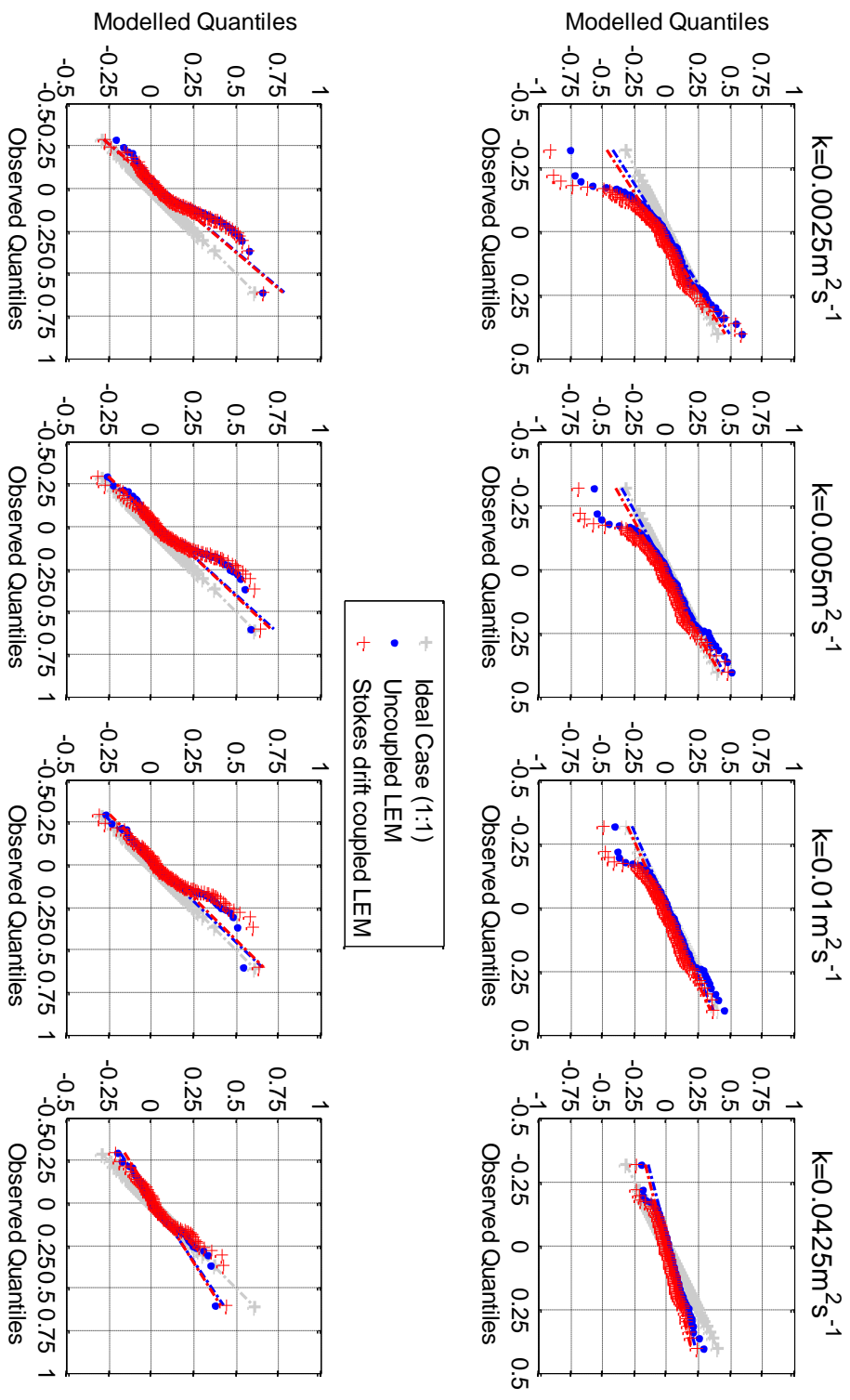


Figure 5.3: QQ plots of zonal (top) and meridional (bottom) velocities. Symbols indicate quantiles at 0.5% intervals; dashed lines are extrapolated from a linear fit to the 1st to 3rd quantiles of the data.

Time-mean performance (Figure 5.1, lower panel) as measured by the correlation between modelled and observed time-mean current profiles suggested maximum performance occurred at higher viscosities than in the time-varying case: the wind driven and shear coupled models displayed maximum performance at $0.043\text{m}^2\text{s}^{-1}$ for both components, the stokes-coupled model displayed maximum performance in the v component at the same value while the u component achieved maximum correlation at $0.1\text{m}^2\text{s}^{-1}$. The wind-forced and shear-coupled models achieved a higher peak zonal correlation ($R=0.890$ and $R=0.887$) than the stokes-coupled model ($R=0.794$). Beyond the viscosities corresponding to peak u-correlation all three models displayed significant declines in performance as measured by correlations. All models displayed a peak meridional correlation of $R=0.992$ at a viscosity of $0.043\text{m}^2\text{s}^{-1}$; at higher viscosities correlations trended downwards but remained elevated ($R=0.804$ - 0.976) relative to correlations at viscosities less than $0.043\text{m}^2\text{s}^{-1}$.

Plots of time-mean velocity profiles for viscosities between 2.5×10^{-3} and $1.0 \times 10^{-1} \text{m}^2\text{s}^{-1}$ are shown in Figure 5.4. Despite the strong correlations seen between the models and observations at certain viscosities no models were able to match the observed profiles at the 95% confidence interval over all of the 0-100m depth range. The shear-coupled model (not shown) was found to display almost identical behaviour to the wind-driven model at all viscosities.

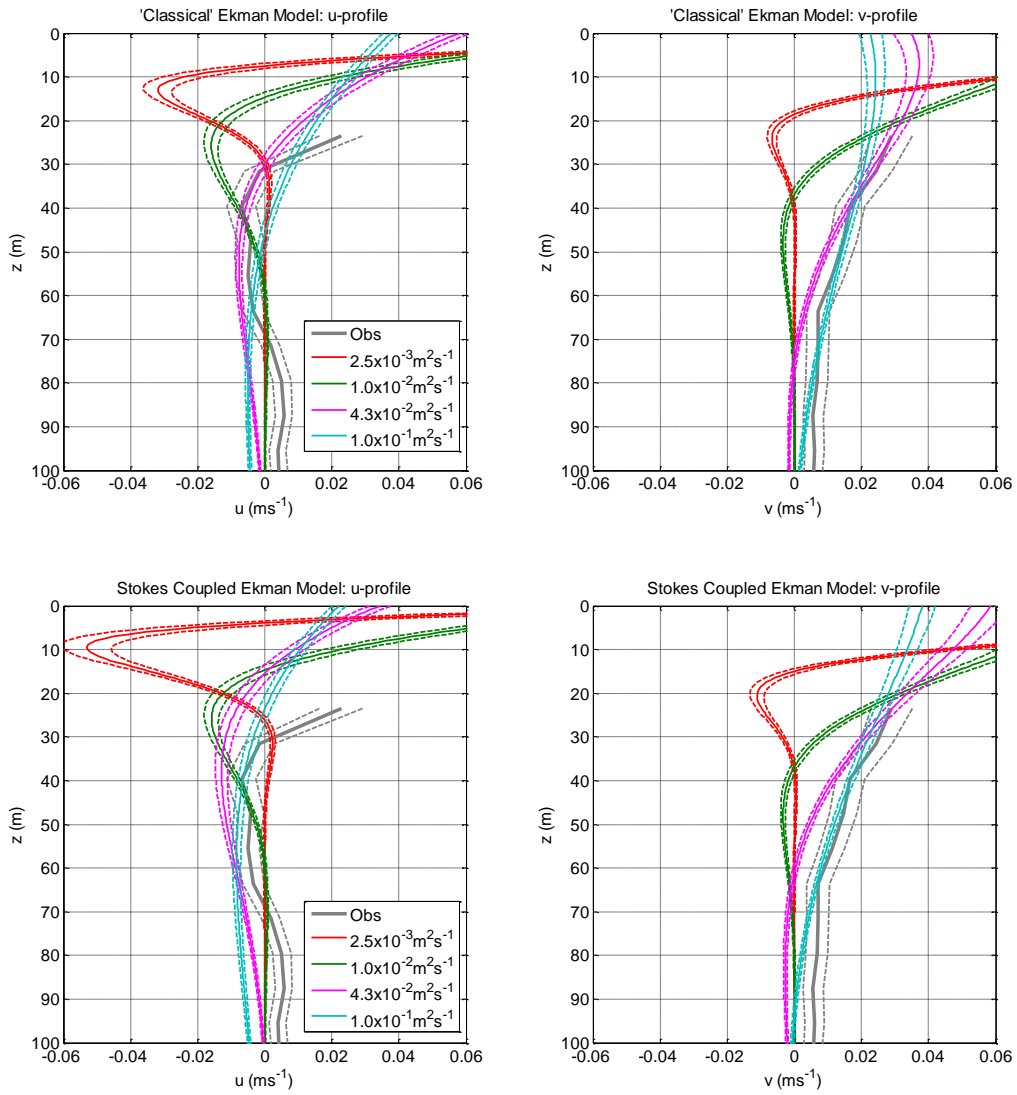


Figure 5.4: Time mean classical Ekman model (top) and stokes-coupled model (bottom) current profiles for a range of viscosities. Solid lines indicate the mean profile and dashed lines the 95% confidence intervals. The shear-coupled model did not produce current profiles significantly different from the classical Ekman model.

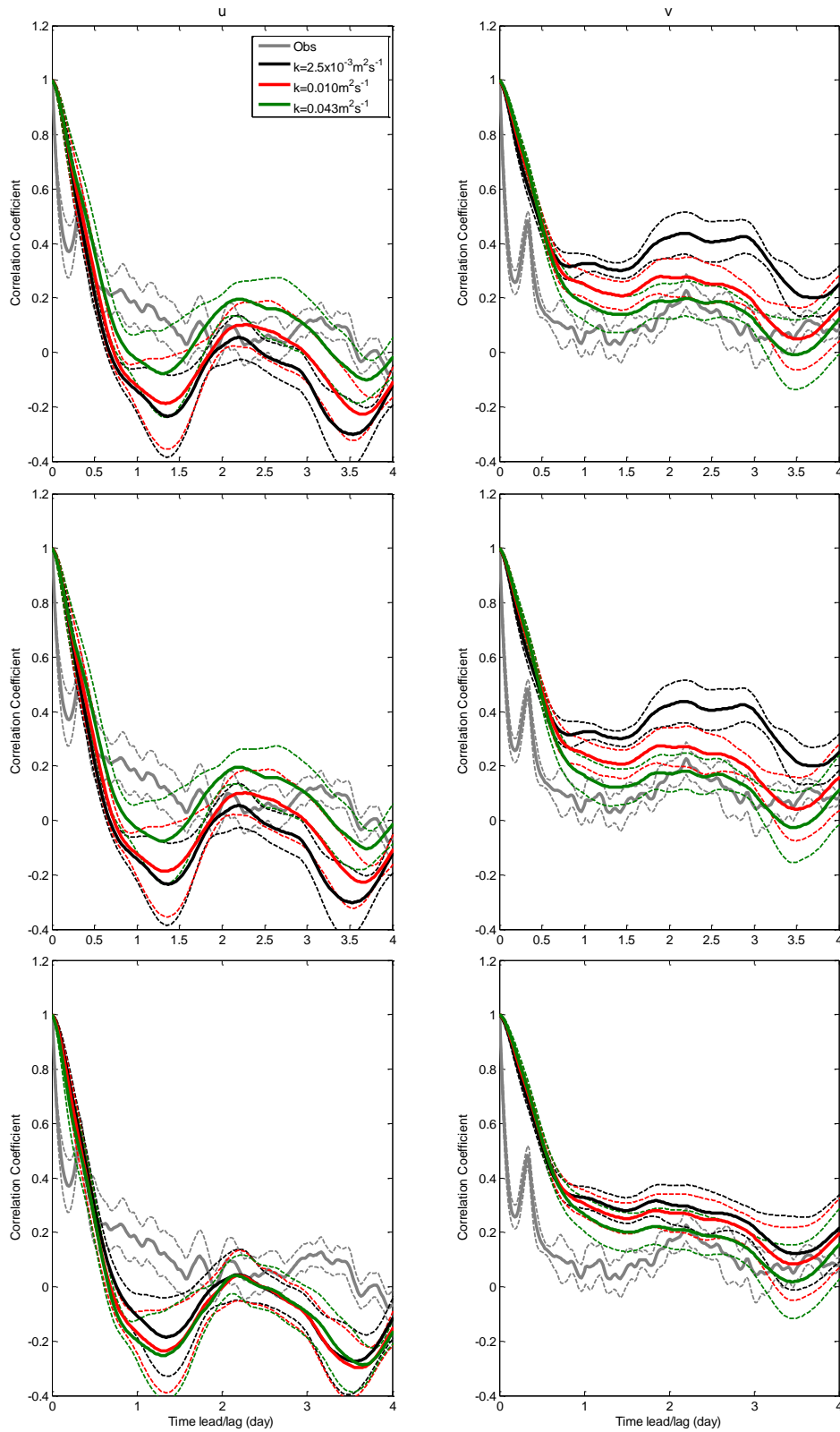


Figure 5.5: Observed (grey curve) and modelled current autocorrelation as a function of time-lag for the u (left) and v (right) components at 23.5m over a range of viscosities for three different LEMs (top, 'classical'; middle, shear coupled, and bottom, Stokes coupled). Solid curves denote the mean values and dashed lines indicate 95% confidence interval.

Plots of autocorrelation as a function of time-lag (Figure 5.5) were found to display little sensitivity to the choice of viscosity or model. The observed autocorrelation was found to display more rapid attenuation than the numerical models in the 0-3 hour range followed by a peak at around the 6 hour mark. This behaviour suggests the observed ageostrophic currents include processes not resolved by the linear Ekman models. Alternatively, it could arise from how the models and observations treat inertial oscillations. The linear models only include inertial currents generated by the local wind forcing while the *in situ* observations also include contributions from inertial currents generated at a distance from the floats or ship that have subsequently been advected by the mean flow. Either way, the difference in behaviour demonstrated in the autocorrelation plots could account for the failure to achieve agreement between the observed and modelled CDFs as measured by the KS test statistic.

b. Finite Depth LEMs

The finite depth linear Ekman models were compared against observed Ekman currents isolated from the ADCP observations by removing the geostrophic shear (identified as described in Chapter 3) with a deep reference velocity here taken at the depth of the model boundary layer (105m or 336m).

Model performance for all finite BLD Ekman model runs with a BLD of 105m is shown in Figure 5.6. All 105m BLD models display general agreement with the corresponding infinite depth models in terms of the optimal viscosities. All models displayed peak time-varying performance between viscosities of 0.005 and $0.01\text{m}^2\text{s}^{-1}$. Peak time-mean performance for the wind-only and Stokes-coupled models occurred at a viscosity of $0.0425\text{m}^2\text{s}^{-1}$; the shear coupled model achieved maximum performance in the u-component at the same viscosity as the other models, but peak v-component performance occurred at a viscosity of $0.1\text{m}^2\text{s}^{-1}$.

Time-varying performance for the zonal current in the 105m BLD wind forced and shear-coupled models was found to be comparable to the equivalent infinite BLD models over most of the

viscosity range. Meridional performance for the same models was found to be equivalent to the infinite BLD models for viscosities less than $0.43\text{m}^2\text{s}^{-1}$ and slightly superior for larger viscosities. The Stokes-coupled 105m BLD model offered equivalent or slightly superior zonal performance to the infinite BLD Stokes-coupled model for all viscosities less than $0.2\text{m}^2\text{s}^{-1}$, but as above, the meridional performance was equivalent to the infinite BLD model. Time mean performance of all 105m BLD models was found to be closely comparable to the equivalent infinite BLD models.

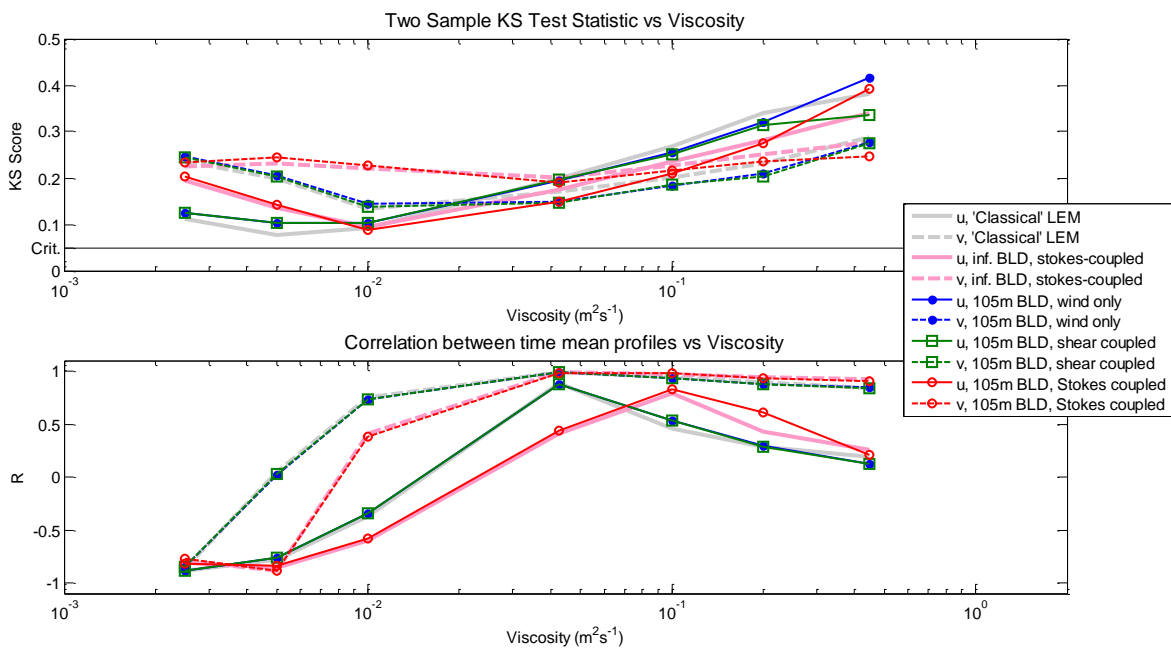


Figure 5.6: KS test statistics for velocity distributions at 24m depth (top) between all finite depth Ekman models with a BLD of 105m and shipboard observations. Correlations between observed and modelled mean velocity profiles (bottom) for all finite depth Ekman models with BLD of 105m. Solid lines indicate u-components and dashed lines v-components.

The 336m finite BLD wind driven and shear coupled models were found to offer generally equivalent zonal time varying performance (Figures 5.7) compared to the infinite BLD wind-forced model, over the majority of the viscosity range. Meridional time-varying performance for all finite depth models was inferior to the infinite BLD models. The zonal time mean performance of all finite depth models was superior to the corresponding infinite BLD models at low viscosities but inferior at high viscosities; while meridional performance was found to closely match the infinite BLD models. In

both cases the viscosities corresponding to maximum performance were the same as the 105m and infinite BLD cases.

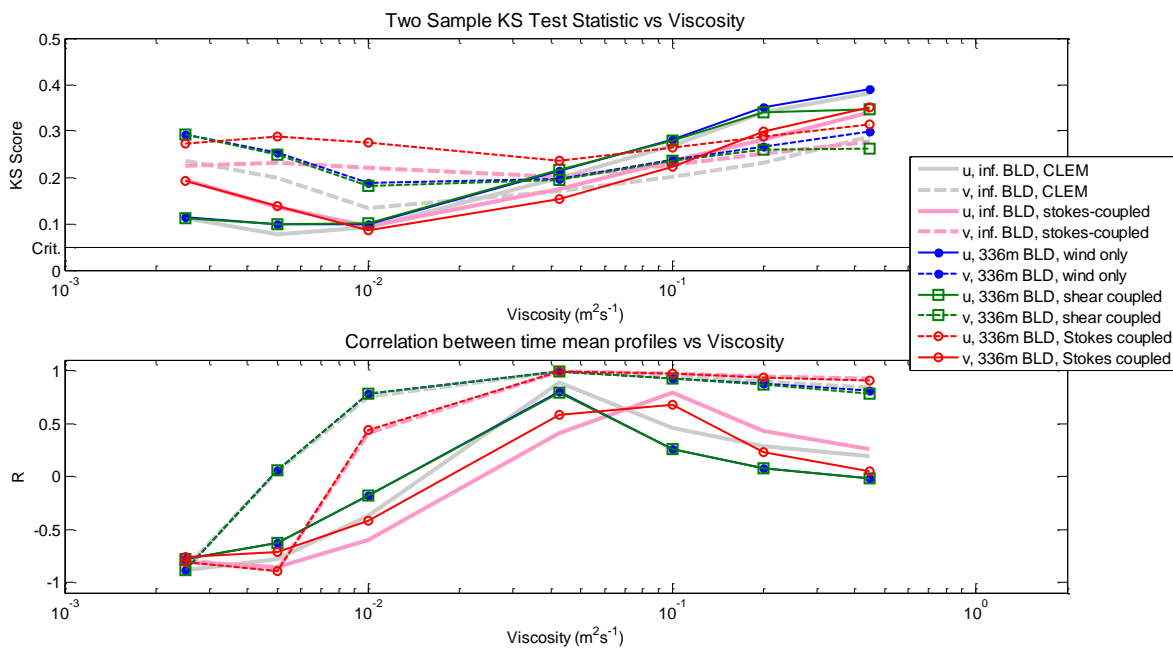


Figure 5.7: KS test statistics for velocity distributions at 24m depth (top) between all finite depth Ekman models with a BLD of 336m and shipboard observations. Correlations between observed and modelled mean velocity profiles (bottom) for all finite depth Ekman models with BLD of 336m. Solid lines indicate u-components and dashed lines v-components.

Examination of modelled PDFs (Appendix 2, Figure A2.1 and A2.3), QQ plots (Appendix 2, Figure A2.2 and A2.4) and mean current profiles indicated that the choice of model BLD and bottom boundary condition had surprisingly little impact on the time-mean and time-varying characteristics of the models. Instead, we found that the primary factor driving differences in model performance as a function of BLD and boundary condition was the change in the observed Ekman current resulting from varying the deep reference velocity.

c. Summary

We have tested a variety of linear Ekman models driven with shipboard wind observations, and compared the resulting Ekman currents to the shipboard ADCP data. All models were found to offer good time-mean performance for viscosities between 0.0425 and 0.1m²s⁻¹. No models were able to

satisfy the KS test at any viscosity, with the best performing (wind-forced) models displaying a zonal KS score of around twice the critical value (0.049). However, examination of QQ plots indicated that the disagreement between the models and observations are primarily limited to the tails of the probability distribution; we speculated that the heavy tails in the modelled data likely arose from neglecting the effects of wind-waves. Minimum KS scores suggested the optimal viscosity for the wind-forced and geostrophic shear-coupled models was between 0.005 and $0.01\text{m}^2\text{s}^{-1}$; while optimal viscosities for the Stokes-drift coupled models were larger, between 0.01 and $0.0425\text{m}^2\text{s}^{-1}$.

The shear-coupled models were found to display equivalent performance to the wind-driven models over the majority of the viscosity domain. Further examination indicated that the QQ plots and probability density functions derived from the shear-coupled models were virtually degenerate to the corresponding wind-driven models. This strongly suggests that within the Southern Ocean context coupling between Ekman currents and geostrophic shear is not significant.

Stokes-drift coupled models were found to be generally inferior to the wind-driven models in a time varying-sense when measured by the KS test. However, examination of QQ plots and PDFs suggests that this is principally due to the Stokes-coupled models displaying heavier tails than either the wind-driven model or observations. Concentrating on the 1st to 3rd quartiles of the data, the Stokes-coupled models appeared to display time-varying performance (as measured by the slope of the QQ plot linear fit) in line with the wind-driven model. Additionally, our assumptions in computing the Stokes stress may have contributed to the poor performance. We used a wave amplitude of half the significant wave height; this would tend to lead to a higher Stokes stress than if we instead used a wave amplitude derived from the mean or RMS wave heights. We also assumed wave activity at any instant was monochromatic (i.e. that waves of only a single frequency were present); *in situ* wave activity is likely to consist of a superposition of waves of multiple frequencies. Finally, we obtained wave forcing data from the ERA-Interim reanalysis fields; it is possible that the spatial and temporal resolution of this dataset does not provide a full representation of the *in situ* wave activity.

The benefit of using models with finite boundary layer depths was found to be small. Examining mean velocity profiles suggested the small changes in performance were principally due to the change of deep reference level used to isolate the observed Ekman currents rather than changes to the model dynamics.

In light of the above evidence, it appears that the most effective and parsimonious model of those tested is one with a time and depth constant viscosity and infinite boundary layer depth; in effect the 'classical' linear Ekman model. However, it must be noted that we still obtain significant disagreement between the viscosities for the best time-mean and time-varying performance.

5.6. EM-APEX Results

a. Infinite Depth LEMs

Time-mean and time-varying performance of all infinite BLD Ekman models applied to the float data is shown in Figure 5.8. Time-varying performance for all models, measured by the KS statistic, was found to be inferior to the model runs for the shipboard data. The wind-forced and shear-coupled models were, again, found to be effectively equivalent to each other. As with the shipboard model runs the Stokes drift coupled model had the highest KS scores and, hence, was the worst performing model across the entire viscosity range; the meridional velocity component had similar KS scores to the uncoupled model but the zonal component KS statistics were significantly inferior. The resulting optimal viscosities did not agree with those obtained in the shipboard model runs (Section 5.5). The wind-forced and shear-coupled models displayed peak zonal performance between 0.01 and $0.043\text{m}^2\text{s}^{-1}$ (against $0.005\text{m}^2\text{s}^{-1}$ for the same models in Section 5.5a) while meridional performance was found to be approximately constant across the entire viscosity range. The Stokes-coupled model gave optimal zonal performance at $0.043\text{m}^2\text{s}^{-1}$ and peak meridional performance at $0.0025\text{m}^2\text{s}^{-1}$.

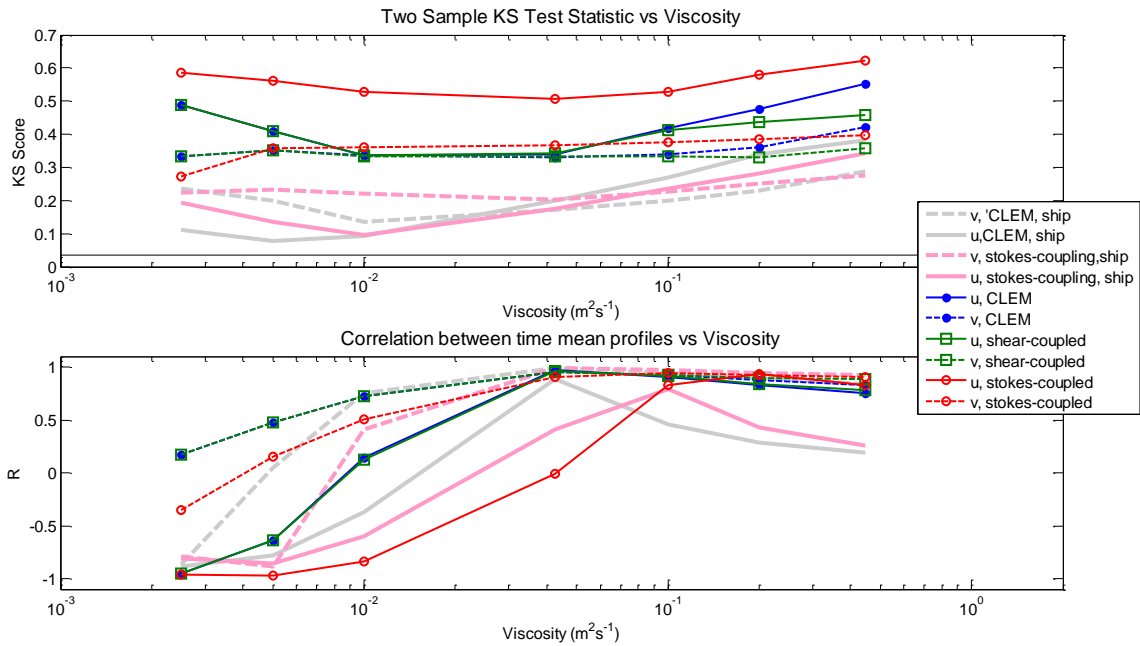


Figure 5.8: KS test statistics for velocity distributions at 24m depth (top) between all infinite depth Ekman models and EM-APEX observations. Correlations between observed and modelled mean velocity profiles (bottom) for all infinite depth Ekman models. Solid lines indicate u-components and dashed lines v-components.

Examination of PDF and QQ plots (Appendix 2, Figure A2.5 and A2.6) reflect the poor time-varying performance identified by the KS test. In both cases the behaviour of the PDFs and QQ plots indicated that the models consistently underestimate the current at 24m depth.

Time-mean performance is shown in the lower panel of Figure 5.8. Again the uncoupled and Shear-coupled Ekman models produced equivalent performance in both components; zonal correlations were found to be higher than the shipboard model runs over all viscosities while meridional correlations were superior for viscosities less than $0.01\text{m}^2\text{s}^{-1}$ and comparable to the shipboard models thereafter. Peak performance was found at the same viscosities as in the corresponding shipboard model runs ($0.0425\text{m}^2\text{s}^{-1}$). The meridional stokes-coupled performance displayed superior performance (relative to the corresponding shipboard model) for viscosities less than $0.01\text{m}^2\text{s}^{-1}$, thereafter model performance was approximately equivalent. Zonal performance was found to be inferior to the shipboard stokes-coupled model for viscosities less than $0.1\text{m}^2\text{s}^{-1}$. The Stokes-coupled model was found to achieve peak correlation at $0.1\text{-}0.2\text{m}^2\text{s}^{-1}$.

b. Finite Depth LEMs

Model performance for the finite depth models using a BLD of 105m is shown in Figure 5.9. Time-mean performance (Figure 5.9, bottom) did not differ significantly from the infinite BLD LEM. Zonal time-varying performance (Figure 5.9, top) improved compared to the infinite BLD model, but at the cost of a comparable decline in meridional performance. As above, the float models displayed inferior performance to the ADCP models (section 5.6). QQ plots and CDF plots (Appendix 2, Figures 9.7 and 9.8) indicate that, similar to the infinite depth case, the 105m BLD models tended to underestimate the oceanic response.

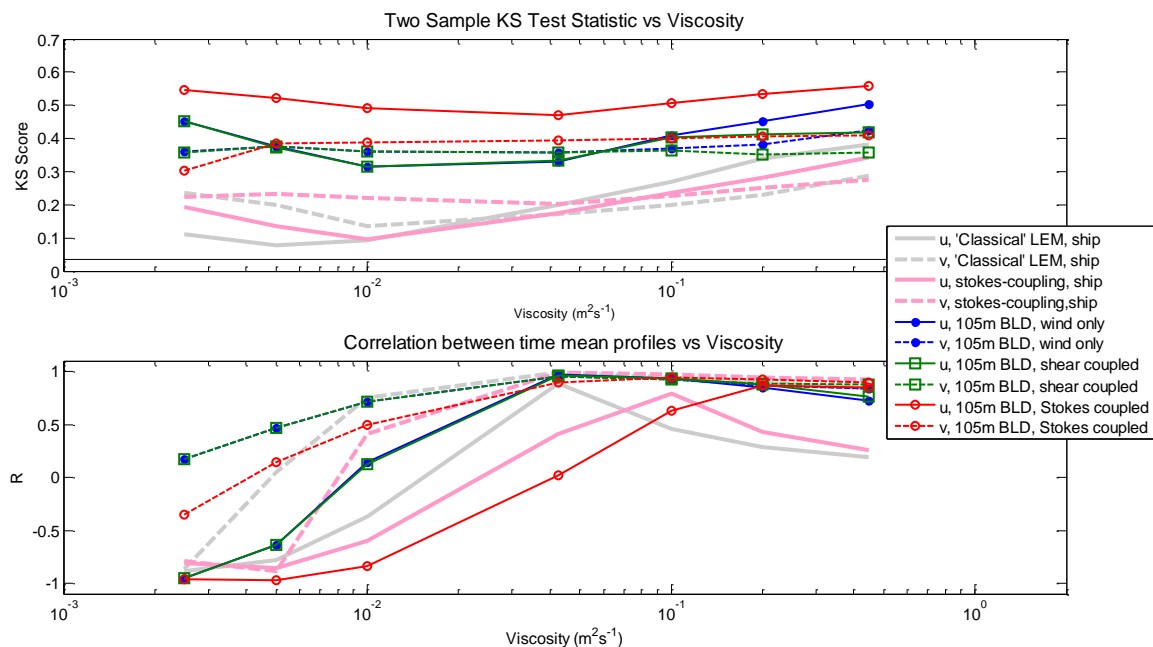


Figure 5.9: KS test statistics for velocity distributions at 24m depth (top) between all 105m BLD Ekman models and EM-APEX observations. Correlations between observed and modelled mean velocity profiles (bottom) for all 105m BLD Ekman models. Solid lines indicate u-components and dashed lines v-components.

The models run with a BLD of 336m (Figure 5.10) were found to offer equivalent time-mean and marginally inferior time-varying performance when compared to the infinite BLD model runs. As above time-varying performance was inferior to the shipboard case, with the models underestimating the velocity response.

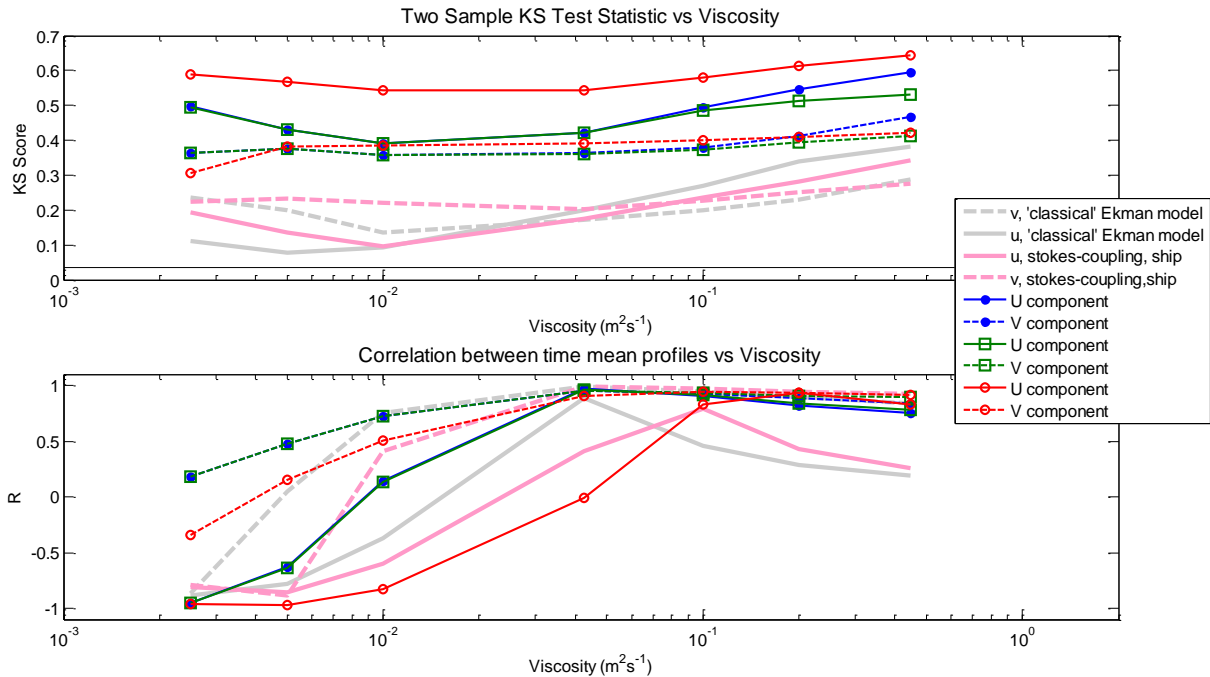


Figure 5.10: KS test statistics for velocity distributions at 24m depth (top) between all 336m BLD Ekman models and EM-APEX observations. Correlations between observed and modelled mean velocity profiles (bottom) for all 336m BLD Ekman models. Solid lines indicate u-components and dashed lines v-components.

c. Price, Weller and Pinkel

We considered three stratified models using the PWP mixing scheme. The ‘simple’ no heat gradient case (equivalent to the standard PWP model) was found to produce zonal and meridional KS coefficients of 0.3976 and 0.3327. The case assuming a meridional temperature gradient and advection from Ekman and inertial currents produced KS coefficients of 0.3732 and 0.3226. The version including advection of the floats up and down the temperature gradient was found to produce KS coefficients of 0.4478 and 0.3406. All stratified models producing KS statistics an order of magnitude larger than the critical value (0.0349). In short, all variants on the PWP mixing schemes display low time-varying model skill.

The low time-varying skill of the PWP models may be a result of errors in the reanalysis air-sea flux; there are significant uncertainties between commonly used reanalysis products (Chaudhuri

et al., 2012). Additionally our data was collected in proximity to the Subantarctic and Polar Fronts. Cerovečki et al. (2011) detected particularly large discrepancies between different reanalysis datasets in proximity to strong fronts, including within the ACC. Alternatively, the low time-varying skill of PWP models may result from other issues such as our source of wind data and the vertical resolution of the model; these possibilities are discussed in Section 5.7.

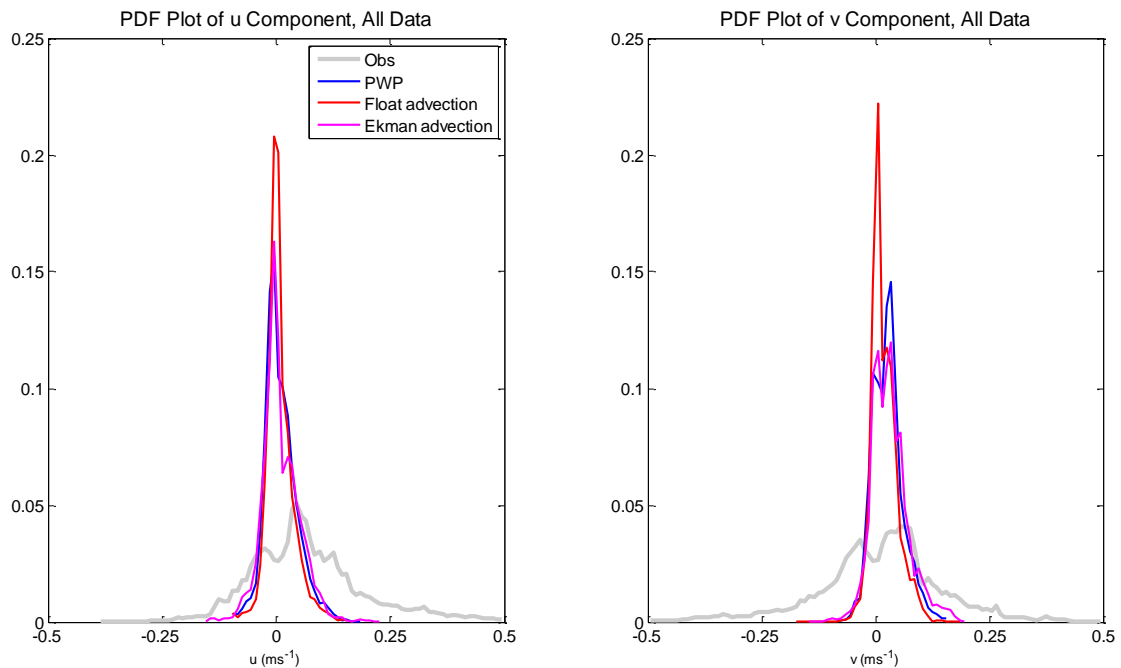


Figure 5.11: PDF plots of u (left) and v (right) components of Ekman currents for float observations and all three PWP models.

PDF plots for the PWP stratified models are shown in Figure 5.11 and QQ plots in Figure 5.12. In line with the KS test results all PDF and QQ plots demonstrated low agreement between the stratified models and the observations. Zonal correlations between the observations and modelled time-mean velocity profiles were found to vary between 0.945 (float advection) and 0.991 (Ekman advection), indicating the PWP models could account for between 89 and 98% of the variance observed in the zonal mean velocity profiles. Meridional correlations were found to lie between 0.904 and 0.961 (accounting for 81-92% of the variability seen in the mean profile). These values indicate that in a time-mean sense stratified models employing the PWP mixing scheme perform as well or better than the linear Ekman models.

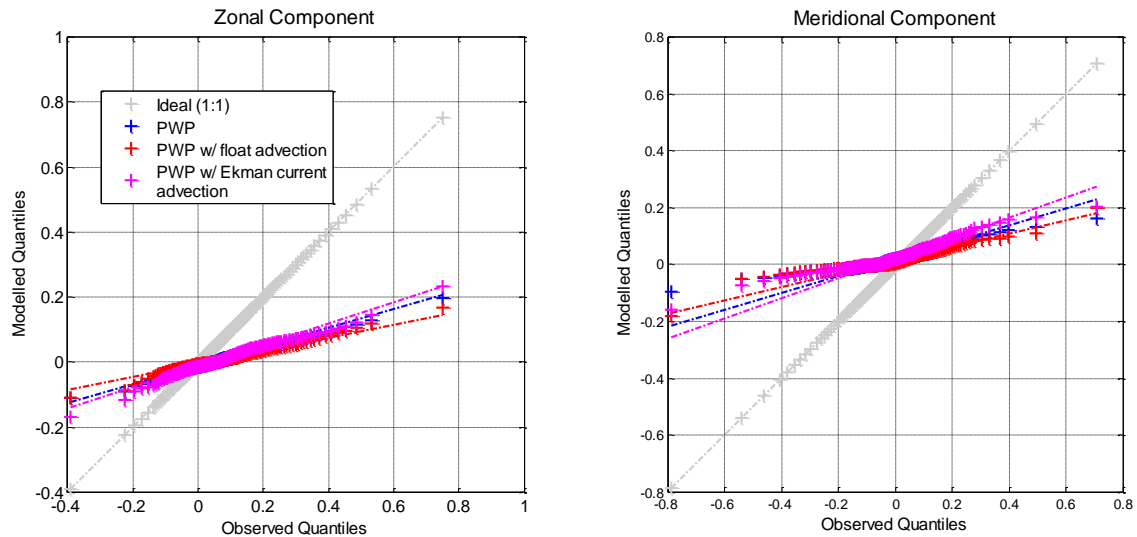


Figure 5.12: QQ plots for all PWP models. Symbols indicate quantiles at 0.5% intervals; dashed lines are extrapolated from a linear fit to the 1st to 3rd quartiles of the data.

d. Summary

All models forced with NCEP/NCAR reanalysis winds interpolated onto the float tracks were found to offer inferior time-varying performance to the same models driven with *in-situ* shipboard winds. The models were found to display comparable characteristics in terms of KS scores and the slope of the QQ plots, suggesting the cause of the failure is universal to all models. These failures suggest it is difficult to properly assess the performance of the models against the EM-APEX float observations and, in particular, we are unable to properly test the stratified models with the PWP mixing scheme. Potential causes of the low model skill are explored in the next section.

Despite all models of the float data displaying low time-varying performance, time-mean performance was comparable to the shipboard model runs, with the models capturing in excess of 80% of the variance observed in the time mean velocity profiles at viscosities between 0.0425 and $0.1\text{m}^2\text{s}^{-1}$.

5.7 Explaining The Differences In Model Performance

In section 5.5, above, we found that several models agree well with shipboard ADCP observations of Ekman currents. Unexpectedly, applying the same models to the float data (section 5.6) resulted in model output showing significant disagreement with the observations. The KS test statistics were found to be much greater over the entire viscosity range than for the ADCP observations, and likewise QQ plots indicated that the models badly underestimated the range of Ekman currents in the float data. The shipboard and float model runs differ in two significant ways:

1. When we applied the models to the shipboard data we used a vertical resolution of 0.5m. Due to additional runtime required to run 8 floats for each viscosity and each version of the model, float model runs used a vertical resolution of 1m. It is possible that the model may display some sensitivity to the vertical resolution.
2. The model runs for the shipboard data used high resolution (30s) *in situ* wind forcing. The float model runs were instead forced with reanalysis winds with 6 hour temporal resolution.

Examination of histograms of the *in situ* wind stresses and NCEP wind stresses interpolated onto both the float tracks and the ship track (Figure 5.13) indicated that the reanalysis winds failed to capture the full range of variability seen in the observed wind stresses. The reanalysis winds interpolated onto the ship track were found to agree well with the distribution of *in situ* stresses up to 1.3Pa but failed to capture any higher amplitude stresses. This would suggest that either the spectral energy content or the resolution of the forcing dataset could account for the difference in model performance.

To investigate the role of vertical resolution and temporal resolution we repeated runs of the shipboard model using coarser vertical resolutions and varying degrees of temporal smoothing. To investigate the sensitivity to the wind forcing dataset, we reran the 'classical' Ekman model for the shipboard observations using NCEP and ERA reanalysis data in addition to the shipboard observations and the CERSAT blended winds.

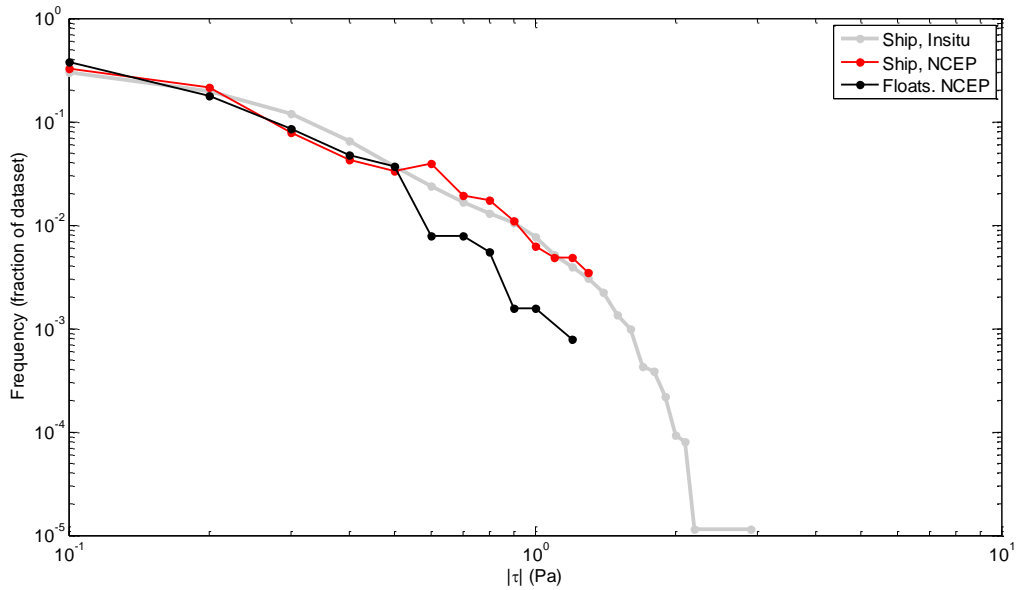


Figure 5.13: Histograms of wind stress amplitude for insitu shipboard winds (grey); NCEP/NCAR reanalysis winds interpolated onto the ship track (red) and NCEP/NCAR winds interpolated onto the float tracks (black).

a. Vertical Resolution

Model performance as a function of vertical resolution is shown in Figure 5.14. The model displayed little sensitivity to vertical resolution for vertical resolutions of less than 1m, and only displayed slight reductions in performance thereafter. Vertical resolution of the models applied above was either 0.5m (shipboard data) or 1m (float data); hence, model sensitivity to the vertical resolution is unlikely to explain the poor performance of the models when compared with the EM-APEX float observations.

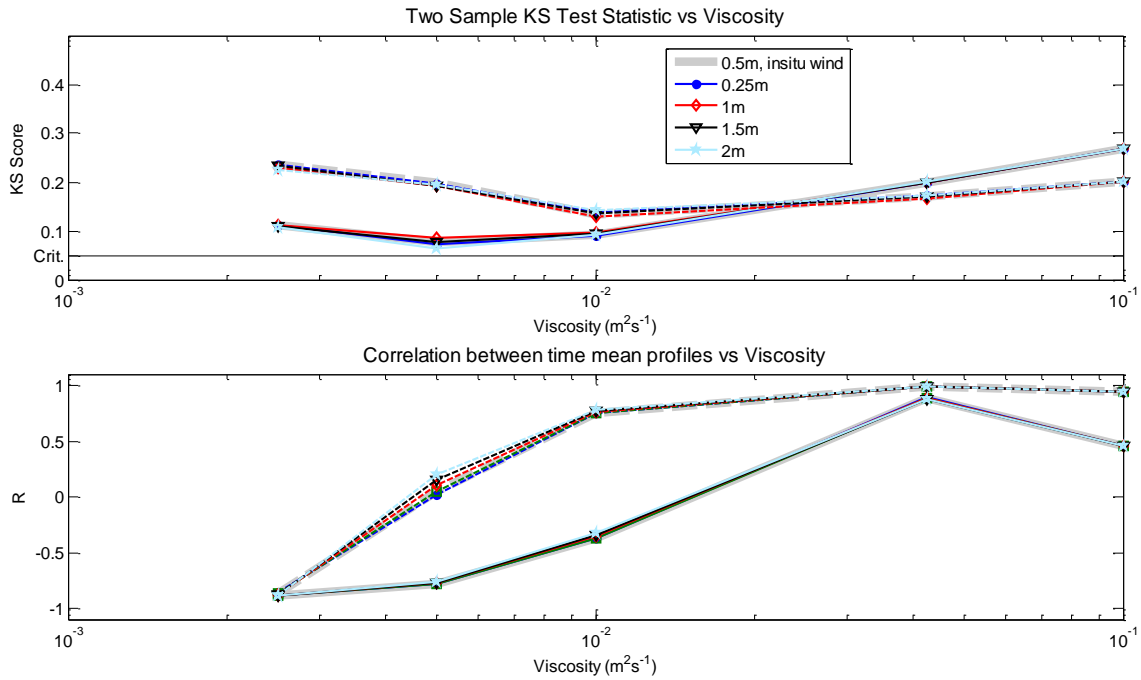


Figure 5.14: KS test statistics for velocity distributions at 24m depth (top) between the infinite BLD

Ekman model run with varying vertical resolution and ADCP observations. Correlations between observed and modelled mean velocity profiles (bottom) for the infinite BLD Ekman models. Solid lines indicate u-components and dashed lines v-components of velocity.

b. Temporal Resolution

We examined the effect of temporal smoothing by taking the observed high resolution (30s) *in situ* winds and smoothing them (using a windowed average) onto temporal grids of 5 minute; 10 minute; 30 minute; 1 hour; 2 hour; 4 hour and 6 hour intervals. We also interpolated the NCEP reanalysis winds onto the ship track. We then re-ran the infinite depth ‘classical’ Ekman model with the new forcing fields over a viscosity range of 0.005-0.1m²s⁻¹. The analysis described above was then repeated. Model performance is summarised in Figure 5.15. Time-mean performance (lower panel) displayed no significant sensitivity to the choice of forcing data.

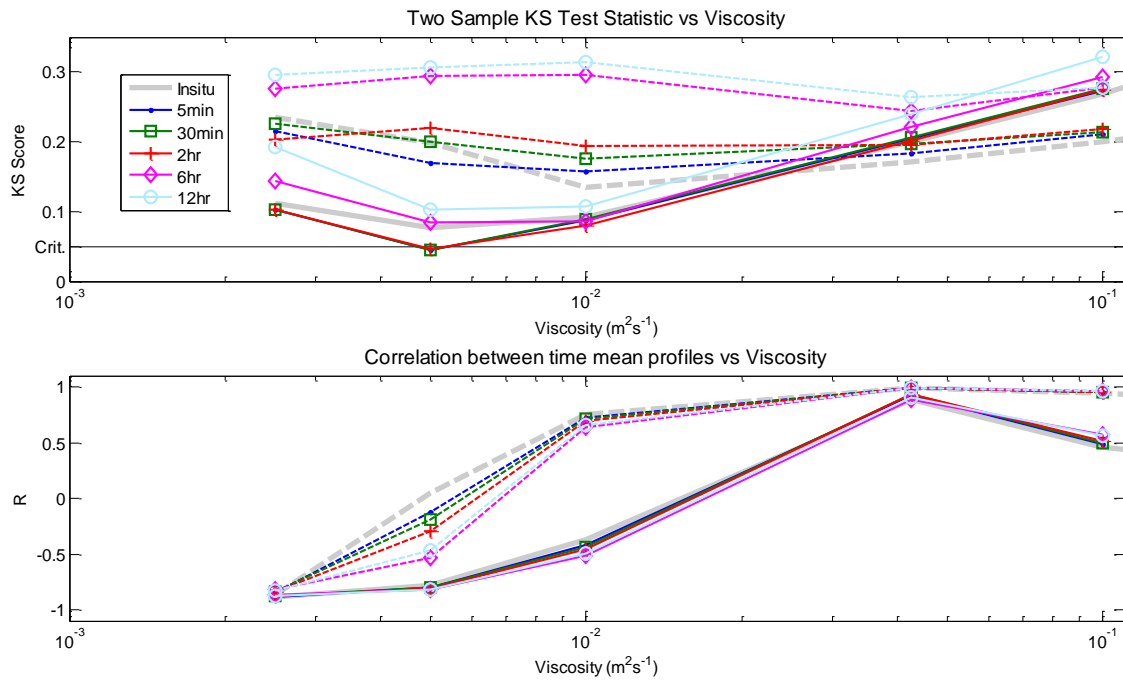


Figure 5.15: Time variable (top, measured by KS test statistic) and time-mean (bottom) model performance for wind forcing data with temporal resolutions between 5 minutes and 12 hours. Solid lines indicate *u*-components and dashed lines *v*-components.

Time-varying performance (upper panel), on the other hand, was found to display sensitivity to the temporal resolution. Smoothing the wind input with windows of between 5 minutes and 2 hours was found to increase zonal performance at low viscosities to the point of meeting the KS test criterion at $0.043\text{m}^2\text{s}^{-1}$. Performance at higher viscosities remained comparable to the unsmoothed case. Temporal smoothing with windows greater than 2 hours was found to result in slightly weaker zonal performance than the unsmoothed case. Meridional performance was found to weaken with increased smoothing across the entire viscosity range. Even with heavy (6-12hr) smoothing it proved impossible to degrade performance to the level seen when comparing the float modelled output and observations.

c. Wind Forcing Dataset

To examine the effect of applying different wind forcing datasets we ran the constant viscosity, infinite BLD Ekman model for the ADCP observations using four alternate wind datasets: NCEP

reanalysis winds; ERA-Interim reanalysis winds; the CERSAT blended scatterometer-reanalysis winds (described in Chapter 3) and the NOAA/NCDC blended satellite winds (Zhang et al., 2006). Details of these datasets are given in Table 5.2 and resulting model performance is summarised in Figure 5.16.

Dataset	Temporal Resolution	Spatial Resolution	Data Source
CERSAT	6 hour	0.25°	QuickSCAT scatterometer, SSM/I radiometers, ERA reanalysis
NCEP/NCAR Reanalysis	6 hour	2.5°	Numerical Model
ERA Interim Reanalysis	6 hour	1.5°	Numerical Model
NOAA/NCDC	6 hour	0.25°	Satellite Scatterometer & Radiometer wind speeds; wind direction from NCEP reanalysis

Table 5.2: Properties of the four wind datasets tested in section 5.7c.

All wind products offered broadly comparable time-mean performance. However, in a time-varying sense CERSAT, ERA and NOAA/NCDC resulted in significantly poorer performance than the models forced with *in situ* winds in both components. The NCEP reanalysis winds were found to offer meridional performance largely comparable with the *in situ* winds, but zonal performance was, with the exception of the lowest viscosities ($0.0025\text{-}0.005\text{m}^2\text{s}^{-1}$), significantly inferior. This suggests that the use of NCEP reanalysis winds contributes to at least part of the reduced performance of the float models runs.

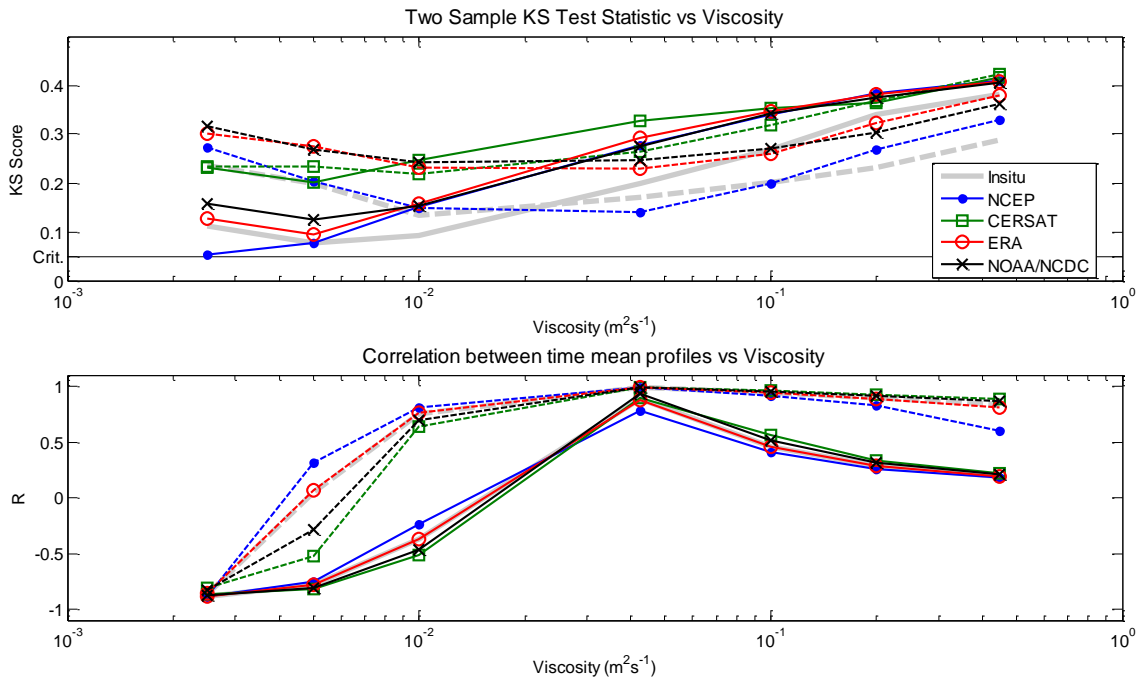


Figure 5.16: Time variable (top) and time mean (bottom) model performance of the constant viscosity infinite BLD linear Ekman model forced with time-series of various gridded wind products interpolated onto the shiptrack. Solid lines indicate u-components and dashed lines v-components.

d. Summary

The evidence outlined above demonstrates that the failure of the float models cannot be attributed to the reduced vertical resolution of the float models compared with the shipboard models. Use of lower resolution ship winds and NCAR/NCEP reanalysis winds was found to result in some loss of model time-varying skill, but neither displayed the decrease in performance seen in the float models. This suggests that the poor performance of the float model runs cannot be solely attributed to either the coarse temporal resolution or the use of the reanalysis winds.

The other gridded wind products tested were found to display inferior performance to the model runs using NCEP, confirming NCEP reanalysis winds are the best available option for forcing the float models.

5.8. Conclusion

We have run a family of nine linear Ekman models over a viscosity range of 0.0025 to $0.447\text{m}^2\text{s}^{-1}$. We have also examined three stratified Ekman models which use the PWP mixing scheme. All nine models were forced with timeseries of *insitu* ship winds and reanalysis winds interpolated onto all float tracks.

For each model run time mean performance was characterized by calculating the correlation between the modelled and observed mean current profiles. Model time varying skill was assessed by examining the probability distributions of the modelled and observed data at 24m depth; we used a two sample Kolmogorov-Smirnov test as a quantitative measure of model skill and quantile-quantile plots as a more qualitative measure.

a. ADCP Data

We found peak correlations between the time-mean modelled and observed Ekman current profiles between $R=0.794$ for the Stokes-coupled model and $R=0.890$ for the 'classical' Ekman model, indicating that the numerical models account for between 63% and 80% of the variability seen in the mean current profile. None of the linear Ekman models managed to meet the KS criteria for a 95% confidence level. Superficially this would imply that in a time-varying sense all numerical models failed. However, examination of quantile-quantile and PDF plots indicated that the models displayed qualitative agreement with the observations over a viscosity range of 0.005 and $0.043\text{m}^2\text{s}^{-1}$. Further examination demonstrated that the numerical models displayed PDFs with heavy tails indicating that the models produced more high amplitude flow than the observations, likely accounting for the failure to match the KS critical value. These heavy tails were associated with high wind stresses; hence we speculate the failure to match the KS critical value results from either overestimating drag coefficients for high wind speeds, or from incorrectly partitioning the wind momentum input between Ekman currents and the wave field.

Model	Viscosity of Min. KS Statistic (m^2s^{-1})		Viscosity of Max. Correlation (m^2s^{-1})	
	u	v	u	v
1 Inf. BLD, no coupling	0.005	0.010	0.043	0.043
2 Inf. BLD, Stokes coupling	0.010	0.043	0.100	0.043
3 Inf. BLD, Shear coupling	0.005	0.01	0.043	0.043

Table 5.3: Viscosities corresponding to the minimum KS statistics (best time-varying performance) and the maximum correlations between current profiles (best time-mean performance) for all infinite depth models run with the insitu shipboard winds.

We next examined how model time-mean and time varying skill varied as a function of viscosity. We identified viscosities corresponding to the maximum time-mean (highest correlation between observed and modelled mean current profiles) and time-varying skill (lowest KS statistic) for both the u and v components (Table 5.3). The ‘classical’ Ekman model and the Shear coupled model were almost indistinguishable. Both displayed peak time-varying skill in the u component at $0.005\text{m}^2\text{s}^{-1}$ and at $0.01\text{m}^2\text{s}^{-1}$ for the v component; in both cases the time-mean skill was maximized at a viscosity of $0.043\text{m}^2\text{s}^{-1}$ for both zonal and meridional components. The Stokes coupled model showed maximum time-varying and time-mean skill at larger viscosities.

The ‘classical’ Ekman and Shear coupled models were found to display higher time-mean and time-varying skill at the optimal viscosities identified in Table 5.3 than the shear coupled model. This could suggest that the Stokes drift coupled model is inferior to the ‘classical’ Ekman model and that the shear coupled model offers no significant advantage over the ‘classical’ Ekman model. However, we must be cautious about this result: we have only investigated coupling in a simple manner by employing modified surface boundary conditions (Cronin and Kessler, 2009, Polton et al., 2005) and we have assumed monochromatic wave forcing for the Stokes coupled model. Using alternate coupling schemes or resolving the full wave spectrum may result in the coupled models displaying better performance.

Finite depth Ekman models were found to display performance closely comparable to the infinite depth models discussed above.

b. EM-APEX Float data

All linear models forced with reanalysis winds interpolated onto the float tracks were found to display inferior time-varying skill compared to the 'classical' Ekman model forced with shipboard wind data. Time-mean model skill was, generally, comparable with the models forced with shipboard winds. PWP models forced with reanalysis winds and buoyancy forcing also displayed low time varying skill, but high time-mean skill, accounting for 81-98% of the variance in the mean Ekman current profile.

To clarify the cause of the difference in performance between the linear models forced with reanalysis winds interpolated onto the float tracks and the same set of models forced with *insitu* shipboard winds we examined the effects of model vertical resolution, the temporal resolution of the wind forcing fields and our choice of gridded wind datasets. The temporal resolution and the reduced spectral energy content from the use of reanalysis winds could explain some of the reduction in time-varying skill relative to models forced with *insitu* winds.

Chapter 6: Discussion and Conclusion

6.1 Summary

a. Detecting and Characterizing Ekman Spirals

The isolation, detection and characterization of Ekman currents are discussed in Chapter 3. Ekman currents were isolated by first filtering out inertial oscillations and then subtracting geostrophic currents. We considered both a constant geostrophic velocity and a constant geostrophic shear (i.e. a geostrophic velocity linearly changing with increasing depth) fitted using a Nelder-Mead simplex search. Ekman currents were then detected and characterized by applying a vectorial fit to current profiles using a simplex search and by applying least-squares fits to profiles of current heading and amplitude. Net Ekman transport was then computed, and profiles of mean viscosity amplitude were calculated using a stress-shear balance.

We found that the number of Ekman spirals, the mean Ekman decay scales, and the ratio between the rotational and amplitude decay scales were dependent on how the geostrophic currents were represented. We detected fewer velocity profiles displaying Ekman-like spirals in the constant geostrophic velocity case than in the constant geostrophic shear case. In the constant geostrophic velocity case the mean Ekman spiral was found to be “compressed” with an amplitude decay scale approximately half the rotational decay scale. In the geostrophic shear case this “compression” of the mean Ekman spiral was dramatically reduced.

We also examined the mean Ekman transport. In both the constant geostrophic velocity and constant geostrophic shear cases, mean Ekman transport was of the right magnitude but with a heading closer to the wind than expected from classical Ekman theory. This anomaly was found to result from a combination of errors in the CERSAT wind fields and inclusion of Stokes drift in the near surface flow into the Ekman velocity profiles. Correcting for these effects, by switching to the NCEP wind fields and removing Stokes drift from the current profiles, brought the observed transport into agreement with the theoretical predictions.

We examined potential links between stratification and the vertical structure of Ekman spirals by considering the relationships between Ekman decay scales and a variety of parameters associated with the strength (e.g. Buoyancy frequency and density differences) and depth (both Mixed layer and thermocline depth) of density stratification. We were unable to identify any significant relationship between stratification and Ekman decay scales. This remains a surprising result in light of the number of prior studies which invoke coupling between stratification and Ekman currents to explain “compressed” Ekman spirals.

b. Fitting Spectral Models

In Chapter 4 we examined our data in the frequency domain following a methodology developed by Elipot and Gille (2009a). Ageostrophic current and wind stress autospectra and the cross-spectrum were estimated using rotary spectral analysis. Using the observed wind autospectrum and wind-current crossspectrum we computed a transfer function at a constant depth level. We then used a Nelder-Mead simplex search to fit nine theoretical transfer functions derived from conceptual models of Ekman currents to the observed transfer function. We subsequently adapted Elipot and Gille’s (2009a) methodology to also allow fits at constant frequency and in a 2D sense (by both frequency and depth).

Fits between the nine models and the data from the EM-APEX float and shipboard ADCP datasets were obtained. Fits to the EM-APEX float data were inconclusive; we found large uncertainty in all parameters (viscosity, viscosity gradient and BLD) for all nine models. Fits to the ADCP data, on the other hand, produced more reliable and consistent results. Over both the 2D and 23.55m constant depth analyses we found the best model was a finite boundary layer depth constant viscosity model. Suitable boundary layer depths were of order 100m and viscosities of the order of $4 \times 10^{-2} \text{ m}^2 \text{ s}^{-1}$. Using this model we then computed the wind energy input into the Ekman layer. With the *insitu* winds we obtained wind energy input for this region of $45.5 \pm 0.4 \times 10^{-3} \text{ Wm}^{-2}$ using model parameters estimated from the constant depth fit, or $42.7 \pm 0.3 \times 10^{-3} \text{ Wm}^{-2}$ using

parameters from the 2D fit. These wind energy inputs are around 50% larger than previous estimates (Elipot and Gille, 2009b, Wunsch, 1998, Wang and Huang, 2004) for the Southern Ocean. If we instead used winds derived from the CERSAT blended reanalysis-satellite wind field wind energy input was lower, around $16 \times 10^{-3} \text{ Wm}^{-2}$. We have previously shown that several reanalysis or blended wind fields fail to reliably capture high amplitude wind stresses (e.g. Figure 5.13) and display lower spectral energy content (e.g. Figure 4.24) than *insitu* wind data. This suggests that the difference between our wind energy input estimates and those obtained in previous studies arises from our use of *insitu* shipboard winds compared to the use of reanalysis winds in both prior studies.

c. Testing Numerical Models

We tested a range of 1D numerical Ekman models in Chapter 5. We considered six linear Ekman models (infinite BLD and finite BLD, each combined with three variations on coupling: uncoupled; coupled with Stokes drift; and coupled with geostrophic shear in the boundary layer) and finally three Ekman models with density stratification and re-stratification in the mixed layer using the PWP mixing scheme. Linear Ekman models were run for both the float and shipboard datasets over a range of viscosities between $0.0025 \text{ m}^2 \text{ s}^{-1}$ and $0.447 \text{ m}^2 \text{ s}^{-1}$ while stratified models using the PWP mixing scheme were run for the float observations. Model time-varying performance was assessed by using a two-sample Kolmogorov-Smirnov test and quantile-quantile plots to compare the cumulative probability-density functions of the observations and model output at 24m depth. Time-mean performance was assessed by examining the correlation between the observed and modelled mean Ekman current profiles.

Analysis of the ADCP data demonstrated that models with Stokes-coupled Ekman physics had a lower performance compared to the uncoupled Ekman models. Shear coupled models were found to be virtually indistinguishable from the uncoupled Ekman model. The use of a finite BLD was found to have little impact on model performance. Ideal viscosities were $O(10^{-2} \text{ m}^2 \text{ s}^{-1})$.

Analysis of the EM-APEX float data was inconclusive. Model skill was generally lower than in the ADCP model runs. This was at least partially the result of using reanalysis winds, which failed to capture the full spectral energy content of the *insitu* winds. This limitation in turn prevented us from properly testing the stratified Ekman models with EM-APEX data.

6.2 Discussion and Conclusions

a. The Utility of EM-APEX Floats

This study has provided a test of the ability of EM-APEX floats to observe the upper ocean. Despite the floats not being able to sample all the way to the sea surface, we were able to isolate Ekman currents from the geostrophic flow and characterise the nature of Ekman spirals in the Southern Ocean.

b. The Vertical Structure of Ekman Currents

Mean eddy viscosities obtained from fits applied to Ekman current decay and rotation were found to range between 3.2×10^{-2} and $44.7 \times 10^{-2} \text{ m}^2 \text{ s}^{-1}$ (decay scales of 25m and 93m), values which are comparable with previous studies in the Southern Ocean for the surface mixed layer (Lenn and Chereskin, 2009). Assuming a constant geostrophic velocity, mean viscosities obtained from the rotational least squares fit were found to be significantly larger than those obtained from the current amplitude least squares fit, resulting in ‘compressed’ spirals. If we instead used a constant geostrophic shear this ‘compression’ was effectively eliminated.

Examination of mean viscosity magnitude profiles as a function of MLD-normalized depth was initially suggestive of either linear or exponential decay of viscosity with increasing depth. We applied linear and exponential fits to all depths between 0.3 and 3MLD. Estimates using data from only within the mixed layer and below 1MLD (i.e. extending into the ocean interior) suggested different behaviour within the mixed layer compared to the interior. However, when we considered the uncertainty around the fits, it became clear that these differences were not statistically

significant. Constant magnitude eddy viscosity was determined from the all-depth fits, and was found to lie between $1.14 \times 10^{-2} \text{m}^2 \text{s}^{-1}$ and $1.60 \times 10^{-2} \text{m}^2 \text{s}^{-1}$.

Constant depth, 2-D and near-inertial frequency spectral fits of conceptual models to the shipboard ADCP current observations revealed that a constant viscosity model with finite boundary layer was the most suitable, in line with previous studies (Elipot and Gille, 2009a). These fits gave viscosities of between $3.52 \times 10^{-2} \text{m}^2 \text{s}^{-1}$ and $4.83 \times 10^{-2} \text{m}^2 \text{s}^{-1}$ and boundary layer depths between 105m and 119m. Given the BLDs were 3-4 times deeper than the decay scales corresponding to the viscosities, the vertical structure of the finite depth Ekman models did differ greatly from an infinite depth model using the same viscosity.

We examined a set of numerical linear Ekman models. When models were forced with shipboard *insitu* winds and compared with ADCP velocity observations we found that an infinite depth constant viscosity model demonstrated the best performance. Viscosities corresponding to maximum model performance varied between $5 \times 10^{-3} \text{m}^2 \text{s}^{-1}$ and $4 \times 10^{-2} \text{m}^2 \text{s}^{-1}$.

This evidence indicates that the ‘classical’ constant viscosity Ekman model with a viscosity $O(10^{-2} \text{m}^2 \text{s}^{-1})$ provides an adequate and simple representation of the vertical structure of Ekman currents. Additionally, our results emphasise the need to properly resolve the vertical structure of geostrophic currents in order to isolate the ageostrophic Ekman velocities.

c. Ekman transport

Ekman currents were computed from the observed Ekman current profiles in Chapter 3. The expected mean transport per unit width (hereafter called transport) computed from the CERSAT blended satellite-reanalysis winds was $1.01 \pm 0.12 \text{m}^2 \text{s}^{-1}$. Using a constant geostrophic velocity to isolate Ekman currents we obtained a mean transport of $0.93 \pm 0.28 \text{m}^2 \text{s}^{-1}$ when integrated from 200m to 14m depth. Transport obtained when using a constant geostrophic shear was $1.18 \pm 0.34 \text{m}^2 \text{s}^{-1}$ at 14m depth. Hence, net transport is consistent in magnitude with Ekman theory.

However, in both cases the mean transport heading was found to be about 50° to the left of the wind, while Ekman theory implies steady state transport should be 90° to the left of the wind in the Southern Hemisphere. Upon examination of the geostrophic shear case we found that this downwind skewing could be a side-effect of our use of the CERSAT blended satellite-reanalysis winds, or the result of aliasing Stokes drift into the Ekman transport. Using NCEP/NCAR reanalysis winds and explicitly removing Stokes velocities brought the observed mean transport into agreement with theory.

We conclude that our results are consistent with both 'classical' Ekman theory and prior studies of Ekman transport (Chereskin, 1995, Chereskin and Roemmich, 1991, Ekman, 1905, Lenn and Chereskin, 2009).

d. The influence of Stratification

As discussed above, when we assumed a vertically-uniform geostrophic current the resulting Ekman spirals were found to be "compressed", and mean viscosities (and decay scales) obtained from the rotational least squares fit were found to be significantly larger than those obtained from the current amplitude least squares fit. This behaviour has been attributed to stratification in previous studies (Price and Sundermeyer, 1999, Price et al., 1987). However, when we instead assumed constant geostrophic shear this "compression" of the Ekman spirals reduced; mean decay scales were brought into agreement and the compression ratio computed on a profile by profile basis was reduced from 1:3 to 1:1.5. This result indicates that the "compressed" Ekman spirals arise as a result of vertical shear in the mixed layer and below. By removing the vertical shear in the ocean currents the classical Ekman problem is being linearised around a sheared state. Examination of the vertical shear removed when isolating Ekman currents indicated that it was statistically consistent with shear observed between the 100m and 200m depth levels (Figure 3.6); a depth at which flow should be principally geostrophic.

In both the constant geostrophic velocity and constant geostrophic shear cases, Ekman transport was found to be surface-intensified with the intensification of transport coinciding with the mixed layer depth. Superficially this result would support the notion that density stratification can act to “surface trap” Ekman currents. However, we find the association is largely coincidental. Mean Ekman decay scales and mixed layer depths are comparable in magnitude, and since Ekman currents decay exponentially with increasing depth, it is logical that current amplitude, and hence net transport, will be weak below the mixed layer.

We also examined the effects of stratification on Ekman currents by considering the relationships between Ekman decay scales and parameters associated with stratification such as buoyancy frequency, mixed layer depth, bulk Richardson number and the density difference between the mixed layer and interior. We only identified a statistically significant relationship between bulk Richardson number (a measure of mixed layer stability) and Ekman decay scales; even this relationship was relatively weak with correlations between 0.19 and 0.5.

Application of three models using the Price-Weller-Pinkel mixing scheme (Chapter 5), which explicitly links momentum mixing (and thus Ekman currents) with density stratification, to the EM-APEX float data proved inconclusive. Model performance was poor, but linear Ekman models applied to the float data displayed similar poor performance. This suggests the poor performance was not intrinsic to the PWP mixing scheme and instead likely arose from limitations of the wind forcing data.

We have demonstrated that the “compression” of Ekman spirals and the confinement of Ekman transport to the mixed layer can be explained in our data without directly invoking effects of density stratification. Examination of the relationships between Ekman decay scales and parameters associated with the depth and strength of stratification yielded few significant results. In addition, as discussed in Section 6.2b, we have demonstrated that the constant viscosity “classical” Ekman model provides an adequate representation of the observed Ekman currents. These lines of evidence

suggest that within the Southern Ocean, and possibly more generally, density stratification does not play a significant role in setting the structure of Ekman currents.

e. Coupling With Geostrophic Shear and Stokes Drift

The effect of coupling between Ekman currents and Stokes drift or geostrophic shear was examined in Chapter 5. Coupling to geostrophic shear was found to have little impact on the performance of model runs compared to the shipboard ADCP data, while coupling to Stokes drift resulted in significant degradation of model performance. This degradation is a surprising result in that we expected the inclusion of Stokes drift to improve model skill. However, these results must be treated with caution since we examined linear Ekman models coupled to the other processes using modified surface boundary conditions (Cronin and Kessler, 2009, Polton et al., 2005). The use of more complex coupling schemes (Heinloo and Toompuu, 2012, Lewis and Belcher, 2004) in a model may give different results. Additionally, due to the nature of the available forcing data, our treatment of Stokes drift was limited to treating the wave input as monochromatic.

f. Wind Data

Throughout this thesis we have encountered issues with reanalysis or blended wind datasets. In Chapter 3 we found that the choice of NCEP rather than CERSAT winds could, when combined with a correction for Stokes drift, explain the down-wind Ekman transport anomaly. In Chapter 4 we observed that the choice of *insitu* shipboard winds over blended reanalysis-scatterometer winds resulted in an increase of around 50% in estimates of wind energy input into the Ekman layer. In Chapter 5 we observed significantly poorer performance in models forced with the CERSAT winds interpolated onto the float track than the same models forced with the *insitu* shipboard winds. These results suggest that the quality of wind data is a limiting factor in understanding near-surface ocean dynamics. This in turn implies a need to improve the temporal resolution of gridded wind data and a need to improve methods of computing wind-stress.

6.3 Further Work

a. Unresolved Questions and Limitations

This study has focused on a relatively limited geographic area. This raises the question of whether our results are applicable on a larger scale, both within the ACC and in other oceans. Our results from examination of the EM-APEX float data are closely comparable with previous studies in the Drake Passage region (Lenn and Chereskin, 2009, Polton et al., 2013). The Kerguelen Island and Drake Passage region are areas of significant topographic intrusion into the ACC with resulting strong eddy activity, which in turn affects the geostrophic currents. This correlation of topography and experimental design is a direct aspect of the design of the SOFINE experiment. The SOFINE experiment was specifically designed to examine the role of topographically generated lee waves and their effect on internal mixing. This strong topography is a significant difference to other regions of the ACC (e.g. the Pacific sector of the Southern Ocean) and large areas of other oceans. This suggests more study is needed to determine the representativeness of the Kerguelen-region and Drake Passage (Lenn and Chereskin, 2009, Polton et al., 2013) results. Options for validating our findings in other regions are discussed below.

We have established that a constant-depth eddy viscosity is the most appropriate parameterization of the vertical structure of Ekman currents. However, we have not examined the effect of a constant-depth but time-varying eddy viscosity on the linear Ekman models. While we have examined the variability of eddy viscosity as a function of some environmental variables (surface wave properties and stratification), we have not examined how eddy viscosity varies with other environmental variables such as sea surface height; surface temperature or internal waves.

The numerical models we have employed in this study have a number of limitations. All models were 1D, which meant we neglected the effects of inertial waves and transient Ekman flows that are generated remotely and propagate into the local region. It is not clear how important these non-local effects are, and what spatial and temporal scales are needed to include these effects. There is evidence that these non-local influences are relevant because the lagged autocorrelation for

the observed data decays much faster than the lagged autocorrelation for the models, plausibly indicating there are oceanographic influences outside the *insitu* winds and surface buoyancy forcing. Additionally, we primarily considered linear models; it is possible that Ekman models resolving non-linear effects would display different responses (Hart, 1996, Tan et al., 2006, Bennetts and Hocking, 1973). Finally, in line with other studies (Cronin and Kessler, 2009, Polton et al., 2005) we have treated coupling in a simple manner using modified surface boundary conditions; more sophisticated representations of coupling between the Stokes drift and the flow field (Lewis and Belcher, 2004, Heinloo and Toompuu, 2012) may result in more realistic flow fields.

c. Further Observational Studies

To address these undetermined questions above, we consider that more observational studies are necessary. We suggest three observation strategies that would resolve some of the questions posed above: repeat EM-APEX float deployments in other regions of the ocean; deployment of free drifting spar buoys, and the deployment of a mooring or mooring array.

A repeat EM-APEX float deployment would provide a relatively simple means of testing whether the “classical” Ekman model applies in other more quiescent regions of the ocean. If focussed primarily on the upper ocean we would be able to configure the floats to profile more rapidly than in this study, providing increased temporal resolution, ideal for the application of spectral fitting. However, as with this study, a repeat EM-APEX deployment would be constrained by the lack of *insitu* winds and would force the use of reanalysis or satellite winds, which we have found to be inadequate for examining the development of Ekman currents. One possibility we have not explored in this thesis is the use of EM-APEX floats to observe wave parameters (Sanford et al., 2011). This would enable us to examine coupling between Ekman currents and Stokes drift in a more explicit fashion.

An alternate approach would be to deploy a number of free-drifting spar buoys with T and S sensors and current meters suspended beneath the buoy in a setup similar to that used by Pollard

and Thomas (1989). This arrangement would provide us with much finer temporal resolution and many of the advantages of the EM-APEX floats with the addition of having *insitu* meteorological data. It may also be possible (Pascal et al., 2010) to use the spar buoys to obtain concurrent wave data. However, the use of a spar buoy would require reduced vertical resolution. Preparation, deployment and retrieval of free drifting spar buoys are likely to be a much more complex, expensive and risky process than a repeat deployment of EM-APEX floats.

Finally, we could consider deploying an array of moorings. Moorings offer most of the advantages of the free-drifting spar-buoys but at the cost of reduced geographic coverage. Mooring designs that include surface meteorological sensors and closely spaced current meters through the upper 200m of the ocean would allow detailed examination of inertial and Ekman currents. The RAMA, TOGA/TAO and PIRATA moorings (Hayes et al., 1991, McPhaden et al., 2009, McPhaden et al., 2010) deployed in the Indian, Atlantic and Pacific Oceans follow this approach. In the numerical modelling phase of this study we have assumed inertial currents are only locally generated, where as in reality our observational data would also include remotely generated inertial currents that have subsequently propagated with the mean flow. A dataset from a properly designed mooring array that resolved non-local inertial oscillations well would allow us to more effectively identify and remove inertial currents, thereby reducing the uncertainty we see in our estimates of Ekman current profiles and mean transport.

In general, repeat deployments of EM-APEX floats would offer an opportunity to confirm our results in another region of the ocean and enhance the spectral view of Ekman currents. However, the data would remain constrained by the lack of *insitu* wind and surface flux data. Meanwhile, the use of free drifting spar buoys or an array of moorings would offer more opportunity to expand our understanding of Ekman currents but are likely to be much more expensive and more risky.

d. Further Modelling Studies

There is substantial opportunity for additional modelling work in the field of Ekman currents. We have thus far taken a fairly simple approach, confining ourselves to considering 1D linear models with a simplistic coupling scheme.

A first improvement beyond our modelling work would be to consider a regional model of Ekman currents forced with reanalysis winds. We could then select profiles along the ship and float tracks for analysis instead of treating the shipboard and float velocity observations as stationary timeseries.

The second major improvement would be to consider coupling in a more complex manner. We have been following two studies (Cronin and Kessler, 2009, Polton et al., 2005) that suggest a simple modification to the surface boundary condition should capture the effects of coupling of Ekman currents to geostrophic shear or Stokes drift. Other studies (Heinloo and Toompuu, 2012, Lewis and Belcher, 2004), however, have suggested more sophisticated means of representing coupling between Ekman currents and Stokes drift. It is possible that these other models of Ekman-Stokes coupling may result in different behaviour throughout the water column instead of just a modified 'effective' surface stress.

Bibliography:

- AMANTE, C. & EAKINS, B. W. 2009. ETOPO1 1 Arc-Minute Global Relief Model: Procedures, Data Sources and Analysis. *NOAA Technical Memorandum NESDIS NGDC-24*.
- BELKIN, I. M. & GORDON, A. L. 1996. Southern Ocean fronts from the Greenwich meridian to Tasmania. *Journal Of Geophysical Research*, 101, 3675-3696.
- BENDAT, J. S. & PERSOL, A. G. 1986. *Random data. Analysis and measurements procedures*, John Wiley & Sons.
- BENNETTS, D. & HOCKING, L. 1973. On nonlinear Ekman and Stewartson layers in a rotating fluid. *Proceedings of the Royal Society of London. A. Mathematical and Physical Sciences*, 333, 469-489.
- BENTAMY, A., CROIZE-FILLON, D., QUEFFEULOU, P., LIU, C. & ROQUET, H. 2009. Evaluation of high-resolution surface wind products at global and regional scales. *Journal of Operational Oceanography*, 2, 15-27.
- CEROVEČKI, I., TALLEY, L. D. & MAZLOFF, M. R. 2011. A Comparison of Southern Ocean Air–Sea Buoyancy Flux from an Ocean State Estimate with Five Other Products. *Journal of Climate*, 24, 6283-6306.
- CHAUDHURI, A. H., PONTE, R. M., FORGET, G. & HEIMBACH, P. 2012. A Comparison of Atmospheric Reanalysis Surface Products over the Ocean and Implications for Uncertainties in Air–Sea Boundary Forcing. *Journal of Climate*, 26, 153-170.
- CHERESKIN, T. K. 1995. Direct evidence for an Ekman balance in the California Current. *Journal Of Geophysical Research*, 100, 18261-18269.
- CHERESKIN, T. K. & PRICE, J. F. 2001. Ekman transport and pumping. *In: STEELE, J., THORPE, S. & TUREKIAN, K. (eds.) Encyclopedia of Ocean Sciences*. Academic Press.
- CHERESKIN, T. K. & ROEMMICH, D. 1991. A Comparison of Measured and Wind-derived Ekman Transport at 11°N in the Atlantic Ocean. *Journal Of Physical Oceanography*, 21, 869-878.
- CRONIN, M. F. & KESSLER, W. S. 2009. Near-Surface Shear Flow in the Tropical Pacific Cold Tongue Front. *Journal Of Physical Oceanography*, 39, 1200-1215.
- DAMERELL, G. M., HEYWOOD, K. J. & STEVENS, D. P. 2013. Direct observations of the Antarctic circumpolar current transport on the northern flank of the Kerguelen Plateau. *Journal of Geophysical Research: Oceans*, 118, 1333-1348.
- DAVIS, R. E., DESZOEKE, R., HALPERN, D. & NILLER, P. 1981a. Variability in the upper ocean during MILE, Part I: The heat and momentum balances. *Deep-sea research*, 28A, 1427-1451.
- DAVIS, R. E., DESZOEKE, R., HALPERN, D. & NILLER, P. 1981b. Variability in the upper ocean during MILE, Part II: Modelling the mixed layer response. *Deep-sea research*, 28A, 1453-1475.
- DE SZOEKE, R. & LEVINE, H. 1981. The advective flux of heat by mean geostrophic motions in the Southern Ocean. *Deep Sea Research I*, 28, 1057-1085.
- DIBARBOURE, G., LAURET, O., MERTZ, F., ROSMORDUC, V. & MAHEU, C. 2008. SSALTO/DUACS User Handbook: (M)SLA and (M)ADT Near-Real Time and Delayed Time Products.
- DONELAN, M. A., DOBSON, F. W., SMITH, S. D. & ANDERSON, R. J. 1993. On the Dependence of Sea Surface Roughness on Wave Development. *Journal Of Physical Oceanography*, 23, 2143-2149.
- EGBERT, G. D. & EROFEEVA, S. Y. 2002. Efficient Inverse Modeling of Barotropic Ocean Tides. *Journal of Atmospheric and Oceanic Technology*, 19, 183-204.
- EKMAN, V. W. 1905. On the Influence of the Earth's Rotation on Ocean Currents. *Ark. Mat. Astron. Fys.*, 2, 1-52.
- ELIPOT, S. 2006. *Spectral characterization of Ekman velocities in the Southern Ocean based on surface drifter trajectories*. PhD, University of California.
- ELIPOT, S. & GILLE, S. T. 2009a. Ekman layers in the Southern Ocean: spectral models and observations, vertical viscosity and boundary layer depth. *Ocean Science*, 5, 115-139.

- ELIPOT, S. & GILLE, S. T. 2009b. Estimates of wind energy input to the Ekman layer in the Southern Ocean from surface drifter data. *Journal Of Geophysical Research*, 114, C06003.
- FAIRALL, C. W., GRACHEV, A. A., BEDARD, A. J. & NISHIYAMA, R. T. 1996. Wind, wave, stress, and surface roughness relationships from turbulence measurements made on R/P FLIP in the SCOPE experiment. *NOAA Tech. Memo. ERL ETL-268*. Boulder, Colorado.
- GNANADESIKAN, A. & WELLER, R. A. 1995. Structure and Instability of the Ekman Spiral in the Presence of Surface Gravity Waves. *Journal Of Physical Oceanography*, 25, 3148-3171.
- GORDON, A. L. 2001. Interocean Exchange. In: SIEDLER, G., CHURCH, J. & GOULD, J. (eds.) *Ocean Circulation And Climate*. Academic Press.
- GOULD, J. 2002. *A brief history of float developments* [Online]. Available: <http://www.noc.soton.ac.uk/JRD/HYDRO/argo/history.php> [Accessed 18 September 2011].
- GOULD, J. 2006. *Argo, an array of profiling floats observing the ocean in realtime* [Online]. Available: http://w3.jcommops.org/FTPRoot/Argo/Doc/Argo_new_brochure.pdf [Accessed 20 September 2011].
- HALPERN, D. 1974. Observations of the Deepening of the Wind-Mixed Layer in the Northeast Pacific Ocean. *Journal Of Physical Oceanography*, 4, 454-466.
- HANAWA, K. & TALLEY, L. D. 2001. Mode Waters. In: SIEDLER, G., CHURCH, J. & GOULD, J. (eds.) *Ocean Circulation And Climate*. Academic Press.
- HARRIS, F. J. 1978. On the use of windows for harmonic analysis with the discrete fourier transform. *Proceedings of the IEEE*, 66.
- HART, J. E. 1996. On Nonlinear Ekman Surface-Layer Pumping. *Journal of Physical Oceanography*, 26, 1370-1374.
- HASSELMANN, K. 1970. Wave-driven inertial oscillations. *Geophysical Fluid Dynamics*, 1, 463-502.
- HAYES, S. P., MANGUM, L. J., PICAUT, J., SUMI, A. & TAKEUCHI, K. 1991. TOGA-TAO: A Moored Array for Real-time Measurements in the Tropical Pacific Ocean. *Bulletin of the American Meteorological Society*, 72, 339-347.
- HEINLOO, J. & TOOMPUU, A. 2012. A modification of the classical Ekman model accounting for the Stokes drift and stratification effects. *Environmental Fluid Mechanics*, 12, 101-113.
- HESELBERG, T. 1954. The Ekman Spirals. *Meteorology and Atmospheric Physics*, 7, 329-343.
- HUGHES, C. W. & ASH, E. R. 2001. Eddy forcing of the mean flow in the Southern Ocean. *Journal Of Geophysical Research*, 106, 2713-2722.
- HUNKINS, K. 1966. Ekman drift currents in the Arctic Ocean. *Deep Sea Research*, 13, 607-620.
- JOHNSON, H. K., HØJSTRUP, J., VESTED, H. J. & LARSEN, S. E. 1998. On the Dependence of Sea Surface Roughness on Wind Waves. *Journal Of Physical Oceanography*, 28, 1702-1716.
- KRAUSS 1993. Ekman Drift in Homogeneous Water. *Journal Of Physical Oceanography*, 98, 20187-20209.
- LAGERLOEF, G. S., MITCHUM, G. T., LUKAS, R. B. & NIILER, P. P. 1999. Tropical Pacific near-surface currents estimated from altimeter, wind, and drifter data. *Journal of Geophysical Research-Oceans*, 104, 23313.
- LEBEDEV, K. V., YOSHINARI, H., MAXIMENKO, N. A. & HACKER, P. W. 2007. YoMaHa'07: Velocity data assessed from trajectories of Argo floats at parking level and at the sea surface. *IPRC Technical Notes*.
- LENN, Y. & CHERESKIN, T. K. 2009. Observation of Ekman Currents in the Southern Ocean. *Journal Of Physical Oceanography*, 39, 768-779.
- LEWIS, D. M. & BELCHER, S. E. 2004. Time-dependent, coupled, Ekman boundary layer solutions incorporating Stokes drift. *Dynamics of Atmospheres and Oceans*, 37, 313-351.
- LIU, Y., WEISBERG, R. H. & SHAY, L. K. 2007. Current Patterns on the West Florida Shelf from Joint Self-Organizing Map Analyses of HF Radar and ACDP Data. *Journal of Atmospheric and Oceanic Technology*, 24.
- MADSEN, O. S. 1977. A Realistic Model of the Wind-Induced Ekman Boundary Layer. *Journal Of Physical Oceanography*, 7, 248-255.

- MASSEY, F. J. 1951. The Kolmogorov-Smirnov Test for Goodness of Fit. *Journal of the American Statistical Association*, 46, 11-121.
- MCNALLY, G. J. 1981. Satellite-Tracked Drift Bouy observations of the Near Surface Flow in the Eastern Mid-Latitude North Pacific. *Journal Of Geophysical Research*, 86, 8022-8030.
- MCNALLY, G. J. & WHITE, W. B. 1985. Wind Driven Flow in the Mixed Layer Observed by Drifting Bouys during Autumn-Winter in the Midlatitude North Pacific. *Journal Of Physical Oceanography*, 15, 684-694.
- MCPHADEN, M. J., ANDO, K., BOURLES, B., FREITAG, H., LUMPKIN, R., MASUMOTO, Y., MURTY, V., NOBRE, P., RAVICHANDRAN, M. & VIALARD, J. 2010. The global tropical moored buoy array. *Proceedings of OceanObs*, 9.
- MCPHADEN, M. J., MEYERS, G., ANDO, K., MASUMOTO, Y., MURTY, V. S. N., RAVICHANDRAN, M., SYAMSUDIN, F., VIALARD, J., YU, L. & YU, W. 2009. RAMA: The Research Moored Array for African-Asian-Australian Monsoon Analysis and Prediction*. *Bulletin of the American Meteorological Society*, 90, 459-480.
- MEIJERS, A. J. S., BINDOFF, N. L. & RINTOUL, S. R. 2011a. Estimating the 4-dimensional structure of the Southern Ocean using satellite altimetry. *Journal of Atmospheric and Oceanic Technology*, 548-568.
- MEIJERS, A. J. S., BINDOFF, N. L. & RINTOUL, S. R. 2011b. Frontal movements and property fluxes: Contributions to heat and freshwater trends in the Southern Ocean. *Journal of Geophysical Research: Oceans* 116, C08024.
- NAVEIRA GARABATO, A., BINDOFF, N. L., PHILLIPS, H. E., POLZIN, K. L., SLOYAN, B., STEVENS, D. & WATERMAN, S. 2009. RRS James Cook Cruise 29, 01 Nov - 22 Dec 2008. SOFine Cruise Report: Southern Ocean *Cruise Report 35*. Southampton: National Oceanography Centre.
- NELDER, J. A. & MEAD, R. 1965. A simplex method for function minimization. *The computer journal*, 7, 308-313.
- NELDER, J. A. & WEDDERBURN, R. W. 1972. Generalized linear models. *Journal of the Royal Statistical Society. Series A (General)*, 370-384.
- ORSI, A. H., WHITWORTH, T. & NOWLIN, W. D. 1995. On the meridional extent and the fronts of the Antarctic Circumpolar Current. *Deep Sea Research I*, 42, 641-673.
- PARK, Y.-H., ROQUES, F., DURAND, I. & FUDA, J.-L. 2008. Large-scale circulation over and around the Northern Kerguelen Plateau. *Deep Sea Research II*, 55, 566-581.
- PASCAL, R. W., YELLAND, M. J., SROKOSZ, M. A., MOAT, B. I., WAUGH, E. M., COMBEN, D. H., CANSDALE, A. G., HARTMAN, M. C., COLES, D. G. H., CHANG HSUEH, P. & LEIGHTON, T. G. 2010. A Spar Buoy for High-Frequency Wave Measurements and Detection of Wave Breaking in the Open Ocean. *Journal of Atmospheric and Oceanic Technology*, 28, 590-605.
- PERRIE, W., TANG, C. L., HU, Y. & DETRACY, B. M. 2003. The Impact of Waves on Surface Currents. *Journal Of Physical Oceanography*, 33, 2126-2140.
- PERSSON, A. 2011. User guide to ECMWF forecast products. European Centre for Medium-Range Weather Forecasts.
- PHILLIPS, H. E. & BINDOFF, N. L. 2014. On the non-Equivalent Barotropic structure of the Antarctic Circumpolar Current: An observational perspective. *Journal Of Geophysical Research*, In Press.
- PHILLIPS, H. E. & RINTOUL, S. R. 2000. Eddy Variability and Energetics from Direct Current Measurements in the Antarctic Circumpolar Current south of Australia. *Journal Of Physical Oceanography*, 30, 3050-3076.
- POLLARD, R. T. & THOMAS, K. J. H. 1989. Vertical Circulation Revealed by Diurnal Heating of the Upper Ocean in Late Winter: Part I: Observations. *Journal Of Physical Oceanography*, 19, 269-278.
- POLTON, J. A., LENN, Y., ELIPOT, S. C., T.K. & SPRINTALL, J. 2013. Can Drake Passage Observations Match Ekman's Classic Theory. *Journal Of Physical Oceanography*, 43, 1733-1740.

- POLTON, J. A., LEWIS, D. M. & BELCHER, S. E. 2005. The Role of Wave-Induced Coriolis Stokes Forcing on the Wind-Driven Mixed Layer. *Journal Of Physical Oceanography*, 35, 444-457.
- PRANDTL, L. 1952. *Essentials of fluid dynamics: with applications to hydraulics, aeronautics, meteorology and other subjects.*, Blackie.
- PRICE, J. F. 1999. upperEk.
- PRICE, J. F. & SUNDERMEYER, M. A. 1999. Stratified Ekman Layers. *Journal Of Geophysical Research*, 104, 20467-20494.
- PRICE, J. F., WELLER, R. A. & PINKEL, R. 1986. Diurnal Cycling: Observations and Models of the Upper Ocean Response to Diurnal Heating, Cooling and Wind Mixing. *Journal Of Geophysical Research*, 91, 8411-8427.
- PRICE, J. F., WELLER, R. A. & SCHUDLICH, R. R. 1987. Wind-Driven Ocean Currents and Ekman Transport. *Science*, 238, 1534-1538.
- REYNOLDS, R. W., SMITH, T. M., LIU, C., CHELTON, D. B., CASEY, K. S. & SCHLAX, M. G. 2007. Daily high-resolution-blended analyses for sea surface temperature. *Journal of Climate*, 20, 5473-5496.
- RINTOUL, S. R., HUGHES, C. W. & OLBERS, D. 2001. The Antarctic Circumpolar Current System. In: SIEDLER, G., CHURCH, J. & GOULD, J. (eds.) *Ocean Circulation And Climate*. Academic Press.
- ROEMMICH, D., BOEBEL, O., FREELAND, H., KING, B. A., LETRAON, P., MOLINARI, R., OWENS, W. B., RISER, S. C., SEND, U., TAKEUCHI, K. & WIJFFELS, S. 1998. *On The Design and Implementation of Argo: A Global Array of Profiling Floats* [Online]. Available: http://w3.jcommops.org/FTPRoot/Argo/Doc/Argo_Design.pdf [Accessed 17 September 2011].
- ROHATGI, V. K. & EHSANES SALEH, A. K. M. 1976. *An Introduction to Probability and Statistics*, New York, John Wiley & Sons.
- RUDNICK, D. L. 2003. Observation of Momentum Transfer in the Upper Ocean: Did Ekman Get It Right? In: MULLER, P. & HENDERSON, D. (eds.) *Near-Boundary Processes and their Parameterization*.
- RUDNICK, D. L. & WELLER, R. A. 1993. Observations of Superinertial and Near-Inertial Wind-driven Flow. *Journal Of Physical Oceanography*, 23, 2351-2359.
- SALLÉE, J.-B., WIENDERS, N., SPEER, K. & MORROW, R. 2006. Formation of subantarctic mode water in the southeastern Indian Ocean. *Ocean Dynamics*, 56, 525-542.
- SANFORD, T. B., DUNLAP, J. H., CARLSON, J. A., WEBB, D. C. & GIRTON, J. B. 2005. Autonomous velocity and density profiler: EM-APEX. *IEEE/OES Eighth Working Conference on Current Measurement Technology*. University of Southampton: IEEE.
- SANFORD, T. B., PRICE, J. F. & GIRTON, J. B. 2011. Upper-Ocean Response to Hurricane Frances (2004) Observed by Profiling EM-APEX Floats. *Journal Of Physical Oceanography*, 41, 1041-1056.
- SCHUDLICH, R. R. & PRICE, J. F. 1998. Observations of Seasonal Variation in the Ekman Layer. *Journal Of Physical Oceanography*, 28, 1187-1204.
- SMITH, W. H. F. & SANDWELL, D. T. 1997. Global seafloor topography from satellite and ship depth soundings. *Science*, 277, 1957-1962.
- SOKOLOV, S. & RINTOUL, S. R. 2007. Multiple Jets of The Antarctic Circumpolar Current South of Australia. *Journal Of Physical Oceanography*, 27, 1394-1412.
- SOKOLOV, S. & RINTOUL, S. R. 2009. Circumpolar structure and distribution of the Antarctic Circumpolar Current fronts: 1. Mean circumpolar paths. *Journal of Geophysical Research: Oceans*, 114, C11018.
- SPEER, K., RINTOUL, S. R. & SLOYAN, B. 2000. The Diabatic Deacon Cell. *Journal Of Physical Oceanography*, 30, 3212-3222.
- STEWART, R. H. 1997. *Introduction To Physical Oceanography* [Online]. Available: http://oceanworld.tamu.edu/resources/ocng_textbook/contents.html [Accessed 15 September 2011].

- SUTHERLAND, B. R. 2010. *Internal Gravity Waves*, Cambridge University Press.
- TAN, Z., FANG, J. & WU, R. 2006. Nonlinear Ekman layer theories and their applications. *ACTA METEOROLOGICA SINICA-ENGLISH EDITION*-, 20, 209.
- THOMAS, J. H. 1975. A Theory of Steady State Wind-Driven Currents in Shallow Water with Variable Eddy Viscosity. *Journal Of Physical Oceanography*, 5, 136-142.
- WALLCRAFT, A., CARROLL, S. N. & RUSHLING, K. V. 2003. *Hybrid Coordinate Ocean Model (HYCOM) Version 2.1: User's Guide* [Online]. Available: http://hycom.org/attachments/063_hycom_users_guide.pdf.
- WAMDI GROUP 1988. The WAM model-a third generation ocean wave prediction model. *Journal Of Physical Oceanography*, 18, 1775-1810.
- WANG, W. & HUANG, R. X. 2004. Wind Energy Input to the Ekman Layer. *Journal Of Physical Oceanography*, 34, 1267-1275.
- WARREN, B. A. & WUNSCH, C. (eds.) 1981. *Evolution Of Physical Oceanography*, Cambridge, Mass.: The MIT Press.
- WATERMAN, S., NAVEIRA GARABATO, A. C. & POLZIN, K. L. 2012. Internal Waves and Turbulence in the Antarctic Circumpolar Current. *Journal Of Physical Oceanography*, 43, 259-282.
- WELCH, P. D. 1967. The Use of Fast Fourier Transform for Estimation of Power Spectra: A Method Based on Time Averaging Over Short, Modified Periodograms. *IEEE Transactions on Audio Electroacoustics*, 15, 70-73.
- WELLER, R. A. 1981. Observation of the Velocity Response to Wind Forcing in the Upper Ocean. *Journal Of Geophysical Research*, 86, 1969-1977.
- WIJFFELS, S., FIRING, E. & BRYDEN, H. 1994. Direct Observation of the Ekman Balance at 10°N in the Pacific. *Journal Of Physical Oceanography*, 24, 1666-1679.
- WILK, M. B. & GNANADESIKAN, R. 1968. Probability Plotting Methods for the Analysis of Data. *Biometrika*, 55, 1-17.
- WUNSCH, C. 1998. The Work Done by the Wind on the Oceanic General Circulation. *Journal Of Physical Oceanography*, 28, 2332-2340.
- YELLAND, M. & TAYLOR, P. K. 1996. Wind stress measurements from the open ocean. *Journal Of Physical Oceanography*, 26, 541-558.
- YOSHIKAWA, Y., ENDOH, T., MATSUNO, T., WAGAWA, T., TSUTSUMI, T., YOSHIMURA, H. & MORII, Y. 2010. Turbulent bottom Ekman boundary layer measured over a continental shelf. *Geophysical Research Letters*, 37.
- ZHANG, H., REYNOLDS, R. W. & BATES, J. J. 2006. Blended and Gridded High Resolution Global Sea Surface Wind Speed and Climatology from Multiple Satellites: 1987 - Present. *American Meteorological Society 2006 Annual Meeting*. Atlanta, GA,.

Appendix 1: Supplementary Material For Chapter 3

1. Temperature and Salinity Plots

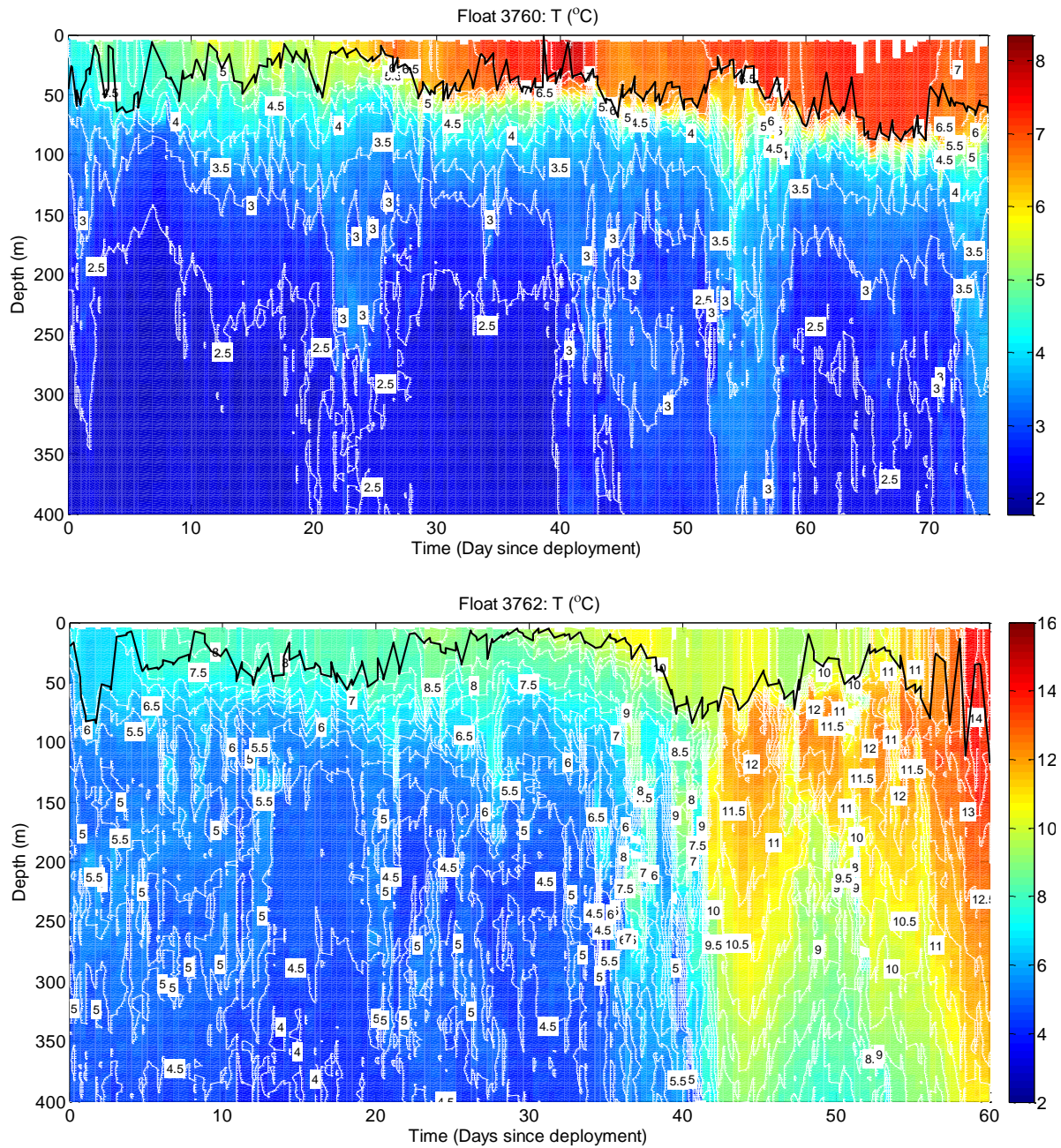


Figure A1.1: Temperature (°C) as a function of depth and time from floats 3760 (top) and 3762 (bottom). White contours indicate regular 0.5°C intervals. The black line marks the mixed layer depth using a density criterion of $\Delta\sigma < 0.03 \text{ kg m}^{-3}$ relative to the upper-most observation (Sallée et al., 2006).

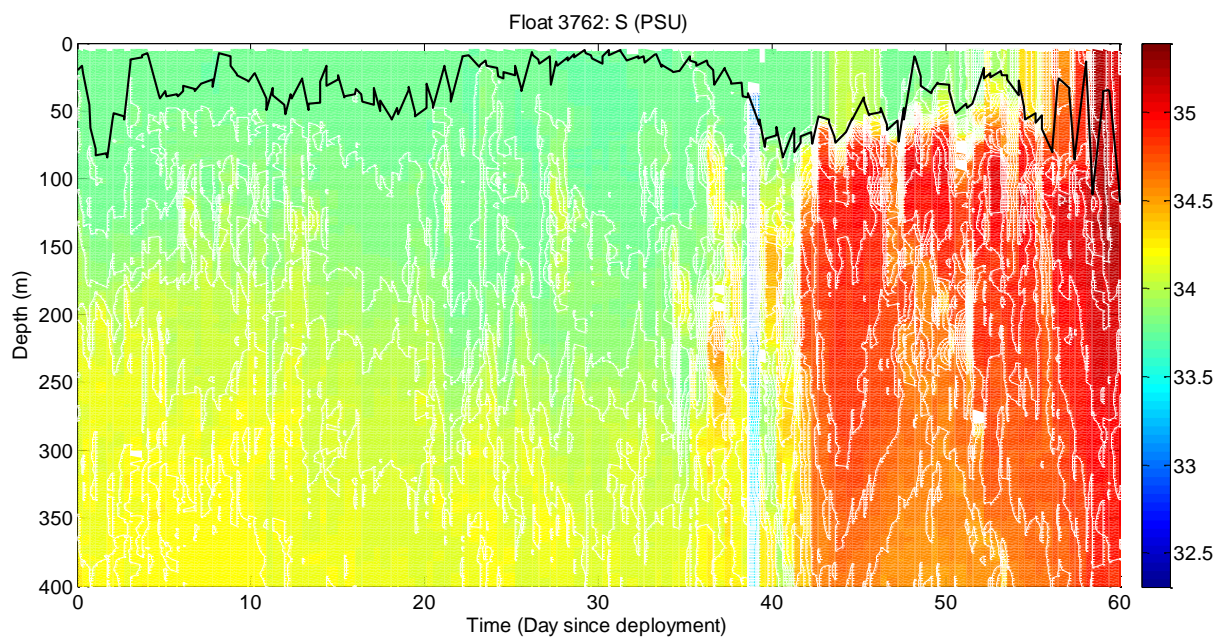
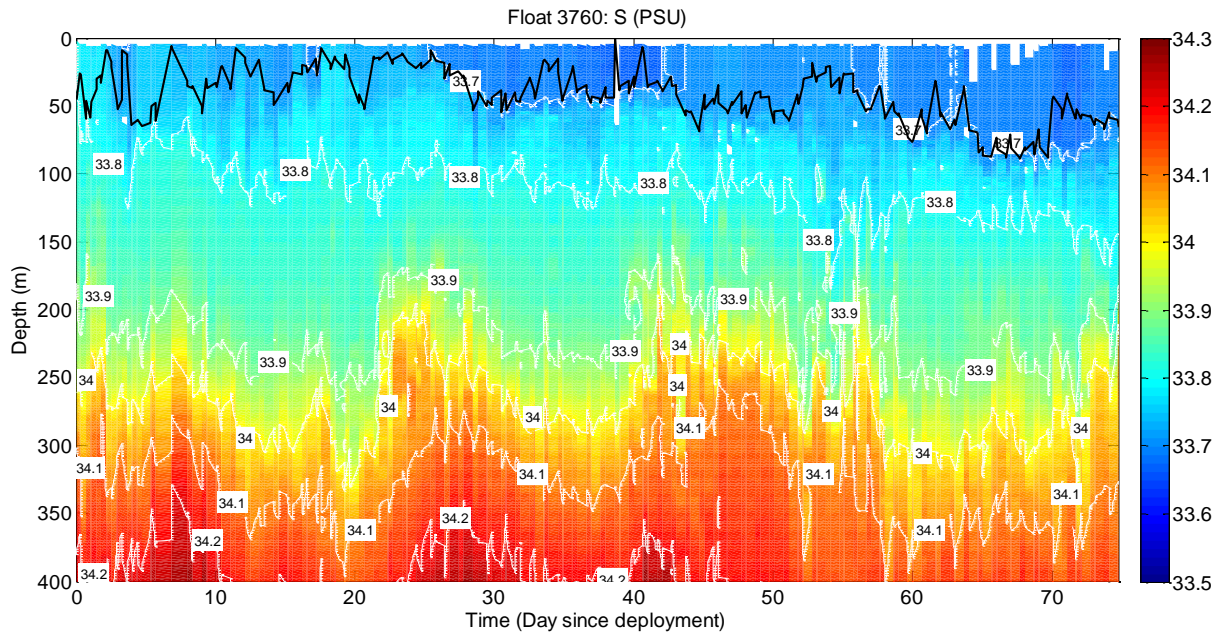


Figure A1.2: Salinity (PSU) as a function of depth and time from floats 3760 (top) and 3762 (bottom). White contours indicate regular 0.1 PSU intervals. The black line marks the mixed layer depth using a density criterion of $\Delta\sigma_t < 0.03 \text{ kg m}^{-3}$ relative to the upper-most observation (Sallée et al., 2006).

2. Wave Parameters and Ekman Decay Scales

Scatter plots of Ekman decay scales as a function of wave period and wave height are shown in Figure A1.3. Examination of the scatter plots indicate that the relationships between Ekman scales and wave parameters are poorly defined. Correlations between wave parameters and D_e or $\log_{10}(D_e)$ are given in Table A1.1. All correlations were weak and few were statistically significant at the 95% level.

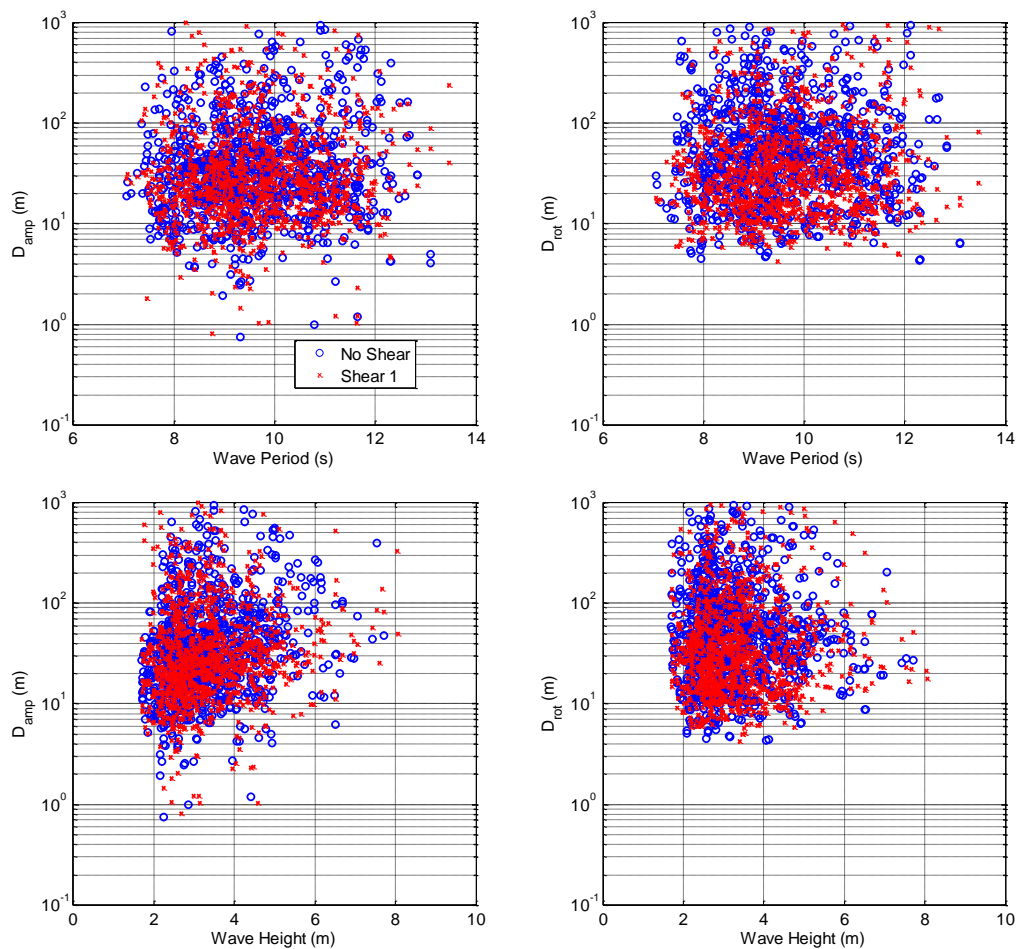


Figure A1.3: Scatter plots of Ekman decay scales (D_{amp} , left; D_{rot} , right) as a function of wave period (top) and wave height (bottom). Blue circles indicate the “No Shear” case while red xs indicate the “Shear 1” case.

<u>Correlations: D_e</u>				
	No Shear		Shear	
	D_{amp}	D_{rot}	D_{amp}	D_{rot}
Wave Height (m)	*0.159	-0.044	0.027	0.025
Wave Period (s)	*0.121	0.052	0.019	*0.087
<u>Correlations: $\log_{10}(D_e)$</u>				
	No Shear		Shear	
	D_{amp}	D_{rot}	D_{amp}	D_{rot}
Wave Height (m)	*0.238	-0.039	*0.126	0.0299
Wave Period (s)	*0.085	0.049	0.049	0.052

Table A1.1: Correlations between wave parameters and Ekman decay scales and correlations for fits between wave parameters and the magnitude (\log_{10}) of Ekman decay scales. * denotes a correlation significant at the 95% level.

3. Stratification and Ekman Decay Scales

Example scatter plots of Ekman decay scales against mixed layer and thermocline depths are shown in Figure A1.4. Likewise, Ekman decay scales are plotted against peak N^2 and bulk N^2 in Figure A1.5. These figures suggest that any relationships between the Ekman decay scales and parameters measuring the strength or depth of stratification are poorly defined.

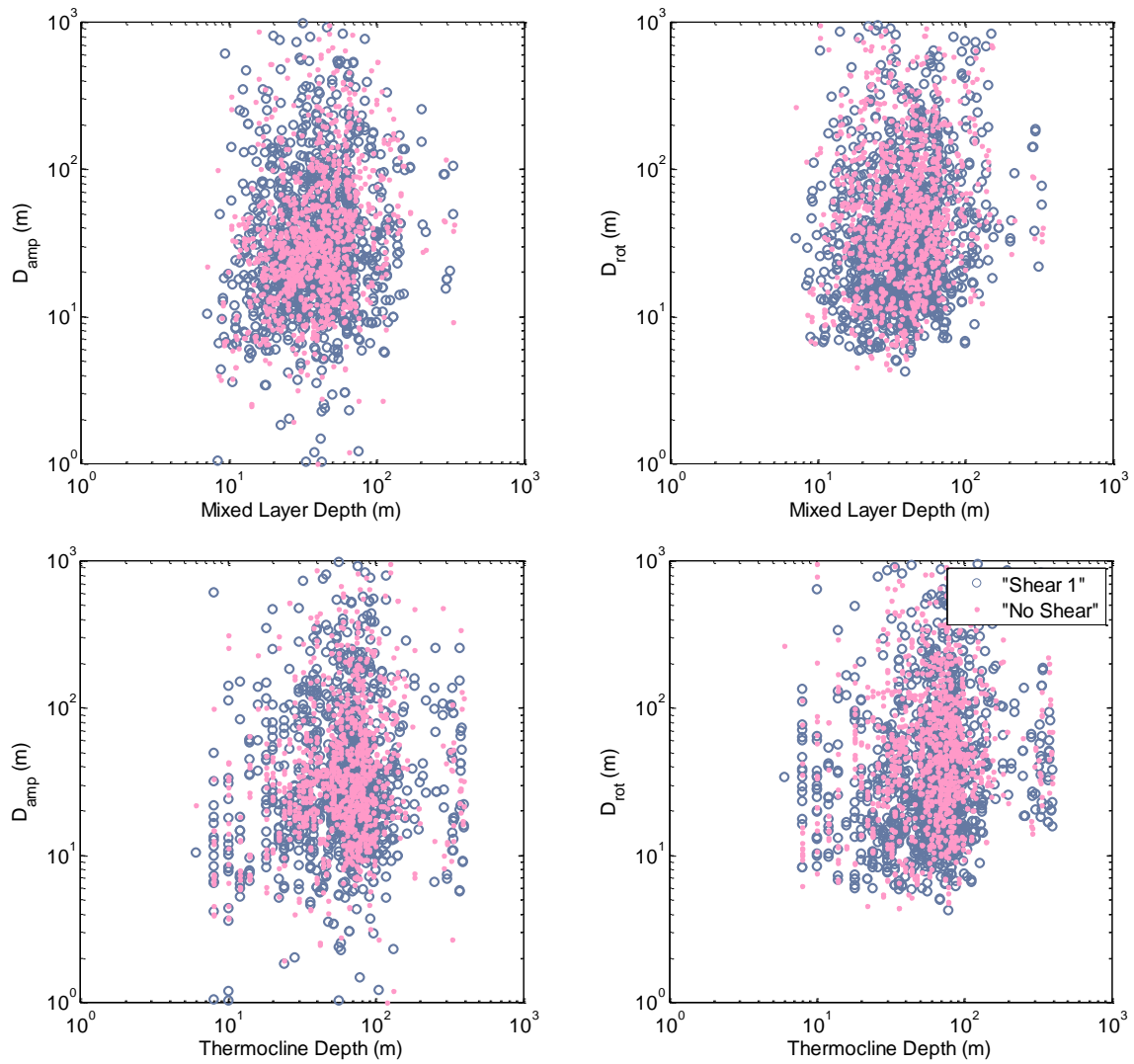


Figure A1.4: Ekman decay scales obtained from current amplitude (D_{amp}) and rotation (D_{rot}) for all EM-APEX profiles plotted as a function of mixed layer depth (top) and thermocline depth (bottom). Open grey-blue circles indicate values plotted for the “Shear 1” case; pale pink dots indicate values plotted for the “No Shear” case.

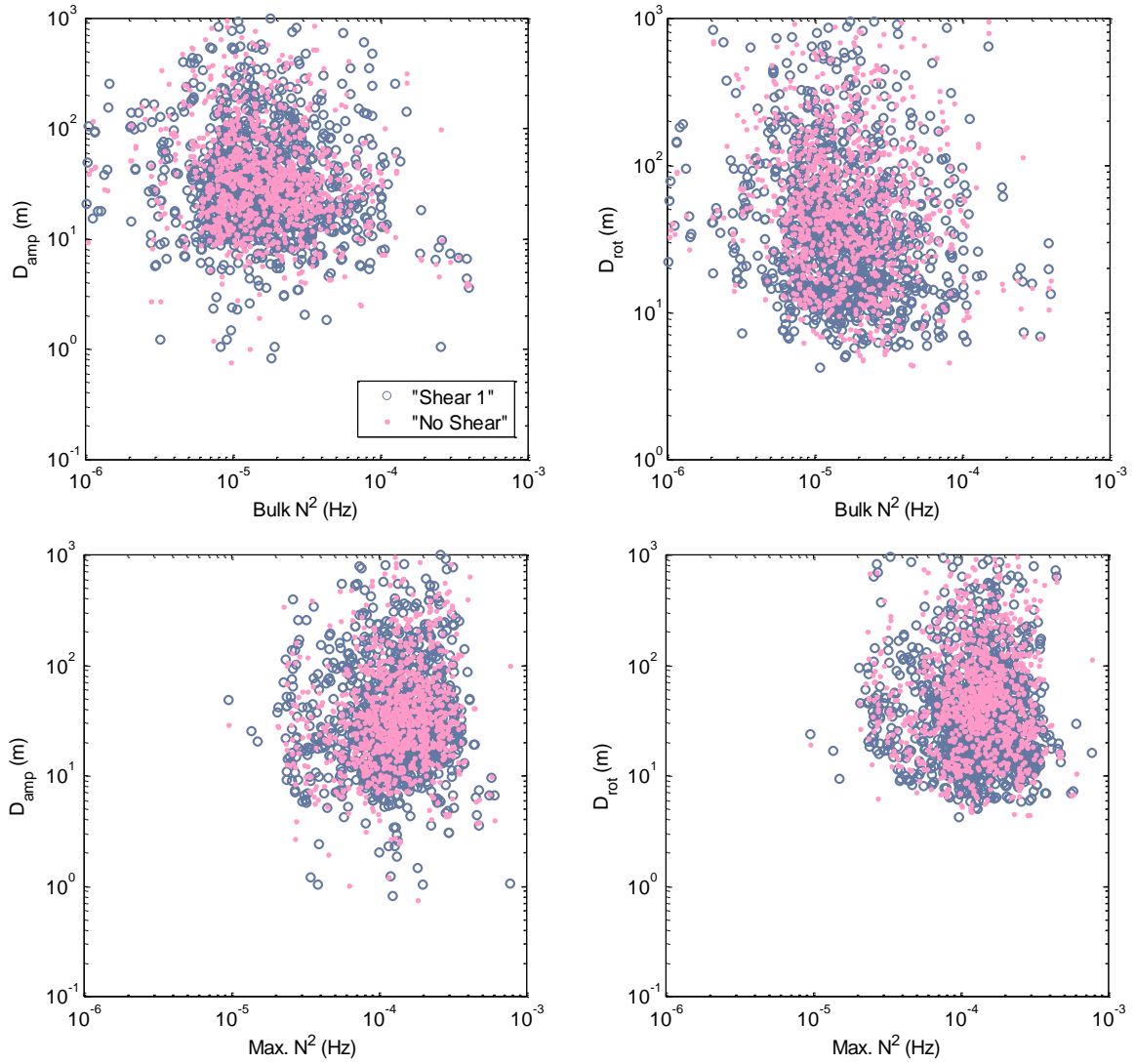


Figure A1.5: Ekman decay scales obtained from current amplitude (D_{amp}) and rotation (D_{rot}) for all EM-APEX profiles plotted as a function of the 'bulk' N^2 (top) and maximum N^2 (bottom). Open grey-blue circles indicate values plotted for the "Shear 1" case; pale pink dots indicate values plotted for the "No Shear" case.

Linear fits were applied to the data in Figure A1.4 and A1.5 using the Matlab polyfit function. Next, exponential fits were then applied to the data using the Matlab polyfit function to apply a linear fit between $\log_{10}(D_e)$ and the \log_{10} of each stratification parameter. Ekman decay scales expected from the fits to the stratification parameters were calculated. Finally, the correlation between the fitted and observed Ekman decay scales was obtained (Table A1.2).

With the exception of the exponential fit between the 'bulk' Richardson number (which produced relatively strong correlations) and Ekman decay scales estimated from current amplitude

all correlations were statistically significant but weak. This would tend to suggest, in line with Figure A1.4 and A1.5, that the Ekman decay scales estimated in Chapter 3 are not strongly influenced by stratification.

Correlation for linear fits				
	No Shear		Shear	
	D_{amp}	D_{rot}	D_{amp}	D_{rot}
Max. N² (Hz)	0.089	0.022	0.038	0.007
'Bulk' N² (Hz)	0.086	0.028	0.044	0.053
R_b	0.054	0.071	0.052	0.053
Thermocline Depth (m)	0.065	0.056	0.009	0.083
Mixed Layer Depth (m)	0.106	0.039	0.036	0.105
Correlations for Exponential Fits				
	No Shear		Shear	
	D_{amp}	D_{rot}	D_{amp}	D_{rot}
Max. N² (Hz)	0.130	0.012	0.048	0.047
'Bulk' N² (Hz)	0.165	0.119	0.101	0.175
R_b	0.584	0.172	0.478	0.193
Thermocline Depth (m)	0.181	0.158	0.121	0.159
Mixed Layer Depth (m)	0.246	0.100	0.133	0.161

Table A1.2: Correlations between the observed Ekman decay scales and Ekman decay scales obtained from linear or exponential fits to parameters measuring depth and strength of stratification including: maximum N²; the 'bulk' N² computed across the mixed layer; the bulk Richardson number; the depth of the thermocline and the depth of the mixed layer.

Another option for assessing the role of stratification depth and strength on Ekman decay scales would be to fit generalized linear models (Nelder and Wedderburn, 1972) to the observations; this would enable us to consider the effects of stratification strength and depth in parallel instead of in isolation (as above). We did not pursue this line of inquiry due to time constraints.

Appendix 2: Supplementary Figures For Chapter 5

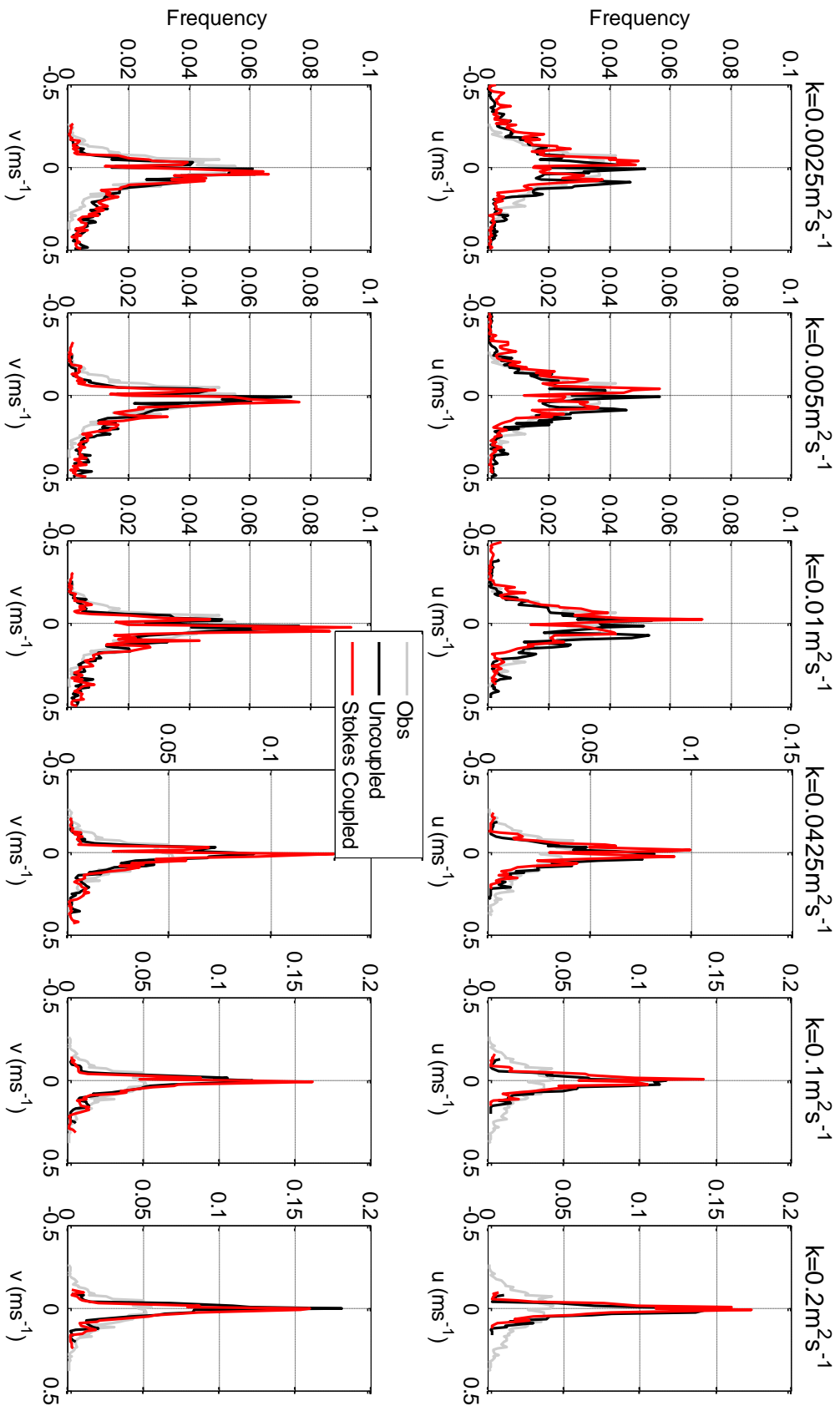


Figure A2.1: Shipboard 105m BLD Linear Ekman Model Probability Density Functions for viscosities between 0.0025 and 0.2m²s⁻¹. The grey curve shows the observed PDF while black and red curves mark the PDFs for the uncoupled and Stokes coupled Ekman models respectively.

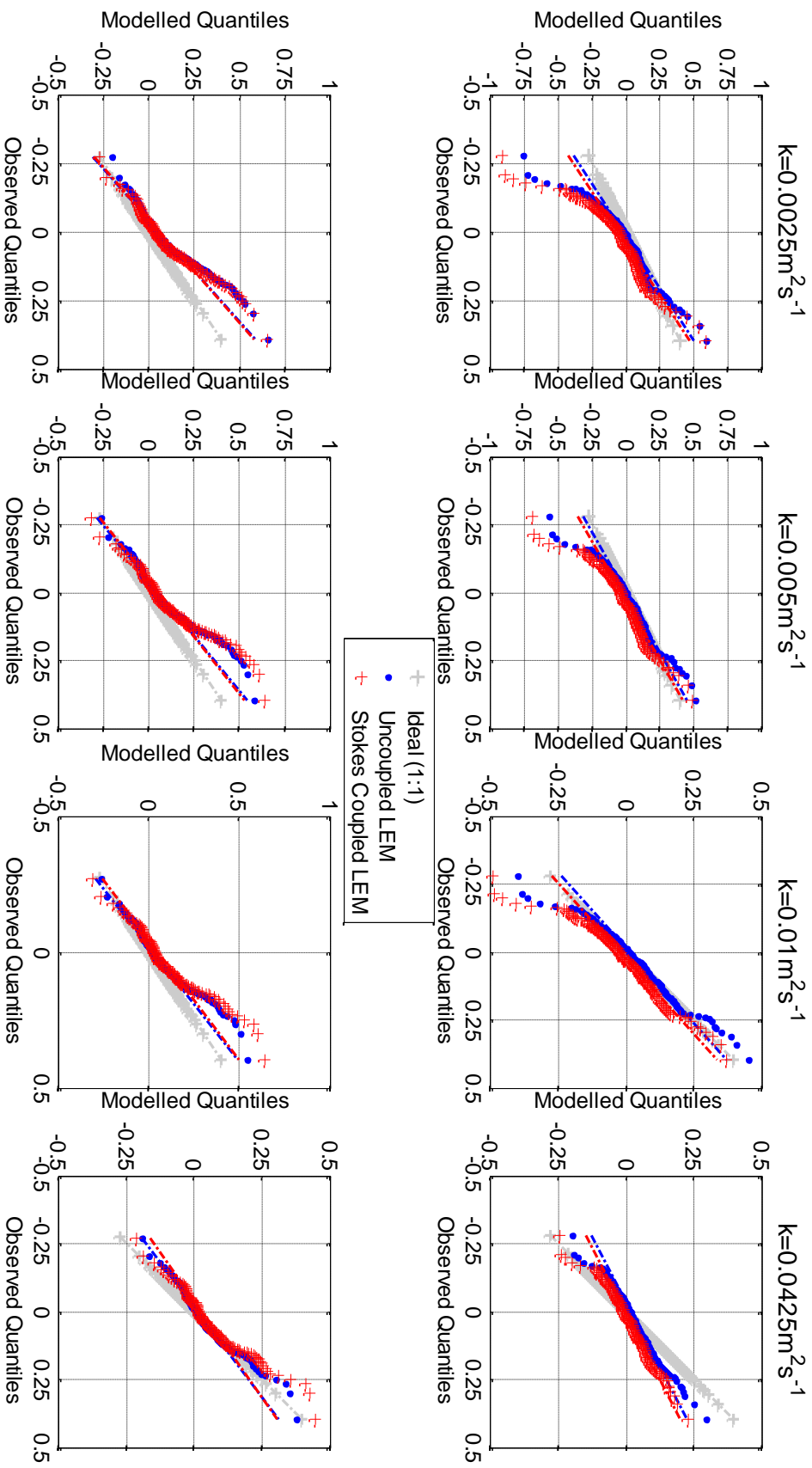


Figure A2.2: Shipboard 105m BLD Linear Ekman Model QQ plots of zonal (top) and meridional (bottom) velocities for viscosities between 0.0025 and 0.0425m²s⁻¹. Symbols indicate quantiles at 0.5% intervals; dashed lines are extrapolated from a linear fit to the 1st to 3rd quartiles of the data.

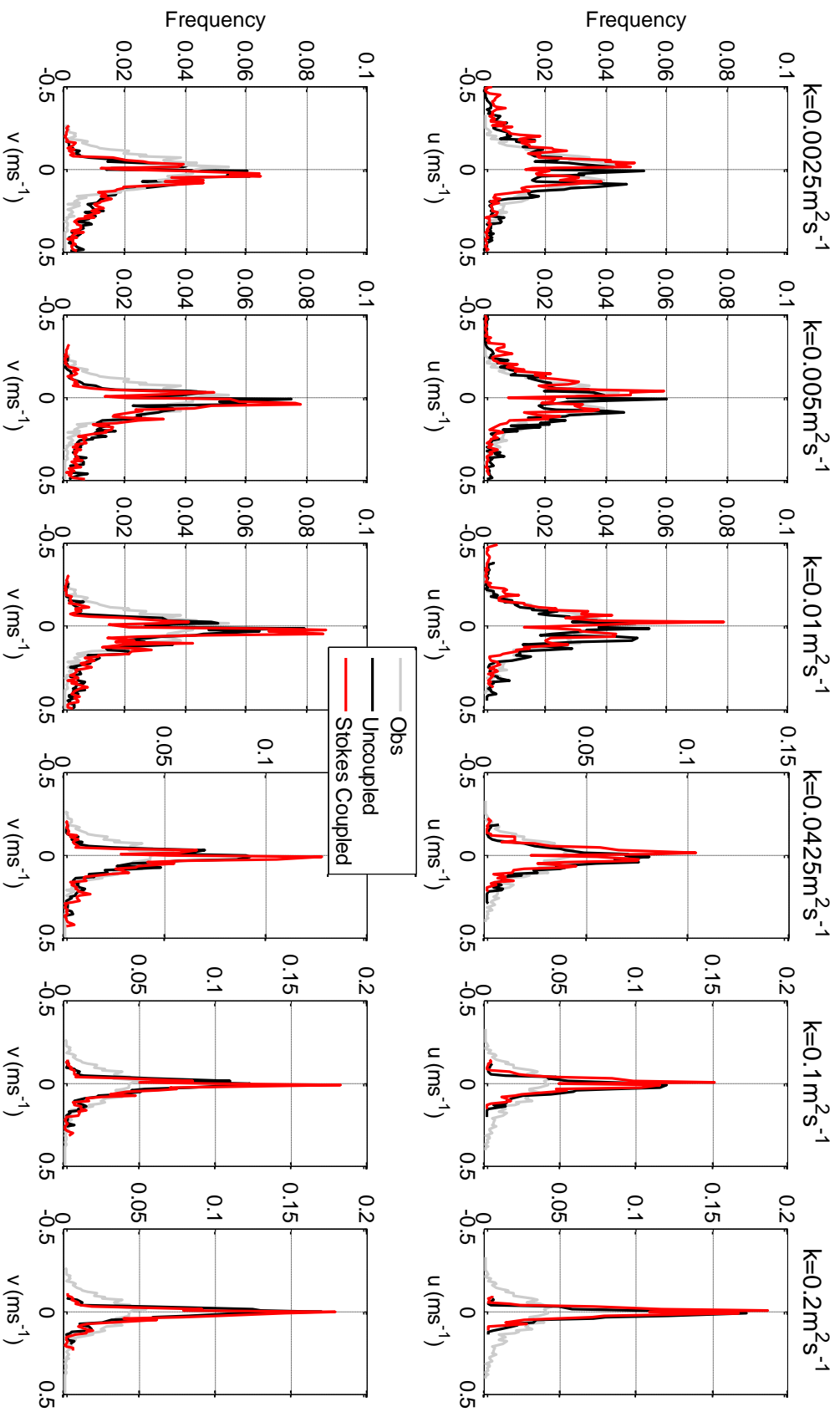


Figure A2.3: Shipboard 336m BLD Linear Ekman Model Probability Density Functions for viscosities between 0.0025 and $0.2\text{m}^2\text{s}^{-1}$. The grey curve shows the observed PDF while black and red curves mark the PDFs for the uncoupled and Stokes coupled Ekman models respectively.

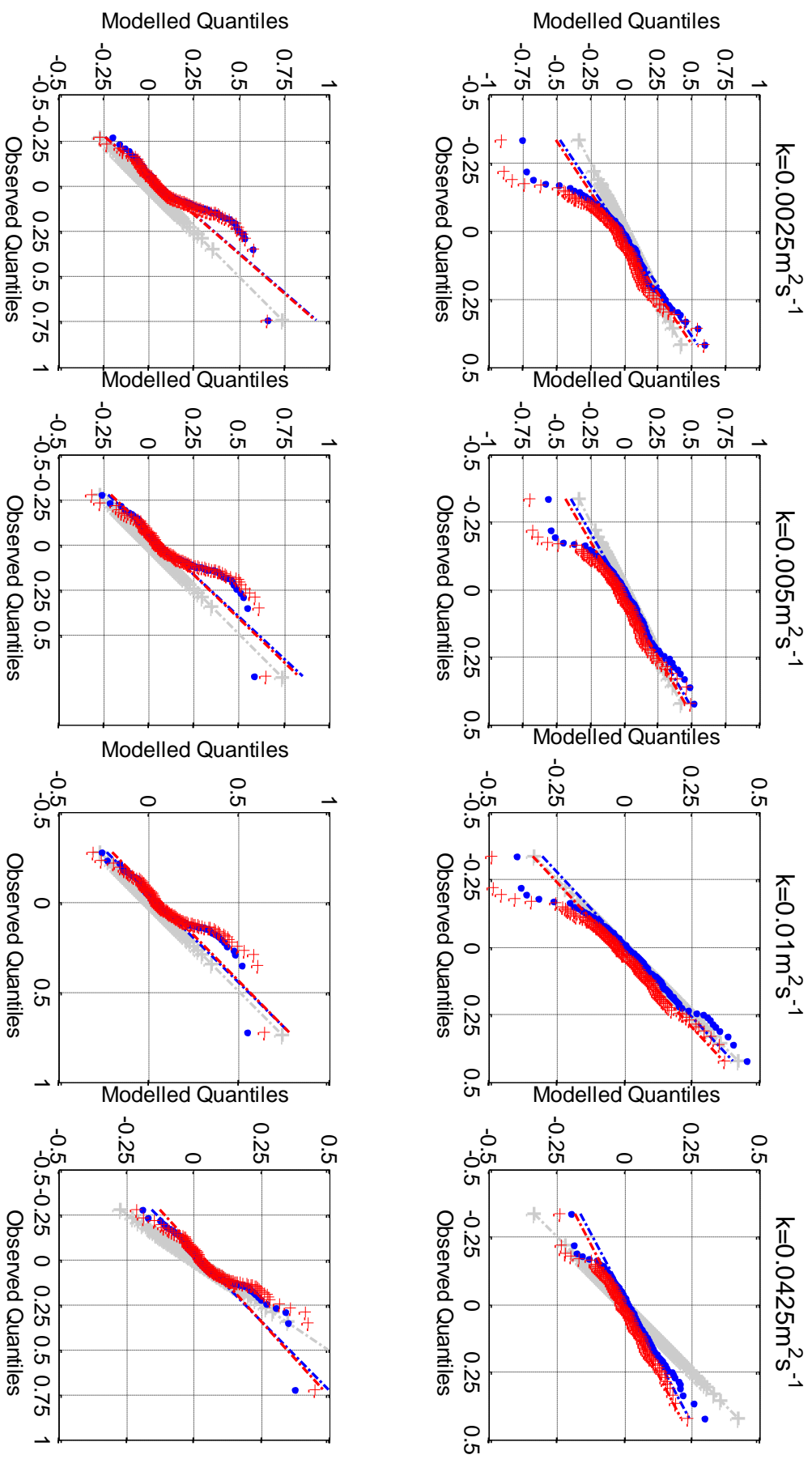


Figure A2.4: Shipboard 336m BLD Linear Ekman Model QQ plots of zonal (top) and meridional (bottom) velocities for viscosities between 0.0025 and 0.0425m²s⁻¹. Symbols indicate quantiles at 0.5% intervals; dashed lines are extrapolated from a linear fit to the 1st to 3rd quartiles of the data.

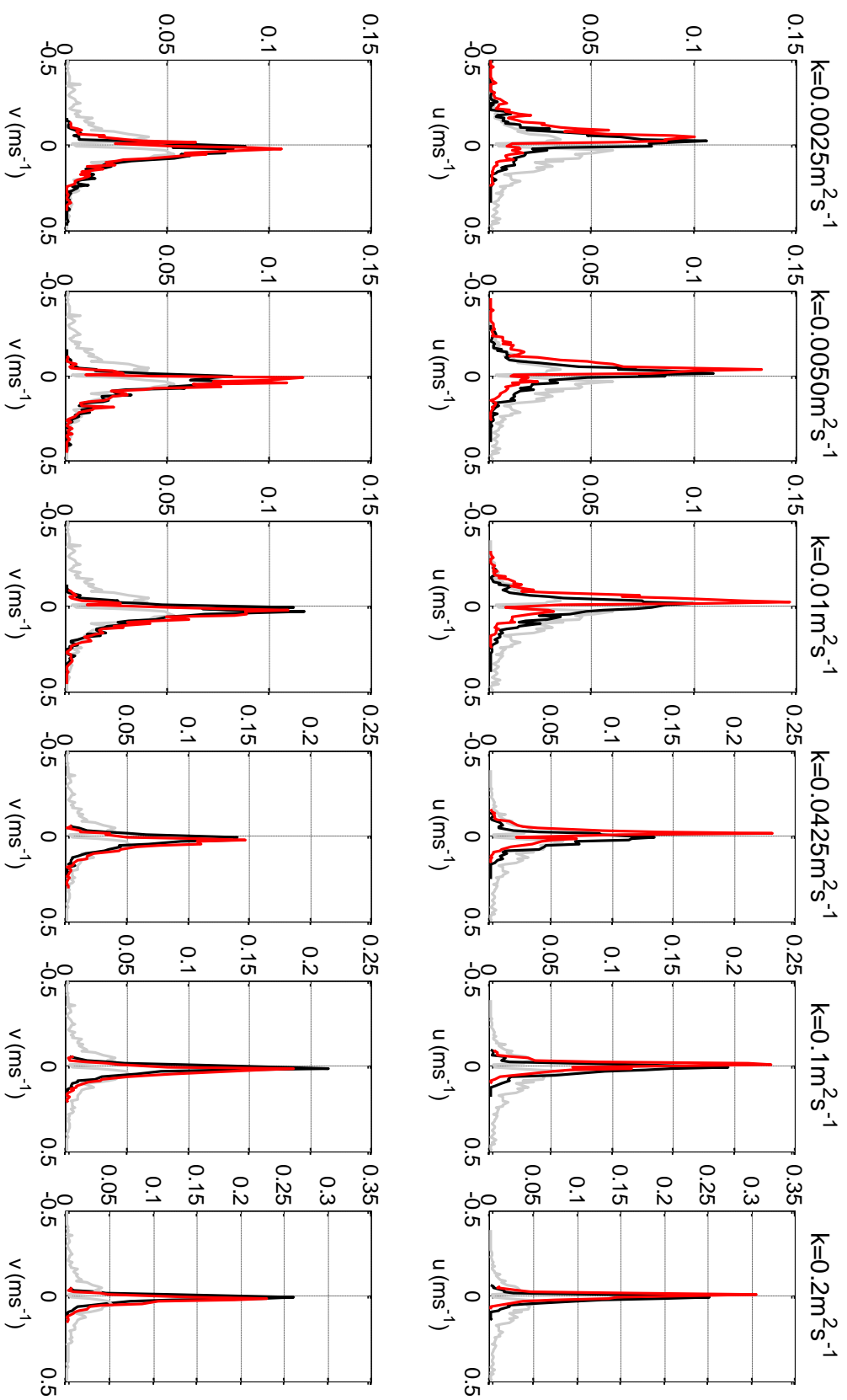


Figure A2.5: Float Infinite BLD Linear Ekman Model Probability Density Functions for viscosities between 0.0025 and $0.2\text{m}^2\text{s}^{-1}$. The grey curve shows the observed PDF while black and red curves mark the PDFs for the uncoupled and Stokes coupled Ekman models respectively.

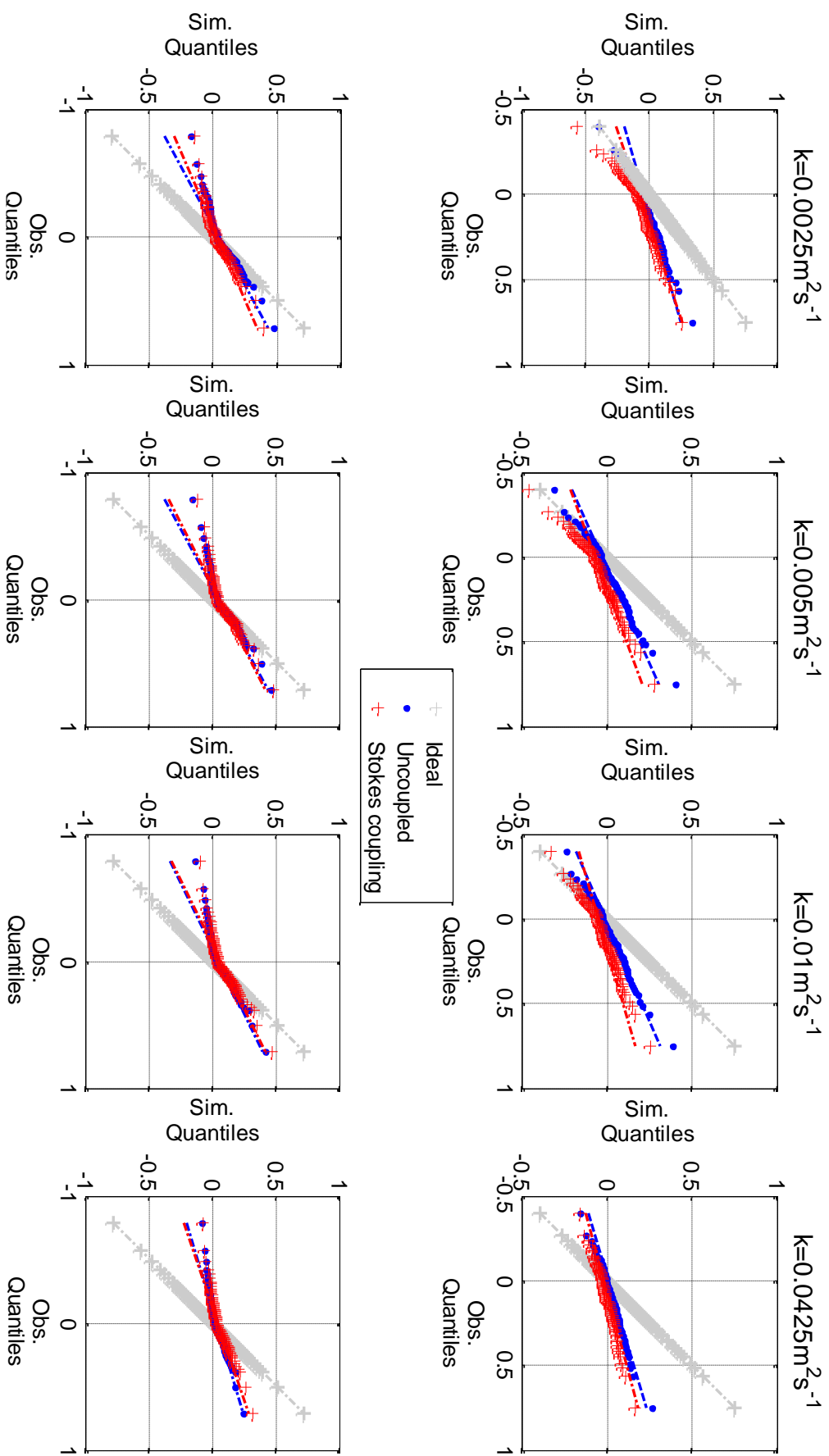


Figure A2.6: *Float Infinite BLD Linear Ekman Model* QQ plots of zonal (top) and meridional (bottom) velocities for viscosities between 0.0025 and $0.0425\text{m}^2\text{s}^{-1}$.

1. Symbols indicate quantiles at 0.5% intervals; dashed lines are extrapolated from a linear fit to the 1st to 3rd quartiles of the data.

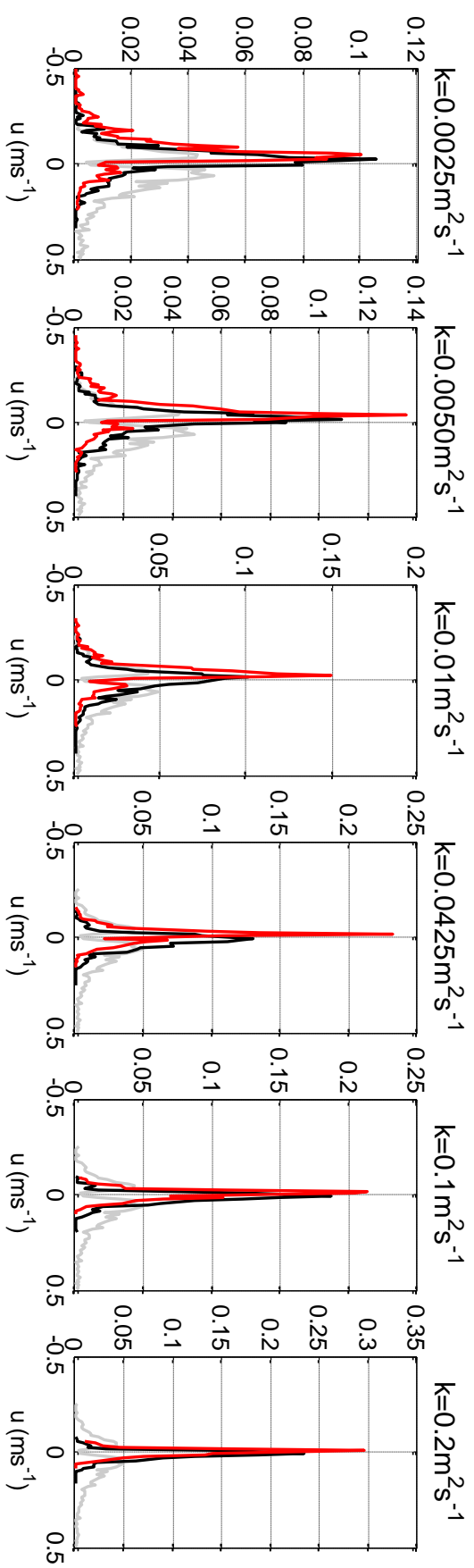


Figure A2.7: Float 105m BLD Linear Ekman Model Probability Density Functions for viscosities between 0.0025 and $0.2\text{m}^2\text{s}^{-1}$. The grey curve shows the observed PDF while black and red curves mark the PDFs for the uncoupled and Stokes coupled Ekman models respectively.

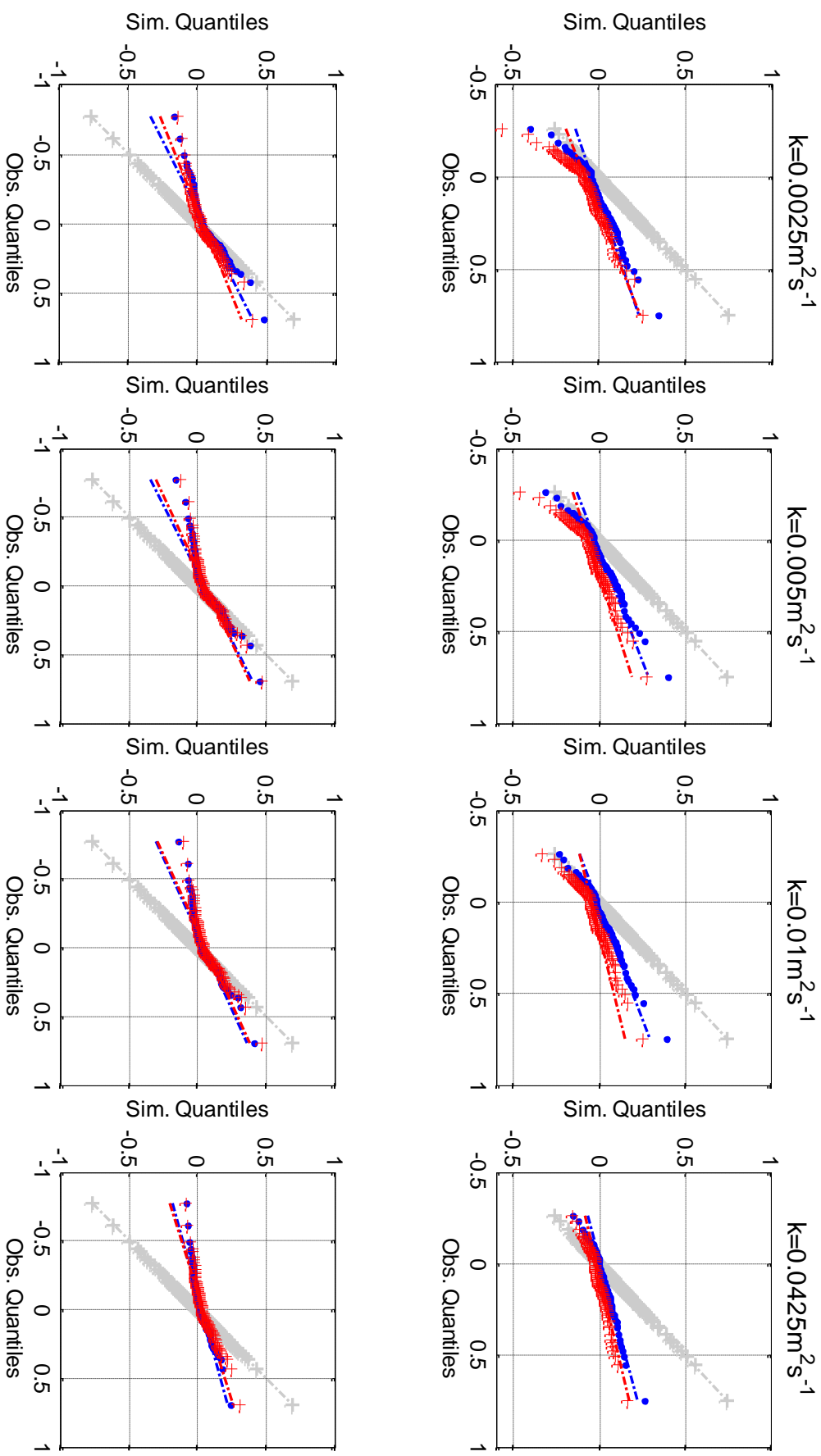


Figure A2.8: Float 105m BLD Linear Ekman Model QQ plots of zonal (top) and meridional (bottom) velocities for viscosities between 0.0025 and 0.0425m²s⁻¹. Symbols indicate quantiles at 0.5% intervals; dashed lines are extrapolated from a linear fit to the 1st to 3rd quantiles of the data.

